Université Paris-Sud
Discipline : Physique ED(517)
Laboratoire : SPP/IRFU CEA Saclay

Thèse de doctorat

Soutenue le 23 Septembre 2014 par

Eftychia-Sofia Protopapadaki

Mesure des dibosons ZZ avec le détecteur ATLAS auprès du LHC et étude des sondes du champ magnétique toroïdal

---

Composition du jury :

Di Ciaccio Lucia	Rapporteur
Laporte Jean-François	Directeur de thèse
Lavignac Stéphane	
Mikenberg George	
Perez Emmanuelle	Rapporteur
Zomer Fabian	Président du jury

University Paris Sud
Disipline : Physics ED(517)
Laboratory : SPP/IRFU CEA Saclay

Doctorat disertation

Defended on the 23 of Septembre 2014 by

Eftychia-Sofia Protopapadaki

ZZ diboson measurements with the ATLAS detector at the LHC and study of the toroidal magnetic field sensors

---

Committee:

Di Ciaccio Lucia	Referee
Laporte Jean-François	Thesis advisor
Lavignac Stéphane	
Mikenberg George	
Perez Emmanuelle	Referee
Zomer Fabian	Jury president

Abstract

Elementary particles and their interactions are described by the Standard Model. Even successful, there are still some unanswered questions which need to be addressed. In this work, the ZZ Standard Model process was studied in the leptonic decay channel. The data used were collected by the ATLAS detector during 2012 and correspond to an integrated luminosity of 20 fb^{-1}. The center of mass energy was 8 TeV. All the analysis elements, such as the signal selection and efficiencies, the background estimation, the measurement uncertainties and the statistical method employed for the cross section extraction, are discussed in this document. The total ZZ on-shell cross section is measured to be $6.98^{+0.42}_{-0.40}(stat.)^{+0.38}_{-0.33}(syst.)^{+0.20}_{-0.19}(lumi.)$pb. A measurement of the on-shell $ZZ \to \ell\ell\ell'\ell'$ "fiducial" cross section, defined in a volume close to the reconstructed one, was also performed. Both total and fiducial measurements are in agreement, within uncertainties, with the SM predictions. The neutral boson-self interactions are forbidden in the SM. Therefore, if triple gauge boson couplings are observed, they will indirectly point to the existence of new physics. Observables sensitive to the presence of anomalous triple gauge couplings, along with the optimal binning were investigated. The traverse momentum of the most energetic boson was among the most sensitive observables, and it was thus used in order to extract 95% CL limits on the anomalous coupling parameters. All observed limits are found to be compatible with the SM expectations.

In the framework of this thesis a performance study was conducted. In order to increase particles mass measurement precision, the accurate knowledge of the toroidal magnetic field inside the detector is essential. The sensors used for the production of the ATLAS toroidal magnetic field map were studied, and it was found that more than 97% of these sensors are reliable. The existing map was probed, and even though inaccuracies were observed, they are not expected to impact muon momentum estimation and thus not to bias the Higgs boson mass measurement.

Contents

Introduction

The most intriguing field of science has always been the one that seeks answers to fundamental questions related to the understanding of our universe. Among others, particle physics has its merit in the 20th century discoveries leading to the better understanding of the microcosm. Today, a solid theory describing the fundamental particles and their interactions exists, the Standard Model. For the investigation of the microcosm, particle accelerators had to be built that are capable to probe very tiny structures inside particles heart. Up to now, one of the milestones to this effort has been the Large Hadron Collider (LHC), which was recently built in the Geneva area, and has started operating in 2008. It collides protons against protons and achieves a center of mass energy of 8 TeV, with the future plans being 14 TeV in 2015. There are two multiple-purpose detectors, able to detect all types of physics that could be potentially seen at the LHC, ATLAS and CMS.

In this thesis two main studies have been conducted within the ATLAS collaboration. The first one was carried out during the first year of my thesis which started at the end of 2011. In this work, which served as my qualification task for the ATLAS collaboration, a general assessment of the ATLAS Toroidal magnetic field sensors was performed. The results of this study were documented in an ATLAS internal note [1]. In the present document, I will discuss the main results of this study.

Then, the last two years of the thesis were devoted exclusively to the main subject of my thesis, which is the study of the standard model $ZZ \to \ell\ell\ell'\ell'$ process. I joined the ZZ ATLAS group in October of 2012, and I keep collaborating with this group until today. We published a preliminary result on the ZZ cross section using the full 2012 dataset of 20 fb^{-1} at a center of mass energy of 8 TeV, at the Moriond 2013 conference [2] [3]. For this analysis I contributed to the determination of part of the measurement inputs, to the data/MC comparison and to the cross sections extraction both for individual Z decay channels and for the combination of these channels, being actually in charge of the edition of the section on the cross sections determination of the ATLAS publication. Even though I had a significant

contribution, this result was preliminary and thus it will not be presented in this document. Here, I will focus only on the extended analysis conducted from mid-2013 until today, which also includes limits on the anomalous triple gauge couplings. The publication procedure for this updated study is still ongoing. A description of the manuscript content follows.

The first two chapters are introductory and form a background for the next chapters. More specifically, in chapter 1, some theoretical aspects of the ZZ process are discussed, and the status of the experimental measurements at the beginning of my thesis is presented. Then, in chapter 2, the LHC and ATLAS detector are described.

Chapter 3 is dedicated to the study I realised on the ATLAS magnetic field sensors. All the content of this chapter is the product of my own work[1].

The last three chapters present the study of $ZZ \to \ell\ell\ell'\ell'$ process. First, in chapter 4 a general description of the analysis is made. Issues such as the cross section definition, the muon and the electron reconstructions, the main background sources, along with the basic concepts of the object and event selection are presented. In chapter 5 all the elements that have been discussed in ch. 4 become quantitative, and the ZZ cross section is extracted. Finally, chapter 6 is dedicated to the extraction of limits on the anomalous triple gauge couplings. All of the results of chapters 5 and 6 have been the product of my own work, excepted some inputs from colleagues, to which reference will be made explicitly.

[1] Work performed under the supervision of L. Chevalier, J-F. Laporte and A. Formica

Chapter 1

Theory aspects of the ZZ production

1.1 The Standard model of particle physics

The standard model (SM) of particle physics describes the properties and interactions of the elementary particles [4] [5] [6]. It is a relativistic quantum field theory that satisfies the local $SU(3)\text{x}SU(2)\text{x}U(1)$ gauge symmetry. The SM was established in the second half of the 20th century by A. Salam, S. Glashow and S. Weinberg. So far, all the particles included in the SM have been discovered.

There are two types of elementary particles incorporated in the SM: the fermions and the bosons. Fermions are matter particles that have a half-integer spin. In figure 1.1, the fermion masses and electric charges are shown. There are two subgroups of fermions, the leptons and the quarks. Leptons come in two types: the electrically charged particles (e, μ, τ) and the neutral particles, the neutrinos (ν_e, ν_μ, ν_τ). Quarks are massive particles which have electrical and color charge and they are six in total (u, d, c, s, t, b). The fermions are organized in three families of increasing mass. The matter particles, besides the well known electric charge Q, can carry weak charge or color charge. These charges are responsible for the particle interactions. Four types of fundamental forces exist with three of them being incorporated in the SM. These forces are mediated by paricles having integer spin which are represented by vector fields, and they are called bosons. The three SM fundamental forces are the electromagnetic the weak and the strong force. The electromagnetic force is related to the electric charge and hence involves all charged particles. The photon is the massless electromagnetic force carrier. The weak force is related to the weak isospin and its carriers are the W^+, W^- and Z bosons. Finally, the strong interaction is the one keeping quarks together and it is due to the quark color charge. The strong force is mediated by eight massless gluons.

The standard model of particle physics is described by an elaborated mathe-

Leptons spin = 1/2		
Flavor	Mass GeV/c^2	Electric charge
ν_e electron neutrino	$<1\times10^{-8}$	0
e electron	0.000511	−1
ν_μ muon neutrino	<0.0002	0
μ muon	0.106	−1
ν_τ tau neutrino	<0.02	0
τ tau	1.7771	−1

Quarks spin = 1/2		
Flavor	Approx. Mass GeV/c^2	Electric charge
u up	0.003	2/3
d down	0.006	−1/3
c charm	1.3	2/3
s strange	0.1	−1/3
t top	175	2/3
b bottom	4.3	−1/3

Figure 1.1: Fermion generations.

matical framework. In the following sections only the parts of the standard model closely related to the diboson ZZ production are discussed.

1.1.1 The local gauge symmetry requirement

In order to understand the origin of particle interactions and the emergence of vector fields that mediate them, the gauge symmetries are discussed in this sub-section. The Quantum Electrodynamic (QED) is taken as an example.

A very important theorem used in particle physics is Norther's theorem. According to this theorem, invariance under a transformation implies the existence of a conserved quantity. This motivates the requirement that the free field Lagrangian is invariant under gauge transformations. Particle interactions, and thus the mediator gauge bosons, arise after applying the requirement of a local gauge transformation to the Lagrangian describing a free fermion field:

$$L = i\bar{\Psi}\gamma_\mu\partial^\mu\Psi - m\bar{\Psi}\Psi \tag{1.1}$$

The simplest case is the U(1) phase transformation $\Psi(x) \rightarrow e^{i\alpha(x)}\Psi(x)$, where α depends on space time, x. This transformation is related to the electric charge Q and thus to the electromagnetic interactions. In order to maintain the Lagrangian invariance under the above local transformation, a modified derivative D_μ must be introduced. By considering $D_\mu = \partial_\mu - ieA_\mu$, where A_μ is a vector field, a new term appears in the Lagrangian $e\bar{\Psi}\gamma^\mu\Psi A_\mu$. This new term represents the interaction between the fermion current density $j^\mu = -e\bar{\Psi}\gamma^\mu\Psi$ and a vector field A_μ. The A_μ corresponds to the photon, which is the force carrier of the electromagnetic

interactions. An additional gauge invariant term that accounts for the photon kinetic energy should be added in the Lagrangian, $-\frac{1}{4}F_{\mu v}F^{\mu v}$, where $F_{\mu v} = \partial_\mu A_v - \partial_v A_\mu$.

To summarize, the complete QED Lagrangian is:

$$L = i\bar{\Psi}\gamma_\mu\partial^\mu\Psi - m\bar{\Psi}\Psi + e\bar{\Psi}\gamma^\mu A_\mu\Psi - \frac{1}{4}F_{\mu v}F^{\mu v} \tag{1.2}$$

No mass term for the photon field is allowed since it would destroy the Lagrangian invariance under the local U(1) phase transformation. This is also the case for all boson fields emerging after a local symmetry requirement such as $SU(2)$ and $SU(3)$: the mass term of the boson fields would destroy the Lagrangian invariance. Even though in the photon case this is not a problem, as it will be discussed in the following section, the absence of mass term for the $W^\pm$ and Z bosons was for many years an important issue for particle physics. The problem was solved by the Brout-Englert-Higgs mechanism [7] [8] [9].

1.1.2 Weak and Electroweak interactions

The Weak interactions were introduced by Fermi to explain the beta decay [10]. In the Fermi theory, they were considered as contact charged current interactions, which have the same current-current structure as the electromagnetic interactions. However, the weak coupling constant G is not massless, as it has dimension of $mass^{-2}$. Later on, experimental data on beta transitions of polarized ^{60}C have shown that weak interactions violate the Parity symmetry, P [11]. In the process under examination $^{60}C \rightarrow^{60} Ni^* + e^- + \bar{\nu}_e$, only left-handed electrons and right-handed antineutrinos were observed. The Fermi theory had to be modified to violate P. Finally, in order to obtain a maximum parity violation, an Axial Vector (P-violating) component had to be included in the mathematical formalism describing the weak interactions. This is why charged weak interactions are called V-A (Vector - Axial vector) interactions.

The existence of neutral weak currents, such as the $\nu q \rightarrow \nu q$ scattering, have been also observed. Contrary to charged weak currents, neutral currents do not have a pure V-A structure, since in addition to the left-handed, they do have as well a right-handed component. However, the right-handed contribution is significantly lower than the left handed.

The fact that the coupling constant in the Fermi theory is not dimensionless, was an indication that there should be a propagator (boson) mediating the weak force. Moreover, the observed lifetime of the weak decays, which is significantly larger than the strong and electromagnetic interactions, was an evidence that if the

weak interaction propagators exist they should be massive.

One step further, there was the aim to combine electromagnetic interactions with the weak interactions under the same mathematical framework. The procedure followed by S. Glashow, S. Weinberg and A. Salam is the same as the one used for the QED formulation. For the electroweak interactions the required local symmetries to be respected are the weak isospin $SU(2)_L$ and the weak hypercharge $U(1)_Y$ with generators $\mathbf{T}$ and Y, respectively. By applying these symmetries, four massless vector fields emerge: a triplet of spin 1 fields $\boldsymbol{W_\mu} = \{W^1_\mu, W^2_\mu, W^3_\mu\}$ and a singlet B_μ, associated to the $SU(2)_L$ and $U(1)_Y$ gauge symmetries, respectively. The generators T^3 and Y must satisfy $Q = T^3 + \frac{Y}{2}$, where Q is the generator of the U(1) gauge symmetry (QED). The above requirement implies a combination of the W^3_μ with B_μ in order to get the photon field A_μ and the neutral weak boson Z. The relation between the neutral fields is:

$$\begin{pmatrix} \gamma \\ Z \end{pmatrix} = \begin{pmatrix} cos\theta_w & sin\theta_w \\ -sin\theta_w & cos\theta_w \end{pmatrix} \begin{pmatrix} B_\mu \\ W^3_\mu \end{pmatrix} \tag{1.3}$$

where θ_w is the weak mixing angle. The charged electroweak bosons are:

$$W^\pm = \frac{1}{\sqrt{2}}(W^1_\mu \mp W^2_\mu) \tag{1.4}$$

The electroweak Lagrangian is:

$$\begin{aligned} L_{EWK} \; = \; & -\frac{1}{4}\boldsymbol{W_{\mu v}} \cdot \boldsymbol{W^{\mu v}} \; - \; \frac{1}{4} B_{\mu v} \cdot B^{\mu v} \\ & + \bar{L}\gamma^\mu (i\partial_\mu - g\frac{1}{2}\boldsymbol{\tau}\boldsymbol{W_\mu} - g^{'}\frac{Y}{2}B_\mu)L \\ & + \bar{R}\gamma^\mu (i\partial_\mu - g^{'}\frac{Y}{2}B_\mu)R \end{aligned} \tag{1.5}$$

where g and $g^{'}$ are the U(1) and SU(2) couplings, respectively, and $\boldsymbol{\tau}$ denotes the Pauli matrix vector. The $W^i_{\mu v}$ and $B_{\mu v}$ are the field strength tensors:

$$\begin{aligned} W^i_{\mu v} &= \partial_\mu W^i_v - \partial_v W^i_\mu + g\epsilon_{ijk} W^j_\mu W^k_v \\ B_{\mu v} &= \partial_\mu B_v - \partial_v B_\mu \end{aligned} \tag{1.6}$$

where ϵ_{ijk} is the SU(2) structure constant. The last term in the $\boldsymbol{W_{\mu v}}$ is due to the non-Abelian structure of the SU(2) gauge symmetry which gives rise to the self coupling of the W bosons, see sec. 1.1.3.

The first two terms in eq. 1.5 account for the kinetic energies and the self inter-

actions of the electroweak bosons. The third term contains the left-handed lepton kinetic energies and their couplings to the bosons. The fourth term represents right-handed lepton kinetic energies and their couplings to the γ and Z bosons. As already discussed, because of the V-A structure of the charged electroweak currents, no coupling of the right-handed leptons to the $W^{\pm}$ bosons appears in the Lagrangian. Moreover, no fermion mass term of the form $m(\bar{L}R+\bar{R}L)$ appears in the Lagrangian either. This is due to the different behavior of the L and R component of the fermion fields under the requirement of the local $SU(2)_L$x$U(1)_Y$ gauge symmetry. Furthermore, as mentioned above, there were evidences for massive gauge bosons due to the significantly longer lifetime of the weak interactions. However, no mass terms for the bosons $W^{\pm}$ and Z appear in the Lagrangian either.

Spontaneous Symmetry Breaking (SSB)

The mass problem was solved in the 1960s by R.Brout, F.Englert and P.Higgs who proposed independently the existence of a new scalar field ϕ. The characteristics of the new scalar field were such that mass can be given to both fermions and bosons via the "spontaneous" symmetry breaking mechanism. The spontaneous symmetry breaking occurs when the Lagrangian describing a system is invariant under a transformation, while the minimum energy state is not. The Lagrangian describing the new scalar field is written as:

$$L_{\phi} = D^{\bar{\mu}}\phi D_{\mu}\phi + m^2|\phi|^2 - \lambda|\phi|^4 \tag{1.7}$$

where D^{μ} is the $SU(2)_L$x$U(1)_Y$ covariant derivative $D^{\mu} = i\partial_{\mu} - g\frac{1}{2}\boldsymbol{\tau}\boldsymbol{W_{\mu}} - g^{'}\frac{Y}{2}B_{\mu}$, and $-m^2|\phi|^2 + \lambda|\phi|^4$ is the potential $V(\phi)$, with m being a term representing the field mass, and λ the scalar field self-coupling constant.

The structure of the complex scalar field to be introduced so that the Lagrangian remains invariant under $SU(2)_L$x$U(1)_Y$ is a isospin doublet with a weak hypercharge Y=1:

$$\phi = \begin{pmatrix} \phi^+ \\ \phi^0 \end{pmatrix} = \frac{1}{\sqrt{2}} \begin{pmatrix} \phi_1 + i\phi_2 \\ \phi_3 + i\phi_4 \end{pmatrix} \tag{1.8}$$

where ϕ_i (i=1,2,3,4) are real scalar fields.

The potential minimum, which is called vacuum, satisfies the condition $|\phi|^2 = \frac{m^2}{2\lambda}$. The choice of the vacuum is driven by the need for a non invariant vacuum state under $SU(2)_L$x$U(1)_Y$ gauge symmetry. This results in a symmetry breaking. The selected vacuum is $\phi_1^2 = \phi_2^2 = \phi_4^2 = 0$ and $\phi_3^2 = -\frac{\mu^2}{\lambda} = v^2$. This specific vacuum is invariant under $U(1)_{em}$ since $Q = T^3 + \frac{Y}{2} = 0$, and thus it keeps the photon

massless, while it gives masses to the other vector bosons. Lastly, the suitable form of the scalar field is:

$$\phi(x) = \frac{e^{i\boldsymbol{\tau\theta(x)}}}{\sqrt{2}} \begin{pmatrix} 0 \\ v + H(x) \end{pmatrix} \tag{1.9}$$

where θ are three real massless fields (Goldstone bosons). The Higgs field $H(x)$ arises from quantum fluctuations around the minimum. When eq. 1.9 is plugged into the complete Lagrangian, these fluctuations will generate the appropriate mass terms. For the Higgs field $H(x)$, a mass term directly appears, while the gauge fields W^i become massive after "absorbing" the Goldstone bosons.

The relevant equations expressing the masses of the $W^{\mp}$ and Z bosons as a function of the coupling constants $g^{'}$, g and the v, are the following:

$$M_Z = \frac{1}{2} v \sqrt{g^2 + g'^2}\,, \;\; M_W = \frac{1}{2} v g \tag{1.10}$$

$$\frac{M_W}{M_Z} = cos\theta_w \tag{1.11}$$

The mass of the W boson has been precisely measured at LEP [12] and Tevatron [13] and the combined results are found to be 80.385±0.015 GeV [14]. The mass of the Z boson, estimated using LEP data, is 91.1876±0.0021 GeV [15].

1.1.3 Triple Gauge Couplings (TGCs)

A very interesting SM feature are the Triple Gauge Couplings. The non-Abelian structure of the $SU(2)_L$ gauge symmetry is responsible for the gauge boson self-interactions because of the $g\epsilon_{ijk}W^j_\mu W^k_v$ term appearing in the eq. 1.6. This term allows self-interactions only between different types of bosons. If there are identical bosons the Levi-Civita symbol ϵ_{ijk}, which is the $SU(2)$ structure constant, is equal to zero. Therefore, the SM allows at tree level only the self-interaction of the charged gauge bosons, which gives rise to vertices of the type $W^+W^-Z(\gamma)$. Neutral triple gauge boson vertices are forbidden in the SM and thus no $Z(\gamma)ZZ(\gamma)$ vertex exists at tree level. Any deviations from these SM predictions can be a sign of new physics.

1.2 Neutral anomalous couplings (nTGCs)

Even though the Standard Model has been a big success of elementary particles physics, especially with the Higgs boson discovery, there are still some remaining questions to answer. In this section, an indirect way to probe new physics is discussed.

1.2.1 Missing pieces of the Standard Model

The remaining questions concerning the SM could be split in two categories, which actually are the two sides of the same coin. From one hand there are experimental observations that can not be explained by the SM, and from the other hand, the theory seem to not be fundamental because of its features, added in an ad hoc way. The most important experimental issues indicating the SM insufficiency are the following:

- Astrophysics and cosmology issues, such as dark matter and energy or inflation that can not be explained by the SM
- Baryon - antibaryon asymmetry, i.e why there is more matter than anti-matter in the universe
- Gravity is not incorporated in the SM.

At theory level, there are serious doubts that the SM is a fundamental theory. Why, for instance, nature would choose to be so complicated having 19 free parameters and coping with problems such as renormalization? Among the most important theory issues are the following:

- There are up to 25 free parameters in the SM if one also includes those related to the representation of neutrino masses. Their values are not predicted by the theory and therefore have to be measured experimentally. A theory having so many parameters does not seem fundamental.
- The scale difference encountered in particle physics is known as the Hierarchy problem. For instance, a significant scale differences exists between the Higgs and the Plank mass.

In order to address the above questions, several alternative theoretical models have been developed over the last decades. Some of these theories are Supersymmetry, Technicolor, extra dimensions and grand unified theories (GUT) [16] [17].

So far, no inconsistencies with the SM predictions have been seen at the LHC. Nonetheless, it is expected that new physics should be around the corner and hence experimentalists continue searching for a sign.

1.2.2 How to probe new physics

The majority of the new physics models predicts heavy new particles and modified interactions between the SM particles. There are two ways to search for new physics of this kind. The first way is to directly search for new particles by looking for unexpected resonances. However, if the available energy in the center of mass is not enough to produce these heavy particles or if their cross section is too small, this method will not show any positive results. The second way is to probe these scenarios indirectly by searching for effects beyond the Standard Model [18]. Deviations on branching ratio values or production rates, will indicate that the couplings between the SM particles are not in agreement with the predictions. Hence, this would be an indirect evidence in favor of new physics.

An example of indirect manifestation of new physics that predicts heavy fermions is the following. Even though the heavy fermions can not be directly produced at the LHC energies, they can appear inside virtual fermion loops. Such loops could result in an enhancement of the SM cross sections. A thorough method to investigate the above scenario is to perform a precision measurement of the Triple Gauge Couplings. As already discussed, the SM forbids at tree level the neutral vertex $Z(\gamma)ZZ(\gamma)$ (s-channel). However, this vertex can be observed if heavy particle loops intervenes, see fig 1.2. These fermion loops at low energy ($m_f >> s$) appear as point-like interactions.

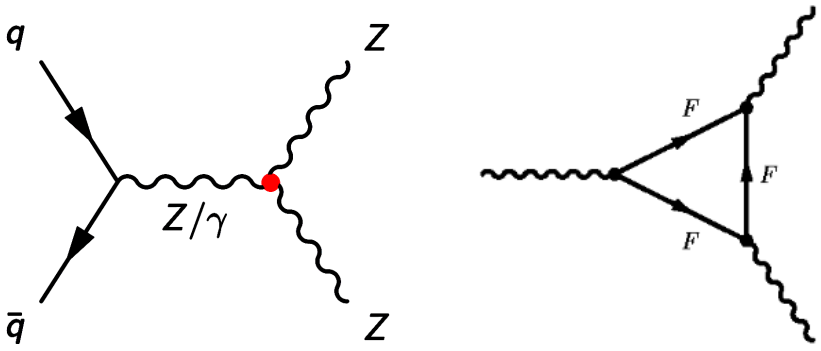

Figure 1.2: Left: Feynman diagram for $q\bar{q} \rightarrow ZZ$ production via the s-channel. Right: triangular fermion loop.

Whatever the new physics is, it can be described with a model independent effective Lagrangian:

$$L_{eff} = L_{SM} + L_{beyond} \tag{1.12}$$

There are two approaches used in order to construct the effective Lagrangian, L_{beyond}. In the following sections these approaches are discussed.

1.2.3 Anomalous couplings approach

The anomalous couplings approach is the one that has been used so far in all diboson analyses within the ATLAS experiment.

The most general way to write a Lagrangian describing the neutral anomalous triple gauge couplings (aTGCs) is by considering all Lorentz and $U(1)_{em}$ invariant terms [19] [20]. There is an infinite number of such terms if higher order derivatives are considered. In the literature only the terms with the lowest number of derivatives (lowest-order) are considered. It can be shown that the Bose statistics and the Gauge Invariance condition in the case V=γ, lead to vanishing vertices if all three bosons are on-shell [1]. As a result of the above requirements the effective Lagrangian for the on-shell ZZ final state is the following:

$$\mathcal{L}_{VZZ} = -\frac{e}{M_Z^2}\left[f_4^V(\partial_\mu V^{\mu\beta})Z_\alpha(\partial^\alpha Z_\beta) + f_5^V(\partial^\sigma V_{\sigma\mu})\tilde{Z^{\mu\beta}}Z_\beta\right] \tag{1.13}$$

where $V = Z, \gamma$ will hereafter denote off-shell Z or γ bosons. There are four f_i^V couplings for the ZZ final state. The couplings f_4^V are CP-violating while the f_5^V are CP-conserving. It should be noted, that no interference terms between the CP-violating couplings and the standard model will be included in the square matrix element needed for the cross section calculation.

There are two insufficiencies in the anomalous couplings approach. The first one is that the Lagrangian contains only the lowest order terms, and the second one is that unitarity violation occurs when computing tree level amplitudes. These two issues were partially solved by working in the momentum space analog to the position space Lagrangian. This is the vertex function framework. The VZZ neutral aTGC vertices can be written as:

[1] This is in contrast to a ZZZ' vertex, studied for example in [21], for which no symmetry prevents all bosons to be on-shell.

$$ie\Gamma^{\alpha,\beta,\mu}_{ZZV}(q_1,q_2,q_3) = \frac{-e(q_3^2-m_V^2)}{M_z^2}[f_4^V(q_3^\alpha g^{\mu\beta}+q_3^\beta g^{\mu\alpha}) - f_5^V\epsilon^{\mu\alpha\beta\rho}(q_1-q_2)_\rho] \quad (1.14)$$

and the neutral $VZ\gamma$

$$ie\Gamma^{\alpha,\beta,\mu}_{Z\gamma V}(q_1,q_2,q_3) = \frac{-e(q_3^2-m_V^2)}{M_z^2}\{h_1^V(q_2^\mu g^{\alpha\beta}-q_2^\alpha g^{\mu\beta}) - \frac{h_2^V}{M_Z^2}q_3^\alpha[(q_3q_2)g^{\mu\beta}-q_2^\mu q_3^\beta] \\ -h_3^V\epsilon^{\mu\alpha\beta\rho}q_{2\rho} - \frac{h_4^V}{M_Z^2}q_3^\alpha\epsilon^{\mu\beta\rho\sigma}q_{3\rho}q_{2\sigma}\} \quad (1.15)$$

where the f_i^V and h_i^V terms are no more constants but functions of the boson momenta. There are eight h_i^V couplings for the $Z\gamma$ final state. The h_1^V and h_2^V are CP-violating while the h_3^V and h_4^V are CP-conserving.

Unitarity issue

In order to overcome the unitarity violation issue the anomalous couplings are considered as decreasing functions of the momentum. This is achieved by introducing an arbitrary form factor [22]. The "dipole" form factor method was widely used to preserve unitarity:

$$f(\hat{s}) = \frac{f_0}{(1+\frac{\hat{s}}{\Lambda^2})^n} \quad (1.16)$$

Where Λ is the scale of new physics and n is an arbitrary number, which in the neutral aTGC case is usually taken to be $n = 2$ or $n = 3$. Using this form factor the cross section regularization is ensured and hence the unitarity violation is prevented.

The upper bounds on the anomalous couplings f_i^V and h_i^V above which the unitarity is violated have been computed here [23] [22]. More specifically for the couplings f_i^γ and f_i^Z the bounds are [2]:

$$|f_{4,5}^\gamma| \leq \frac{1}{\alpha}\Big[\frac{3}{5}(3-6\sin^2\theta_w+8\sin^4\theta_w)\Big]^{1/2}\left(\frac{M_Z}{\Lambda}\right)^3\frac{(\frac{2}{3}n)^n}{(\frac{2}{3}n-1)^{(n-3/2)}} \quad (1.17)$$

$$|f_{4,5}^Z| \leq \frac{4}{\alpha}\sqrt{\frac{3}{10}}\sin\theta_w\cos\theta_w\left(\frac{M_Z}{\Lambda}\right)^3\frac{(\frac{2}{3}n)^n}{(\frac{2}{3}n-1)^{(n-3/2)}} \quad (1.18)$$

[2] Only the bounds on the parameters associated with the VZZ vertex are given here, since in this document the analysis focuses on the ZZ final state

where α is the QED fine structure constant and θ_w is the weak mixing angle and Λ the scale of new physics. The upper bounds on the coupling parameters f_i^γ and f_i^Z for various Λ values, computed according to eq. 1.17 and 1.18, are given in table 1.1.

	Λ = 2 TeV	Λ = 5 TeV	Λ = 10 TeV
$\lvert f_i^\gamma \rvert$	0.1149	0.0074	0.0009
$\lvert f_i^Z \rvert$	0.0960	0.0061	0.0008

Table 1.1: Upper bounds on the f_i^γ and f_i^Z parameters extracted using eq. 1.17 and 1.18, respectively.

1.2.4 Effective Field Theory (EFT) approach

In the Effective field theory approach, the new physics is parametrized by an expansion in higher dimension operators [24] [25] [26]:

$$L_{eff} = L_{SM} + \sum_{d>4} \sum_{i} \frac{C_i}{\Lambda^{d-4}} O_i^d \tag{1.19}$$

where Λ is the scale of new physics, C_i are the coupling strengths and O_i are the operators. The latter are constructed using all the standard model fields. It should be noted, that theorists have also included in their calculations the standard model Higgs boson, discovered at the LHC in 2012 [27].

The Lagrangian has mass dimension four, and thus, the higher order operators must have coefficients of inverse mass powers $\Lambda^{-(d-4)}$ to respect dimensionality. The new physics is assumed to be at scale Λ, which is much larger than the available energy, $\Lambda >> \hat{s}$. Therefore, only the first operators appearing in this expansion are expected to contribute, as all the next order operators will be highly suppressed. If however they are not suppressed, the theory is not valid anymore and has to be revised. This will indicate that new physics is present at the energies probed at the experiment.

The operators are required to be Lorentz and $SU(3)\mathrm{x}SU_L(2)\mathrm{x}U_Y(1)$ invariant. After imposing the gauge symmetries and the spontaneous symmetry breaking occurs, the fields are re-organised and several different vertices with common coefficients emerge. This is an important virtue of the effective field theory, as now the parameters of different final states can be linked. Therefore, experimentally, the EFT parameters can be constrained using several independent triple gauge coupling measurements. It is of a great importance that Higgs couplings are also related to

the charged vertex $Z(\gamma)WW$ parameters and thus, independent measurements can be combined to further constrain the charged anomalous couplings [28] [29].

The lowest dimension operators used to describe neutral triple gauge couplings have dimension eight. This is because odd dimension operators (dim 5 and 7) violate lepton and/or baryon numbers and no dimension six operator contributes to the neutral TGCs. Finally, there are four operators respecting the imposed symmetries and generating the neutral TGCs [30]:

$$\begin{aligned} O_{BW} &= iH^{\dagger}B_{\mu v}W^{\mu\rho}\{D_{\rho}, D^{v}\}H, \\ O_{WW} &= iH^{\dagger}W_{\mu v}W^{\mu\rho}\{D_{\rho}, D^{v}\}H, \\ O_{BB} &= iH^{\dagger}B_{\mu v}B^{\mu\rho}\{D_{\rho}, D^{v}\}H, \\ O_{\tilde{B}W} &= iH^{\dagger}\tilde{B}_{\mu v}W^{\mu\rho}\{D_{\rho}, D^{v}\}H \end{aligned} \tag{1.20}$$

where H is the Higgs field.

The relations between the ZZ final state anomalous couplings (f_i^V) and the effective field theory parameters ($\frac{C_i}{\Lambda^4}$) are:

$$\begin{aligned} f_4^{\gamma} &= \frac{v^2 M_Z^2(-c_w s_w \frac{C_{BB}}{\Lambda^4} + (c_w^2 - s_w^2)\frac{C_{BW}}{\Lambda^4} + 4 s_w c_w \frac{C_{WW}}{\Lambda^4})}{4 c_w s_w} \\ f_4^{Z} &= \frac{v^2 M_Z^2(c_w^2 \frac{C_{BB}}{\Lambda^4} + 2 c_w s_w \frac{C_{BW}}{\Lambda^4} + 4 s_w^2 \frac{C_{WW}}{\Lambda^4})}{2 c_w s_w} \\ f_5^{\gamma} &= \frac{v^2 M_Z^2}{4 c_w s_w}\frac{C_{\tilde{B}W}}{\Lambda^4} \\ f_5^{Z} &= 0 \end{aligned} \tag{1.21}$$

The relations between the $Z\gamma$ final state anomalous couplings (h_i^V) and the effective field theory parameters ($\frac{C_i}{\Lambda^4}$) are:

$$
\begin{aligned}
h_1^\gamma &= \frac{v^2 M_Z^2 (-s_w^2 \frac{C_{BB}}{\Lambda^4} + 2c_w s_w \frac{C_{BW}}{\Lambda^4} + 4c_w^2 \frac{C_{WW}}{\Lambda^4})}{4 c_w s_w} \\
h_1^Z &= \frac{v^2 M_Z^2 (-c_w s_w \frac{C_{BB}}{\Lambda^4} + (c_w^2 - s_w^2) \frac{C_{BW}}{\Lambda^4} + 4 s_w c_w \frac{C_{WW}}{\Lambda^4})}{4 c_w s_w} \\
h_2^\gamma &= 0, \quad h_2^Z = 0 \\
h_3^\gamma &= 0 \\
h_3^Z &= \frac{v^2 M_Z^2}{4 c_w s_w} \frac{C_{\tilde{B}W}}{\Lambda^4} \\
h_4^\gamma &= 0, \quad h_4^Z = 0
\end{aligned}
\tag{1.22}
$$

There are relations between the f_i^V and the h_i^V:

$$
f_5^\gamma = h_3^Z, \quad and \; h_1^Z = -f_4^\gamma \tag{1.23}
$$

1.2.5 One loop level estimates: SM and beyond

In sec. 1.1.3 it was discussed that the SM does not predict triple neutral gauge couplings at tree level. However, small contributions are expected from fermion loops. These contributions have been computed here [31]. Within the SM only the CP-conserving couplings f_5^V, h_3^V and h_2^V can be generated. More specifically, the f_5^γ and h_3^V couplings get contributions from charged fermion loops whilst the f_5^Z coupling takes contributions also from neutrino loops. Moreover, anomalous cancellations of the fermion loops may occur. These cancellations are related to the masses of the fermions considered in the model, and can lead to the suppression or even the vanishing of the coupling.

SM prediction

The anomalous cancellations in each fermion family consists a feature of the SM, as cancellations occur due to the specific fermion charges in combination with the fact that there are three colors associated to each quark. The importance of these cancellations depends on the relative magnitude of the available energy compared to the fermion mass scale. The neutral anomalous couplings are complex numbers since they acquire an imaginary part of about the same magnitude as the real one in the

case $\sqrt{s} > 2m_t$. When this happens, i.e $\sqrt{s} > 2m_t$, a bump on the total f_5^V and h_3^V magnitude is seen for both real and imaginary components, which however rapidly decreases with $\sqrt{s} > 2m_t$. The decreasing positive and negative contributions from the various fermions finally cancel out for $m_F \ll \sqrt{s}$. As the LHC the available energy is significantly higher than the SM fermion masses the anomalous cancellations are important. Theoretical computations have shown that the SM next-to-leading order TGC are of the order $O(10^{-4})$ [31].

Specific models beyond the SM

In the beyond SM case, it is much more complicated to estimate the order of the aTGC for new physics. The coupling can be estimated only when a specific model is considered. Most of the new physics models predict the existence of heavy fermions. If these models are right, the new physics will manifest itself via triangular fermion loops that will enhance the $ZZ(\gamma)$ cross section. Such models are for instance the Minimal SuperSymmetric Model (MSSM) and the TechniColor (TC) [16] [17].

In the MSSM example [31], the new heavy fermions are two charginos, which contribute to both f_5^V and h_3^V couplings, and four neutralinos, which contribute only to the f_5^Z coupling. In the MSSM, as in the SM, the magnitude of the anomalous cancellations will determine the expected coupling order of magnitude. In contrast to the SM, in the MSSM, mixed fermion contributions are allowed in the loop. The anomalous cancellations depend on the differences between the mass scale of the involved fermions. In the case where all fermions are almost degenerated at scale Λ, the coupling will vanish. There are two more scenarios giving non-vanishing couplings. In the first scenario, the fermion multiplets have mass differences of the order of the electroweak scale. This will result in a suppressed coupling, of the same order as the SM couplings. In the last case, one of the fermions has significantly lower mass than the other fermions of the family. This scenario is the less suppressed, as the coupling is expected to be of the order m_Z^2/M_F^2, i.e up to $O(10^{-3})$.

1.2.6 Experimental limits on neutral aTGC

From the LEP1 era up to now at the LHC, the experiments extract limits on the aTGCs. While LEP sensitivity to the charged aTGCs was very high, as the LEP charged limits are still better than the LHC 7 TeV limits, this was not the case for the neutral aTGCs due to the limited statistics. Hence, the LHC results on the neutral aTGCs are very important. The limits on the neutral aTGC at LEP have been mainly extracted using the polar angle observables, θ_γ and θ_Z, for the Zγ and

ZZ final states, respectively [32] [33] [34] [35]. At hadron collides the anomalous couplings have been extracted using the mass of the system or the P_{T} of the photon and the leading Z, for the Zγ and ZZ final states, respectively [36] [37] [38] [39].

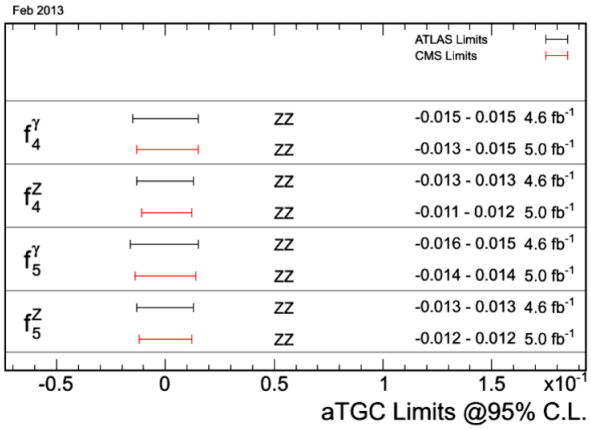

Figure 1.3: Experimental limits on the neutral anomalous Triple Gauge Couplings f_i^V.

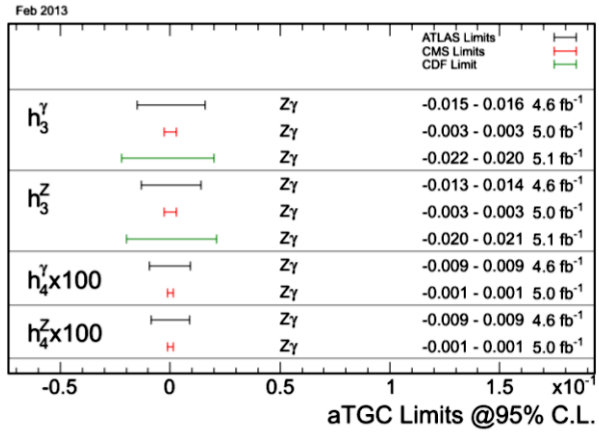

Figure 1.4: Experimental limits on the neutral triple anomalous couplings h_i^V.

In fig. 1.3 and 1.4 the LHC limits for the VZZ and $VZ\gamma$ vertices are presented, respectively. These limits are computed using the ATLAS and CMS data, taken in 2011 at $\sqrt{s} = 7$ TeV for $\Lambda = \infty$. The limits are significantly looser compared to the theoretical predictions discussed in sec. 1.2.5. This implies that for the moment the experimental sensitivity is below the sensitivity required to probe new physics, which according to calculations is expected to be of the order of $O(10^{-4})$ to $O(10^{-3})$.

1.3 The Standard Model ZZ production at the LHC

In this section the Standard model ZZ production at the LHC is presented.

There are two leading order (LO) Feynman diagrams contributing to the ZZ standard model production: the u and the t channel, see fig. 1.5. At NNLO there is an additional contribution from gluon-gluon fusion via quark box diagrams. This is estimated using the MCFM generator [40] to be of the order of about 5% for $\sqrt{s}$ = 8 TeV.

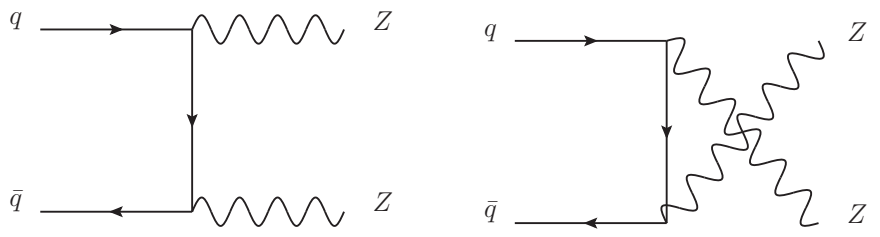

(a) $t-$channel ZZ production. (b) $u-$channel ZZ production.

Figure 1.5: The SM tree-level Feynman diagrams for ZZ production through the $q\bar{q}$ initial state in hadron colliders.

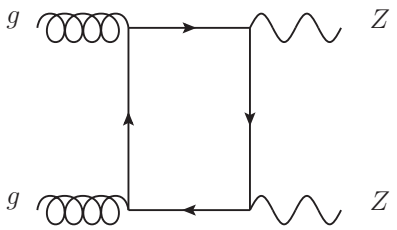

Figure 1.6: Feynman diagram for $gg \to ZZ$ production.

As described in sec. 1.1.3, the s-channel (TGC) is forbidden at tree level and only very small contributions of the order of $O(10^{-4})$ are expected at NLO via fermion loops. The ZZ on-shell cross section for a center of mass energy of 8 TeV is computed at NLO with MCFM [40] and it is found to be 7.06±0.25 pb.

1.3.1 Motivation for the $ZZ \to 4l$ study

In this document, the analysis will focus on the production of Z-pairs that decay in the fully leptonic final state. There are two measurements that will be presented in this analysis: the standard model ZZ production cross section and the limit

extraction on the anomalous couplings f_i^V. Both are realized using all the 2012 data, taken by the ATLAS detector.

More specifically, only decays in electron (e) and muon (μ) pairs will be considered. The branching ratio of a single Z boson going to e or μ pair is of the order of 3.36% [14]. Therefore, the branching ratio for $ZZ \to \ell\ell\ell'\ell'$, where $l = e$ or $l = \mu$, is of the order of 0.45%. A final state composed of four high energy leptons is easily discriminated from background processes. This is an important advantage when the aim is to perform a precision measurement. Furthermore, the deep understanding of the ZZ standard model process is important because it is an irreducible background to the $H \to ZZ$. However, because of the low ZZ cross section and the small branching ratio of the fully leptonic decay channel, the statistical error is still expected to be important, even for the full 2012 dataset.

1.3.2 Previous cross section measurements

The ZZ standard model cross section have been measured since LEP. Fig. 1.7 shows the cross section measurement at LEP as a function of $\sqrt{s}$.

The two hadron colliders, first the Tevatron and then the LHC, have measured the ZZ production cross section as well. In fig. 1.8, measurements and theoretical predictions of the total on-shell ZZ production cross section are compared and plotted against the center of mass energy $\sqrt{s}$. Experimental measurements from CDF and D0 in $p\bar{p}$ collisions at the Tevatron at $\sqrt{s} = 1.96$ TeV, and experimental measurements from ATLAS in pp collisions at the LHC at $\sqrt{s} = 7$ TeV and $\sqrt{s} = 8$ TeV[3] are shown. The blue dashed line shows the theoretical prediction for the ZZ production cross section in $p\bar{p}$ collisions, calculated at NLO in QCD using MCFM with PDF set CT10. The solid red line shows the theoretical prediction for the ZZ production cross section in pp collisions, calculated in the same way. All measurements are in good agreement with the theory predictions.

The latest results on neutral anomalous couplings f_i^V, which are related to the ZZ final state, have been already shown in sec. 1.2.6

1.3.3 What to expect from 8 TeV 2012 data

As discussed in the previous sections, the aim of this analysis is to perform a precision measurement of the ZZ cross section and to extract limits for the neutral anomalous couplings. The key for the precision increase is to properly understand the analysis uncertainties, and then to try to decrease them.

[3]The ATLAS 8 TeV measurement was performed using a small sub-set of the 2012 data

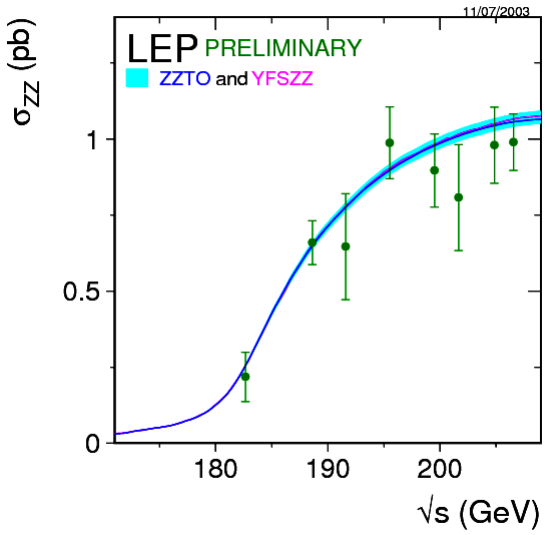

Figure 1.7: Measurements of the Z-pair production cross-section at LEP [15], compared to the theoretical predictions as a function of $\sqrt{s}$. The shaded area represent the $\pm$ 2% uncertainty on the predictions.

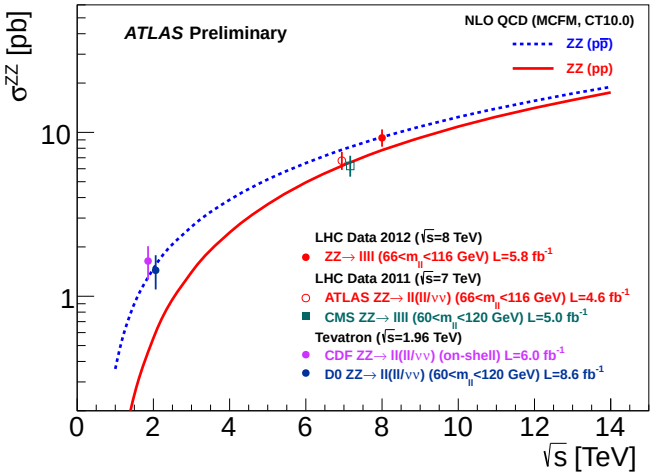

Figure 1.8: ZZ production cross section measurements at hadron colliders and theoretical predictions as a function of centre of mass energy $\sqrt{s}$.

The error on the cross section can be decomposed in two categories. The first one is the statistical error which can be reduced if more data are collected. This can be achieved by increasing the instantaneous luminosity and the data-taking period, see sec. 2.1.2, and by improving the detector efficiency. The second error accounts for all the uncertainties present in the measurement. These systematic errors quantify the potential ignorance we have on the final state particles, the theoretical simulations, the background and the luminosity estimations.

In order to have a numerical example the latest cross section measurement using the ATLAS detector is examined. It was performed with all 2011 data $\approx$ 4.7 fb^{-1} at $\sqrt{s} = 7$ TeV and yield: $\sigma_{tot}^{ZZ} = 6.7^{+0.7}_{-0.7}(\text{stat.})^{+0.4}_{-0.3}(\text{syst.}) \pm 0.3(\text{lumi.})(\text{pb})$ [37]. As it can be seen, the statistical error is still dominant.

In this document the full 2012 dataset at $\sqrt{s} = 8$ TeV will be used. The 2012 integrated luminosity is $\approx$ 20.7 fb^{-1}. Since the statistical error scales with the luminosity as $\sqrt{L}^{-1}$, one expects a factor of 2 decrease of the error. Moreover, since the 2012 collisions where performed for $\sqrt{(s)} = 8$ TeV, the ZZ cross section will be increased of about 20% with respect with the 7 TeV data and thus the ZZ production rate will be further increased, see *pp* theory curve in figure 1.8. Therefore, for the first time the statistical error is expected to have the same magnitude as the total systematic error, and thus now it is even more important to restrain the latter.

The errors related to the final state particles, the background estimation and the luminosity uncertainties, can be further reduced if the detector operation is well understood. For this reason, in the following chapter, 2, a description of the LHC and the ATLAS detector is presented. In chapter 5 all systematic sources affecting the analysis are discussed.

Chapter 2

The LHC and The ATLAS Detector

2.1 The LHC

The Large Hadron Collider (LHC), which is the last part of the CERN accelerator complex illustrated in Fig. 2.1, is the most powerful particle collider ever built. It is designed to collide protons against protons (p-p) at a nominal center of mass energy (CME) of $\sqrt{s} = 14$ TeV. Heavy ions as lead (Pb) will also be accelerated in order to perform Pb-Pb collisions. The accelerator ring is 27 km long and it is located underground the Geneva area. It can reach an instantaneous luminosity of 10^{34} cm^{-2}s^{-1} for p-p collisions, and 10^{27} cm^{-2}s^{-1} for Pb-Pb collisions. Two general purpose detectors are installed at two points of the accelerator ring, CMS and ATLAS. There are two more detectors: ALICE and LHCb, which are dedicated to heavy ion collisions and the b-physics studies, respectively. In this document, only the ATLAS detector will be described since this thesis was conducted within the ATLAS collaboration.

2.1.1 Protons in the accelerator ring

Design motivation

The motivation for the LHC construction is to probe the standard model of particle physics, and to search for new physics beyond it. This is achieved by colliding two proton beams. The available energy in the CM is $\sqrt{s} = 2E_{beam}$. During the collision, the quarks and gluons interact with each other and produce new particles. The observation of these particles probes the fundamental laws that rule particles behavior. This very complicated and challenging experimental setup demands, in addition to an excellent detector device, the development of a powerful accelerator

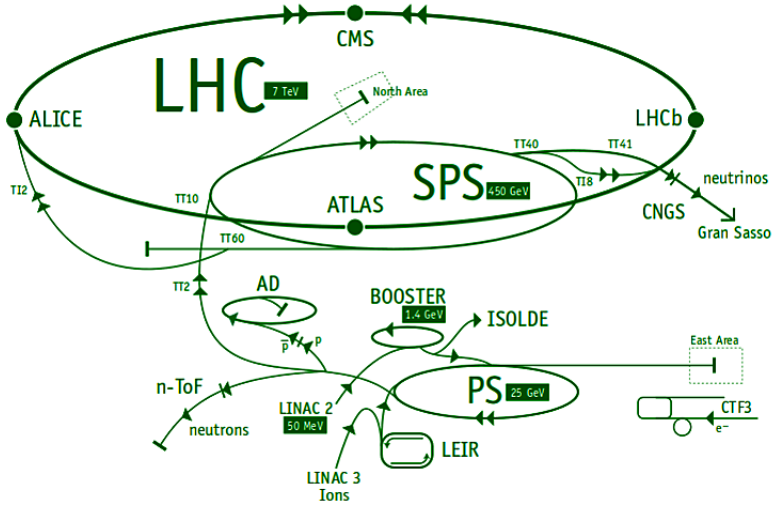

Figure 2.1: The CERN accelerator complex.

machine able to reach high enough energies to probe new physics.

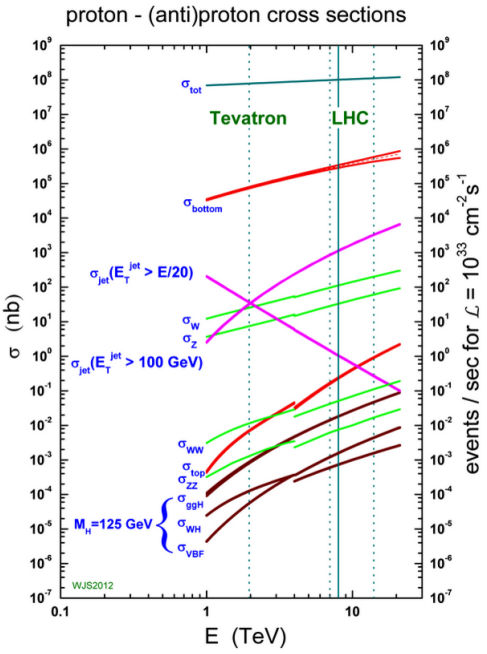

Figure 2.2: Cross sections as a function of $\sqrt{s}$.

Fig. 2.2 shows the cross section of several processes as a function of the $\sqrt{s}$. The physics processes of interest have a low cross section, even at the LHC nominal center of mass energy. Therefore, in order to make a precision measurement, one

needs to increase the production rate, which is given by the cross section times the instantaneous luminosity:

$$\frac{dR}{dt} = L_{inst} \times \sigma \tag{2.1}$$

The instantaneous luminosity, L_{inst}, depends on the number of particles per bunch and the number of bunches per beam, but also to other more technical parameters which characterize the beam. Such characteristics are the beam revolution frequency and the beam width, which is related to the proton compression in each bunch.

The LHC ring design, which determines the beam properties and thus the instantaneous luminosity, was driven not only by the need for high energy and instantaneous luminosity, but also by the construction cost. The optimal solution chosen gives a machine powerful enough to investigate interesting physics areas, such as Higgs below 1 TeV, while keeping the budget under $\approx$ 3.1 bn €.

The design

All starts from a bottle filled with hydrogen atoms exposed to a strong electric field. Because of this field, the orbiting electrons are stripped off the atoms and then the hydrogen nucleus can start their journey in the accelerator complex. The complex is composed of consecutive linear and circular acceleration units, see fig 2.1. The first one is the Linac 2, that provides the protons with an energy up to 50 MeV. Then the beam is injected in a circular booster, the PSB, such that when leaving it, each proton has up to 1.4 GeV. There are two more circular accelerators preceding the beam entrance in the 27 km long LHC, the PS and the SPS, rising the proton energy to 25 GeV and 450 GeV, respectively. The final acceleration, up to the nominal proton energy (7 TeV), is done in the LHC. Furthermore, before the beam is kicked in the LHC, it is split in two parts. The two beams are accelerated using the same pipe but in the opposite direction, allowing them to cross at the detector center, called interaction point (IP).

The LHC ring is built up of eight sectors (octant), as shown in Fig. 2.3, connected together to form the beam pipe, see Fig. 2.4. In the beam pipe there is an ultra high vacuum (10^{-13} atm) to prevent beam erosion due to proton interactions with gas molecules.

Each sector has a part containing 154 dipole superconducting magnets that keep the protons in a circular orbit. Each dipole is 15 m long and weighs around 35 t. It produces a 8.3 T field, which is capable to bend 7 TeV proton beams. Such

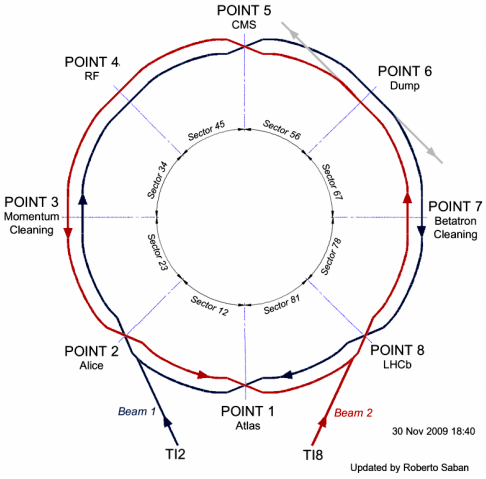

Figure 2.3: The octants of the LHC ring.

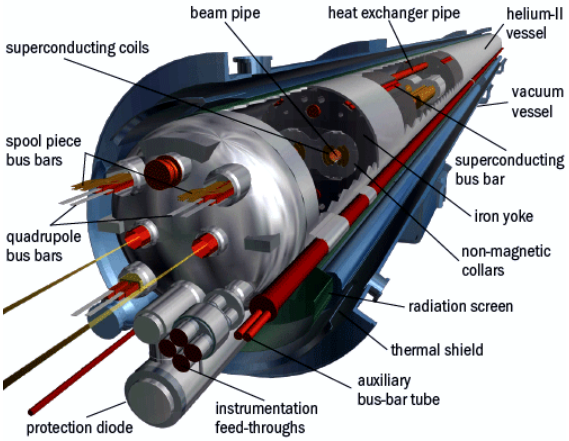

Figure 2.4: The LHC beam pipe.

high bending power is attained by keeping dipoles niobium-titanium (NbTi) cables in a superconducting state, using superfluid Helium at a temperature of 1.8 K. The second part of the sector is linear. It serves for the beam injection, cleaning, collision, dumping and acceleration, depending on the sector position. This beam handling is achieved using a set of magnets and radio frequency (RF) cavities. The magnets are responsible for the beam focusing while the RF cavities are used for the beam acceleration.

Because of the RF acceleration, the beam is split in discreet proton groups called "bunches". The number of bunches per beam and the number of protons per bunch is bounded by the accelerator design. The accelerator is designed to deliver 2808 bunches per beam, each one containing 1.2 10^{11} protons.

2.1.2 The LHC Performance

The LHC physics runs started on 2010 with a CME of $\sqrt{s} = 7$ TeV and an instantaneous luminosity of 10^{32} cm^{-2}s^{-1}. By the end of the year 45 pb^{-1} of data have been collected by each multipurpose experiment. In 2011 the CME remained the same while some beam characteristics were changed, such as the number of bunches per beam and the bunch "squeezing", so that an increased instantaneous luminosity of 10^{33} cm^{-2}s^{-1} is obtained. Approximately 5 fb^{-1} have been collected during 2011. The last physics run, performed before the 2 years shutdown, took place in 2012 at a CME of 8 TeV and an instantaneous luminosity rising up almost to the nominal one, i.e 10^{34} cm^{-2}s^{-1}. The total integrated luminosity delivered in 2012 was 20.3

fb^{-1}. In Fig. 2.5 the integrated luminosity during the year 2010, 2011 and 2012 is shown for the ATLAS detector.

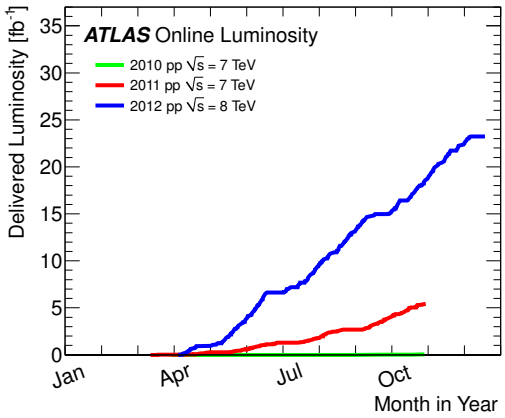

Figure 2.5: Integrated luminosity versus day delivered to ATLAS during stable beams and for p-p collisions. This is shown for 2010 (green), 2011 (red) and 2012 (blue) running. The online luminosity is shown.

The physics analyses, especially those aiming at a precise cross section measurement and to a less exted those performing search studies, are highly concerned by the luminosity calculation and its accuracy. The final integrated luminosity quoted, is estimated experimentally using the data themselves, by measuring the observed interaction rate per bunch crossing, and not just integrating over time the instantaneous luminosity. Furthermore, there are systematic uncertainties associated to the above estimation, which can be dominant for clean analysis such as $ZZ \to \ell^-\ell^+\ell^-\ell^+$.

Luminosity measurement

The instantaneous luminosity for a storage ring, operating at a revolution frequency f_r and with the number of bunches per beam n_b, can be also expressed by the following equation:

$$L = \frac{\mu_{vis} n_b f_r}{\sigma_{vis}} \tag{2.2}$$

Where σ_{vis} is the inelastic interaction cross section, corrected for detector and reconstruction efficiency. The μ_{vis} is the number of inelastic interactions per bunch crossing. In order to determine the luminosity, the average μ_{vis} has to be measured. There are two main approaches using dedicated algorithms for the μ_{vis} estimation.

The first algorithm is based on an event counting. It just applies a threshold to the global event activity to decide if an inelastic interaction has occurred. For

a given time interval where N_{BC} bunch crossings took place and N inelastic events were recorded, μ_{vis} is given by $\mu_{vis} = \frac{N}{N_{BC}}$. This method can be used for $\mu_{vis} << 1$, however, as already discussed, the aim is to have as much as possible inelastic interactions per bunch crossing. This means a $\mu_{vis} >> 1$, a condition referred as pile-up.

The second algorithm takes as input the signal of each detector readout channel. The channels recording a signal above some predefined threshold are counted as "hits". In this method, the hits are converted to μ_{vis} using calibration techniques [41]. Because of the greater complexity of the "hit counting" method, more systematic errors are included.

The μ_{vis} measurement has multiple uncertainty sources, such as the efficiency correction of the interaction cross section, and thus is important to cross check its estimation. For this reason, data from several detectors are processed independently. The total luminosity uncertainty was estimated to be 1.8% [42] and 2.8% for the 2011 and 2012 data, respectively. The 2012 luminosity uncertainty is derived following the same methodology as for the 2011 uncertainty estimation, using a preliminary calibration of the luminosity scale, derived from beam-separation scans performed in November 2012.

2.2 The ATLAS detector

The ATLAS (A Toroidal LHC ApparatuS) detector is one of the two general purpose detectors built along the LHC. It measures 44 m long, 25 m hight and weighs 7000 t, see Fig 2.6.

With a designed instantaneous luminosity of 10^{34} cm^{-2}s^{-1} and a total cross section of about 100 mb at $\sqrt{s} = 7$ TeV, the p-p interaction rate turns out to be of the order 1 GHz. In order to properly exploit this significantly high rate, excellent detector performance is needed.

- A tracking detector is needed for the reconstruction of the charged particle trajectory and for the primary and secondary vertex reconstruction. Thanks to this detector electrons can be distinguished from photons and a better τ-lepton and heavy-flavour identification is performed.

- A high resolution energy measurement of the electrons and photons is required. This is obtained using a high granularity electromagnetic calorimeter. Both objects interact electromagnetically with the calorimeter material, depositing their energy by producing an electromagnetic shower.

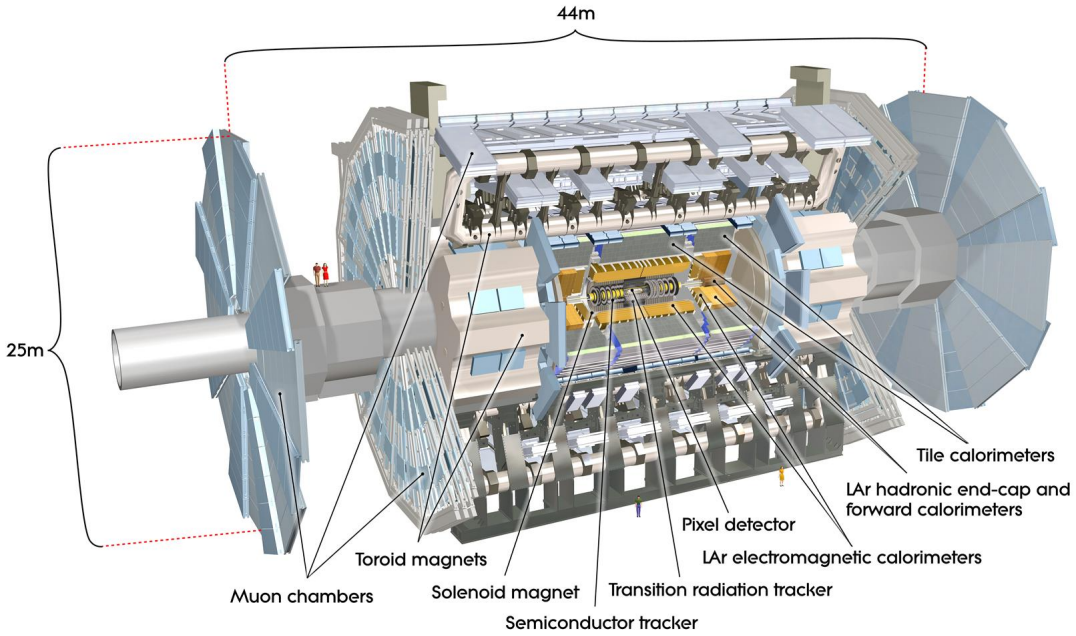

Figure 2.6: The ATLAS detector.

- For the particles interacting strongly with the matter, a dedicated calorimeter is used. Its granularity and depth should be adapted to precisely measure the energy deposit of the hadronic shower. Moreover, a precise energy measurement leads to a better estimation of the event missing energy.

- For the precise muon momentum measurement there is a need for a detector located away from the iteration point in order to) avoid the high radiation noise, b) have a large lever arm. The detector should be immersed in a strong magnetic field, providing a high enough bending power even for the most energetic muons.

- The high event rate should be filtered. A fast detector response will allow to determine online if an event passes some predefined baseline criteria, and only if it does proceed to its storage.

- The phase space covered by the detector should be as wide as possible in order to be able to meaure all types of physics phenomena. Moreover, by doing so, a better estimation of the missing energy is ensured and one also prevents from adding systematic errors on the measurements due to extrapolations to the uncovered phase space.

In the next sections more details about the ATLAS detector are given. First, the ATLAS coordinate and trigger systems are described, then the four sub-detectors: the inner detector, the electromagnetic and hadronic calorimeters and the muon spectrometer follow, and finally the toroidal magnetic field system.

The coordinate system

The ATLAS detector uses a right-handed coordinate system, as shown in Fig. 2.7. The z-axis is aligned with the beam and the z=0 position is the interaction point (IP). The $x - y$ plane is transverse to the z-axis. The positive y direction points upwards and the positive x direction points to the center of the LHC ring. A quantity widely used is the pseudorapidity $\eta = -ln\, tan\, \frac{\theta}{2}$, where θ is the polar angle in the cylindrical coordinate system. Other quantities used are the azimuthal angle ϕ and the distance ΔR, which is defined as $\Delta R = \sqrt{\Delta\eta^2 + \Delta\phi^2}$.

There are two detector areas. The main one is the central area, which is named Barrel as it has a cylindrical shape which surrounds the IP. Then, in each detector side there is a complementary detector ensemble. These two detectors are wheels, called End-Caps and they are placed perpendicular to the z-axis. The detector side positioned at a positive z, is called "A" side, while the one located at negative z, "C" side.

2.2.1 Data Aquisition and Trigger System

The extremely high instantaneous LHC luminosity produces approximately 1 G of proton-proton collisions per second. However, the majority of these events are not interesting for the studies performed at the LHC, which mainly focus on the investigation of high energy "rare processes". In addition, the material cost of the online event processing and the limited storage space, put a constrain on the amount of data that can be finally recorded. For all the above reasons the ATLAS detector is equipped with a three-level trigger system, see Fig. 2.8, which finally reduces the number stored events by a factor of 10^9.

The level one trigger (L1) requires a very quick time response in order to cope with the high events rate. It is thus a hardware based trigger which uses very simplified algorithms. It collects low granularity inputs from the calorimeter trigger towers, muon trigger detectors (TGC and RPC), and from the forward detectors. The final decision on whether an event is kept or not is made by the Central Trigger Processor (CTP) on less than 2.5 μsec. The event rate recorded after the L1 filtering is around 75 KHz. The L1 also provides the next trigger level with the information

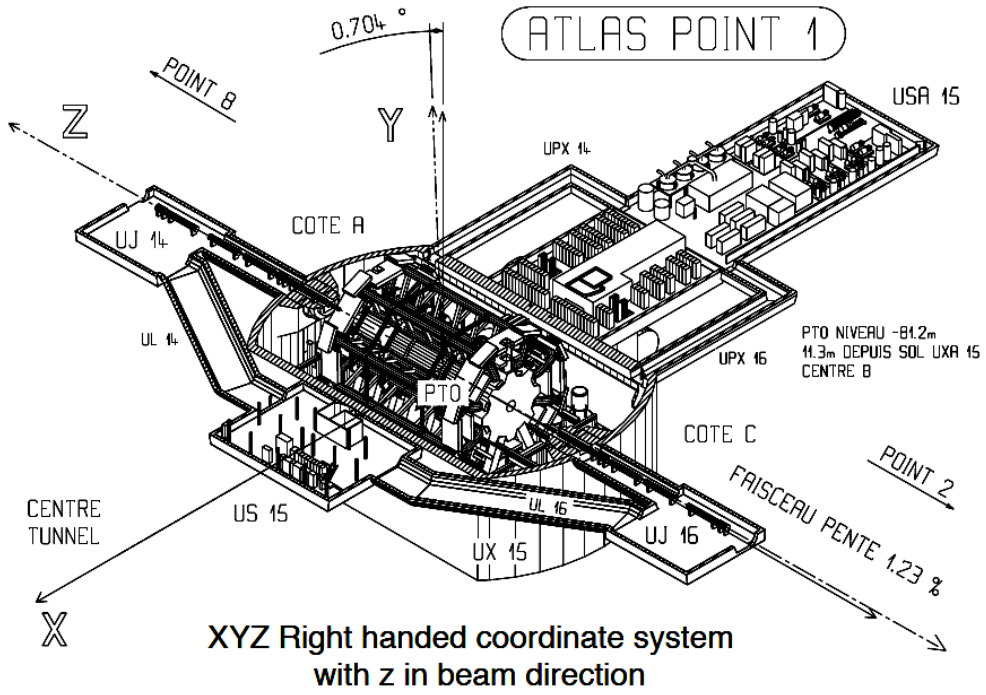

Figure 2.7: The coordinate system of the ATLAS detector.

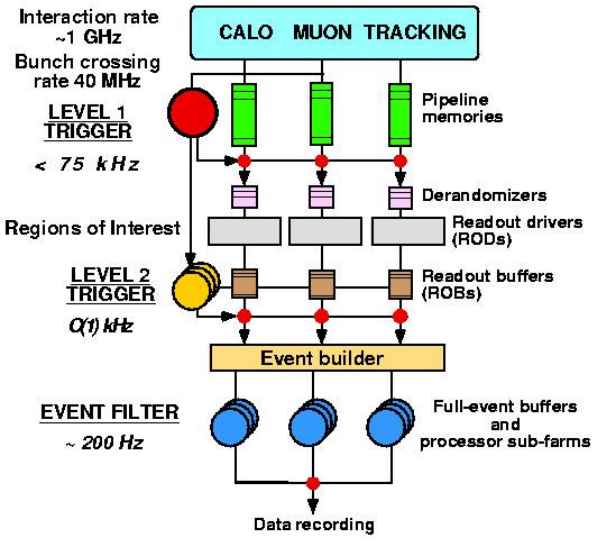

Figure 2.8: Schema of the ATLAS trigger system.

of the detector regions where a interesting signal is observed (RoI).

The High Level Triggers (HLT) follow the L1 and consist of the Level two (L2)

and Event Filter (EF) triggers. Both are based on software tools, performing a more sophisticated selection. More specifically, at L2, a finer investigation of RoI takes place. The interesting event data are transferred to readout buffers, where dedicated algorithms process the full granularity information. The procedure can last up to 40 ms. The event rate fulfilling the L2 requirements is of some kHz. Finally at the EF level, all the event information is processed by offline-like reconstruction algorithms. It takes less than 4 seconds to the filtering procedure to be completed. The final event rate delivered is $\approx$ 200 Hz.

2.2.2 Inner Detector

The inner detector (ID) is located in the innermost part of the ATLAS detector. It is designed to reconstruct the trajectory of the charged particles. The ID is composed of three sub-detectors that give a fine-granularity position measurement. Fig. 2.9 shows a cut away view of the ID. The outer radius of the ID is 1.15 m, and the total length is 7 m covering a fiducial region up to $|\eta| < 2.5$. Within this area both the primary and the secondary vertices can be identified. The ID is immersed in a 2 T solenoid magnetic field that ensures the correct charge identification and the good momentum determination. The momentum resolution in the ID is of the order of $\frac{\Delta P_T}{P_T} = 0.05\% \times P_T[GeV] \oplus 2\%$.

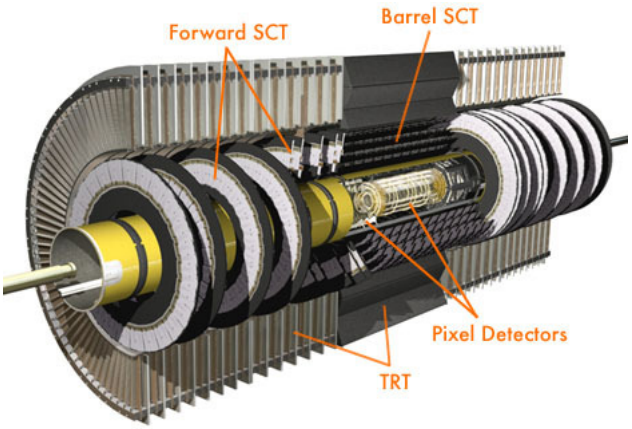

Figure 2.9: Cut away view of the Inner Detector.

Central Solenoid Magnet

The ID is surrounded by the Central Solenoid (CS) magnet. The coil measures 5.3 m long and has an inner radius of 1.2 m. A current of 7600 A flows through the

superconducting cable and generates a 2 T field. Since the CS is located right before the electromagnetic calorimeter, the coil had to be as thin as possible in order to prevent particles from losing their energy before entering the calorimeter. For this reason the CS is installed in a vacuum vessel common with the calorimeter. The coil thickness is of 0.66 radiation lengths, see [43].

Silicon Pixel Detector

The silicon pixel detector is the closest detector unit to the beam axis. It provides a high precision track measurement and is able to reconstruct well the secondary vertices produced by in flight hadron decays. The pixel detector is composed of three Barrel layers, and in the two End Cap regions of three disk layers. The layers are equipped with modules, with a size of 50x400 μm^2 each. The modules are composed, in total, of 80 million silicon sensors. A charged particle traversing the semi-conductor silicon pixel creates electron-hole pairs. Because of the applied voltage, the electrons flow towards the anode where the signal is recorded. The position of the signal can be reconstructed with great accuracy, using the information of adjacent pixels position. The pixel detector design has been optimized to tolerate the high radiation conditions present at the LHC. In order to minimize the radiation damage, modules are kept at low temperature, -10 $^{\circ}C$.

Semi Conductor Trackers (SCT)

The SCT is located in the intermediate ID area and it consists of four Barrel layers and two End Cap with nine disks each. There are in total 4088 modules on which 16000 silicon micro-strip sensors are mounted. In order to achieve high precision tracking with a resolution down to 16 μm x 500 μm, the modules are made of two pairs of daisy-chained silicon strip sensors, glued back to back at a stereo angle of 40 mrad. The above configuration permits the measurement of the three position components.

Transition Radiation Tracker (TRT)

The TRT detector is the outermost part of the ID. It consists of 370 K straw trackers each of 4 mm diameter. Straws are filled with a mixture of $70\%Xe, 27\%CO_2$ and $3\%0_2$. A 1.78 kV potential is applied between the anode wire, passing through the straw center, and the straw wall (cathode). The position information provided by the TRT is in the $R-\phi$ plane in the Barrel region, and along the z-axis in the End Cap region. The intrinsic accuracy is 130 μm per straw.

In order to increase the electron identification efficiency, the space between the straws is filled with material, so that particles passing through it emit transition radiation photons. When these photons enter the straw, they contribute to the enhancement of the gas ionization, and thus amplify the signal. Since the electrons are more likely than hadrons to emit photons at low energy, one can distinguish an electron from a pion in the TRT.

The TRT resolution is lower comparing to the previously described ID sub-detectors. However, because of the larger volume it occupies, a greater number of particle hits can be recorded, up to 36 measurements per track. The TRT covers an area up to $|\eta| = 2$.

2.2.3 Calorimeters

The ATLAS detector calorimetric system is located outside the solenoid magnet and covers an area up to $|\eta| < 4.9$. It is designed to absorb, and therefore to measure, the energy of the incident charged and neutral particles using a sampling technique. For this purpose, it is made of metal plates sandwiched together to form a dense environment (absorber) that will cause incoming particles to interact with it and produce a shower of secondary particles. For the measurement of the energy deposit, another material is used (Liquid Argon or plastic scintillators), which alternates with the absorber plates.

There are two types of particles to be measured. Those interacting mainly electromagnetically (electron and photons) and those interacting mainly via the strong force (hadrons). Therefore, two different calorimeters had to be build, see Fig. 2.10. In each case, for a better energy reconstruction, the calorimeter material thickness has to be large enough to contain the entire shower.

Electromagnetic calorimeter

The electromagnetic calorimeter is located in the same cryostat with the solenoid magnet, right after the wall which separates it from the coil of the solenoid. It is designed in such a way that a good electron and photon identification along with a high energy resolution are obtained. Moreover, if the above requirements are fulfilled, a well grounded missing energy reconstruction is ensured. The electromagnetic calorimeter characteristics are: a large fiducial volume coverage, a high detector granularity and a uniform resolution over the full azimuthal angle.

The EM calorimeter has an accordion shape, as presented in Fig. 2.11. It is made of lead plates and liquid argon gap layers of 2.1 mm width. The lead works as an

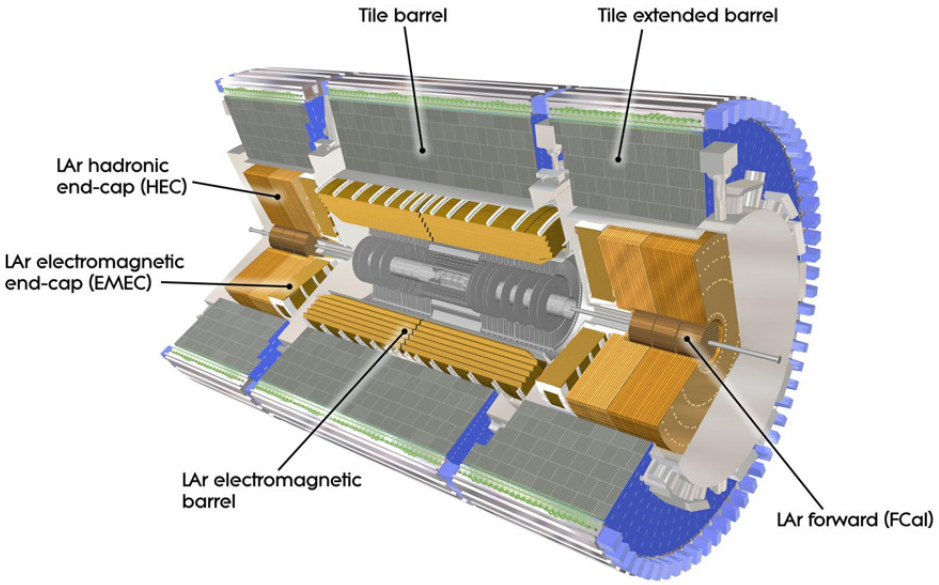

Figure 2.10: The ATLAS calorimeters.

absorber due to its high atomic number (Z = 82). When an incoming particle passes through the plate, it interacts with the lead atoms. Secondary electrons are produced which ionize the liquid argon. The electron signal is read out by copper electrodes, kept at a potential of +2000 V. The induced electrical current is proportional to the energy deposit.

The EM calorimeter has three main areas. The Barrel area consists of two half cylinders with a 4 mm gap at z = 0 covering an η region up to 1.48, and two coaxial wheels on each End Cap side, the first covering from $|\eta|$>1.38 to $|\eta|$<2.5 and the second from $|\eta|$=2.5 to $|\eta| = 3.2$. For a better energy and position resolution in the central Barrel area, there are three samplings, each one with a different thickness. Furthermore, in order to correct for energy loss in the material preceding the EM calorimeter (ID, solenoid and cryostat) there is a liquid argon pre-sampler. The EM calorimeter in the Barrel area is 24 X_0 thick in total, while the End Cap is 26 X_0.

The energy resolution of a calorimeter is given by:

$$\frac{\sigma(E)}{E} = \sqrt{\frac{\alpha^2}{E} + b^2 + \frac{c^2}{E^2}} \tag{2.3}$$

In this equation, α is the so called sampling term. It is related to the statistical fluctuations of the number of produced electrons (N) in the electromagnetic shower developed in the absorber. Since N $\propto$ E, and N follows a normal distri-

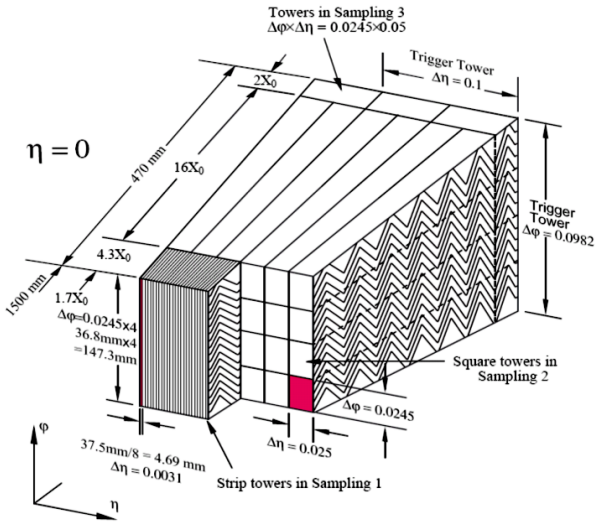

Figure 2.11: The structure of the barrel accordion calorimeter.

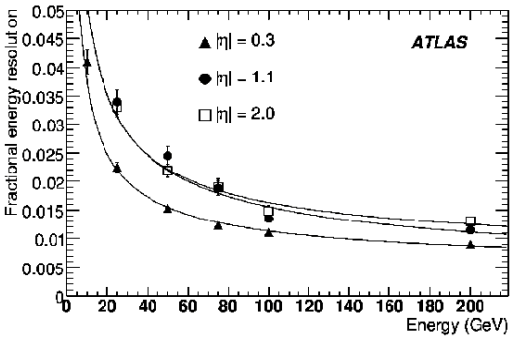

Figure 2.12: Electron resolution as a function of the energy.

bution, $\sigma_{sample} = \sqrt{N} \propto \sqrt{E}$. The b term accounts for the non-uniformity of the detector response, mainly due to temperature fluctuations, geometrical deformations and inhomogeneities in the liquid-argon. Finally, the last term c, is related to the electronic noise. In Fig. 2.12, the electron energy resolution is shown as a function of the energy. For an electron energy greater than 100 GeV, the resolution is up to 1%.

Hadronic calorimeter (HC)

In order to measure the energy of strongly interacting particles, the HC follows the EM calorimeter, both in the Barrel and End Cap region. In the Barrel area, it covers a fiducial volume up to $|\eta| < 1.7$. It consists of plastic tile scintillators embedded in steel plates. Each scintillator is coupled to two optical fibers that transmit the produced light to a photomultiplier. The scintillators are grouped together to form cells of various dimensions, depending on the η region and the depth, so that the cell granularity is optimal. There are in total 5182 cells in the Barrel HC. The End Cap hadronic calorimeter (HEC) consists of two cylindrical wheels, one in each detector side. The HEC is a liquid argon sampling calorimeter with copper-plate absorber. It covers a pseudorapidity range between 2.1 and 3.2. The designed resolution of the HC is $50\%/\sqrt{E} \oplus 3.0\%$ [44].

Forward calorimeters (FC)

The main purpose of the forward calorimeters is to improve the missing energy measurement by extending the detector coverage to almost 4π. Furthermore, it is used for the measurement of forward jets, emitted with a very small angle with respect to the z axis i.e $1 < \theta < 5$ degrees. The FC is made of three detector units: FC1, FC2 and FC3. Each unit consists of a copper matrix with tube holes, filled with copper tubes. Inside the tube there is an absorber rod acting as an anode. The gap between the tube wall and the rod is filled with liquid argon.

The FC1 is the closest unit to the interaction point and it is thus used also for EM calorimetry. It has a copper rod and the liquid argon gap is very small (250 μm) to prevent an ion build-up effect that would be induced by the significant radiation level present in this area. The FC1 resolution has a sampling term of $34\%/\sqrt{E}$ and 2% constant term. The last two detector units are used for measuring the hadronic component. The rod is made of tungsten and the gap thickness is 375 and 500 mm for the FC2 and FC3, respectively. The resolution is estimated to be $80\%/\sqrt{E}\oplus$ 2.7%.

2.2.4 Muon Spectrometer

The muon spectrometer (MS) is located in the outermost part of the ATLAS detector and it is the main muon detector. It covers an area up to $|\eta| = 2.7$. More explicitly, the barrel area goes up to $|\eta| \approx 1.6$, with the $1.4 < |\eta| < 1.6$ being a transition region with the End Cap. The MS is immersed in a strong toroidal magnetic field of $\approx$ 0.5 T. In Fig. 2.13 the MS layout is shown. It should be noted that for $|\eta| < 0.06$ no muon chambers exist due to a hole allowing service passages inside the ATLAS detector. The muon spectrometer purpose is to perform an excellent muon identification along with a high momentum resolution for a large momentum spectrum using precision chambers. It also collects information for the muon trigger system, using fast response chambers.

The higher particle flux in the forward detector region, has led to a different choice for the precision and trigger chambers. In the following, the four types of muon chambers (two precision and two trigger chambers) and the alignment of these chambers are presented. The magnetic field system of the MS is described in sec. 2.2.5.

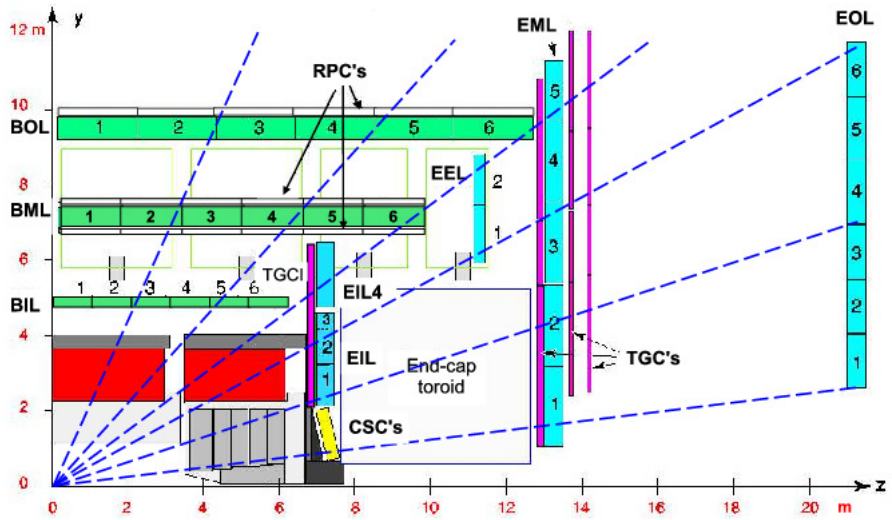

Figure 2.13: Cross-sectional view of ATLAS in the r-z projection at $\phi \approx \pi/2$. The Barrel MDT chambers are shown in green, the End Cap MDT chambers are blue. In the Barrel (End Caps), the RPC (TGC) chambers are shown outlined in black (solid purple)

Muon Drift Tubes chambers (MDTs)

The MDTs are precision tubes located both in the Barrel and End Cap region. They are filled with gas that gets ionized when a charged particle traverses it. The ionization electrons are collected by the wire in the center of the tube (anode), as shown in Fig. 2.15. The drift time of the electrons is used to estimate the position of the muon. Once several "hits" are recorded on different tubes along the muon trajectory, the muon track can be reconstructed using as well the inner detector information.

The drift tubes are made of aluminum with a wall thickness of 0.4 mm and have a diameter of 3 cm. The MDTs length can vary from 0.9 m to 6.3 m, depending on the detector area in which they are mounted. The potential applied between the aluminum tube (cathode) and the gold-plated tungsten-rhenium wire (anode) traversing the tube is set to 3 kV. The tubes are filled with $Ar(93\%)$ and $CO_2(7\%)$ mixture, kept under 3 bar pressure. These characteristics ensure the detector tolerance to the high particle flux over time. The electron maximum drift time is 700 ns and the single hit resolution of a tube is estimated to be ≈ 80 μm.

In order to build a chamber, up to 72 tubes are gathered together, one next to the other, to form a layer. Chambers consist of two multi-layers, with each multilayer

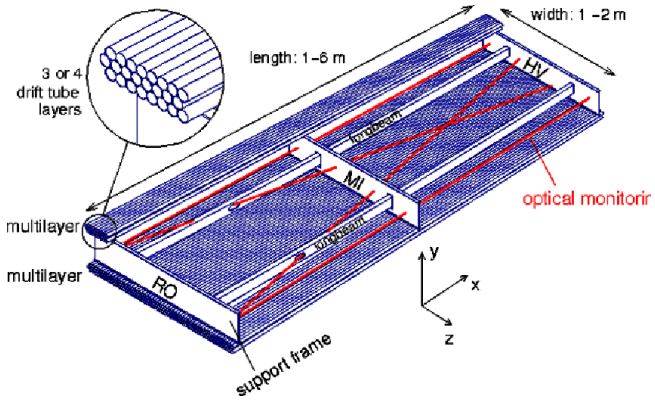

Figure 2.14: A detailed view of a muon chamber.

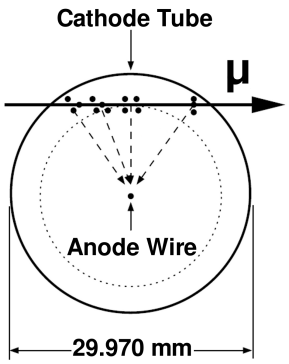

Figure 2.15: Cross section of a MDT tube.

composed of four tube layers in the innermost part of the MS, and three tube layers in the other MS regions, as shown in Fig. 2.14. MDT chambers are located in the central and forward areas of the ATLAS detector, covering an $|\eta|$ region up to 2.7.

There are two chamber sub-types: the Large chambers, which are located between the magnet toroid coils, and the Small chambers, which are located right on the coils. In the Barrel area, there are 8 magnet coils, thus, one ends up with 16 chambers per Z section. In total there are 7 Z sections per detector side.

The MDT chambers are positioned around the z-axis with the MDT wires oriented along the ϕ coordinate. Even though the tubes length can reach 6 m, a rough estimate of the second coordinate (non-bending plane), ϕ, can be performed using the information of the signal propagation time along the wire. The second coordinate resolution is of the order of 20 cm.

Cathode Strip Chambers (CSCs)

The CSCs are precision measurement chambers, located in the inner part of the first End Cap detector wheel. The need for the CSCs has emerged because of the high radiation in the forward detector region. MDTs have up to 150 Hz/cm^2 radiation tolerance while the CSCs can go up to 1K Hz/cm^2. The CSCs are multi-wire chambers, filled with $Ar(80\%)$ and $CO_2(20\%)$, providing a drift time of 30 ns with a time resolution of 7 ns. Each chamber is composed of four layers. Each layer contains 192 cathode strips orthogonal to the anode wires, and 48 strips parallel to the anode. The cathode to anode distance is 2.54 mm.

When a muon passes through the chamber it ionizes the medium. Because of the 1.9 kV potential applied, the free electrons will drift toward the anode producing an avalanche. The charge induced by the avalanche is read-out by the two sets of cathode strips that are mutually perpendicular to each other. The above structure

of the read-out electronics provides both a η and ϕ coordinate measurements. The final position information is obtained by a charge interpolation over the adjacent strips. The position resolution in the bending plane, η, is 60 μm per layer while the resolution of the non-bending plane drops to 5 mm because of the lower strip granularity.

There are in total 16 CSC chambers per End Cap side, split in 8 Large and 8 Small sectors. The covered $|\eta|$ area goes from 2.0 to 2.7.

Resistive Plate Chambers (RPCs)

The RPCs are chambers located in the Barrel detector area, covering an $|\eta|$ region up to 1.04. In the Middle Barrel area, RPCs surround the MDTs, while in the Outer region there is only one chamber. Fig 2.16 shows the RPCs location. The information collected by the RPCs is used for the muon Level 1 trigger. RPCs provide also the muon track position in the non bending plane.

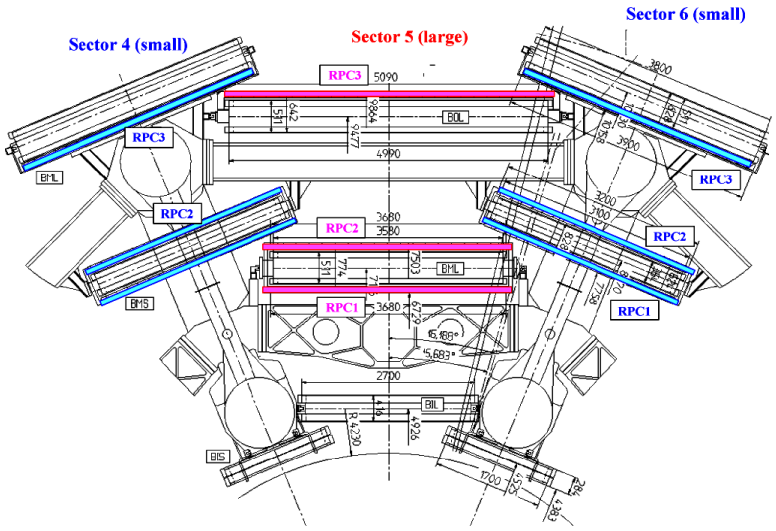

Figure 2.16: RPCs location on the middle and outer Barrel layers.

RPCs are made of two resistive (up to $10^{12}\,\Omega$cm) bakelite plates of 2 mm thickness each, with their surfaces coated by thin layers of graphite, allowing an uniform voltage distribution along the plates. The distance between the plates is 2 mm, and the enclosed space is filled with a gas mixture of $C_2H_2F_4(94.7\%)$, $C_4H_{10}(5\%)$ and $SF_6(0.3\%.)$ kept under high pressure. When a charged particle passes through the saturated medium, it ionizes the gas, and because of the 9.5 kV potential applied, an avalanche on the anode is produced. Then, the signal induced on the copper pick-up

strips is read out via capacitive couplings. The read-out strips are organized in two planes perpendicular to each other, and therefore both η and ϕ information is provided. A RPC chamber is composed of two such layers (two-plates system). Each RPC layer can reach a spatial resolution, in both directions, of 10 mm.

Thin Gap Chambers (TGCs)

The TGCs are chambers developed to trigger muon events in the forward region and to provide the ϕ coordinate information. As already discussed, the radiation rate is significantly higher in the End Cap region than in the Barrel area. For this reason TGCs have similar design as the CSC i.e they are multi-wire chambers. The TGCs are located on four End Cap wheels in each detector side and cover a detector area from $|\eta| = 1.04$ up to 2.6. The first TGC wheel is situated in front of the Inner wheel and the last three wheels surround the Middle wheel.

In order to achieve an efficient muon trigger under such luminosity conditions (25 ns bunch crossing), an as high as possible time resolution is required. This is fulfilled owing to the small anode-cathode distance and the high operating voltage of 3.1 kV. The gas mixture used is CO_2 (55%) and $n-C_5H_{12}$ (45%). The resolution of the $|\eta|$ and ϕ coordinates depend on the chamber location and ranges from 10 mm to 60 mm.

Muon chambers alignment

In order to achieve a high muon momentum resolution the precise knowledge of the muon chamber position is required. A simplified example of muon measurement is shown in figure 2.17. If one assumes an uniform magnetic field, one gets:

$$P_T = \frac{L^2 B}{8s} \tag{2.4}$$

where s is the sagitta as shown in Fig. 2.17, L is the distance between the Inner and Outer chamber and B is the uniform magnetic field. An uncertainty on the chambers position is directly propagated to the muon momentum measurement. For a very energetic muon of about $P_{\mathrm{T}} = 1$ TeV the sagitta is ≈ 500 μm, thus, in order to obtain a 10% momentum resolution one needs a chamber position accuracy better than 50 μm. For this purpose, an advanced MDTs alignment technique is used, based on optical sensors.

The different geometry of the Barrel and End Cap regions require an individual approach for each one, therefore two alignment softwares exist. The aim is

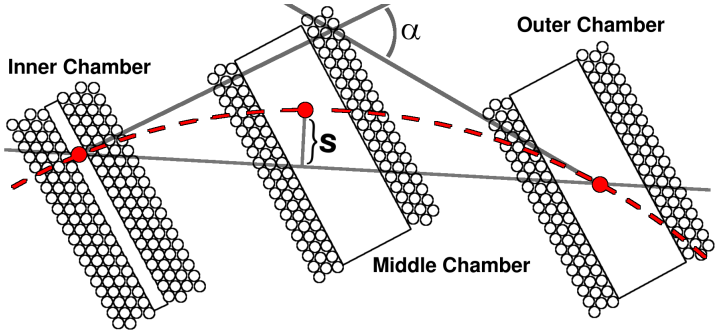

Figure 2.17: Sagitta illustration of a muon hitting the three MS layers.

to measure the changes of the relative position of the chambers as well as their deformations.

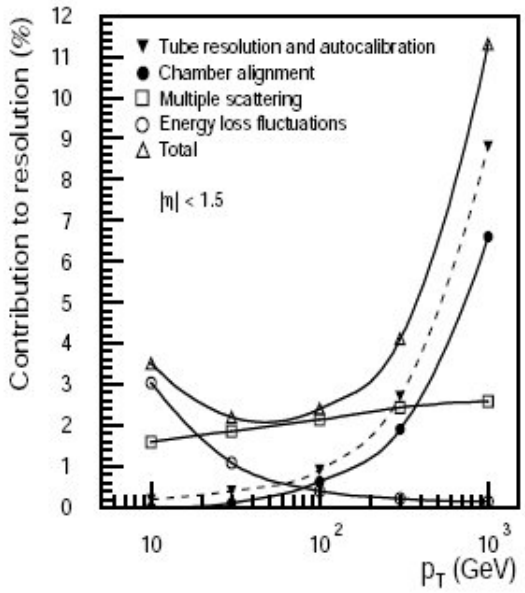

Figure 2.18: Contributions to the momentum resolution for muons reconstructed in the Muon Spectrometer as a function of transverse momentum for $|\eta|<1.5$.

Figure 2.18 shows the various contributions to the muon momentum resolution. One observes that at low energies the resolution is primary affected by the energy loss, while for higher energies by the tube resolution and the chamber alignment. The multiple scattering contribution to the resolution is small and constant, of 2%, all along the muon momentum range [45].

2.2.5 Toroidal Magnet system

In this section the ATLAS Toroid superconducting magnets and the muon spectrometer magnetic field map (B-map) are presented. The description will be detailed in order to introduce the study of the magnetic field sensors and the B-map that follows in chapter 3.

The motivation for a strong and well modeled magnetic field in the muon spectrometer (MS) area is driven by the need of an excellent muon transverse momentum measurement. For this reason the MS is immersed in a toroidal magnetic field, produced by three toroid superconducting magnets, located one in the Barrel area and one in each End Cap area. Fig. 2.19 illustrates the position of the magnet coils.

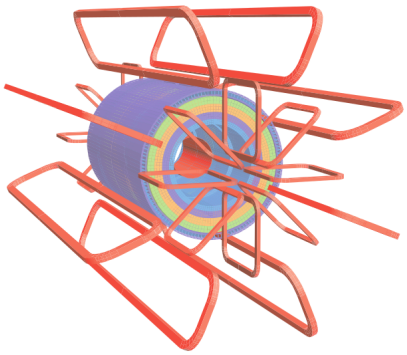

Figure 2.19: The coils of the Barrel and End Cap Toroids.

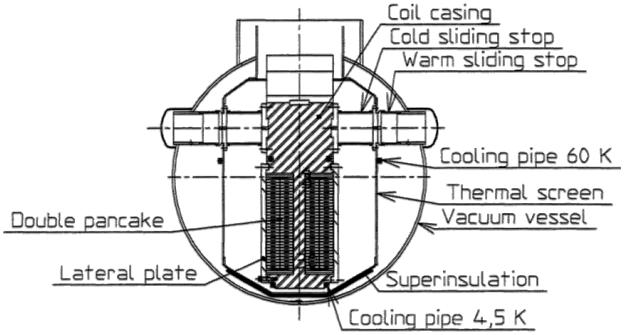

Figure 2.20: Barrel coil cross section.

Barrel Toroid (BT)

The BT consists of eight coils. Each coil is 25 m long, has 5 m width and weighs about 300 t. In the center of a coil there are 4 rows of 32 Nb-Ti superconducting filaments cables (two pancakes), encapsulated in a pure Aluminum casing. The cooling of the cables is achieved thanks to four tubes filled with helium kept at 4.3 K which pass through the casing, as shown in Fig. 2.20. The Aluminum casing is then enclosed in a vacuum stainless-steel vessel, which is called cryostat. The nominal current passing through the superconducting cables is 20.4 kA. To prevent an operation asymmetry between the 8 coils provoked by magnet quenches, safety dampers are installed along all the coils. When a quench is detected, the dampers will immediately increase the cable resistivity so that the magnets are set out of operation. The magnetic field surrounding the MS starts from 0.15 T, for regions

far away from the coils, and goes up to 2.5 T close to the coils, with a mean value of approx 0.5 T.

Besides the important coil weight, the coils are also exposed to a strong magnetic force, of $\approx$ 1400 t. Hence, the detector designers had to put a great effort to ensure coil stability. For this reason, along each coil there are seven metallic supports embedded in the cryostat. These supports stabilize the coil itself, avoiding its deformation, especially due to the tensions produced while turning On/Off the magnets. The coils are linked with each other in such a way that they are assembled radially around the beam axis. The overall toroid mechanical support consists of eight inner, middle and outer rings. The magnetic system shares the same rigid metallic structure as the muon chambers. The Large muon chambers are located directly on the metallic structure, while the small chambers are located on the coil. The whole structure is supported by the ATLAS "legs".

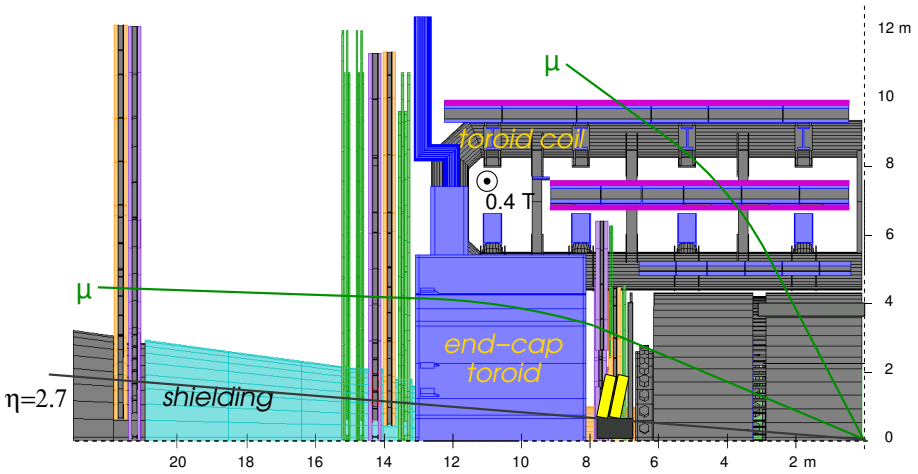

Figure 2.21: Muon track in the MS.

In Fig. 2.21 one can see the deflection of a muon track passing through the Barrel area.

End Cap Toroid (ECT)

There are two ECTs, one at each detector side, providing the necessary bending power to the muons traversing the forward detector area. The ECT is a compact object composed of eight cold masses consisting of coils, each one put inside a keystone box, as shown in Fig 2.22. The boxes are then grouped together and placed inside one single vacuum cryostat.

In contrast with the BT, the installation and maintenance of the ECT is much

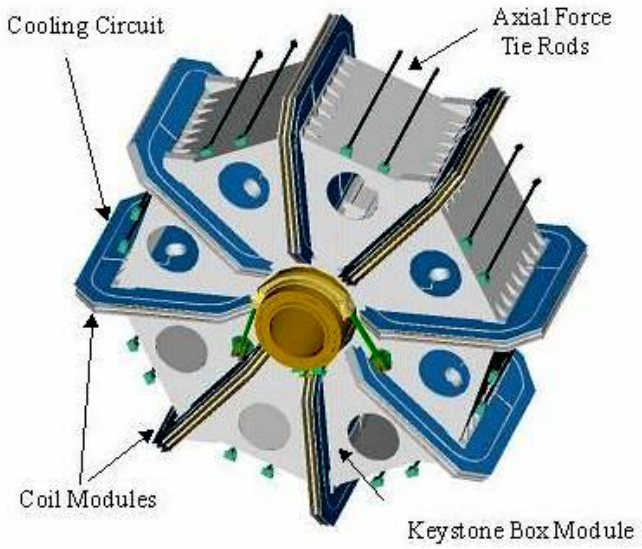

Figure 2.22: The End Cap Toroid cold mass.

easier, because of its easy-access location. The total weight of each coil reaches 220 t. The ECT provides the forward region with a magnetic field of the order of 0.2 to 3.5 T.

Magnetic field map (B-map)

Among the most important and challenging tasks is the modeling of the toroid magnetic field. For the muon momentum determination, the field integral along the muon trajectory needs to be as accurate as possible. However, the highly heterogeneous magnetic field, along with the gradient of the field, reaching 1 mT/mm close to the coil, makes this task very complicated. More precisely, the difficulties involved are:

- Coil position: The magnetic field produced by the toroid magnet can be easily estimated using the Biot-Savat law. However this requires a precise knowledge of the coil position. The nominal coil positions is known with a 5 mm accuracy. Furthermore, additional deformation and position shifts over the time are expected, mainly due to the gravitational force, the magnetic loads permanently applied to the system, and finally, the important mechanical stresses that a coil undergoes during the magnets switch On/Off.

- Magnetic perturbation: Inside the ATLAS detector there are a lot of magnetic materials which can provoke magnetic perturbations. The most important

sources of perturbation affecting the field are the tile calorimeter, its return-yoke and the ID and MS shielding disks. The effect of the above sources on the magnetic field has been evaluated to be of the order of 4%, using the ATLM B-field simulation package [46]. There are additional, less significant, magnetic structures that can produce up to 10% local magnetic perturbations in the inner MDT layer. Such structures are the traction cylinders enabling the movement of the detector horizontally along the z-axis. These perturbations are modeled by the TOSCA package [47]. In Fig. 2.23 the detector elements distorting the Biot-Savat field lines are shown, with a color code indicating their significance.

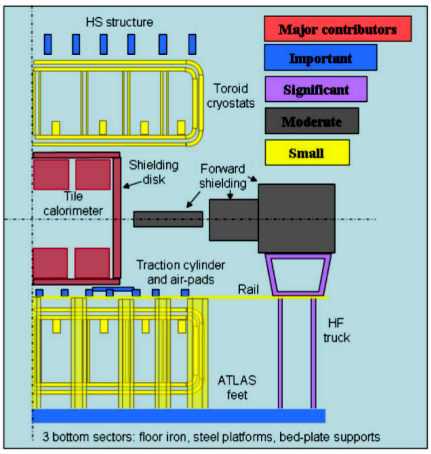

Figure 2.23: Sketch of the ATLAS detector material causing magnetic perturbations.

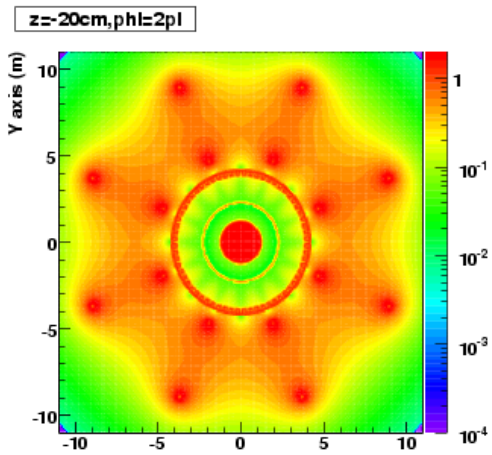

Figure 2.24: Magnetic field of the toroid magnet in the Barrel $r-\phi$ plane.

The problem of the coil position determination was worked out with the installation of 1840 3D hall cards, mainly on the MDTs, which measure the Toroidal magnetic field. These measurements are used for the reconstruction of the coil position. The coil positions estimated with the above method have a good accuracy, and thus these are used for the magnetic field map production. In Fig. 2.23 the field strength in the $r-\phi$ plane is shown. A detailed study on these sensors follows in chapter 3.

Chapter 3

Study of the ATLAS Magnetic field sensors

This chapter presents a study of the Toroidal magnetic field sensors, which are mounted on the chambers of the Muon Spectrometer [48], and it is based on the sensor measurements taken during 2011. This work was performed in the framework of my qualification task for the ATLAS collaboration, aimed to be a step towards the implementation of an online monitoring system of these sensors. I focussed on the stability of the measurements and the definition of quality criteria in order to be able to spot badly behaving probes, and to build a set of "good" sensors. The "good" sensors can be used as reference for the monitoring of the system and to define effective criteria to automatize as much as possible the detection of possible abnormal behaviour. In the course of this assessment study, some unexpected variations have been spotted which were explained in term of influence of nearby block of steel for Barrel sensors and in terms of misalignment of the Toroids for the End Cap sensors. For the latter study, the magnetic field map has been used and thus a study of its accuracy has been also performed.

3.1 Introduction

As it has been discussed in the previous chapter, the ATLAS detector is equipped with one Solenoid and three Toroids magnets, one Barrel and two End Caps [49] [48]. The reconstruction of muon tracks requires precise knowledge of the magnetic field amplitude at every position in the detector. The magnetic field in an air-core magnet can be computed once the positions of all conductors are known and the perturbation from magnetic elements, such as the iron return yoke of the Solenoid, are taken into

account. The position of the conductors is determined using the measurements of the magnetic field taken by sensors mounted mainly on the MDT Stations, see figure 3.1 and 3.2 [50]. Once the positions of the conductors are known, they are used to build a map of the magnetic field, the B-map, which is used for the particle reconstruction.

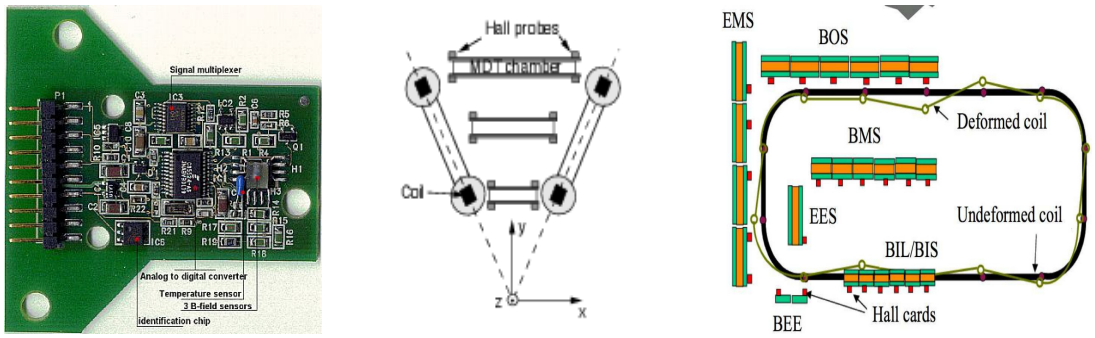

Figure 3.1: Left: 3D Hall probes, Middle: Transverse plan of ATLAS muon chambers, Right: Positions of Barrel muon chambers and B-sensors in the plane of a magnet coil.

Each sensor is a 3D Hall card. There are 1776 active 3D Hall cards, 985 located on Barrel muon chambers and 619 located on End Cap muon chambers, see table 3.1. The position of these sensors is determined using dedicated alignment algorithms. The presentation of the sensors study is organised in sections as follows:

- The variables that will be used in this analysis are discussed in section 3.2.
- In section 3.3, a set of quality requirements on sensor measurements is defined.
- In section 3.4, sensors are classified according to their magnetic field measurements stability in time.
- Groups of sensors that exhibit an abnormal behavior are examined in section 3.5.
- In section 3.6, the B-map predictions are compared with sensor measurements for 2011 and 2012.
- Finally, in section 3.8, two ways of implementing an online monitoring system for sensors are suggested.

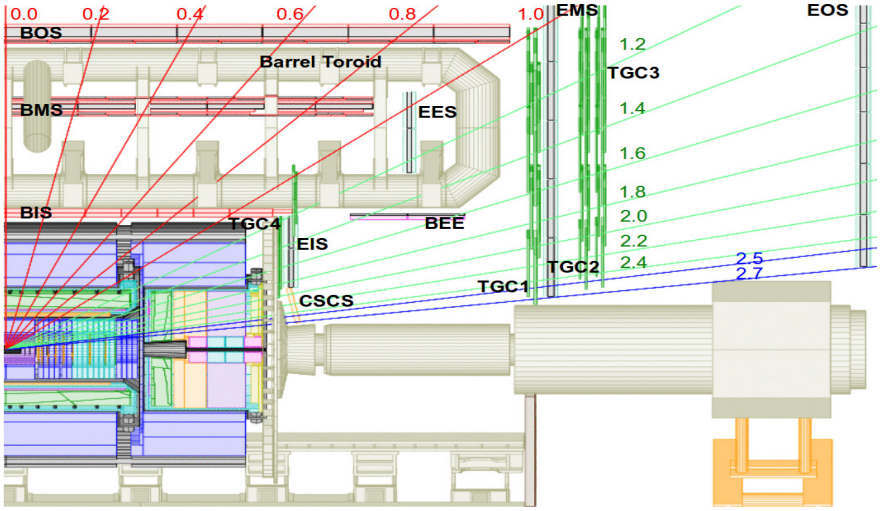

Figure 3.2: ATLAS detector, longitudinal plan.

Barrel	sensors	End Cap	sensors	Other	sensors
BIS	254	CSC	64	TEC	64
BIL	213	EMS	256	BEE	64
BOS	144	EIL	127	PB	40
BOL	104	EML	160	LAR	3
BMS	142	EEL	12	TEB	1
BIM	20				
BIR	16				
BMF	24				
BOF	32				
BOG	36				
total	985		619		172

Table 3.1: Number of sensors located on muon chambers.

3.2 The available information

Each Hall card has four probes that measure the three components of the magnetic field along the local xyz axis of the sensor, and the temperature, every 5 minutes. Each sensor output is calibrated according to its temperature [51]. The achieved resolution precision is better than 2 G. These measurements are stored in an Oracle database.

Additional useful information for the analysis is the current amplitude in the Toroids (I_T) and Solenoid (I_S) magnets and the sensor positions, which are derived

using the alignment algorithm. Until now, the update of sensor positions in the database is a complex procedure which is done approximately once per month but there are plans to automatize the sensor positions insertions every time an update is done at the level of the MDT alignment [52]. Finally, a flag variable ($ErrFlag$) related to the calibration procedure is available. It is a decimal number which should be converted to binary, to recover information about the handling of the calibration procedure. All the above information is also stored in the database.

Due to the large number of measurements and the interface difficulties to handle large amounts of data, mean values over 4 hours periods (about 48 measurements) are used. The mean values of the magnetic field components and the temperature over 4 hours, are henceforth noted: B_x, B_y, B_z and T. The standard deviation of these values are noted dB_x, dB_y, dB_z and dT, respectively. The time interval containing the measurements used for the computation of the mean values is also stored in the database. Finally the stored measurements are tagged with the name of the sensor[1]

3.3 Measurements quality

In order to probe the sensor stability during 2011, the mean value and the standard deviation of the magnetic field amplitude and the temperature, are computed using 2011 measurements for each sensor. These values will be noted as $\bar{B}$, $\sigma_{\bar{B}}$, $\bar{T}$ and $\sigma_{\bar{T}}$, respectively.

A first attempt was made using all the available measurements when Toroids and Solenoid magnets were simultaneously on. A noticeable number of sensors had large $\sigma_{\bar{B}}$, despite the fact that they seemed stable in time. These large $\sigma_{\bar{B}}$ values are due to few bad quality measurements. Hence, the solution was to protect the analysis of defective measurements. This was done by defining a set of requirements on the variables $B_x, B_y, B_z, T, dB_x, dB_y, dB_z$, dT and $ErrFlag$.

3.3.1 Requirements on measurements

Here are presented all cuts used to select good quality measurements. The exact value of each requirement is chosen in such a way that potentially bad measurements

[1] An example of the structure of sensor names is BIL6A13_BSE_ORO; where the first field $BIL6A13$ gives the name of the station on which the sensor is mounted BIS, and its location along the Z axis in the Barrel area, 6 (or in radius if it is located in the End Cap area). The A indicates the detector side, i.e possitive or negative z-possition, and 13 indicates the ϕ sector. The last two fields indicate the sensor position on the station

are excluded, while the statistics is kept high. However, an optimisation is still possible.

- Toroid and Solenoid currents: During 2011 several shut-downs took place. Thus, only measurements taken when both magnets were operating in stable conditions should be used. The nominal current for the Toroids is considered to be 20.4 kA and for the Solenoid 7.730 kA. Actual requirements in this analysis are: $I_T >$ 20399.9 A and $I_S >$ 7729.9 A. The value of the current amplitude is known with precision better than 0.2 A.

- $ErrFlag$ cut: As mentioned in section 3.2, $ErrFlag$ is a variable related to the calibration procedure. Each decimal of the value corresponds to a binary number. The averaging of all variables over four hour periods is a problem for the treatment of this flag variable. Finally, the cut applied was $ErrFlag<200$ and $ErrFlag!=12$ [53].

- B-related cuts: As seen in section 3.2, B_x, B_y and B_z values are the mean of about 48 measurements taken during 4 hours. Therefore, interesting variables are their standard deviation dB_x, dB_y and dB_z.

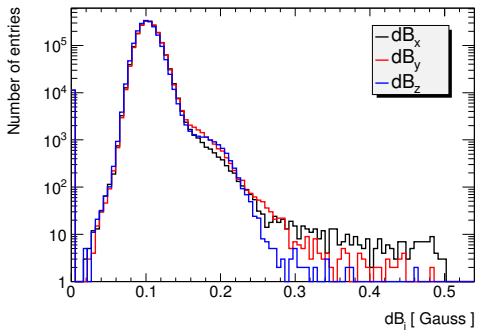

Figure 3.3: Distributions of dB_x, dB_y and dB_z (G) measuremets taken by all sensors during 2011.

Magnetic field measurements should be stable over time. Consequently, the dB_x, dB_y and dB_z values are expected to be very low. The requirement for them is to be below 0.25 G, so that the distribution tail of dB_i, shown in figure 3.3 is removed. A lower cut is also used, since some sensors provide the exact same measurement of the magnetic field components for a long period of time. Such behavior could be an indication of electronics damage, or failure of the read-out procedure. Therefore, dB_x, dB_y and dB_z are required to be above

0.01 G. Finally, an upper limit cut on the magnetic field modulus, noted B, requires $B < 2\ 10^4$ G, since higher values of B are not expected in the detector areas where the sensors are located. This requirement rejects measurements which are not properly calibrated or measurements which were taken while an electronic problem occurred.

- T related cuts: A temperature measurement out of the expected range and/or hight dT value could indicate a sensor malfunctioning. In order to suppress such measurements, two cuts are used.

  Expected temperature lies in the interval 15 °C $< T <$ 30 °C. This range is large because some sensors are expected to measure mean temperatures dispersed away from 23°C, which is the mean predicted temperature in the cavern. Such variation inside the detector is due to the sensor location inside the cavern. For instance, sensors located close to the climatisation systems are expected to have a much lower temperature. The distribution of all T and dT measurements taken by all sensors during 2011 is shown in figure 3.4. Temperature measurements above 40 °C, which produce the bumps observed in the right tail of the temperature distribution, come from two specific sensors, see section 3.4.2. From the right plot in figure 3.4 one sees that sensor temperature measurements are very stable during the year. Hence, dT is not expected to be large, and thus the cut was set to 0.2 °C.

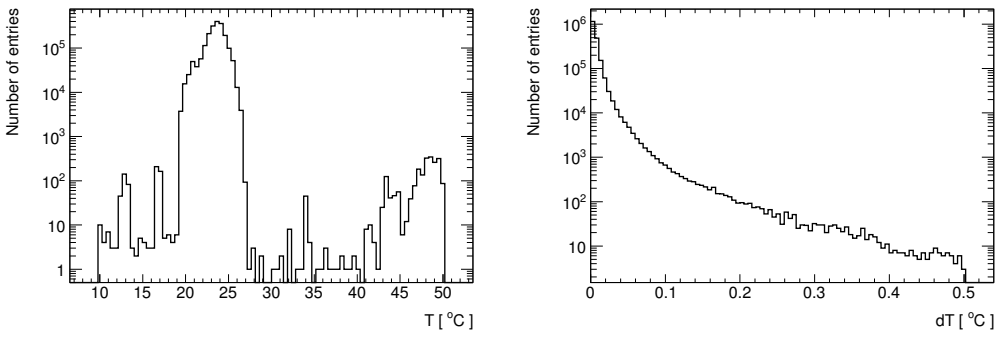

Figure 3.4: Distribution of T and dT [°C] measuremets taken by all sensors during 2011.

The impact of each set of cuts on 2011 measurements, when both Toroids and Solenoid magnets were on, is shown in table 3.3.1. When the detector operates under nominal conditions, only 0.9% of the recorded measurements in the database, are excluded, mainly due to B-related cuts. As can be seen, there is an overlap

between the cuts. When a measurement fails the T-related or the Error flag-related cuts, it likely fails also the B-related cuts. As will be shown in section 3.4.2, the majority of the probes have all (100%) or almost all (99%) of their measurements passing the selection cuts, however a small number of sensors have some (>1%) of their measurements failing the cuts.

Cut used	% of measurements cut
Error flag	0.15
B-cuts	0.71
T-cuts	0.51
All cuts	0.89

Table 3.2: Percentage of measurements trimmed after applying each set of cuts separately.

3.4 Sensor classification

In section 3.3, a set of cuts was defined in order to sort out measurements taken during stable sensor operation from measurements taken during a sensor malfunction. All measurements passing the selection requirements were used for the computation of the magnetic field mean value during 2011, $\bar{B}$ and its standard deviation $\sigma_{\bar{B}}$. Each sensor $\sigma_{\bar{B}}$ quantifies its B measurements stability in time. A second sensor quality discriminative variable is F_{value}, which is defined as the fraction of good measurements used to compute $\bar{B}$. The closer the F_{value} is to 1, the better the sensor response is.

3.4.1 Stability in time: $\sigma_{\bar{B}}$

The first classification variable is $\sigma_{\bar{B}}$. It is computed using all 2011 measurements that satisfy the criteria defined in section 3.3.

$\sigma_{\bar{B}}$ G range	without cuts	with cuts
< 0.02	4	0
$[0.02 - 1[$	1607	1649
$[1 - 2[$	59	54
$[2 - 10[$	74	59
$[10 - 50[$	10	4
>50	22	1
total	1776	1767

Table 3.3: Number of sensors in each $\sigma_{\bar{B}}$ range.

In table 3.3 the sensors are splitted in six groups according to their $\sigma_{\bar{B}}$ value. This categorisation is performed for both cases where the selection on the measurements is applied or it is not applied. One observes that after applying all cuts, a significant shift of sensors $\sigma_{\bar{B}}$ towards lower values occurred. The number of sensors with $\sigma_{\bar{B}} < 1$ G is increased by 2.3%. Therefore, measurements filtering presented in section 3.3 is justified.

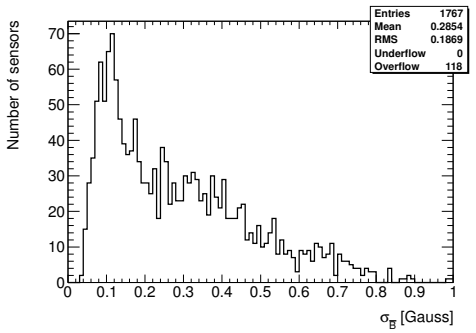

Figure 3.5: $\sigma_{\bar{B}}$ value after applying all cuts on measurements.

Figure 3.5 shows the distribution of $\sigma_{\bar{B}}$ for all sensors with $\sigma_{\bar{B}} < 1$ G. Each part of the distribution is mainly filled by sensors sharing common characteristics, such as location inside the detector (BOS, BIS etc), their distance from electronics and the strength of the magnetic field which they measure. One also sees in table 3.3, as well as in figure 3.5, that the total number of sensors after applying the cuts is 1767. As will be discussed in section 3.4.2, nine sensors have all their measurements failing the requirements.

Figure 3.6 shows the sensor percentage of each category that have a $\sigma_{\bar{B}}$ in the ranges indicated in the Y axis. The X axis indicates the sensor categories. The first bin "All" includes all the 1776 sensors. The next 12 bins are for the main sensors categories, i.e those wich have more than 40 sensors. Finally, the last X axis bin "ELSE" includes all the remaining sensors, which belong in smaller categories. One notes that:

- Sensors located on EMS and EML chambers have the most stable magnetic field measurements.
- Sensors located on large chambers have more stable magnetic field measurements than those located on small chambers.
- $\approx$ 15% of sensors located on BOS and BOL chambers have $\sigma_{\bar{B}}$>0.8 G. These sensors will be studied in section 3.5.1.

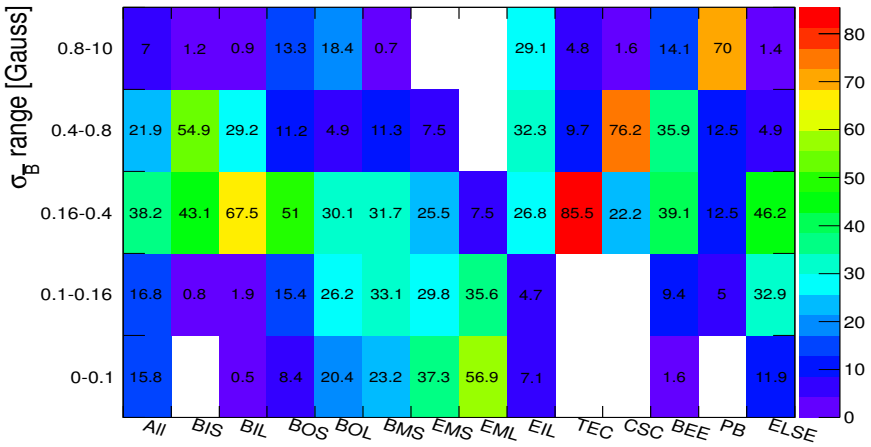

Figure 3.6: Percentage of sensors of each category which have a $\sigma_{\bar{B}}$ value in the range indicated in the Y axis.

- Sensors located on EIL chambers seem unstable. They will be studied in section 3.5.2.

It has to be stressed that the criteria defined in section 3.3 are expected to exclude contribution of B measurements with high fluctuations caused from malfunctioning sensors. However, a high $\sigma_{\bar{B}}$ value could still indicate a sensor instability which the cuts were not able to detect. Additionally, a high $\sigma_{\bar{B}}$ value could also be due to sensor position shift or magnets movement, which is completelly independent of the sensor operation. Consequently, one should use the $\sigma_{\bar{B}}$ values with precaution, since they are computed using measurements taken during a long period of time and thus picture the fluctuation of the B measured without directly indicating the reason of the fluctuation.

3.4.2 Fraction of good measurements: F_{value}

F_{value} represents the fraction of each sensor measurements that pass the criteria defined in section 3.3. It allows to identify sensors with low $\sigma_{\bar{B}}$ but with a noticeable number of measurements vetoed. It's defined as:

$$F_{value} = \frac{number\ of\ good\ measurements}{total\ number\ of\ measurements} \tag{3.1}$$

In table 3.4 and figure 3.7, it can be seen that 66% of sensors have all their measurements satisfying the requirements. All categories, except sensors located on

F_{value} range	number of sensors
1	1170
$[0.99 - 1[$	563
$[0.9 - 0.99[$	21
$]0 - 0.9[$	13
0	9
total	1776

Table 3.4: Number of sensors in each F_{value} range.

EMS and EML chambers, have a significant fraction of their sensors with a F_{value} in the range $[0.99, 1[$. There are nine sensors with all their measurements failing the requirements, i.e. with $F_{value} = 0$. Table 3.5 shows the values of $\bar{B}, \sigma_{\bar{B}}, \bar{T}$ and $\sigma_{\bar{T}}$ of these defective sensors without applying any cut on their measurements.

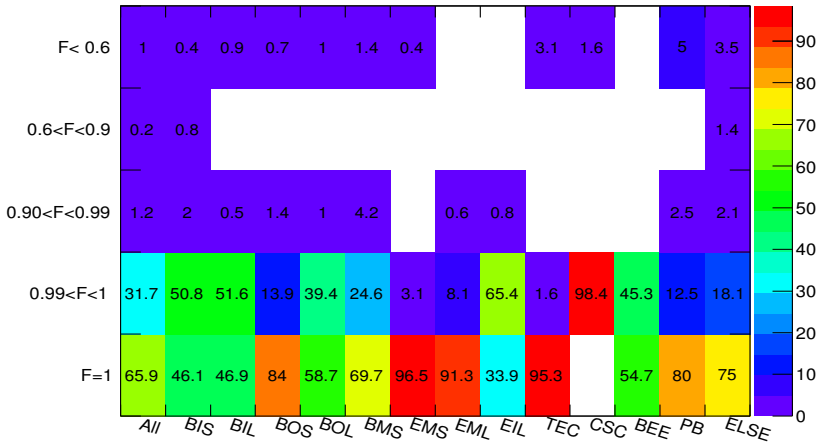

Figure 3.7: Percentage of sensors of each category which have a F_{value} value in the range indicated in the Y axis.

name	$\bar{B}$ (G)	$\sigma_{\bar{B}}$ (G)	T (°C)	$\sigma_{\bar{T}}$ (°C)
TEC1A14_BSE_OUR	0.9	0.0	19.6	0.0
TEC1C04_BSE_OUR	0.6	0.0	20.4	0.0
CSCLC01_BSE_IHS	1.02	0.0	22.9	0.0
BIS6C14_BSE_OHV	11.5	0.0	100.0	0.0
EEL1A05_BSE_IHS	173187839.7	119.6	22.3	0.16
BOL1A05_BSE_ORA	173188103.7	1.8	16777.2	0.0
BIL6A01_BSE_OHV	7040.2	348.6	23.6	0.81
BOS4A06_BSE_IHV	4554.1	1.2	49.1	0.9
EMS3A12_BSE_IRL	1001.2	0.7	46.5	2.3

Table 3.5: List of sensors having all their measurements failing the requirements.

The first four sensors of table 3.5 have all their dB_x, dB_y, dB_z and dT values equal to zero, and furthermore, the B central values are much below expectations. Sensors located in TEC, CSC and BIS chambers are expected to measure a B greater than 1000 G. Such a behavior probably indicates a problem of electronics. The EEL1A05_BSE_IHS sensor had all its $ErrFlag$ values equal to 12. This indicates a calibration problem, and explains why the B has a large value, much above the expected limit of 2 T. Nevertheless, the temperature probe seems to operate normally. One gets the same behaviour for the BOL1A05_BSE_ORA sensor. During all 2011, $ErrFlag$ was equal to 65280. In addition to the magnetic field probes, the temperature probe is also defective. The sensor BIL6A01_BSE_OHV had all its dB_x and $dB_y \approx 10$ G. These values are much above the expected, (dB_x and $dB_y < 0.25$ G), something which indicates high sensor instability over time. Finally, sensors BOS4A06_BSE_IHV and EMS3A12_BSE_IRL had all their temperature measurements much above 30 °C.

3.4.3 Classification

The previous two sections have shown that the vast majority of sensors are stable during 2011. Using the two quality variables, $\sigma_{\bar{B}}$ and F_{value}, a sensors classification can be built (see table 3.6) which makes it possible to:

1. Identify all sensors that need to be more closely examined.
2. Use this classification as a reference for future sensors stability checks.
3. Use it for the implementation of the sensors monitoring system. Depending on the category in which the sensor belongs, different threshold on the deviation of an individual B measurement from the sensor mean value can be used.

	$0.01<\sigma_{\bar{B}}<0.8$ (G)	$0.8<\sigma_{\bar{B}}<2$ (G)	$2<\sigma_{\bar{B}}<10$ (G)	$10<\sigma_{\bar{B}}<50$ (G)	$\sigma_{\bar{B}}>50$ (G)
$F_{value}=1$	perfect	good	unstable	bad	very bad
$0.99<F_{value}<1$	good	good	unstable	bad	very bad
$0.9<F_{value}<0.99$	unstable	unstable	bad	very bad	very bad
$0.6<F_{value}<0.9$	bad	bad	bad	very bad	very bad
$F_{value}<0.6$	very bad	very bad	very bad	very bad	very bad

Table 3.6: Sensor classification based on its $\sigma_{\bar{B}}$ (G) and F_{value} values.

Low $\sigma_{\bar{B}}$ in combination with a F_{value} value close to 1 indicates high stability. Sensors with low $\sigma_{\bar{B}}$ and low F_{value} are those having some B outliers not fulfilling the requirements. The opposite configuration, i.e high $\sigma_{\bar{B}}$ and high F_{value}, indicates

a significant fluctuation of sensor B measurements over time, which however pass the cuts. This could be due to a sensor or magnet (mainly ECT) position shifts. Finally when both values are bad, i.e high $\sigma_{\bar{B}}$ and low F_{value}, the sensor is defective and needs to be closely examined and probably replaced.

Henceforth, PB, LAR and TEB sensors will not be taken into account in this analysis, since they are used to measure magnetic perturbations, and thus they are not directly used for the B-map production. Consequently, the total number of sensors that will be used is 1732. The previous classification leads to the following results:

	$0.01<\sigma_{\bar{B}}<0.8$ (G)	$0.8<\sigma_{\bar{B}}<2$ (G)	$2<\sigma_{\bar{B}}<10$ (G)	$10<\sigma_{\bar{B}}<50$ (G)	$\sigma_{\bar{B}}>50$ (G)
$F_{value}=1$	1095	29	13	0	0
$0.99<F_{value}<1$	505	25	26	0	0
$0.9<F_{value}<0.99$	16	2	1	0	1
$0.6<F_{value}<0.9$	0	4	0	0	0
$F_{value}<0.6$	3	0	0	0	0

Table 3.7: Number of sensors in each category: perfect, good, unstable, bad and very bad.

Table 3.7 shows how many sensors belong to each category. There are 1723 sensors in the table. As mentioned in section 3.4.2, there are nine more sensors which belong in the very bad category, see table 3.5. These sensors are not included in this table as all their measurements fail the requirements, and thus the $\bar{B}$ and $\sigma_{\bar{B}}$ cannot be computed for them. One can deduce that 94.1% of the sensors were perfect or good during 2011, and only 18 sensors (1%) belong to the bad or very bad categories.

3.5 Large $\sigma_{\bar{B}}$ sensors

As shown in section 3.4, some groups of sensors located in specific detector areas, have $\sigma_{\bar{B}}$ values significantly higher than expected. These sensors are mainly located in the Barrel on BOS and BOL stations, and in the End Cap on EIL chambers. A closer examination of these 2 categories follows.

3.5.1 BOS/L problematic sectors

As seen in section 3.4.1, 14% of the BOS and 18 % of the BOL sensors have $\sigma_{\bar{B}}$ larger than 0.8 G, while all other sensors located on these chambers have $\sigma_{\bar{B}}$ lower than about 0.5 G.

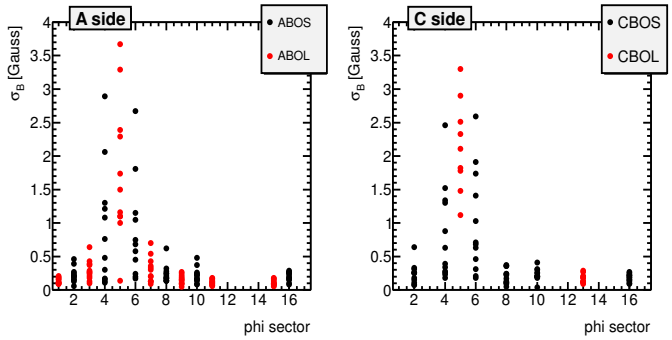

Figure 3.8: $\sigma_{\bar{B}}$ against phi sector.

In figure 3.8 the $\sigma_{\bar{B}}$ is plotted against the phi sector. One sees that the most affected phi sectors are the 04, 05 and 06. These sectors are located in the top of the detector. An investigation of these sectors shows that the more affected sensors are: BOSxx04_BSE_RO, BOSxx06_BSE_HV and BOLxx05_BSE_xx, i.e these located on the BOS muon chambers, in the 04 and 06 phi sector, near to the read-out (RO) and high voltage (HV) electronics, respectively, see fig. 3.9. For sensors located on BOL chambers, both RO and HV sensors in the 05 phi sector are affected.

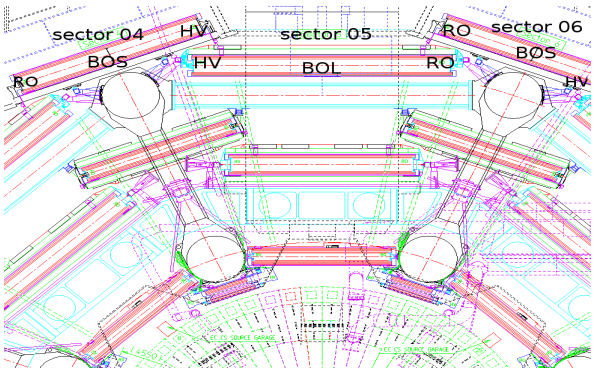

Figure 3.9: Location of the bad sensors.

In figures 3.10 and 3.11, the difference B - $\bar{B}$ is plotted as a function of time, using different color for each sensor. A magnetic field jump of the order of 1 to 6 G can be seen, which starts and ends at exactly the same date (3rd May 2011 and 1st of September 2011, respectively) for BOS and BOL sensors. The jump seems related to the detector shut-down, as it starts and ends right after the magnets were switched On/Off. Work realized inside the detector during this period or the switch On/Off of the magnets could destabilize sensor operation, or even cause sensor/magnets displacement.

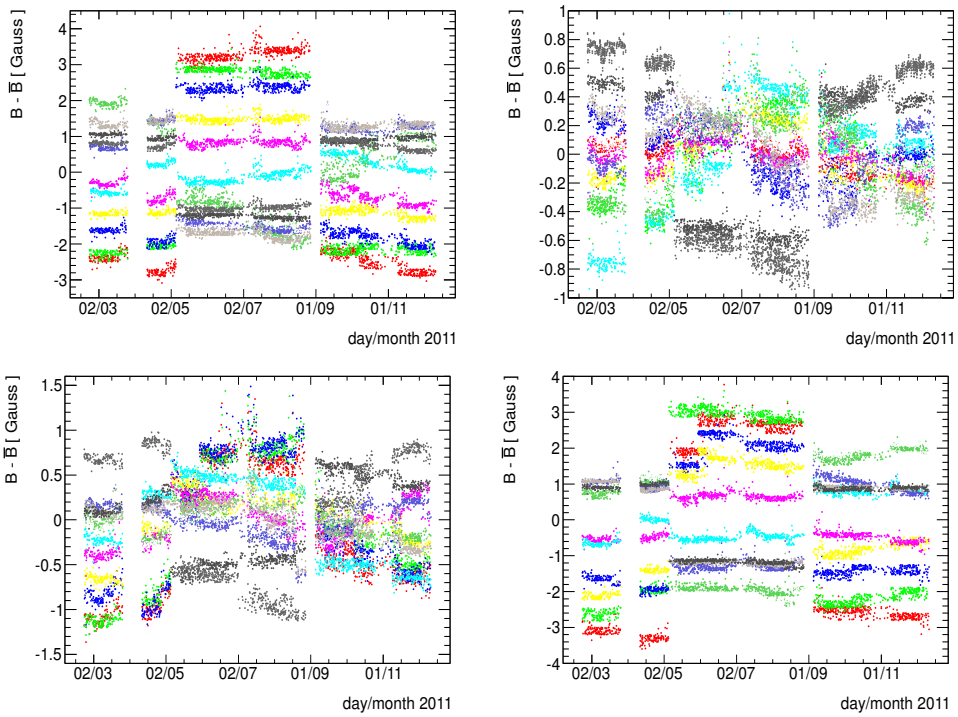

Figure 3.10: B - $\bar{B}$ as a function of time. Top: BOS phi sector 04, Bottom: BOS phi sector 06. Left RO and right HV.

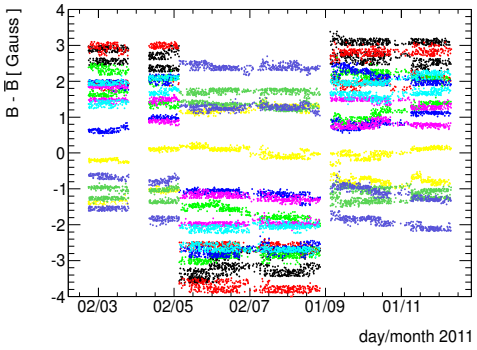

Figure 3.11: B - $\bar{B}$ as a function of time for sensors located on BOL chambers in the 05 phi sector.

In order to explore this behavior several checks were performed. First, possible temperature fluctuations were investigated since they could affect sensor functioning. However, as shown in figure 3.12 no such correlations between the ΔT and ΔB are observed. A shift in the position of the sensors could also be an explanation of the magnetic field jump, as sensor position shifts of 100 μm can induce changes of B up

to 1 G. Figure 3.13 shows the correlation between ΔB and ΔR, where ΔB is the difference in the magnetic field measurement between May and June and ΔR is the difference in radial sensor position over the same period. The sensor position shifts are too small to explain the variations of B, and moreover, no correlations between ΔB and ΔR are seen. Finally, the reset stages of the sensor calibration procedure had been suspected, still, this could not be directly checked as, unfortunately, the time of these resets had not been recorded during 2011. In order to probe this scenario a cycle of sensor electronic resets followed by a read-out procedure has been conducted during July 2012. The results of this study have shown that the effects are too small to explain the observed jumps.

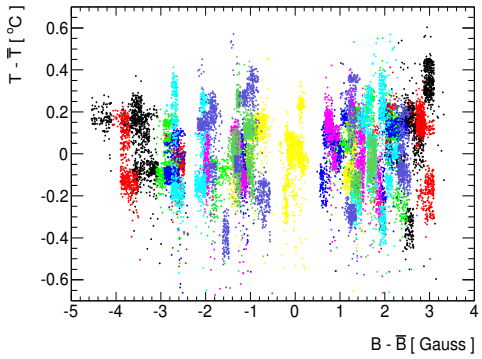

Figure 3.12: Temperature fluctuations vs magnetic field fluctuations for BOL phi sector 05 sensors.

The more telling clue regarding the observed jumps is their clear geometrical pattern. As we have seen, sensors located on phi sectors at the top of the detector have the largest sigma.

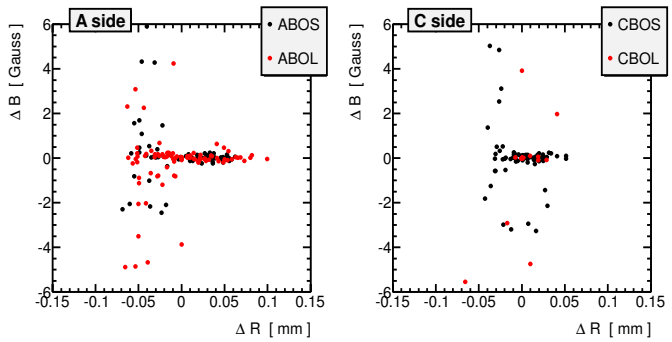

Figure 3.13: ΔB vs ΔR for BOS and BOL sensors.

An additional potent geometrical pattern comes from the following observation.

As discussed, sensors located on phi sector 05 situated at both ends of the chambers, i.e both HV and RO sensors, indicate changes of the magnetic field, while only sensors on HV side for sector 06 and on RO side for sector 04 show similar changes. The "stable" sensors, i.e on RO side for sector 06 and on HV side for sector 04, although they measure a stable B, their magnetic field components do exhibit a "jumpy" behavior. Figure 3.14 shows the B component variations over time for all BOSxx04_BSE_HV sensors. The magnetic field jump goes up to 9 G. This behavior can be explained by a rotation of the sensor around a fix point in such a way that only the components and not the magnitude are affected. This scenario explains the behavior of all sensors located at both ends of the 04 phi station, if a rotation around a point at the level of the HV sensors is applied. Very symmetrically, all the measurements of the sensors of sector 06 can be explained by a rotation around a point at the level of the RO sensors, see fig. 3.9.

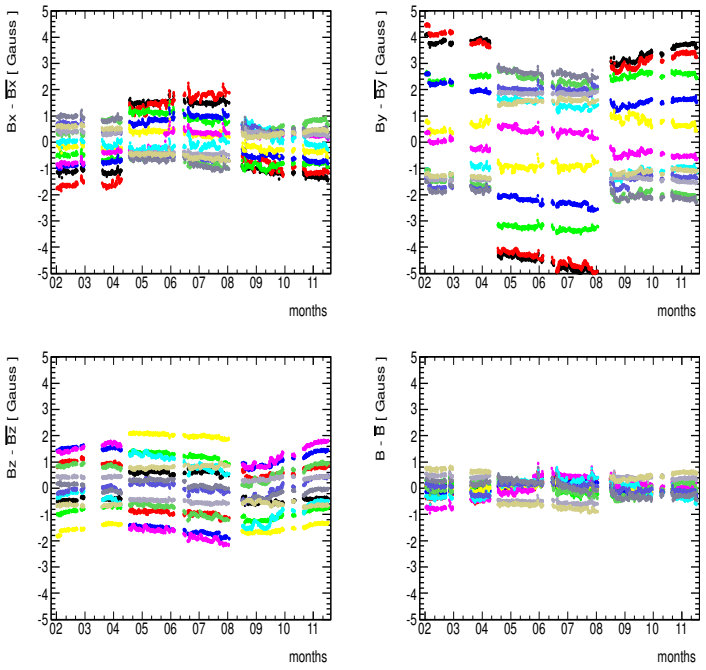

Figure 3.14: Fluctuations of the magnetic field magnitude B and the field components B_i against time for BOS sensors, phi sector 04 HV.

Finally, a correlation of the ΔB with the z position along the beam for the affected group of sensors is examined in figure 3.15. One sees that there is a clear pattern. In both detector sides, and for both BOS and BOL sensors, the largest ΔB is observed for Z=1,2, i.e in the central area. The ΔB sign of this difference is inversed after Z=3. BOL and BOS sensors exhibit a mirrored behavior, in all Z

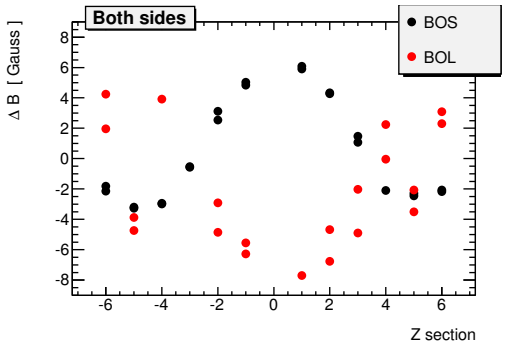

Figure 3.15: ΔB vs Z section for BOS and BOL sensors.

sections but 5.

People responsible for the tasks performed on the muon chambers were contacted, and confirmed that during the shut-down period, no interventions that could explain the jump have been realized in the vicinity of BOS and BOL areas.

The last potent explanation, which is very intriguing, but requires an additional study for its validation, is that the ATLAS portable cranes affect the magnetic field. There are two metallic cranes, which weight about 140 t each, located few meters above the Z=1 section of the detector. When a shut-down takes place these cranes are used in order to move objects, i.e the wheels etc. If after a shut-down the cranes are not placed at the same position, the sensors located at the top of the detector (phi sectors 03 to 07) and at low Z, will eventually measure a different magnetic field than before the shut-down. This is a very promising scenario. However, for its validation, it needs a new simulation which includes perturbations coming from the crane.

To summarize, in the above study, BOS/L sensors with high σ_B values were analyzed. It came out that the high σ_B values were due to magnetic field jumps, observed between 3/5/2011 and 1/9/2011. The main potential reasons explaining the jumps have been examined. A geometrical pattern is observed, which involves sensors located on chambers of the top phi sectors. A pattern is also observed along the Z axis. The behavior seems related to the magnets switch On/Off, and to the ATLAS metallic cranes. However, more detailed studied involving simulations are needed in order to verify the above scenarios.

3.5.2 EIL problematic sectors

As seen in section 3.4.1, 70% of EIL sensors have a $\sigma_{\bar{B}}$ higher than 0.8 G. A more detailed study has shown that the defective sensors are those located in the inner

part of the wheel (noted R=1,2 for the first and second ring, respectively) on the negative Z side of the detector. All phi sectors but 01 and 03 are affected.

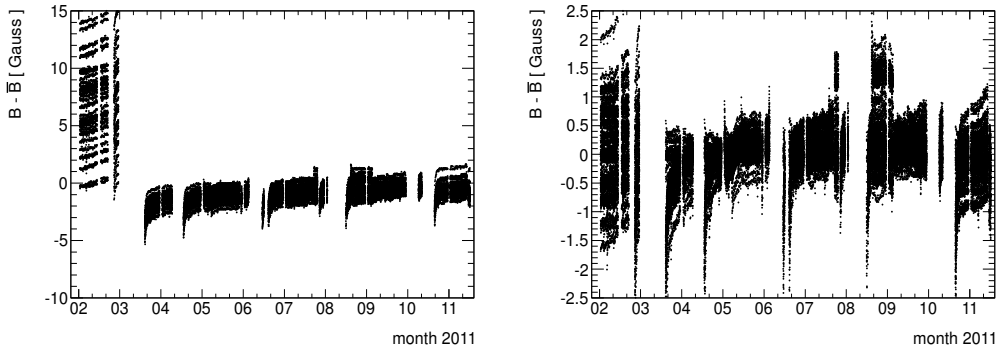

Figure 3.16: $B - \bar{B}$ as a function of time for sensors located on EIL chambers. Left: C side, R=1,2 and all phi sectors but 01 and 03, Right: R=1,2 phi sectors 01 and 03, and R=4 all phi sectors.

Figures 3.16 show the difference $B - \bar{B}$ as a function of time. From the left plot, it can be seen that the jump occurred between 25/3/2011 and 14/4/2011, periods corresponding to a shut-down. Studies similar to these described in section 3.5.1 have been performed, and no evidences of sensor malfunctioning or sensor position shifts were found.

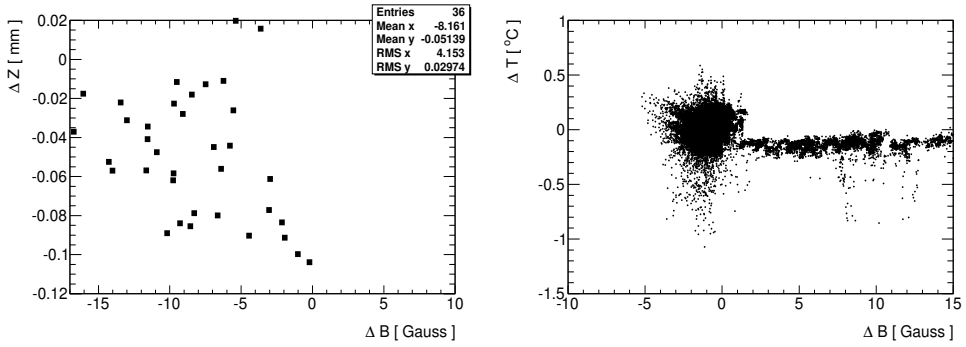

Figure 3.17: Distributions are for sensors located on the C side of the detector on EIL chambers, with R=1,2 and all phi sectors but 01 and 03, Left: ΔZ position vs ΔB between March 1st and May 1st, Right: temperature fluctuation vs magnetic field fluctuations.

The left plot in figure 3.17 shows the difference in the Z position (ΔZ) against ΔB. The left plot shows the temperature fluctuations as a function of ΔB. Differences are evaluated between March 1st and May 1st. No clear correlation between the B jump and the ΔZ or the temperature variation is observed. For End Cap

sensors, such significant B - jumps correlated with shut-down periods, could be due to a displacement of the End Cap Toroids (ECT). A detailed study probing this scenario is presented in section 3.6.2.

3.6 B-map study

The field amplitude at every position in the ATLAS detector is determined using a magnetic field map (B-map). The B-map was last computed in 2010. The production of the B-map is a complex procedure that requires:

1. Sensor measurements of the magnetic field amplitude.
2. Sensor positions, computed using the available alignment algorithm.
3. A modeling of the coil geometry.

Sensor measurements and their positions are used in order to reconstruct the positions and deformation of the coils. Then, in order to model the total magnetic field inside the detector, Biot-Savart law is applied and whenever possible, additional magnetic field perturbations due to the detector material are taken into account.

In the next section, the agreement between the amplitude of the magnetic field, computed at each sensor position using the B-map (B_{calc}), and the one measured by the sensors, in 2011, is studied. Furthermore, a comparison of the two different versions of alignment constants is performed. Then, a comparison between 2011 and 2012 measurements and the B-map predictions is made. The aim is to examine if, after the shut-down that took place in the end of 2011, the ECT position was the same as in 2011.

3.6.1 Comparison of the B-map computations with 2011 measurements

The only requirement for the computation of B_{calc}, at a specific point in the detector, is its exact coordinates: x, y and z. Therefore, an accurate measurement of the sensor position is needed. It should be mentioned that sensor positions actually used are derived with a new alignment algorithm. The new algorithm is improved with respect to the one used for the B-map production [54]. A comparison of the two different versions of the alignment algorithm follows at the end of this section.

For this study, positions evaluated on the 1st of May 2011 are used. The $\bar{B}$ which is compared to the B_{calc} is evaluated using B measurements taken within a

2-days time interval after the moment an update on the sensor position was made available. Sensors belonging to the Bad or Very Bad category are not included in the analysis. Moreover, Barrel and End Cap sensors are studied separately for two main reasons:

- End Cap sensors feel mainly the magnetic field induced by the ECT, while Barrel sensors feel the Barrel Toroid magnetic field. Edge Barrel sensors (BIS Z=7,8) and sensors located on the outer part of the End Cap wheel (R=3,4,5) feel the combination of both fields. Sensors located in the inner parts of the End Cap wheels are more sensitive to position shift of the End Caps. As the ECTs can move independently in the two detector sides, the A and C sides will be treated separately.

- Different alignment algorithms are used for the two detector areas.

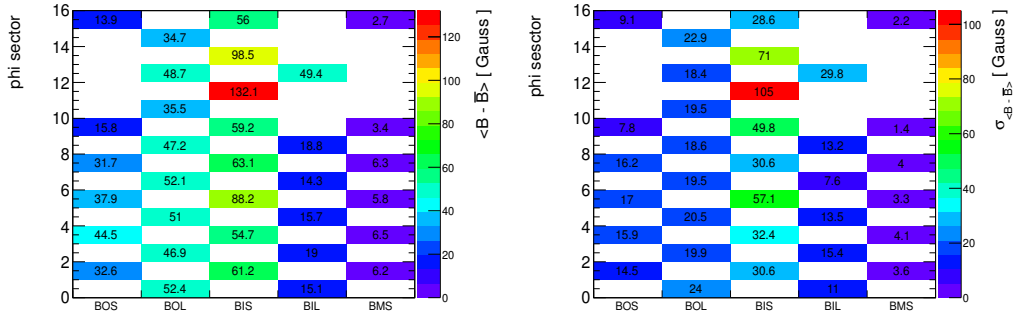

Figure 3.18: Barrel phi sectors, Left: $\overline{|B_{calc} - \bar{B}|}$, Right: standard deviation of $|B_{calc} - \bar{B}|$.

Plots in figures 3.18 and 3.19 concern sensors located on BOS, BOL, BIS, BIL and BMS Barrel muon chambers. The left plot in figure 3.18 shows the mean value of $|B_{calc} - \bar{B}|$, while the right plot shows the standard deviation of $|B_{calc} - \bar{B}|$ for each category of sensors. Plots in figure 3.19 picture the same quantities, for different Z sections along the beam axis.

The agreement between the B-map and the measurements is better for sensors located on BMS and BIL chambers. High discrepancies are observed for sensors located on BIS chambers, which probably indicate insufficient modeling of the magnetic perturbations due to the Tile calorimeter. The highest discrepancy is observed for sensors located on BIS muon chambers, on edge Z sections (Z=7,8), where both central values and their standard deviations are large. About the 68% of sensors

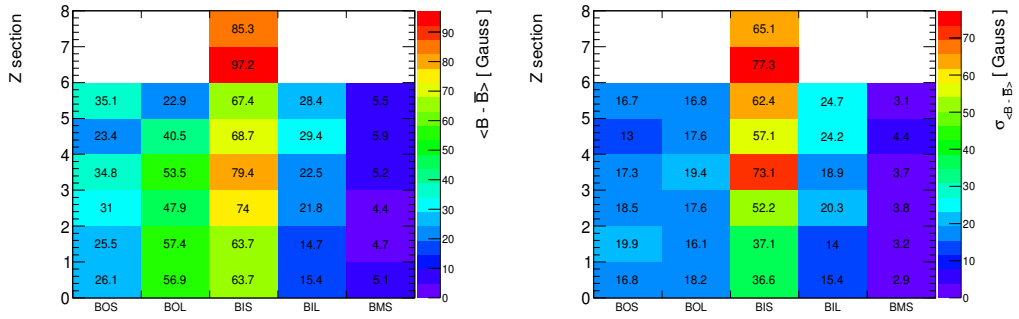

Figure 3.19: Barrel z sections, Left: $\overline{|B_{calc} - \bar{B}|}$, Right: standard deviation of $|B_{calc} - \bar{B}|$.

belonging to this group, have a $|B_{calc} - \bar{B}|$ value in the range 20 - 160 G. A worse agreement between the B-map predictions and the measurements is expected in this detector area, since the magnetic field is the superposition of the ECT and Barrel Toroid fields and is more difficult to model. Additionally, in 2010, the alignment for the muon chambers located in the edge Z sections (Z=7,8), wasn't enough accurate, and thus measurements from sensors located on these chambers weren't taken into account for the production of the B-map.

Among the phi sectors, the highest discrepancies appear in the sectors 12 and 14 with about 68% of the sensors having a $|B_{calc} - \bar{B}|$ value in the range 30 to 230 G. This is expected as it is known that for these specific sectors the perturbations due to the Tile calorimeter were not taken into account in the B-map production.

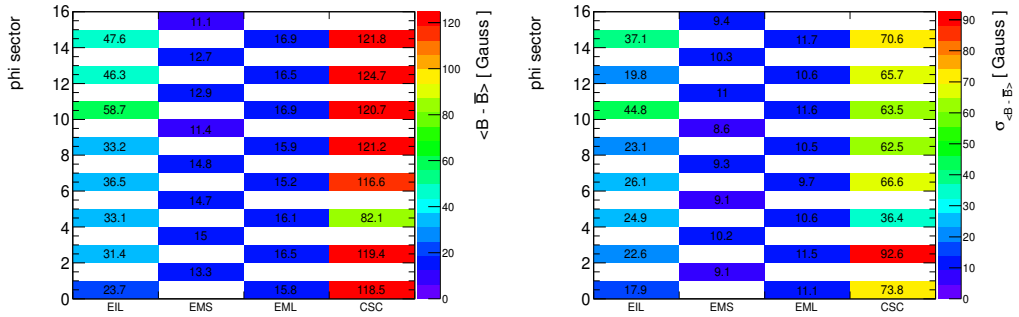

Figure 3.20: End Cap phi sections, Left: $\overline{|B_{calc} - \bar{B}|}$, Right: standard deviation of $|B_{calc} - \bar{B}|$.

Plots in figures 3.20 and 3.21 picture the same quantities as the plots in figures 3.18 and 3.19, respectively, but they are made for End Cap sensors located

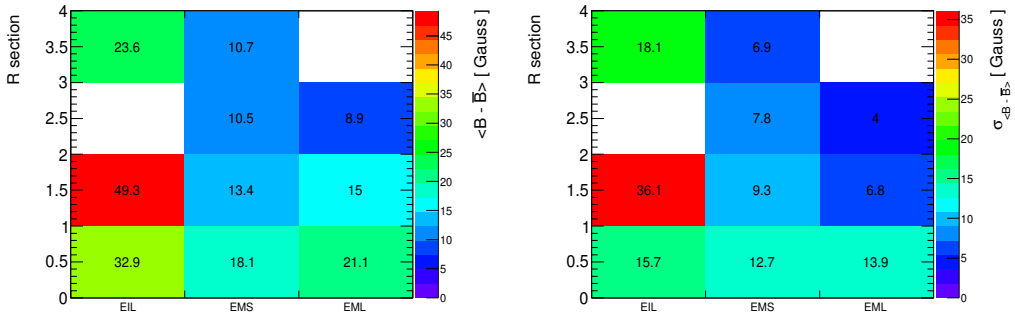

Figure 3.21: End Cap R sections, Left: $\overline{|B_{calc} - \bar{B}|}$, Right: standard deviation of $|B_{calc} - \bar{B}|$.

on the EIL, EMS, EML and CSC End Cap muon chambers. One observes that sensors located on EMS and EML chambers, in both R and phi position plots, have central and standard deviation values below 20 G. The agreement for these sensors is remarkably better than for EIL and CSC sensors. For instance, the mean B_{calc}-$\bar{B}$ value for sensors located on CSC chambers can reach 120 G.

The above End Cap plots include sensors located on both A and C sides and were made for positions and measurements taken the 1st of May. As a second step of this analysis, End Cap sensors located on the positive and the negative side are examined separately, and the mean $|B_{calc} - \bar{B}|$, is computed for the following five dates in 2011: 1 March, 1May, 17 June, 1Agust and 18 September. This allows to: 1) determine if the measured magnetic field and the B_{calc} agreement is better in one side than in the other, 2) examine if the B-jump observed in March for sensors located on EIL chambers in the C side of the detector, shown in section 3.5.2, is closer to the B-map predictions compared to May measurements.

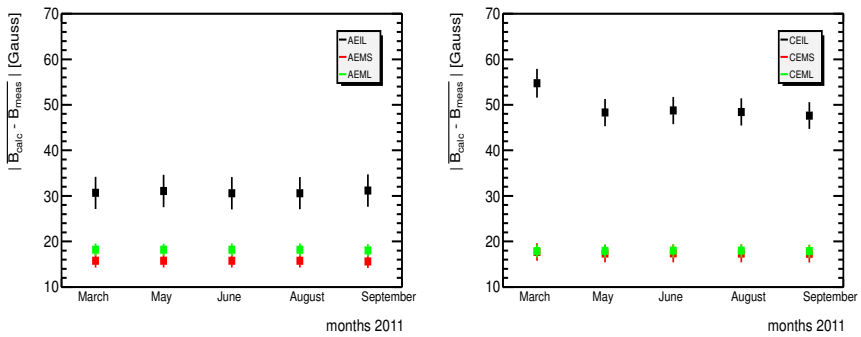

Figure 3.22: $\overline{|B_{calc} - \bar{B}|}$ for EIL, EMS and EML. Left: A side, Right: C side

Plots in figure 3.22, show the $\overline{|B_{calc} - \bar{B}|}$ value for the main three categories of End Cap sensors, for five different dates in 2011. One observes that:

1. Sensors located on the C side on EIL chambers have significantly higher $\overline{|B_{calc} - \bar{B}|}$ value in comparison with the A side, during all 2011. This could indicate that the C side ECT has moved after the B-map production. Moreover, it seems that the ECT has moved slightly closer to its 2010 position for which the B-map was produced. The $\overline{|B_{calc} - \bar{B}|}$ value has decreased of about 7 G.

2. Sensors located on EMS and EML chambers in both detector sides have a mean B_{calc}-$\bar{B}$ value of ≈17 G, i.e, two times lower than the EIL sensors located on the A side. As it will be discussed in the following section, such discrepancies between the sensors located on EMS/EML and the EIL chambers are expected because of the large difference in the gradient of the magnetic field near the coil.

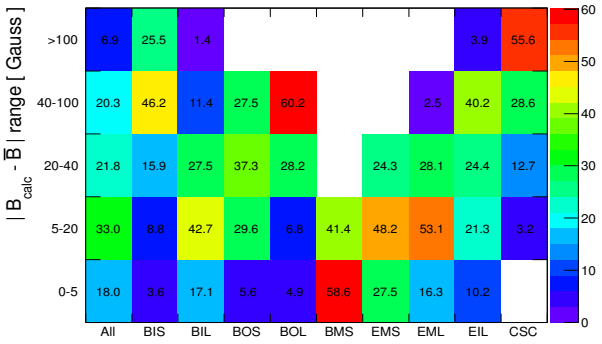

Figure 3.23: Percentage of sensors of each category, which have $|B_{calc} - \bar{B}|$ in the range indicated on the Y axis.

In order to summarize previous observations, figure 3.23 shows the percentage of sensors of each category, which have $|B_{calc} - \bar{B}|$ in the range indicated in the Y axis. Values are calculated for May 2011. Table 3.8 shows the percentage of sensors of each category which have $|B_{calc} - \bar{B}| > 40$ G. From the above figure and table one sees that ≈ 80% of the sensors have $|B_{calc} - \bar{B}|$ above 5 G and 27% above 40 G.

Finally, as it has been already stressed, the B-map was produced using sensor positions determined by the old alignment algorithm while this study is done using positions determined by the new improved alignment algorithm. Figure 3.24 shows

Sensors categories	All	BIS	BIL	BOS	BOL	BMS	EMS	EML	EIL	CSC
% of sensors with $\lvert B_{calc} - \bar{B}\rvert > 40$ G	27%	72%	13%	27%	60%	0	0	3	44%	84%

Table 3.8: Percentage of sensors of each category which have $|B_{calc} - \bar{B}| > 40$ G.

the differences ΔZ and ΔR computed using sensor positions evaluated with the two different versions of the alignment algorithm. The ΔZ distribution has a mean of $\approx$ 200 μm and a RMS of $\approx$ 700 μm. There are 30 sensors with $|\Delta Z| > 3$ mm. The ΔR distribution has a mean of $\approx$ 1.3mm and a RMS of $\approx$ 1.2 mm. There are 17 sensors with $|\Delta R| > 6$ mm. As it can be seen, the new alignment algorithm significantly shifts sensor positions with respect to the old algorithm which was used for the B-map production. A position shift larger than 1 mm is expected to have an impact of $\approx$ 10 G on the B. Thus, the production of the B-map might be affected by the alignment algorithm version used for its production. This could add an additional systematc error to the B-map.

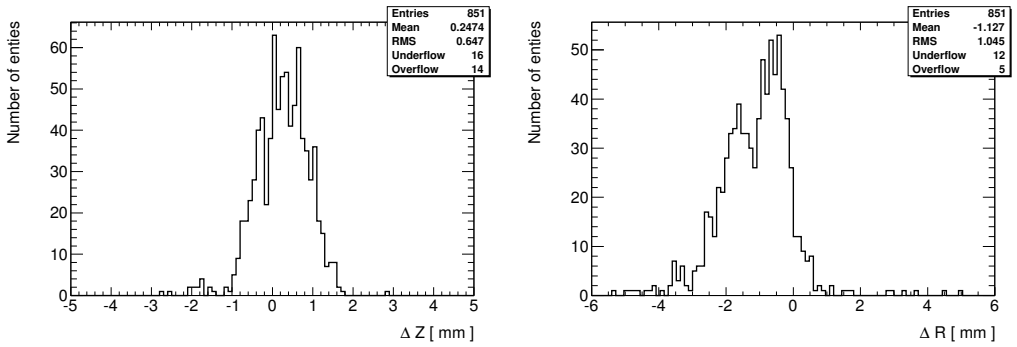

Figure 3.24: Left: ΔZ, Right: ΔR. Differences are evaluated using all Barrel sensor positions derived by the two alignment algorithms for March 2011 1st.

To conclude this section, here are summarised the most important points to be considered for the B-map production:

1. Only measurements taken from sensors that are considered perfect, good and, in some cases, unstable should be used, see section 3.4.

2. Only measurements passing the criteria defined in section 3.3 should be used.

3. The newest alignment technique should be used for the estimation of the sensor positions.

3.6.2 Comparison of 2011 with 2012 measurements

In this section, the impact of the shut-down, which took place in the end of 2011, on the magnetic field measurements of Barrel and EC sensors will be examined. Then, the observed variations on the EC sensor measurements will be interpreted in terms of ECT position shift. More specifically, the sensors magnetic field measurements performed in the end of 2011 (September 18th, B_{2011}) are compared with the measurements performed in the beginning of 2012 (March 18th, B_{2012}). The quantities that will be used in this analysis are the difference B_{2012} - B_{2011}, noted ΔB, and the $B_{calc2012}$ - $B_{calc2011}$, noted ΔB_{calc}. The $B_{calc2011}$ and $B_{calc2012}$ are computed using the B-map, for the sensor positions on the two dates above.

Barrel sensors

First, sensors located on the Barrel muon chambers are examined.

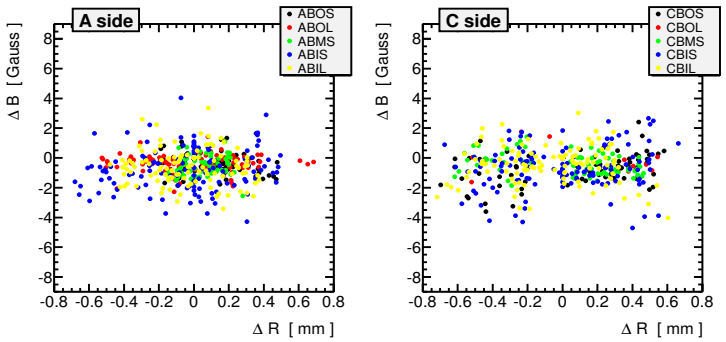

Figure 3.25: ΔB vs ΔR for sensors located on Barrel chambers. Left: A side, Right: C side.

Plots in figure 3.25 show the ΔB vs ΔR for Barrel sensors located on the A and C sides of the detector. One sees that some Barrel sensors have moved up to 0.8 mm in the radial direction. However, there is no correlation between the position shift and the variations in the magnetic field measurements. Additionally, some sensors located on BIL chamber in edge Z sections (Z=5,6) have moved significantly in the Z direction, up to 6 mm. However, the impact on the magnetic field measurement is not important, as the amplitude of the magnetic field is expected to change only slightly in the Z direction. For this reason, this analysis focuses on the radial shift for the Barrel sensors.

Plots in figure 3.26 show the ΔB_{calc} vs ΔR. The B-map predicts the impact of the measured ΔR on the magnetic field to be significant. There is a clear correlation

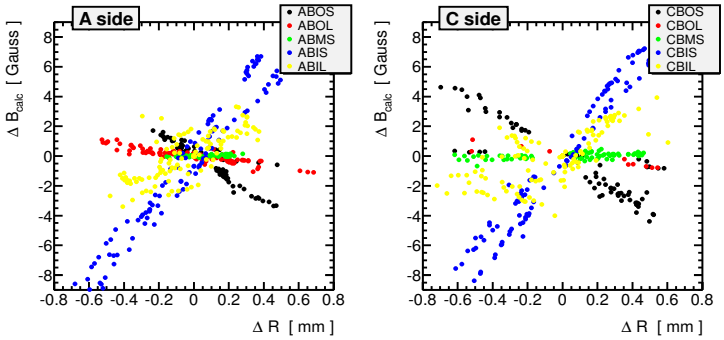

Figure 3.26: ΔB_{calc} vs ΔR for sensors located on Barrel chambers. Left: A side, Right: C side.

between the position shift and the variation in the predicted magnetic field. The ΔR impact is linear but not with the same coefficient for the different sensor categories. This behavior is expected, since the magnetic field gradient varies according to the detector area in which the sensors are located.

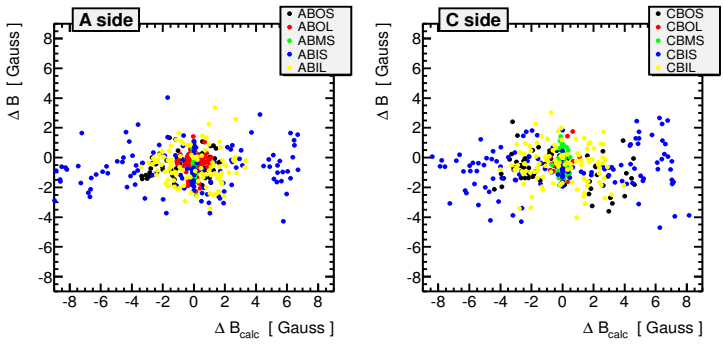

Figure 3.27: ΔB vs ΔB_{calc} for sensors located on Barrel chambers. Left: A side, Right: C side.

Figure 3.27 shows the ΔB vs ΔB_{calc}. No correlation between the observation and the expectation is seen. The absence of correlation between the measured magnetic field and the shift in the position, while the B-map predicts it, could be due to a global movement of the coils-chambers system. In this scenario, sensor positions have changed and the alignment algorithm detect it, however, magnetic field measurements do not change, as the sensors have moved in the same way as the coils did, consequently ΔB is not equal to $\Delta B_{calc}(\Delta R)$.

It has to be stressed that the observed ΔB for the sensors located on the BIS and BIL muon chambers is $\approx 3\ \sigma_{\bar{B}}$, where $\sigma_{\bar{B}}$ is the 1 standard deviation around the mean magnetic field measurement in 2011, see figure 3.28. In section 3.4.1, it

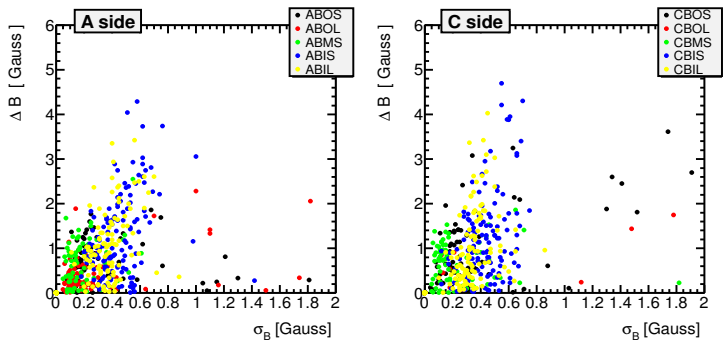

Figure 3.28: ΔB vs $\sigma_{\bar{B}}$ for sensors located on Barrel chambers.

has been shown that 70% of the sensors had $\sigma_{\bar{B}}$<0.4 G, while here the mean ΔB is $\approx$ 1.5 G. Therefore, new reference mean values have to be computed for each sensor using 2012 measurements.

End Cap sensors

In this sub-section End Cap sensors will be examined. Contrary to Barrel sensors, End Cap sensors exhibit a behavior easier to interpret. Sensors located on EIL muon chambers have a significantly large ΔB, up to 50 G. As it will be demonstrated, these jumps do not seem related to sensor position shifts but rather to ECTs relocation after the shut-down.

For the purpose of this study only sensors located in the inner part of the wheel, i.e R=1,2, will be used. This because outer wheel sensors feel also the BT magnetic field and thus this would blur the study.

In figure 3.29 the ΔB is plotted against ΔZ for each detector side, and for the EML/S and EIL sensors separately. There are high magnetic field variations, up to 50 G, which however are not correlated with the sensor position shifts. Figure 3.30, verifies this observation as the observed difference ΔB is not predicted by the B-map, ΔB_{calc}. Again, EIL sensors are plotted separately from EMS and EML.

Although the variations of the measured magnetic field are not due to the new sensor positions, there are clear correlations between measurements and predictions. Moreover, the systematic offset of the correlation between the magnetic field variations and the ΔZ indicates that a shift of the ECT toroids along the z axis probably occurred after the 2011 shut-down.

In order to verify this scenario and, if true, to derive a numerical value for the ECTs position shifts, one should minimize the ΔB - ΔB_{calc} difference. It is not possible to directly shift the position of the ECTs in the B-map. Nevertheless, one

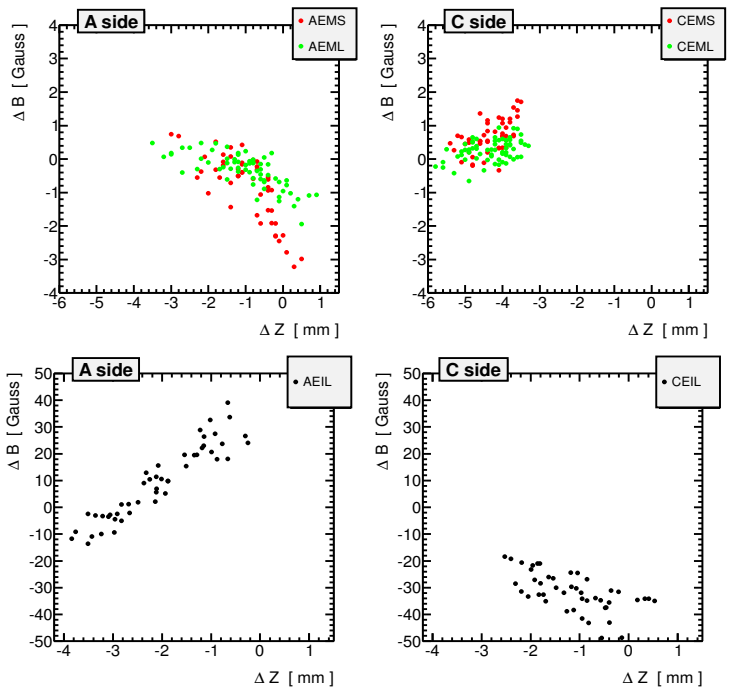

Figure 3.29: ΔB vs ΔZ. Top: EMS and EML sensors, bottom: EIL sensors. Left: A side, Right: C side.

can work the other way around by applying a global shift on the 2012 Z position of each sensor till the ΔB - ΔB_{calc} difference gets a minimum value.

Sensors located in the inner (EIL) and the middle End Cap wheel (EMS/L) will be examined separately due to their different sensitivity. The results deduced using the EIL sensors will be considered as more reliable since the gradient of the magnetic field is significantly higher for them, and therefore they are more sensitive to ECTs position shift, see figure 3.31 and table 3.9.

Sensors groups	EIL	EMS	EML
$\approx$ |Z| positions [mm]	7860	13730	14150
$\approx$ |Gradient| G/mm	12.1	0.99	0.23

Table 3.9: |Z| positions and |Gradient| G/mm for each group of sensors.

The optimal z shift (Z_{shift}) to be applied on sensor positions so that the real distance between the ECT and the sensors is reproduced, is the one which minimizes the χ^2:

$$\chi^2(Z_{shift}) = \frac{\Sigma(\Delta B - \Delta B_{calc}(Z_{shift}))^2}{\sigma^2} \tag{3.2}$$

The σ^2 value is chosen so that χ^2= n-1 (n = number of sensors). Its value will be

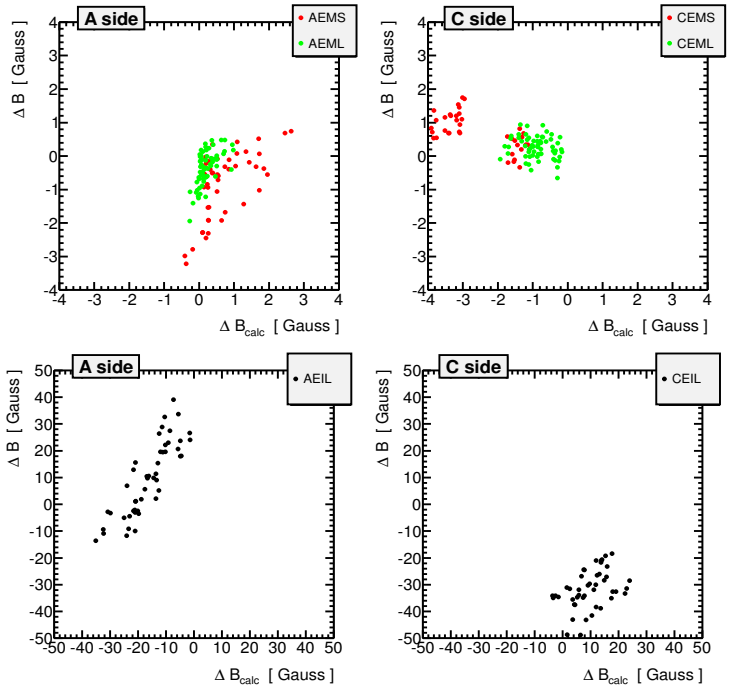

Figure 3.30: ΔB vs ΔB_{calc}. Top: EMS and EML sensors, bottom: EIL sensors. Left: A side, Right: C side.

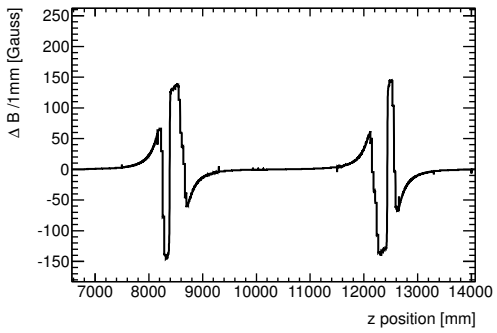

Figure 3.31: Magnetic field gradient G/1mm vs z position for x=2000mm and y=2000mm .

discussed in the end of this section. The results of the minimum χ^2 method, for both A and C sides, are shown in figure 3.32. The numerical results of the fit are summarized in tables 3.10 and 3.11, for the A and C detector side, respectively.

One sees that indeed, ECTs at both detector sides seem to be placed at a slightly different position after the 2011 shut-down. The small discrepancy on the extracted Z_{shift} value between the EIL and EMS/L estimation is justified because of the big difference in the sensitivity. The most sensitive fit (EIL) indicates that the ECT

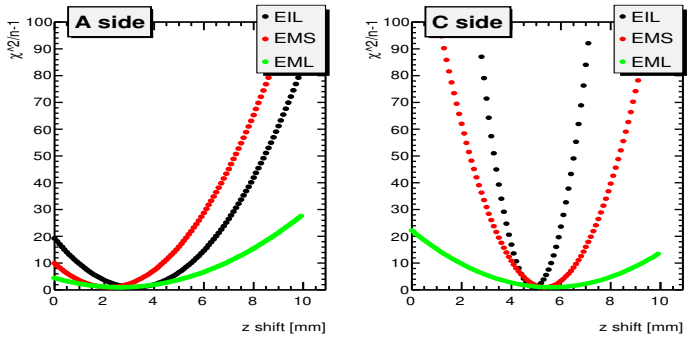

Figure 3.32: $\chi^2/n-1$, Left: A side, Right: C side

A side	EIL	EMS	EML
Z_{shift} [mm]	3.2	2.2	2.6
n-1	47	47	63
σ to use so that: χ^2=n-1 [G]	6.24	0.55	0.33
Estimate of errors (from χ^2 min+1) [mm]	0.1	0.12	0.17

Table 3.10: Fit results, A side.

C side	EIL	EMS	EML
Z_{shift} [mm]	4.9	5.3	5.6
n-1	47	47	63
σ to use so that: χ^2=n-1 [G]	1.99	0.31	0.28
Estimate of errors (from χ^2 min+1) [mm]	0.02	0.1	0.15

Table 3.11: Fit results, C side.

position shift is of the order of 3.2 mm and 4.9 mm for the A side and C side, respectively.

In figures 3.33, one sees that after the Z_{shift} correction, there is a clear improvement of the ΔB and ΔB_{calc} agreement for both A and C EIL sensors. The linear fit on the corrected values gives an intercept at the origin (p0) of -1.64 $\pm$ 0.4 and a slope (p1) of 1.39 $\pm$ 0.046 G, for the A side, see top right plot. For the C side, see bottom right plot, the p0 and p1 values are -0.27 $\pm$ 0.19 and 0.99 $\pm$ 0.01 G, respectively. The agreement, after the z correction, is also better for the EMS and EML sensors, but since these sensors are not very sensitive to position shifts of the order of some mm, the plots are not that indicative and thus are not presented here.

Even though the results are satisfactory, the discrepancy of the σ value between the A and C sides, 6 and 2 G see tables 3.10 and 3.11, respectively, is not expected. Assuming that the position shift of the ECT occurred exclusively in the z direction, both fits should have the same σ error, since EIL sensors should have the same behavior in this symmetric configuration (A and C sides).

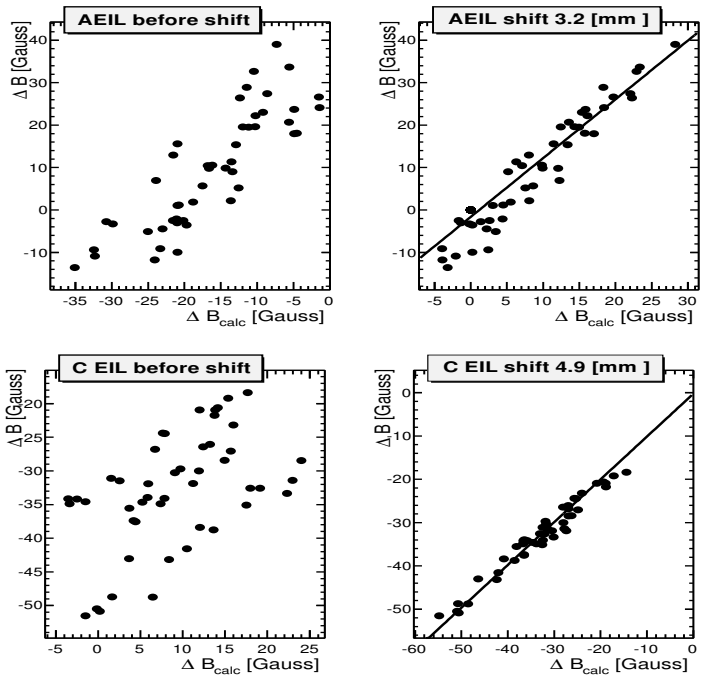

Figure 3.33: ΔB vs ΔB_{calc} for sensors located in the A side (top) and C side (bottom), Left: before shift, Right: after shift.

Figure 3.34 shows the ΔB - ΔB_{calc} difference as a function of the phi sectors for the A side. One observes a sinusoidal shape which indicates that the A side ECT has been probably slightly rotated around an axis perpendicular to the z axis.

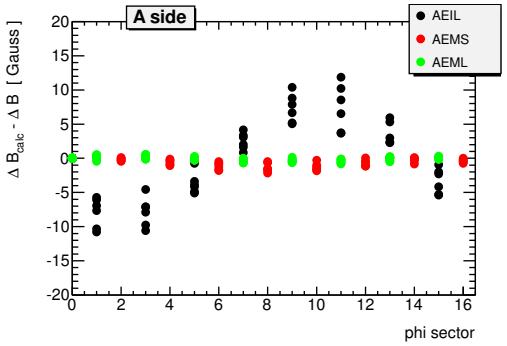

Figure 3.34: ΔB vs phi sector, A side.

In order to confirm this scenario and find the rotation angle, a new fit should be done, using the already shifted by 3.2 mm sensor positions. In this fit an additional shift due to a rotation will be applied. The rotation axis is set to contain the point x=0, y=0 and z=7860 mm (average EIL sensor position), located in the transverse

plan, and to form an angle of 117.5 ° with the x axis, since from plot 3.34, one sees that the ΔB - ΔB_{calc} difference is ≈ 0 for the 06 and 14 phi sectors. The results of the fit for the EIL A side sensors, are shown in table 3.12. One sees that after applying a rotation of 3.15 mrad on their positions, the σ is getting compatible with the C detector side error.

A side	EIL
θ [mrad]	3.15
n-1	47
σ to use so that: χ^2=n-1 [G]	1.57
Estimate of errors (from χ^2 min+1) [mrad]	0.044

Table 3.12: Fit results, A side.

In figure 3.35, the ΔB vs ΔB_{calc} is plotted for the EIL sensors, before any correction, after the first order correction i.e the Z_{shift}, and after the second order correction, i.e the θ rotation, which gives the final result. In the last case, the difference between the observed and the calculated magnetic field is further reduced. The linear fit on the corrected values, gives an intercept at the origin of 0.06 ± 0.06, and a slope of 0.99 ± 0.01 G.

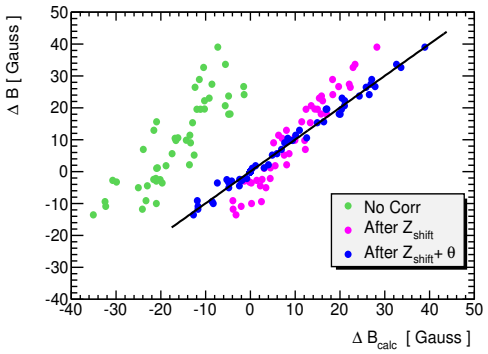

Figure 3.35: ΔB vs ΔB_{calc}, A side EIL sensors.

The improvement in the ΔB and ΔB_{calc} agreement, after rotating sensor positions, supports the assumption that a slight ECT rotation occurred after shut-down. Moreover, due to this very good agreement the σ value used in order to get $\chi^2 = n-1$ was significantly reduced, from 6.2 to 1.57 G. After the successive two corrections for the A side, both sides have a σ below 2 G. One should consider as representative error of EIL sensors, the one coming from those located on the A side (1.57 G see table 3.12), since a second order correction was applied to them.

The σ value used in the fit, should be the sum in quadrature of the measurement error (σ_{Bmeas}) and the error onn the ΔB_{calc} estimation (σ_{Bcalc}):

$$\sigma = \sqrt{\sigma^2_{Bmeas} + \sigma^2_{Bcalc}} \tag{3.3}$$

Both σ_{Bmeas} and σ_{Bcalc} errors are related to the magnetic field gradient in the detector area where the sensors are located. The former was estimated in section 4.1. A rough estimate for the latter is the gradient, known from table 3.9, times 100 μm, which is the expected alignment uncertainty.

	EIL	EMS	EML
σ_{Bcalc} [G]	1.21	0.10	0.02
σ_{Bmeas} [G]	0.60	0.30	0.20
σ_{exp} [G]	1.35	0.32	0.20
σ_{fitA} [G] C side	1.99	0.31	0.28
σ_{fitC} [G] A side	1.57	0.55	0.33

Table 3.13: Comparison of σ fit value with σ expected.

In table 3.13, the σ_{exp} values are compared with those found from the fit. One sees that the factor 5, between the σ_{fit} of the sensors located in the inner End Cap wheel, and those located in the middle wheel, is well understood. More in details, for the C side, where a first order correction was applied, for EMS and EML sensors there is a good agreement between the σ_{exp} and the σ_{fit}, while for EIL sensors there is still a slight discrepancy. For the A side, where a first order correction was applied on the EMS and EML sensors, and a second order on the EIL, the EMS and EML σ_{fitA} values are slightly higher than the expected values, while the EIL σ_{fitA} value is very close to the expected value.

3.7 Energy scale

The study in section 3.6.1 has shown discrepancies between the sensor measurements and the B-map predictions, which can reach 100 G in some detector areas. Therefore, it is of great interest to evaluate the impact of these inaccuracies on the momentum of the muons.

So far, the studies of the agreement between the magnetic field measurements and the B-map predictions have been performed on the modulus of the magnetic field. In order to assess the impact on the muon momentum, it is more relevant to examine the toroidal component of the magnetic field, B_ϕ. Moreover, as the amplitude of the magnetic field varies depending on the detector region, a more relevant quantity is the relative deviation with respect to the expected magnetic field value in the detector area on which the sensor is located. In the case this

relative deviation is constant over the entire detector volume, it induces a relative momentum deviation of the same order:

$$\frac{B_{\phi}^{meas} - B_{\phi}^{B-map}}{B_{\phi}^{meas}} \quad \propto \quad \frac{P^{true} - P^{reco}}{P^{true}} \tag{3.4}$$

One should examine the $\Delta B_{\phi}/B_{\phi}$ behavior along the path of the muon, since what matters are the integrals $\int Bdl$ and $\int Bldl$ over the muon trajectory, l. In the Barrel area, where there are three chamber layers, this can done by comparing the shape of $\Delta B_{\phi}/B_{\phi}$ between the layers. If all stations have a significant systematic shift in the same direction, this would indicate a problem.

Figure 3.36 shows the ΔB_{ϕ} and $\Delta B_{\phi}/B_{\phi}$ as a function of the phi sector for the inner, middle and outer Barrel layers, for both sensors located on large and small stations. One observes that even though for some sensors located on specific phi sectors on BOS and BIS chambers, the relative deviation can reach 3%, there is no correlation between the two patterns. The biggest disagreement is found in the region of the ATLAS feet (sectors 12 and 14), where magnetic perturbations from the iron in this region are not taken into account in the magnetic field map. Moreover, the BMS results show a very good agreement between the measurement and the B-map, with the disagreement being down to of some ‰. This is very important since the BMS results are representative of the large middle area in which the major part of a muon trajectory is.

Therefore, the above plots indicate that the observed discrepancy between the B-map and the sensor measurements is not expected to affect the muon momentum reconstruction and hence the determination of their mass. This study was used as a supporting material for the note investigating the Higgs mass discrepancy between the $H \rightarrow ZZ \rightarrow llll$ and the $H \rightarrow \gamma\gamma$ channel in 2012 [55] for what concerns the muon reconstruction, arguing in favor of the accurate $H \rightarrow ZZ \rightarrow llll$ result.

It should be stressed that these results are in line with studies that probe the impact of the magnetic field on the mass of the J/ψ and Z particles [56]. These studies find an impact inferior to 0.5% after taking into account the B-field uncertainty, MS and alignment uncertainties.

3.8 Monitoring system

As already mentioned, one should use only reliable magnetic field measurements for the B-map production. In order to avoid the duplication of the work described in

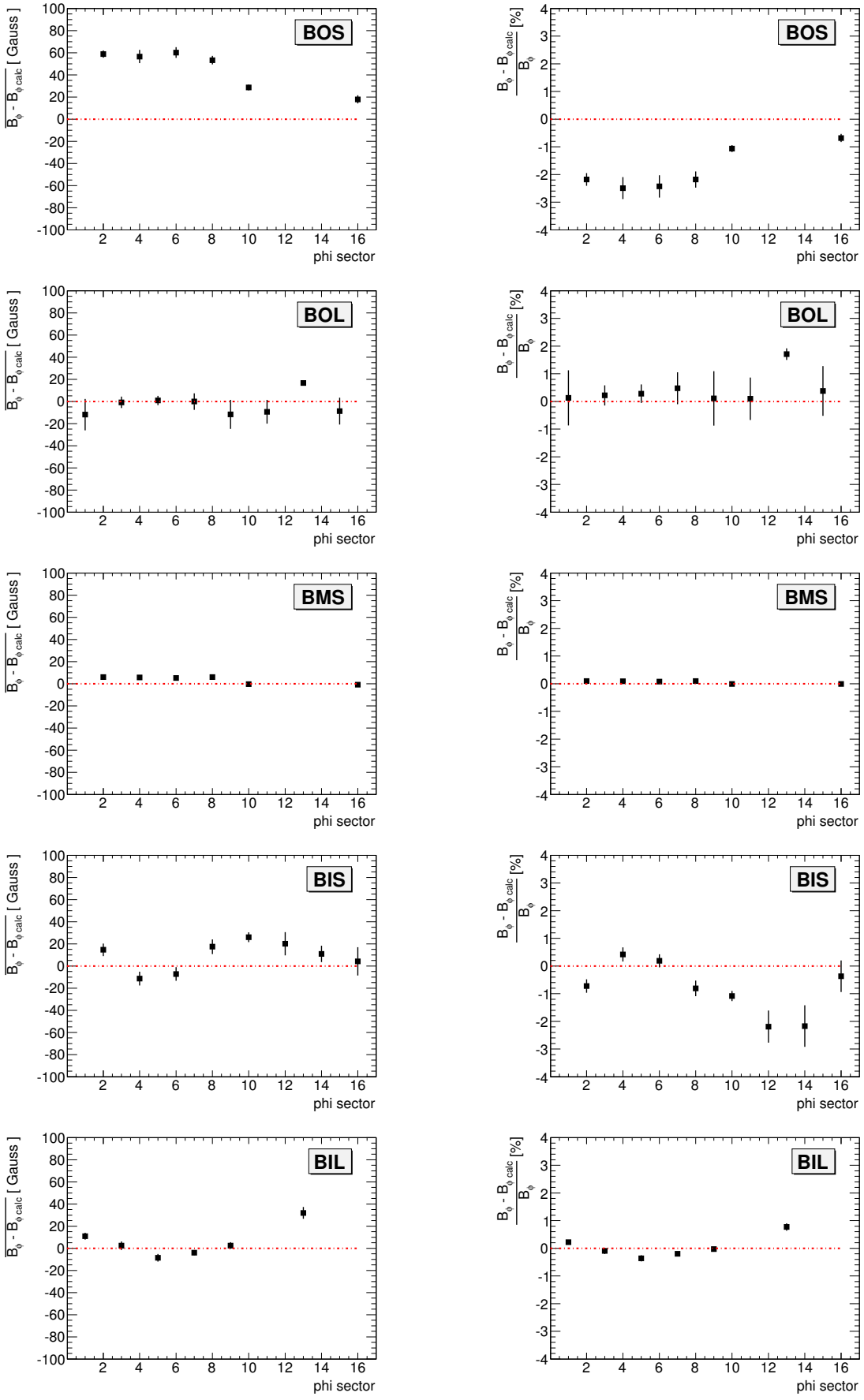

Figure 3.36: $B_\phi^{meas} - B_\phi^{B-map}$ (left) and $\frac{B_\phi^{meas} - B_\phi^{B-map}}{B_\phi^{meas}}$ (right) as a function of the phi sector for all three Barrel layers.

sections 3.3 and 3.4 for the measurements selection, an on-line monitoring system of the sensor measurements should be implemented.

Two possible methods will be discussed in this section. In the first method one compares the measured values B with the B_{calc}, directly calculated form the B-map. In the second method B is compared to $\bar{B}$, computed using measurements taken in a small time interval before the date in question. The basic idea is to flag the measurements having $|B_{calc}\text{-}B|$ or $|B\text{-}\bar{B}|$ above the expected threshold, and send an alert message to the field experts, when an anomaly is observed. People in charge could then use the information from the monitoring program in order to detect defective sensors and to closely examine their behavior. Once the reason for the deviation is identified, they should act accordingly by for instance replacing the sensor. Moreover, if there are evidences of ECT movement a new B-map should be produced.

B-map as a reference

The best way to apply an effective sensor monitoring, is to use as a reference the B_{calc} calculated by an improved B-map. The study presented in this document has underlined new needs at the level of the existing DB structure. Even though the usage of the B_{calc} can be very useful for future sensor monitoring, for the moment there are practical constrains on the implementation of a monitoring system based on the B-map calculations. The main constrains are summarized here.

The first issue is related to the sensor position estimation which is needed for the B_{calc} estimation. In a first place, one could use constant values of the sensor positions, which have been estimated off line. The possibility to use B sensors position updates in an automatic way is also under discussion among experts. One possible solution would be to trigger insertions of new positions every time that the alignment monitoring system detects a large position change for at least one sector, either in the Barrel or in the End Cap. Nevertheless, Such a procedure needs a few developments inside the alignment monitoring system (mainly for the End Cap), so it can not be implemented in a short time scale.

An additional complication on using the B_{calc} as a reference, comes from the fact that the B-map precision is not the same at every detector position. Detector regions exposed to magnetic perturbations or regions where alignment is not accurate enough, are expected to have lower precision. Consequently, the limit on $|B_{calc}\text{-}B|$ deviation should also depend on the sensor location.

As soon as the above open issues related to the software and the threshold to

apply, will be studied and solved, the monitoring system based on the B-map could be implemented. Finally, the definition of the appropriate output information that should be stored in the data-base is under discussion.

Mean values as a reference

A simpler way, in terms of software upgrades, to implement an on-line sensor monitoring, is to use as a reference the mean values computed in this work. This method requires as an input a table with the $\bar{B}$ values of each sensor.

As was shown in this work, when a shut-down occurs, sensor measurements may change slightly, or in some cases significantly. Hence, for a future monitoring one can not use the 2011 mean values computed in this work. The optimal solution would be, following exactly the same procedure as shown in sections 3.3 and 3.4, to compute new sensor mean values after each shut-down. One should wait untill the detector operation is completely stabilized after the switch On of the magnets, and then proceed to the computation of mean values. Measurements taken in a 5 days time interval would probably be enough for the determination of the mean magnetic field value and its standard deviation. The new mean values should be also compared with those computed before the shut-down. If the difference is significant, and not correlated with a sensors position shift, then this probably indicates that the ECT has moved and a new B-map production might be considered.

The $|\bar{B}\text{-}B|$ threshold to apply, could be set to 3 $\sigma_{\bar{B}}$, where the $\sigma_{\bar{B}}$ value is the standard deviation of the mean magnetic field value, computed in the 5 days time interval. Sensors which were characterized as unstable, based on 2011 analysis, or had a F value inferior to 1, could have a larger threshold, i.e 4 $\sigma_{\bar{B}}$. However, in order to decide the exact threshold value, so that the monitoring system is optimized, a more detailed analysis may be performed.

The disadvantage of this method compared to a method that uses the B-map as a reference, is that it is sensitive to sensor position shifts. Even though one does not expect a sensor position shift to occur during stable detector operation, it is not excluded. If this happens, the sensor will measure a different magnetic field, probably above the defined threshold. As a result, the measurement will be flagged, even though no malfunctioning occurred.

3.9 Conclusions

In this work a general assessment of the 3D Hall cards that measure the Toroidal magnetic field was made.

First, sensor measurements were probed and some cuts were introduced to exclude potentially bad measurements from the analysis. Using these cuts, sensor stability during 2011 was examined and a categorization table was built, taking into account: 1) the $\sigma_{\bar{B}}$, computed using all 2011 measurements passing the cuts and 2) the F_{value} value, which is the fraction of good measurements used for the mean value computation. According to this table sensor stability during 2011 was evaluated and the defective sensors were identified.

Groups of sensors with high $\sigma_{\bar{B}}$ value, were more systematically examined and it was found that they show a magnetic field jump between two shut-down dates. Possible correlation with temperature variations, electronics stability and sensor position shifts were examined without finding clear evidences. However, a geometrical pattern was found, which probably relates these jumps to the presence of the two massive metalic cranes.

A B-map study, using 2011 measurements, shows that the discrepancy between $\bar{B}$ and B_{calc} for 27% of sensors exceeds 40 G. However, the impact on the muon momentum is not expected to be significant. Sensors located on EIL muon chambers, have measured a significantly different magnetic field in 2012 comparing to 2011. This magnetic field jump was not related to sensor position shifts. The B-map was used in order to investigate if the ECTs have been relocated in a slightly shifted position after the 2011 shut-down. The outcome of this study supports this assumption, and suggests that the ECTs have moved 4.9 mm and 3.2 mm, in the C and A sides, respectively.

Finally, based on the findings of this work, two different ways to implement an on-line monitoring system of the sensors were proposed.

Chapter 4

Physics analysis description

4.1 Introduction

The main subject of this thesis is the study of the $ZZ \to \ell\ell\ell'\ell'$ process, where $\ell, \ell' \in \{e, \mu\}$. In the following sections the elements needed in order to perform the cross section measurement of this process are discussed [1].

The total ZZ cross section is defined as:

$$\sigma^{tot}_{ZZ} = \frac{N^{obs}_{ZZ\to\ell\ell\ell'\ell'} - N^{bkg}_{ZZ\to\ell\ell\ell'\ell'}}{\mathcal{L} \times BR\{ZZ \to \ell\ell\ell'\ell'\} \times A_{ZZ\to\ell\ell\ell'\ell'} \times C_{ZZ\to\ell\ell\ell'\ell'}} \tag{4.1}$$

where $N^{obs}_{ZZ\to\ell\ell\ell'\ell'}$ denotes the number of observed ZZ events in data, and $N^{bkg}_{ZZ\to\ell\ell\ell'\ell'}$ the number of expected background contamination. $\mathcal{L}$ is the integrated luminosity and $BR\{ZZ \to \ell\ell\ell'\ell'\}$ is the branching ratio for a Z to decay leptonicaly, i.e in a muon or electron pair. The $C_{ZZ\to\ell\ell\ell'\ell'}$ and $A_{ZZ\to\ell\ell\ell'\ell'}$ are correction factors related to the object reconstruction efficiency and the detector acceptance, respectively.

In order to avoid uncertainties due to the extrapolation to the total phase space, the cross section is also measured in a restricted phase space which is close to the analysis one. This is the "fiducial" cross section and it is provided separately for each decay channel:

$$\sigma^{fid}_{ZZ\to\ell\ell\ell'\ell'} = \frac{N^{obs}_{ZZ\to\ell\ell\ell'\ell'} - N^{bkg}_{ZZ\to\ell\ell\ell'\ell'}}{\mathcal{L} \times C_{ZZ\to\ell\ell\ell'\ell'}} \tag{4.2}$$

In this chapter, first in sec. 4.2, the reconstruction of the electrons and muons is described. Then, in sec. 4.3, the main background processes to the $ZZ \to \ell\ell\ell'\ell'$ analysis are presented. In sec. 4.4, the guidelines for the event and object selection are

[1] The elements that are needed to set limits on the neutral anomalous couplings are similar, and will be discussed in sec. 6

introduced. Finally, in sec. 4.5, the total and fiducial volumes are defined, and the two correction factors along with the theoretical uncertainties related to their estimation are discussed.

4.2 Object reconstruction: muons and electrons

In this section, the muon and electron reconstruction is presented. Main issues related to their identification and energy resolution will be discussed, taking into account the detector structure, as shown in chapter 2.

In the introduction of this document it was mentioned that by exploiting the full 2012 data a significant decrease of the statistical error is expected. Figure 4.1 shows the η distribution of the most forward lepton of an on-shell ZZ event at truth level. The plot was made using a *Pythia* $ZZ \to \ell\ell\ell'\ell'$ sample. One sees that almost 40% of ZZ events have at least one lepton in the region $|\eta| > 2.5$ and thus it is essential to extend the measurement volume up to the possible detector acceptance. Working in this direction, all leptons that are inside the ATLAS detector acceptance are included in the analysis. The ATLAS acceptance is up to $|\eta| = 2.7$ for muons and up to $|\eta| = 4.9$ for electrons. Attention will be given to the particles behavior within the different parts of this fiducial volume.

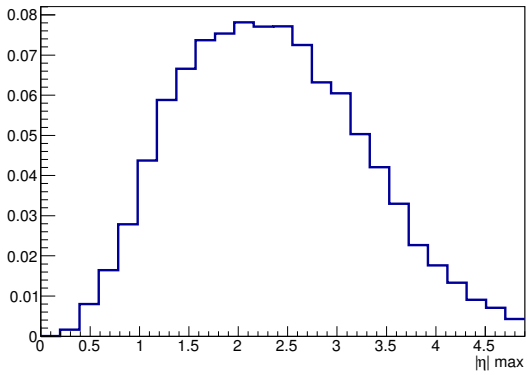

Figure 4.1: Normalized pseudorapidity distribution of the most forward lepton of on-shell ZZ events at generator level.

4.2.1 Muons

Muons are detected mainly using the inner detector (ID) and the muon spectrometer (MS). When a muon traverses the ATLAS detector it first passes through the

ID where it leaves "hits" in the three ID sub-detectors. Since muons are heavy mass particles compared to the electrons, they can traverse the electromagnetic calorimeter almost without deposing any of their energy. Then, muons arrive at the main muon detector, the muon spectrometer (MS), carrying the greater part of their initial energy. The MS was designed in such a way that muons can be efficiently reconstructed relying exclusively on the MDT measurements.

Issues affecting the muon reconstruction

The muon reconstruction is a complicated procedure that depends on several parameters. These parameters have been discussed in the detector chapter, see ch. 2. Here are briefly listed:

- The operation status of the muon drift tubes can affect the drift time estimation which is needed for the determination of the hit position. The drift time depends on the gas parameters, such as temperature and pressure, the tube anode-cathode potential and the electronics response.

- Chambers accurate alignment is also important in order to precisely determine the hit positions.

- The modeling of the detector material plays an important role for the muon reconstruction. For instance, the muon energy loss inside the electromagnetic calorimeter is estimated to be of the order of 4 GeV, something that can significantly affect the muon momentum estimation.

- A detailed modeling of the Toroidal magnetic field is necessary for the muon momentum estimation, see ch. 2.2.5. This task is complicated due to perturbations induced by the detector material and the need for an accurate knowledge of coil positions.

Muon reconstruction description

In this paragraph the idea behind the main muon reconstruction algorithm, the so called STACO chain [57], follows. The algorithm first explores the muon spectrometer and searches for "regions of interest". A muon that passes through a chamber will most probably hit all the tubes located on the sub-layers of the muon chamber. The first step is to reconstruct the muon path in a single chamber using all these hits. The resulting segments of tracks, hereafter called simply segments, are straight lines tangent to the global muon track with precisely known position and angle.

Once the segments on each of the three muon chambers are reconstructed, a global fit between the three segments is performed. This is called a 3-point reconstruction, and it is the optimal one since the full MS information is exploited. However, as some detector areas have a weaker coverage due to missing chambers or passages allowing detector access, there is a possibility to reconstruct MS tracks using only two segments. This is called an angle-angle reconstruction, because the angles of the two segments are used to re-build the muon path. Finally, a third type of MS track reconstruction is performed for End Cap muons with $|\eta| > 1.3$. Such muons have only the first two segments inside the magnetic field, as the area between the second and third wheel is not covered by the End Cap magnetic field. Thanks to the large distance between the second and the third wheel, of about 8 m, the direction of the straight line passing by the two last segments is precisely determined. The muon momentum is then estimated taking into account the distance between the straight line extrapolation and the point located in the first wheel. This type of reconstruction is called angle-point. For all reconstruction types several fit iterations are performed.

The next step is to try to match the reconstructed track inside the muon spectrometer, hereafter called MS track, with a track reconstructed inside the inner detector, hereafter called ID track. This is done by extrapolating the MS track towards the interaction point, correcting for the energy loss in the calorimeter, and searching for an ID track within a cone $\Delta\eta$x$\Delta\phi$ around the MS track. If an ID track is found, a statistical combination of the MS and ID tracks takes place using the covariance matrices of both track parameters [58]. If this procedure is successful, one obtains a combined muon track (CB). If however no associated ID track is found, the muon is called stand alone (SA) since it is reconstructed using only the MS hits. The failure of the MS - ID matching occurs when for instance the muon is emitted outside the ID acceptance in the forward detector region. Contrariwise, there are some cases where no MS track can be reconstructed at all, either because of missing chambers or because the muon had too low momentum to track safely its path inside the strong MS magnetic field. In these cases, there is an attempt to match the ID tracks with at least one MS segment. If the matching is successful, these muons are called segment tagged (ST).

Finally, in order to extend the muon reconstruction acceptance in the detector area where no MS chambers exist at all due to the service hole around $|\eta| \approx 0$, there is a fourth type of muons. These are muons having an ID track matched to an energy deposit in the electromagnetic calorimeter and thus are called "Calorimeter-Tagged". Muons contrary to hadrons deposit only a small and constant fraction of their energy

in each layer of the calorimeter. As a result, muon tracks are easily disentangled and thus reconstructible. However, calorimetric muons are lower quality muons with poor purity due to the high activity present in the calorimeter, mainly coming from jets and the multiple proton-proton interactions occurring during a bunch crossing (pile-up).

It is clear that CB muons are expected to have the greatest quality compared to SA, ST and calorimetric muons, since the maximum possible information (MS+ID) is used for their reconstruction.

To summarize, here are listed the four muon categories:

- Combined (CB) muons are the outcome of the statistical combination of MS with ID tracks.
- Stand alone (SA) muons are those reconstructed using only the MS hits.
- Segment tagged (ST) muons are those having a reconstructed ID track that is matched with at least one segment in the MS.
- Calorimeter-Tagged (CaloTag) muons have an ID track associated to an energy deposit in the electromagnetic calorimeter.

Muon reconstruction efficiency

Generally, in order to estimate the reconstruction and identification efficiencies of particles a data-driven method is used, called "tag and probe". In this method, usually, a Z or a J/ψ particle has to be reconstructed using one high quality lepton, the so called "tag", together with one lepton that fulfill only some of the regular requirements, the so called "probe". Then, by imposing the mass of the dilepton pair to fall in a restricted mass window one increases the probability that the probe is indeed a lepton. Additional cuts are also applied, for instance on the lepton isolation and the event trigger, in order to further suppress background contamination from non-Z leptons in data. The remaining background contamination must be evaluated and subtracted.

For the computation of the reconstruction efficiency of a CB or ST muon the probe is an ID track. The efficiency is defined as the ratio of the number of probe muons finally fulfilling all the quality requirements i.e being ST or CB muons, over the total number of probes. It can be written as:

$$\varepsilon(type) = \varepsilon(type|ID) \cdot \varepsilon(ID) \quad with\ type\ =\ CB, ST \tag{4.3}$$

In fig. 4.2 the data and MC muon reconstruction efficiency is presented, along with their ratio [59]. The reconstruction efficiency is found to be slightly different in MC compared to the data. Thus, a scale factor (SF) should be applied on the MC simulated events:

$$SF = \frac{\varepsilon(type)_{Data}}{\varepsilon(type)_{MC}} \tag{4.4}$$

The uncertainties on the reconstruction efficiency SFs mainly come from the estimation of the background, the size of the cone used for matching the probe with the reconstructed muon, and approximations of the tag and probe method. These uncertainties are small, of the order of 0.1% to 0.2% for muon with $P_T > 10$ GeV. For muons with $P_T < 10$ GeV, the uncertainties are estimated using J/ψ events, and they are found to be of the order of 0.5% to 2%. Finally, for muons having P_T above ≈ 100 GeV the SF determination is not reliable because of low statistics in data. However, as the SF has little dependence on the muon transverse momentum a constant central value can be considered. The systematic error for these high P_T muons was estimated using MC simulations with built-in imperfections and was found to be of the order of 0.05%, growing linearly with the momentum as 0.42% x $P_T[TeV]$ [59].

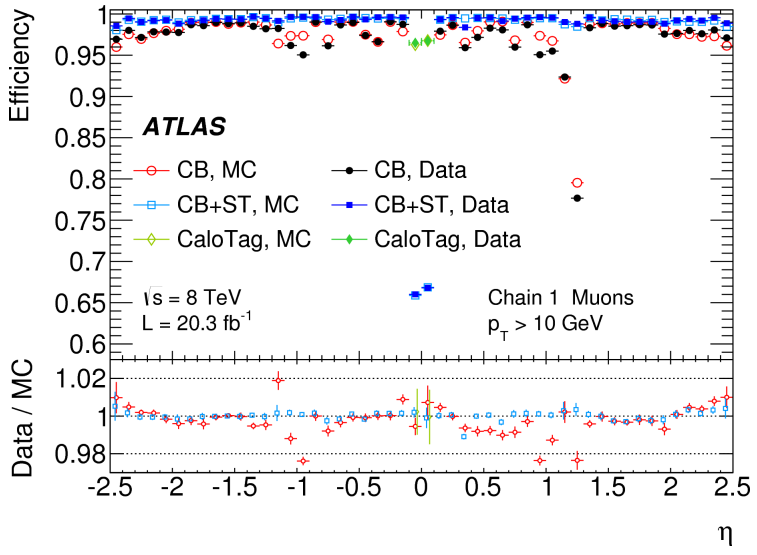

Figure 4.2: Muon reconstruction efficiency as a function of η for muons with $p_{\mathrm{T}} >$ 10 GeV in data and MC. Calorimetric muons are used only for $|\eta|$<0.1.

Since the inner detector does not cover the area above $|\eta| > 2.5$, the forward CB and SA muon reconstruction efficiency cannot be estimated with the method

described above. In order to obtain the forward muon SF, instead of counting muons, one counts the number of Z events in data and MC simulations which have one muon in the high η region. More specifically the SF is defined as the ratio of the data versus MC Z events having one muon in the region $2.5 < |\eta| < 2.7$ and the second in $|\eta| < 2.5$, over the number of data over MC events having one muon in the region $2.2 < |\eta| < 2.5$ and the second in $|\eta| < 2.2$. The systematic uncertainties on the SF are of the order of 1.2%.

Momentum scale and resolution

The muon momentum is estimated from the deflection of the track inside the toroidal magnetic field in the MS, or the solenoid magnetic field in the ID. In the MC simulations, the momentum scale and resolution are expected to suffer from modeling insufficiencies, related for instance to the inaccurate knowledge of the ID material budget and to alignment inaccuracies. Thus, one should correct the simulated P_T distribution in order to match the data distribution. This procedure is called smearing. The muon momentum resolution can be parametrised as [60]:

$$\frac{\sigma(P_{\mathrm{T}})}{P_T} = \frac{a}{P_T} \oplus b \oplus c \cdot P_T \tag{4.5}$$

where the first term accounts for uncertainties in the energy loss, induced by the detector material, and it is inversely proportional to the muon momentum. The second term is constant with the momentum and is related to the muon multiple scattering occurring along its trajectory. The last term accounts for the spatial detector resolution and it increases linearly with the momentum. For the ID momentum, no uncertainties related to the energy loss are considered, since no significant material density precedes the inner detector.

Hence, the corrected muon momentum can be written as:

$$P_T^{Cor.det} = P_T^{MCdet} \cdot s^{det}(\eta,\phi)[1 + \frac{\Delta a^{det}(\eta,\phi)G(0,1)}{P_T^{MC,det}} + \Delta b^{det}(\eta,\phi)G(0,1) + \Delta c^{det}(\eta,\phi)G(0,1)P_T^{MC,det}] \tag{4.6}$$

with det=MS, ID, s^{det} is the scale correction, and G(0,1) a normal distribution. The correction parameters s^{det}, Δa^{det}, Δb^{det} and Δc^{det} are estimated for the various η and ϕ detector regions, using MC template fit methods on the Z and J/ψ mass spectrum. Several distributions are produced after varying the Δa, Δb and Δc parameters. Then, the values that give the best matching to data are selected. The CB muon momentum corrections are the weighted average of the ID and MS corrections.

The associated systematic uncertainties on the resolution parameters and the scale are mainly due to assumptions on the muon momentum correction model, along with the template fit implementation. However, these are small compared to the other muon related uncertainties. The evaluation of these uncertainties mostly involves fit variations. Details on the systematics extraction can be found in [59]. The ID and MS scale corrections in almost all the detector areas are of the order of 0.1% with associated uncertainties up to 0.2%. The dimuon mass resolution is of 1.2% for low P_{T} muons in the central detector area, $|\eta| < 1$, and rises to 2% for hight P_{T} muons. In the detector are with $|\eta| > 1$, the dimuon mass resolution ranges from 2% for low P_{T} muons to 3% for high P_{T} muons.

4.2.2 Electrons

Electrons are reconstructed using a combination of the information taken by the inner detector and the electromagnetic calorimeter. The Barrel area covers up to $|\eta| = 1.47$ and the End Cap covers from 1.37 to 3.2. Electrons emitted in the very forward region can be measured as well using the two forward calorimeters, up to $|\eta| = 4.9$.

Issues affecting the electron reconstruction

The electron reconstruction is challenging because of the high activity present in the electromagnetic calorimeter. Hadrons or converted photons can be mis-identified as electrons. The important issues affecting the electron reconstruction are the following:

- The accurate ID and EM calorimeter alignment is essential, since the matching of the calorimeter energy cluster to the inner detector track requires a precise knowledge of the ID - EM calorimeter relative position.

- The calibration of the electromagnetic calorimeter.

- The electron energy deposit outside the electromagnetic cluster must be carefully recovered. This energy loss mainly happens either due to bremsstrahlung radiation when a high energy electron interacts with the ID material, or due to energy leakage in the hadronic calorimeter.

- The pile-up activity in the electromagnetic calorimeter affects the electron energy estimation. Thus, corrections must be applied to account for this.

Electron reconstruction description

An electron deposits the greater part of its energy in the electromagnetic calorimeter. In the central detector area, the energy recorded by neighbour towers is gathered together by special algorithms to form a fix-size seed cluster [61]. The reconstruction procedure continues only if the seed cluster energy is greater than 2.5 GeV. Then, a scan is performed in order to find if there are inner detector tracks that can be matched with the cluster. Inner detector tracks must have a minimum number of hits in the ID sub-detectors. If the track requirements are fulfilled, then the distance between the cluster and the track has to be $\Delta\eta < 0.05$ and $\Delta\phi < 0.1$. If several tracks are matched to the cluster, the one with the more silicon hits and the smallest $\Delta R = \sqrt{\Delta\eta^2 + \Delta\phi^2}$ is selected. The matching with the track can only be realized in the central detector area, because of the restricted inner detector acceptance, $|\eta| < 2.5$.

For the forward area, $2.5 < |\eta| < 4.9$, more sophisticated reconstruction algorithms are used in order to compensate the lack of track information. These are "topological" algorithms, optimized in order to form clusters with a variable number of cells. The clustering starts from a seed cell having a large signal over noise ratio and then the cluster is expanded to include all the neighbour cells having a lower, but still above a minimum value τ_{min}, signal over noise ratio [62].

In order to achieve a precise energy estimation after the successful cluster-track matching, in both detector areas, the energy is re-calculated taking into account the energy deposit in: the material in front of the EM calorimeter, outside the cluster (lateral leakage), and beyond the EM calorimeter, i.e in the hadronic calorimeter (longitudinal leakage).

Electron reconstruction efficiency

The computation of the electron reconstruction efficiency is performed using the tag and probe method on $Z \to ee$ events, as described in the muon section. Here, one "tag" electron that satisfies all the selection criteria is paired with one cluster energy seed, the "probe". The invariant mass of the pair is then required to fall in a tight mass window around the Z pole mass. Again, in order to reduce the background contamination in the electron channel, mainly coming from electrons from heavy flavor decays, converted photons, and hadrons misidentified as electrons, tight criteria are applied on the "'tag" and on the event. The remaining background contamination is estimated using data-driven methods. Since the electron reconstruction starts with the formation of a seed cluster, the reconstruction efficiency is defined as

the ratio of the number of fully reconstructed probes (cluster + track) to the total number of probes (cluster). A probe fails the cluster - track matching if the ID track requirements are not fulfilled.

The reconstruction efficiency is computed in bins of E_T and η. In each bin the efficiency central value is the average of the different efficiencies results obtained after varying the main parameters involved in the background estimation and the tag and probe method, such as the tag electron definition and the mass window around the Z. The reconstruction efficiency is found to be of the order of 99% in all the detector regions for very energetic electrons, $E_T > 80$ GeV, and to drop down to 95% for low energy electrons, $E_T < 20$ GeV, in the Barrel-End Cap transition region. Data and MC give results of the same order, and thus the SF that should be applied on the simulated distribution in order to match the data, is found to be close to 1. The total uncertainty on the efficiency is of the order of 0.5% for electrons with $25 < E_T < 80$ GeV, and it can go up to 2% for lower energy electrons [63].

Electron energy scale and resolution

The electromagnetic calorimeter was calibrated using test-beam measurements. In order to further improve the electron energy scale correction Z, J/ψ and W events are used. The energy can be parametrized as:

$$E_{meas} = E_{true}(1 + \alpha_i) \tag{4.7}$$

where E_{meas} is the measured energy using the MC calibration, E_{true} is the true energy, and α_i is the residual mis-calibration for a given "i" η region. The α is then determined by an unbinned log-likelihood fit on the mass spectrum of $Z \rightarrow ee$ events. At low energies the results have been complemented using $J/\psi \rightarrow ee$ events. Studies have shown that α dependence on the E_T is minimal, however, the η dependence is significant. The α value is 2% in the Barrel area, and rises up to 5% in the forward area, see fig. 4.3. Calibration cross checks have been performed using $W \rightarrow e\nu$ events [64].

There are several sources of systematic uncertainties related to the electrons energy scale determination. Such uncertainties are:

- The imperfect knowledge of the material in front of the EM calorimeter and the presampler energy scale which is used for the energy loss correction

- Calibration of the electronics and non-linearities in the read out electronics

- Requirements on the calorimeter operating conditions i.e exclusion of detector areas with dead material

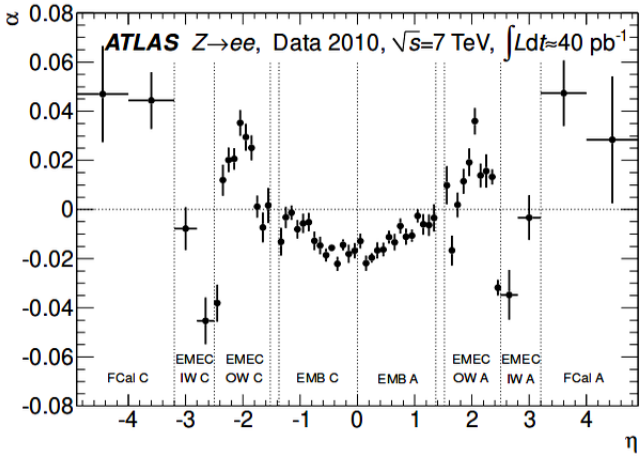

Figure 4.3: The energy-scale correction factor α as a function of the pseudorapidity of the electron cluster derived from fits to $Z \to ee$ data

- Theoretical assumptions related to the choice of the Z lineshape

The above sources result in a scale systematic error of the order of 0.3% to 1.6%, for electrons in the central detector area, $|\eta| < 2.47$. More precisely, the systematic uncertainties are below 0.4% for high energy electrons $E_T > 40$ GeV, however, lower E_T central electrons have an uncertainty that grows linearly with decreasing energy, and can reach 1%. Forward electrons have higher uncertainties which can rise up to 3%.

Finally, a correction on the energy of simulated events is applied, in order to correct for small differences in the energy resolution observed in data compared to MC.

Electron identification

Electron signatures can be confounded with background objects such as jets or converted photons. A set of highly discriminating requirements on the object characteristics should be applied in order to eliminate these backgrounds. For instance, cuts are applied on the variables related to the longitudinal and transverse shape of the electromagnetic shower, on the number of hits in the inner detector and on the track-cluster matching. The latter two cut categories can only be applied on central electrons ($|\eta| < 2.5$), as only these have an inner detector track.

Depending on the need of each analysis several different sets of cuts are available, encapsulated in "menus", providing different identification efficiencies and background rejection rates. For central electrons there are four cut based menus: *loose+*

+, *medium++*, *tight++* and *multilepton*. The cuts encapsulated in the first three menus are basically a sub set of each other. The *tight++* menu is the one that applies the most stringent cuts, and thus that provides the higher background rejection. The *loose++* menu is the one applying the looser cuts and thus has the higher efficiency. The *multilepton* menu is optimized for low energy electrons, since it has similar efficiency as the *loose++* menu but also a better background rejection. More details on these menus can be found here [63]. Moreover, the above cut-based menus are also available in a version based on Multivariate analysis (MVA) techniques. All the menus are optimized in bins of η and E_T.

The identification efficiency is estimated in bins of η and E_T with a tag and probe method, as described in the reconstruction efficiency section. Results from data and MC studies on Z and J/ψ particles are combined [2] to get the final efficiency. The efficiency central value and its systematic uncertainty are obtained by varying the parameters involved in the tag and probe method. These variations concern the size of the mass window around the Z or J/ψ particle, the fit parameters, the "tag" definition and the background estimation and the way it is subtracted from the signal. Fig. 4.4 shows the measured electron identification efficiency as a function of η and E_T in data and MC, for the cut-based menus [63]. One sees that higher identification efficiency is obtained with *Loose* and *multilepton* menus, as even for low energy electrons it is above 90%, and reaches 98% for high energy electrons. The total uncertainty on the identification efficiency is of the order of 5-6% for electrons with E_T below 25 GeV and drops to 1-2% for higher energy electrons. The ratio plot shows that the efficiencies in data and MC are in reasonable agreement, as the ratio is between 95% and 1.

For the forward electron identification there are three menus, the *forward loose*, *forward medium* and *forward tight*. These are exclusively based on cuts on the cluster energy deposit in the calorimeter and the shower shapes since no track information is available. Thanks to the good transverse and longitudinal segmentation of the calorimeter a good discrimination against the jets is possible. The identification efficiency in the forward region is estimated using a tag-and-probe method on $Z \rightarrow ee$ events in nine η bins. The identification efficiency for the *loose* and *medium* menus depending on the η bin vary from 80 to 100%, and between 60% and 95% for the tight menu. The data-to-MC efficiency ratio vary from 0.8 to 1 with a total uncertainties of 2-4% in the EMEC and 4-8% in the FCal. The larger uncertainty contribution comes from the choice of the background model and the signal fit range [65].

[2] J/ψ data are used only for the low E_T region, i.e in the range 7-20 GeV

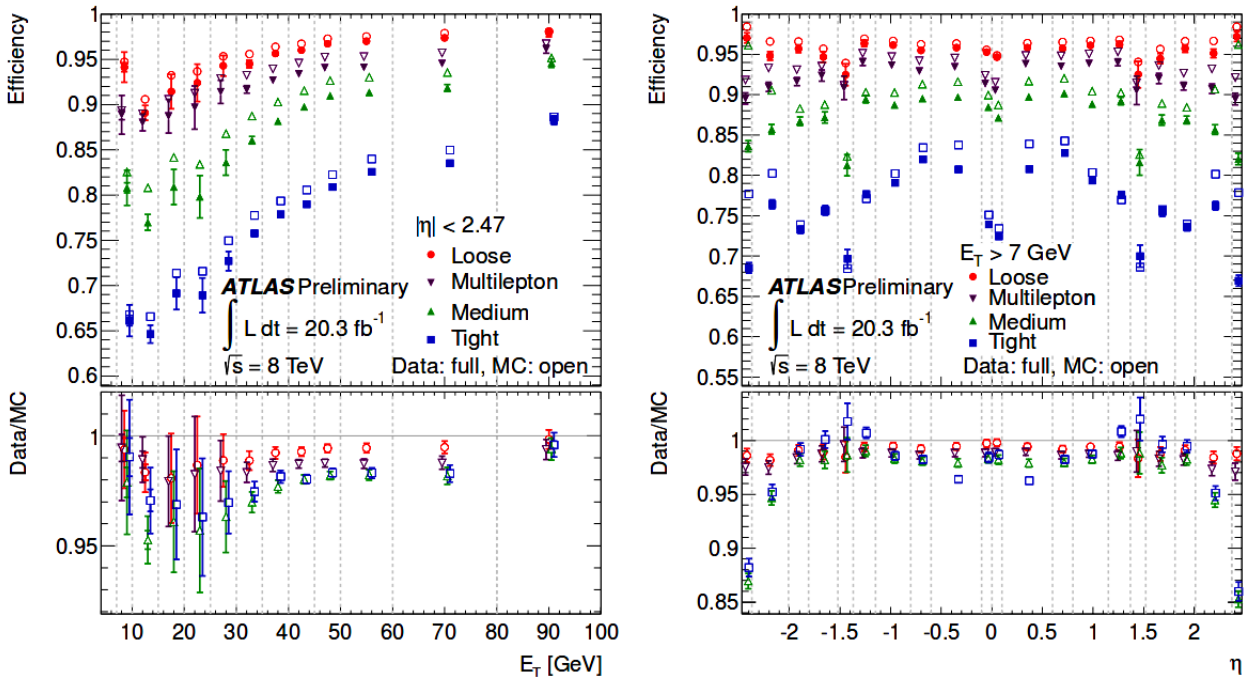

Figure 4.4: Measured electron identification efficiency for the cut-based menus as a function of η for different E_T in data and MC.

4.3 Background

The $ZZ \to \ell\ell\ell'\ell'$ process has one among the cleanest signatures. The 4 high momentum final state leptons make the analysis almost free of background contamination. Contrary to leptons coming from hadronic background sources, the signal leptons do not have activity observed around their ID track neither around their energy deposit in the calorimeter, and thus they are called isolated. The "isolation" criterion can eliminate the majority of the background events having jets. However, there are also backgrounds mimicking the $ZZ \to \ell\ell\ell'\ell'$ process when they have the same final state signature. Hence, the backgrounds can be split into two categories: those that can not be reduced by applying requirements on the leptons as they have an identical final state signature, and those that can be reduced by applying tight requirements on the lepton characteristics, such as the isolation, the impact parameter and the identification. In the following sections the two background types are introduced.

4.3.1 Irreducible background

The irreducible background consist of processes with four prompt high energy, isolated leptons. The main irreducible background sources are: the production of three gauge bosons (triboson), the $t\bar{t}$ process and the double parton interactions (DPI). More specifically, the triboson background consists of the $ZZZ \to 2\nu 4\ell$ and $ZWW \to 4\ell 2\nu$ processes. However, these processes are not expected to significantly contaminate this analysis since they have very small production cross sections, of the order of 10^{-2} fb and 1 fb, respectively. The $t\bar{t}Z$ process can also yield four prompt leptons. This happens if the Z and both Ws from the top quark decay leptonically. The cross section of this final state is also very small. Finally, the DPI affecting this analysis occurs when during a proton-proton collision two Z bosons are produced by two independent parton-parton interactions. The cross section of multi-parton interactions is very difficult to evaluate and thus has very large uncertainties. Luckily, the ZZ DPI contamination is still very small, with less than 1 event expected for the total 2012 integrated luminosity.

As it will be discussed later on, even though these backgrounds are irreducible at the level of the lepton selection, they can be reduced by applying a requirement on the mass window of the two Zs. By doing so, all the irreducible background sources, but the DPI and the ZZZ, are drastically suppressed. The estimation of the irreducible background contamination is performed using MC simulations and will be presented in section 5.3.1.

4.3.2 Reducible background

The second and more important background type to the $ZZ \to \ell\ell\ell'\ell'$ process consists of high cross section processes with a final state containing real good leptons plus fake leptons. Fake leptons can eventually pass all the selection requirements, when objects from hadronic decays happens to be reconstructed as isolated electrons or muons.

The most important reducible background sources are the $Z{+}jet$ and $WW{+}jets$, where the jet is produced from the hadronisation of a light or heavy quark. Such events will produce two prompt leptons from the Z or the two W leptonic decays, and two fake leptons produced inside the jet. These fake leptons originate mainly from semileptonic heavy flavor decays, muons from in-flight decays of pions and kaons [66], jets misidentified as an electron or electrons from converted photons. Furthermore, the $t\bar{t}$ process can yield two "good" leptons in the case where both W from the top decay disintegrate leptonically. Another important background is the

WZ process when both bosons decay in the leptonic channel, giving three prompt leptons. The background contamination from processes containing fake leptons are usually estimated using data-driven methods. This will be discussed in section 5.3.

4.4 Analysis selection

Taking into account the elements discussed in the previous sections regarding the lepton characteristics and the background processes to the ZZ signal, in this section the guidelines for the event and particle selection are discussed.

The ZZ analysis can be split in three parts. First, a pre-selection on the event is applied, such that only "interesting" events that have been recorded under stable detector operation are processed. Then, in order to disentangle between the ZZ signal and the various backgrounds the prompt electrons and muons of the event are selected, and finally specific requirements on the Z-pair are imposed.

4.4.1 Event pre-selection

The following two types of event pre-selection are applied.

Data Quality and event reliability

During the LHC operation dysfunctions may occur that deteriorate the data quality. Such dysfunctions may involve unstable beam, magnets ramping, or too many detector noisy cells. Information from more than 100 operation quality flags are compiled together, in order to decide if the data taken during a small period of time are reliable. This information is stored in the so called "Good Run List" (GRL). Besides the global LHC and detector operation, problems may occur in localized areas in the calorimeters. In order to prevent a deterioration of the measurement quality such events are also rejected.

Event trigger and primary vertex

As discussed in section 2.2.1, due to the very high bunch crossing rate, which is of the order of 20 MHz for the 2012 LHC run, only events fulfilling some criteria pointing to the existence of an interesting process are finally recorded. For the four lepton final state the candidate events must be triggered by a high momentum isolated electron or muon. For the electrons the trigger is based on the calorimeter and tracking information while for muons it is based on the fast-response MS trigger

chambers. The final trigger information used is given by the Efficiency Filter (EF) that combines all the event information.

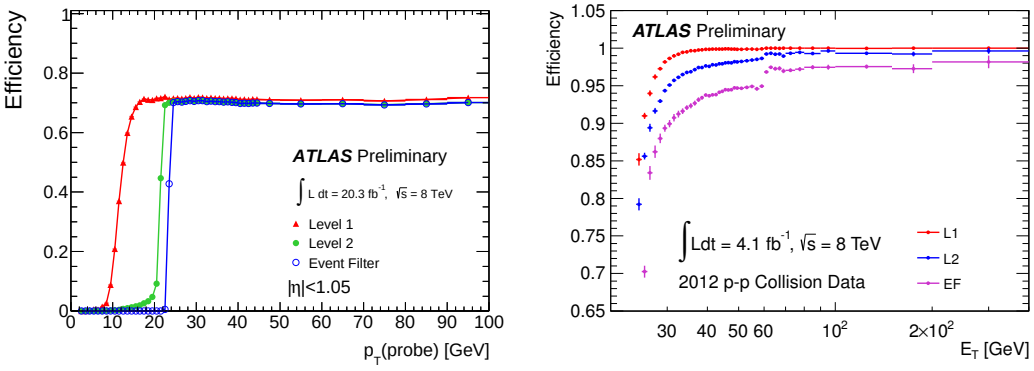

Figure 4.5: Single lepton trigger efficiency for central muons (left) and central electrons, excluding the crack region (right).

The single lepton trigger efficiencies for the 2012 data have been computed using tag and probe methods on $Z \rightarrow ll$ events. In fig. 4.5 the trigger efficiencies of electrons and muons as a function of the P_T of the probe are shown [3] [67] [68] [69].

Moreover, the event is required to have at least three tracks associated to the primary vertex. The primary vertex is defined as the vertex that has the highest transverse momentum sum of associated tracks, more details on its definition can be found here [70].

4.4.2 Object selection

The object selection is crucial for the analysis results. It impacts both the statistical and systematic errors of the cross section measurement. If a loose selection is applied, the statistical error will decrease since more ZZ candidates will be selected. However, the background contamination and the systematic errors will probably also increase. For instance, in section 4.2, it has been discussed that low energy leptons and those emitted in the forward region have higher uncertainties related to their reconstruction. This is also the case for particles in the Barrel-End Cap transition region and the calorimetric muons.

As the $ZZ \rightarrow \ell\ell\ell'\ell'$ analysis suffers from high statistical errors in order to increase the acceptance, in addition to the central leptons, the forward leptons and

[3] The signle trigger requirement for electrons is: $e24vhi\_medium1$ OR $e60\_medium1$ i.e one "medium" electron either isolated with P_T>24 GeV or with P_T>36 GeV without any isolation requirement, while for muons the signle lepton triggers are $mu24i$ OR $mu36$, i.e either one isolated muon with P_T>24 GeV or a muon having P_T>36 GeV without any isolation requirement

the calorimeter muons will be also considered. Hereafter, all leptons besides the central are called "extension" leptons. Moreover, the requirement on the transverse momentum will be also lowered for the higher quality leptons.

When lower quality objects, such as "extension" or low P_{T} central leptons are included in the analysis, in order to maintain the analysis as "clean" as possible, one should apply additional requirements on the leptons. Here, quantities that can be used to increase the analysis purity are presented. The precise requirements applied on these quantities for all object types will be presented in sec. 5.2.1.

Reconstruction and identification

In the sections describing the electron and muon objects, 4.2.2 and 4.2.1, respectively, it was shown that several different types of muon reconstruction and electron identification exist. By requiring the leptons to fulfill tight reconstruction and identification criteria, one can fight against the background mimicking the signal objects, and thus reject the reducible background. The muon reconstruction type, i.e CB, SA etc, reflects only the quantity of information used for the track reconstruction. On the other hand, the electron identification "menu" encapsulates a multitude of requirements, for instance, on its shower shape in the calorimeter and the number of inner detector hits (central electrons). The reconstruction and identification cuts are very important, especially for forward leptons which do not have an ID track, an thus the track quality and impact parameter cuts cannot be applied.

Track quality

A minimum number of hits in each sub layer of the inner detector is required in order to avoid reconstructed tracks with poor inner detector information. This cut should also take into account the dead sensors and the holes present in the ID. In the central electron case, this cut is embedded in the identification menu. The track quality cut can only be applied to leptons emitted in the $|\eta| < 2.5$ detector area.

Isolation

The isolation cut is the most powerful cut to reject background with fake electrons and muons. Two types of isolation can be defined: track and calorimetric isolations.

- The track isolation is defined as the ratio of the sum of the transverse momentum in a cone of ΔR around the lepton, excluding the track of the lepton itself, over the transverse momentum of the lepton. In order to exclude the pile-up contribution

from the sum computation, only tracks of good quality, coming from the primary vertex and having p_{T} above ≈ 1 GeV are considered.

- The calorimetric isolation is defined as the ratio of the sum of the transverse energy deposited in the calorimeter cells in a cone of ΔR around the lepton, excluding the lepton contribution, over the transverse energy of the lepton. The sum of the energy is corrected for energy leakage due to the lepton itself and for soft contributions coming from underlying events and the pile-up.

Impact parameter

There are two impact parameters, the transverse and longitudinal. The most important one is the transverse impact parameter ($d0$), which is defined as the distance of the closest approach of a track particle to the interaction point in the plan transverse to the beam-line. Usually, the significance of the impact parameters is used instead, $\frac{d0}{\sigma_{d0}}$, where σ_{d0} is the resolution of the impact parameter. This quantity plays an important role in order to discriminate against background events containing leptons from B hadron decays. Because of the B hadron lifetime, those leptons are expected to have larger $d0$ significance compared to the signal leptons which emerge from the primary vertex.

The longitudinal impact parameter is defined as the z coordinate at the point of the track closest approach to the interaction point. This parameter is also used to discriminate against particles with large lifetime. In most analysis, instead of directly applying the requirement on the z value, the $|z \cdot sin(\theta)|$ quantity is used instead. By doing so, one ends up with a quantity that is independent of the track direction, and thus independent of the track resolution.

Transverse momentum

While for central leptons one can lower the requirement on the P_{T} in order to increase the analysis acceptance without including too much background, this is not the case for the "extension" leptons. For the latter the cut on the P_{T} is a tool against the background helping increasing their purity.

Overlap removal

It can happen that two particles are found as emitted in the same direction. In such cases, the reconstruction has been defective. For this reason only the higher quality object is kept. The removal of one of the objects reconstructed in a very close region,

will also prevent from a double counting of one single object, twice reconstructed. This procedure is called overlap removal.

4.4.3 Event related cuts

Once the objects have been selected more requirements on the lepton system follow which can significantly suppress both the "reducible" and "irreducible" background contamination. Such requirements for instance are: to have two pairs of same flavor opposite sign leptons, to never allow more than one extension leptons per Z, both Zs to be on shell, etc. More details on these requirements are given in section 5.2.

4.5 Acceptance and Efficiency corrections

The limited detector acceptance along with the object and event selection requirements would lead to an observation biased by the detector layout and the specific analysis choices, if no corrections are applied to account for these. A cross section measurement is useful only if it can be directly compared to the theoretical predictions and to results obtained with other experimental setups. For this reason, the most commonly quoted cross section is the "total" ZZ cross section. Moreover, a "fiducial" cross section measurement that is defined in a simple and restricted fiducial volume, close to the reconstructed one, is useful, especially for comparison with theoretical estimations as it requires less extrapolations than the "total" one.

There are two correction factors that have to be computed. The first accounts for the loss of the signal events due to the selection cuts and it is noted C_{ZZ}, and the second accounts for the limited detector acceptance, noted A_{ZZ}. Only the first is needed for the computation of the "fiducial" cross section see eq. 4.2, while both the reconstruction efficiency and detector acceptance correction factors are needed for the "total" cross section computation, see eq. 4.1.

4.5.1 Reconstruction Efficiency C_{ZZ}

In section 4.4, the requirements that should be applied on the leptons and the event in order to reject background were discussed. The correction factor C_{ZZ} accounting for the ZZ event loss due to these cuts can be defined as the product of all cut efficiencies:

$$C_{ZZ} = \epsilon_{event} \times \epsilon_{lep} \tag{4.8}$$

where ϵ_{event} represent all the efficiencies related to the event pre-selection, such as the trigger and primary vertex cut, and ϵ_{lep} is the product of the individual efficiencies for the four leptons to pass the lepton selection cuts, such as P_T, isolation, d0 significance etc.

The above definition of the C_{ZZ} can indeed correct for reconstruction efficiencies, however, a problem arises as the fiducial volume in which the measurement is performed has to be defined. Thus, one usually first precisely define the reference fiducial volume in which the fiducial cross section will be measurement, and then compute the C_{ZZ} using the signal MC. The correction factor is then defined as the ratio of the number of MC signal events fulfilling the reconstruction level cuts over the number of events passing the fiducial volume cuts at generator level:

$$C_{ZZ} = \frac{N_{\text{Rec. } ZZ}^{\text{MC Pass All Cuts}} \times \text{SF}}{N_{\text{Gen. } ZZ}^{\text{MC Fiducial Volume}}} \tag{4.9}$$

where both the numerator and denominator have all the event-related weights that correct for simulation mis-description related to the pile-up and the z-vertex modeling, see 5.1. The SF is an event-by-event scale factor, correcting the simulation for all discrepancies between data and MC lepton efficiencies, such as the trigger and reconstruction. The C_{ZZ} correction essentially accounts for the probability of reconstructing a ZZ event inside the fiducial volume as it corrects for both the limited reconstruction efficiency and for the difference between the reconstruction and reference fiducial volume.

Another important issue in this analysis is the treatment of Z bosons decaying to a tau pair, $ZZ \to \ell\ell\tau\tau$ and $ZZ \to \tau\tau\tau\tau$ with the τ decaying in e and μ. In this analysis we made the choice to embed the correction for this contamination inside the C_{ZZ}. This means that the tau samples are considered as signal samples, and thus they contribute to the C_{ZZ} numerator, but not to the denominator. This additional correction encapsulated in the C_{ZZ}, contrary to the previous two correction sources that tend to pull the correction factor value down, will push the C_{ZZ} value slightly higher. The tau contamination in the $ZZ \to \ell\ell\ell'\ell'$ analysis is quite low, less than 1%, thanks mainly to the mass cut on the Z bosons.

Finally, it should be mentioned that since the selection cuts for electrons and muons are different, the fiducial volume corresponding to each channel will also be different. Therefore, the calculation of a combined fiducial correction factor is not possible, unless an additional extrapolation to a common fiducial volume is performed. The fiducial volume definition for each decay channel is presented in section 4.5.3.

4.5.2 Total Acceptance A_{ZZ}

In order to calculate the integrated cross section for the production of both Z bosons being on-shell, one must also apply a correction accounting for the limited detector acceptance. This is obtained by extrapolating the truth-level fiducial volume to the truth-level full phase space. The A_{ZZ} is defined as:

$$A_{ZZ} = \frac{N_{\text{Gen. } ZZ}^{\text{MC Fiducial Volume}}}{N_{\text{Gen. ZZ}}^{\text{MC All}}} \tag{4.10}$$

The denominator of the A_{ZZ} is the total number of on-shell $ZZ \to \ell\ell\ell'\ell'$ events with $\ell = e$, or μ, generated in the total phase space, while the numerator of the A_{ZZ} is actually the denominator of C_{ZZ}, i.e the on-shell ZZ events in the fiducial phase space. The computation of the total cross section needs the A_{ZZ}xC_{ZZ} and thus it would be sufficient to compute the ratio of the reconstructed events to the generated on-shell ZZ events. However, the factorisation of these two corrections helps to better understand the two different correction origins. Again, A_{ZZ} is calculated for each channel separately.

4.5.3 Total and Fiducial volume definitions

Total volume definition

The analysis performed in this document aims to an on-shell cross section measurement. Thus, for the total volume definition a restriction on the mass of the Z bosons is applied. The truth level cut on the Z mass is:

- $66 < m_{a^+a^-}(Z/\gamma^*) < 116$ GeV, where $m_{a^+a^-}(Z/\gamma^*)$ is the mass of the pair with a reconstructed mass closest to the PDG value, and it is called "primary" Z.
- $66 < m_{b^+b^-}(Z/\gamma^*) < 116$ GeV, where $m_{b^+b^-}(Z/\gamma^*)$ is the mass of the pair further away of the PDG value, and it is so called "secondary" Z

where the a index represents the leptons of the primary Z, and the b index the leptons of the secondary Z boson.

Fiducial volume definition

In order to provide a fiducial cross section measurement, as already discussed, one needs first to define the fiducial phase space. There are two guidelines for the fiducial volume choice:

- First, the more natural way to proceed is to define a fiducial volume the closest possible to the reconstructed-level selection. By doing so, the C_{ZZ} will be as high as possible since it will only correct for the limited reconstruction efficiency, and will not include "extrapolations" in regions where the detector does not measure, or measure with poor efficiency.

- Second, the simplicity of the fiducial volume definition is essential, as it makes easier the comparison with theory and other experimental results.

In this analysis, same flavor particles with different features (i.e central, forward and calorimetric muons) are considered and thus at reconstruction level slightly different cuts are applied to each type. It is probably preferable to have the same truth-level definition for all same flavor sub-type particles. With this choice, the fiducial volume will be kept simple with the cost of lowering the C_{ZZ} since it will also account for differences between the reconstruction volume and fiducial volume.

Besides the on-shell requirement on both Z bosons, truth-level cuts on the pseudo rapidity $|\eta|$ and on the transverse momentum P_T of the final state leptons will be applied. In the introduction of this chapter it was said that all lepton inside the detector acceptance should be used in order to decrease the measurement statistical error, hence this will be the guideline for the fiducial volume definition. In figure 4.1 it was shown that almost 40% of the ZZ events have at least an electron or muon with $|\eta|>2.5$ and thus it is important to include all leptons that can be potentially reconstructed by the ATLAS detector. In Figure 4.6, a true-level study of the minimum transverse momentum of the electrons and muons composing on-shell ZZ events which have all of their 4 leptons inside the detector fiducial volume is shown. One sees that there are about 2% of 4μ and $2e2\mu$ events having a muon with $P_T < 10$ GeV, and about 3% of 4e and $2e2\mu$ events having an electron with $P_T < 10$ GeV. At reconstruction level, in order to still be protected of background leptons and do not increase too much the systematic uncertainties, central leptons with a momentum down to 7 GeV will be included.

Here are summarized the fiducial volume cuts that will be applied on the electrons and muon per channel in addition to the on-shell requirement :

Four electron channel:

- All leptons are required to have a transverse momentum greater than 7 GeV
- Require at least three electrons with $|\eta| < 2.47$, and allow at most one electron in the range $2.47 < |\eta| < 4.9$

Four muon channel:

- The momentum requirement for all muons of the event is the same as for the electrons, i.e $P_T > 7$ GeV

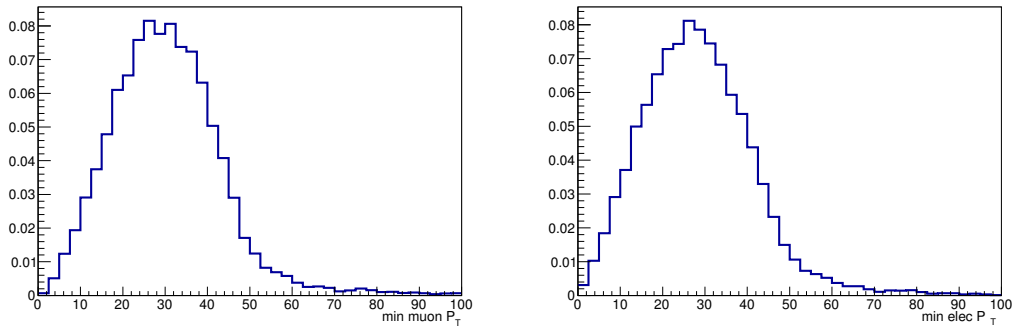

Figure 4.6: Distribution of the minimum transverse momentum of the muon (left) and electron (right) that is inside the fiducial volume of an on-shell ZZ event at generator.

- All muons are required to be emitted within the detector acceptance, i,e $|\eta| < 2.7$

Two electrons two muons channel:

- Both electrons and muons are required to have $P_T > 7$ GeV
- Cuts on the $|\eta|$:

  - For the electron pair, either both electrons can be emitted in the central detector area, i.e $|\eta| < 2.47$, or, at most one electron can be emitted in the forward area, i.e $2.47 < |\eta| < 4.9$

  - For the muon pair both muons must have $|\eta| < 2.7$

Finally, all four leptons of the ZZ event are required to be spatially separated with the minimum allowed distance being $\Delta R(\ell, \ell) > 0.2$. The fiducial volume definition is summarized in table 4.1.

Two pairs of opposite sign same flavor leptons
$66 < m_{Z_{1,2}} < 116$ GeV
$\Delta R(\ell, \ell) > 0.2$
$P_{T_\ell} > 7$ GeV
$\|\eta_\ell\|$:
$eeee$: $\|\eta_e\| < 2.5$ OR ($\|\eta_{e_{1,2,3}}\| < 2.5$ AND $\|\eta_{e_4}\| < 4.9$)
$\mu\mu\mu\mu$: $\|\eta_\mu\| < 2.7$
$2e2\mu$: $\|\eta_\mu\| < 2.7$, $\|\eta_{e_{1,2}}\| < 2.5$ OR ($\|\eta_{e_1}\| < 2.5$ AND $\|\eta_{e_2}\| < 4.9$)

Table 4.1: The fiducial volume definition.

It should be stressed that due to the different fiducial volume definitions for each decay channel, no combined fiducial cross section measurement can be provided.

The values of A_{ZZ} can be found in table 4.2 for the three decay channels. These values have been computed using the nominal signal samples of this analysis which are $POWHEG$ and $gg2VV$, see 5.1. As expected, the A_{ZZ} value for the four electron channel is closer to 1 compared to the four muon channel because of the larger electron fiducial volume, $|\eta| < 4.9$ for at most one electron, to be compared to $|\eta| < 2.7$ for muons.

$llll$	$eeee$	$\mu\mu\mu\mu$	$ee\mu\mu$
A_{ZZ}	0.817 ± 0.001	0.645 ± 0.001	0.726 ± 0.001

Table 4.2: The acceptance correction factor A_{ZZ} for the three $ZZ \to \ell\ell\ell'\ell'$ decay channels. Only the statistical error is shown.

4.5.4 Theoretical systematic uncertainties

There are theoretical uncertainties affecting the correction factors C_{ZZ} and A_{ZZ} that should be taken into account for the cross section extraction. These include differences due to the simulation frameworks, the choice of the parton distribution functions (PDF) and the QCD scales. The impact of all these uncertainty sources on the $ZZ \to \ell\ell\ell'\ell'$ analysis will be discussed in the next chapter. Here a general description follows.

The differences between the simulation frameworks can appear at all steps of the simulation chain: the hard process generation, the parton shower modeling (ISR, FSR), the hadronisation process and the underlying event modeling. Processes probed in the leptonic final states are expected to be affected mainly by the choice of the simulation packages for the hard process modeling, the ISR and FSR while the modeling of the hadronisation is expected to rather affect processes probed in the hadronic final state.

The uncertainties related to the parton distribution functions used for the MC generation are also expected to impact the measurement. The PDFs give the probability of finding a parton i involved in the hard scattering of momentum transfer Q^2 which has a fraction of the proton momentum x_i, $f_i(x_i, Q^2)$, see [71] [72] [73]. The PDFs are primarily extracted from lepton-nucleon deep inelastic scattering experiments, such as HERA. The neutral and charged current cross sections can be expressed as a function of the proton structure functions which are directly related to the PDFs in the perturbative QCD framework. Results from TEVATRON and LHC experiments have been used as well to further improve the PDF estimation.

For instance, an important contribution to the constrain of quark-anti quark PDFs came from Drell-Yan dimuon studies in Tevatron fixed target experiments E605, E772 and E866 [74] [75] [76]. There are several groups that work independently for the PDF determination. The main differences between these groups come from the used data-sets, the order on which the perturbative QCD calculations are performed, the parametrisation assumptions and the treatment of the systematic uncertainties.

Lastly, the cross section of a process should not depend on the choice of the renormalization and factorisation scales when all higher order correction are considered in the calculations. However, as the calculations for the ZZ process are up to NLO in QCD, the simulations are expected to depend on the choice of the QCD scales.

Chapter 5

Cross section measurement

In this chapter the analysis performed in order to obtain the ZZ cross section measurement is presented. First, in section 5.1, details on the dataset and the signal simulation samples are given. In section 5.2, specificities on the $ZZ \to \ell\ell\ell'\ell'$ selection are presented, based on the explanations of section 4.4. In section 5.3 the background contamination from reducible and irreducible sources is estimated, and details on the data-driven method used to extract the reducible background are presented. In section 5.4 the data event yields are compared to the signal plus background prediction. Then, in section 5.5 all the systematic errors affecting the measurement are given. The statistical procedure followed in order to perform the measurement is described in section 5.6. Finally, in section 5.7, after having discussed all the ingredients needed for the cross section measurement, the results on the total and fiducial cross sections are presented and the impact of each systematic source on the total cross section measurement is discussed. These results are compared to theoretical prediction and previous measurements.

5.1 Data and MC

The ZZ cross section measurement that will be presented in this document is based on LHC proton-proton collision data, recorded by the ATLAS detector during 2012, at a center-of-mass energy of $\sqrt{s} = 8$ TeV. After cleaning the dataset from subperiods with defective detector operation, the effective integrated luminosity [1] is found to be 20.3 fb^{-1}. As it was discussed in section 2.1.2 the preliminary estimation of the integrated luminosity uncertainty is $\pm 2.8\%$.

[1] based on the latest Good Run List for W/Z analysis data12_8TeV.periodAllYear_DetStatus-v58-pro14-01_DQDefects-00-00-33_PHYS_StandardGRL_All_Good.xml

Monte Carlo simulation samples have been generated for all the processes that can be potentially observed at the 8 TeV LHC run. In the following paragraph, before entering in the description of our signal simulation samples, the corrections that need to be applied on the 2012 MC simulation in order to match the 8 TeV data are discussed.

5.1.1 Experimental corrections on the MC

It has been already mentioned that one needs to apply scale factors (SF) on MC simulations in order to account for the lepton mis-modelling. These SF are derived from the comparison of lepton efficiencies in data and MC. It can happen that the simulation of general collision features, such as the number of collisions per bunch crossing ($< \mu >$) and the z-position of the primary vertex, may also suffer from mis-modeling.

During the 2012 run, the $< \mu >$ is estimated to be ≈ 21, see fig. 5.1. However, MC simulations do not reproduce this profile correctly, and thus one has to perform a "pile-up reweighting" of the MC distributions. The applied weight can change the shape of the kinematic distributions, but it should not modify the sample cross section.

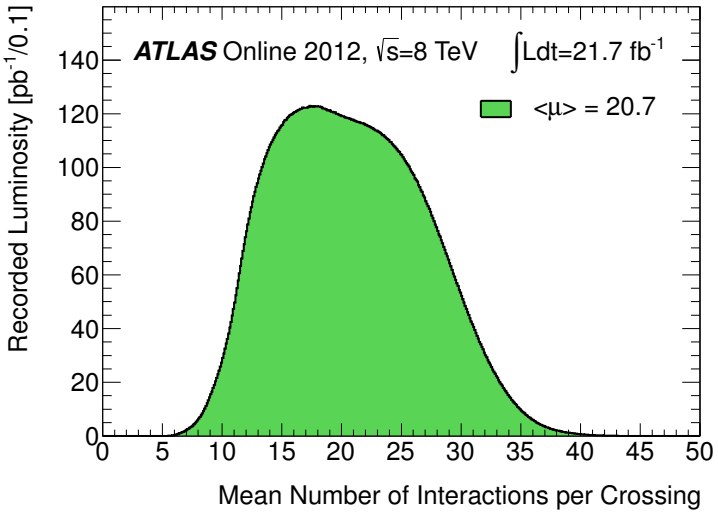

Figure 5.1: Luminosity-weighted distribution of the mean number of interactions per crossing for the full 2012 pp collisions dataset.

The second feature that needs to be corrected is the spread of the z-vertex. For instance, a larger z-vertex position can lower the reconstruction efficiency since

particles can artificially end up outside the detector acceptance. The observed data-MC discrepancy for 2012 simulations could have an impact up to 2% on the electron identification efficiency due to missing ID tracks. This was corrected by reweighting the beamspot z0 width distribution.

5.1.2 Signal process modeling

A pair of two Z bosons can be directly produced either by quark-antiquark interaction via the t and u-channels, or by gluon-gluon fusion, see fig. 1.5 and 1.6, respectively. The latter is a NNLO QCD diagram which is estimated to contribute approximately 5% to the total ZZ cross section for a center of mass energy of 8 TeV.

The simulation of the ZZ signal is performed using two different generators: $POWHEG$ [77] for the quark-antiquark interaction modeling and $gg2VV$ [78] for the gluon-gluon interaction. $POWHEG$ is a NLO QCD generator and thus it takes into account, at matrix element level, all NLO corrections such as loop diagrams and parton emissions. The $gg2VV$ generator does not include QCD corrections at higher orders, but it does include $H \rightarrow ZZ^*$, and also the interference between the SM ZZ process and the $H \rightarrow ZZ^*$. Still, this contribution is not expected to affect our measurement as the low Higgs mass results to an off-shell ZZ decay, while our measurement focuses on the on-shell ZZ production. Furthermore, the interference between the Higgs and the SM ZZ production is expected to be rather small, and only slightly decrease the on-shell cross section [79] [78]. Both generators are interfaced with $Pythia8$ [80] for the parton emission and hadronisation modeling.

While the NLO QCD corrections are well known and already implemented in the majority of the generators, the NLO electroweak and the NNLO QCD corrections for the ZZ production are not yet directly implemented in the generator level. So far, higher order effects are partially taken into account by the showering algorithms, such as $PHOTOS$ [81] and $Pythia$, that model the extra photon and parton emissions, respectively. However, lately a great effort has been carried out by theoreticians so that a complete calculation of these higher order effects is obtained.

The NLO EW virtual corrections have been recently computed by Kasprzik et al, and are found to decrease the total $q\bar{q} \rightarrow ZZ$ cross section by 4% [82] [83] [84]. The dependence of this correction with the energy of the Z boson was found to be significant, as it can reach 20% for high Z transverse momentum. This dependence makes this correction important for this analysis, as the sensitivity on the anomalous couplings is at high energies. To account for these NLO EW effects, theorists provided us with a differential k-factor, and an interface specifically developed to be used on the $POWHEG$ samples [85].

The NNLO QCD corrections to the total $q\bar{q} \to ZZ$ cross section have been recently computed by Grazzini et al [86], and they are found to increase the total cross section approximately 4%. However, the differential calculation is still missing and thus it is not possible yet to incorporate them in our analysis. The lack of these NNLO QCD corrections is indirectly taken into account in our analysis by the scale uncertainties.

Both simulation samples use the CT10 [71] parton distribution function and they were generated with a dynamic normalization and factorization scale, equal to the invariant mass of the four leptons, m_{ZZ}.

5.2 The Selection and its efficiency

In the previous chapter, and more specifically in section 4.4, an analysis overview and the guidelines for an optimal lepton selection have been introduced. In this section, the details on the event and lepton selection are given and the efficiencies of the applied requirements are presented.

5.2.1 Object selection

When the ZZ production results in two charged lepton pairs, it has the cleanest signature among all diboson processes. As already discussed, such a final state allows an almost background free analysis. However, because of the already small ZZ cross section and the small $Z \to ll$ branching ratio, which is of the order of 3.3%, this analysis suffers from high statistical uncertainties. Hence, for both electrons and muons a common aim was established: maximize the acceptance while keeping the background and the associated systematics as low as possible. The acceptance has been maximised by also including all types of extension leptons. In order to maintain a high purity among these "lower" quality particles tighter selection criteria have to be applied on them. In the following paragraphs the exact criteria on each lepton category are presented.

Muons

The muon categories included in this analysis are: central muons ($|\eta| < 2.5$), forward muons ($2.5 < |\eta| < 2.7$) and calorimetric muons ($|\eta| < 0.1$). The latter help to recover reconstruction efficiency in the central detector area where no muon chambers exist due to the detector service hole.

All types of muon tracks must have a minimum number of hits recorded by the inner detector. This allows to fight against cosmic muons or muons from in flight decays of heavy hadrons. More specifically central and calorimetric muons must have at least 1 hit in all Pixel layers, 5 in the SCT, and less than 3 holes (no hit in a layer crossed by the track) in all silicon layers. For all those hit conditions, dead sensors are counted as observed hits, not as holes. Forward muons must fulfill the same requirements except for the minimum number of SCT hits which drops from 5 to 3 hits.

While central muons can be Segment-Tagged, i.e they are allowed to have only few segments in the muon spectrometer matched with an ID track, forward muons must have hits to all three stations of the muon spectrometer in order to compensate for insufficient inner detector coverage above $|\eta| > 2.5$. For calorimetric muons, in order to cope with the high multiplicity recorded by the electromagnetic calorimeter and the lack of muon spectrometer information, there are two additional quality discriminants. Both discriminants (one is cut-based, the other uses a likelihood method) aim to increase the reconstruction purity, for instance by looking at the likelihood of seeing an energy deposit in the calorimeter layers which is due to the passage of a minimum ionizing particle, such as a muon [87]. Furthermore, a removal of calorimetric muons close to the central muons within a cone of $\Delta R < 0.1$ is performed. By doing so, double counting is avoided and priority is given to the central muons, since these have the higher quality.

A muon coming from a Z decay is expected to have high momentum. A selection requirement based on the muon kinematic is essential to dig-out the signal and reject the background. The central muons used in this analysis are required to be Combined or Segment-Tagged. These muons have higher reconstruction efficiency and higher reconstruction purity with respect to the forward and calorimetric muons, and thus one can go as low as 7 GeV in the transverse momentum range without losing significantly in purity or increasing the systematic uncertainties. For the forward muons this threshold is 10 GeV and for calorimetric muons is 20 GeV, owing for their lower intrinsic purity.

Another very important mean to discriminate against the background leptons coming from heavy flavor decays or particle conversions, is to cut on the transverse and longitudinal impact parameters. All three muon categories share a common cut on the significance of the transverse impact parameter, of $|\frac{d0}{\sigma_{d0}}| < 3$, and on the longitudinal impact parameter, of $|z_0 \cdot sin(\theta)| < 0.5$ mm.

Finally, the last mean to fight the background coming from fake leptons inside a jet, is the isolation criterion. Between the two isolation types, (calorimetric and

track), the track isolation is usually preferred to the calorimetric isolation because of the higher uncertainties involved in the calculation of the latter. Such uncertainties are mainly due to the difficulty in the precise estimation of the pile-up noise in the electromagnetic calorimeter. For the above reason the track isolation is used for central and calorimetric muons as they both have a high precision inner detector track. On the other hand, forward muons lack a good ID track, consequently, the calorimetric isolation is used for these. In all cases, a cone of 0.2 around the track(cluster) is considered, in which the fraction of the momentum(energy) around the muon over the momentum(energy) of the muon should be less than 15%.

The prompt leptons of this analysis are supposed to fulfill the impact-parameter and isolation requirements, however, this may not always be the case. The efficiency of these cuts has been computed with a tag and probe method in both data and MC and small differences have been observed. Scale factors were introduced to correct MC for this mis-modeling. The uncertainties related to their estimation are propagated to the cross section measurement.

In table 5.1 the cumulative efficiency of the selection cuts for the three muon categories is shown as computed using an exclusive $ZZ \to \ell\ell\ell'\ell'$ *Pythia* sample. In order to make sure that only the reconstructed muons coming form Z decays are considered, they are required to be reconstructed within a cone of 0.2 around a true muon which has as a parent an on-shell Z boson. The yields are normalized to the total number of muons of each category present in the signal sample having an on-shell Z parent.

Requirement	Central μ [%]	Forward μ [%]	Calorimeter-tagged μ [%]
Transv. momentum	97.5 ± 0.0	92.6 ± 0.4	91.0± 0.4
Calo-Tagg quality	-	-	90.4± 0.4
ID hits	97.3 ± 0.1	90.9 ± 0.5	90.4± 0.4
$\lvert z_0 \cdot sin(\theta)\rvert$	97.0 ± 0.1	90.5 ± 0.5	90.0± 0.5
$\lvert d_0\rvert/\sigma(d_0)$	95.6 ± 0.1	90.0 ± 0.5	89.1± 0.5
Track isolation	94.3 ± 0.1	-	88.4± 0.5
Calo. isolation	-	88.2 ± 0.5	-
Overlap removal	-	-	26.8 ± 0.7

Table 5.1: Cumulative efficiency (%) of the successive selection requirements on the three muon types.

Electrons

As for the muon case, all types of electrons that can be measured with the ATLAS detector are considered in this analysis. This raises the $ZZ \to eeee$ acceptance up

to $|\eta| = 4.9$. Central electrons are those emitted below $|\eta| < 2.5$. They are required to have a cluster transverse energy greater than 7 TeV. It should be noted that for electrons with more than four silicon (SCT and Pixel) hits in the inner detector, the η and ϕ are taken from the track measurement, otherwise these parameters are taken from the cluster. The forward electrons are emitted in a pseudorapidity range of $2.5 < |\eta| < 4.9$. The threshold on the forward electrons transverse energy is significantly higher, set at 20 GeV, in order to compensate for their lower intrinsic purity due to the lack of inner detector track.

Electrons main signature is the energy deposit in the electromagnetic calorimeter. Due to the important background activity in the EM calorimeter, special attention is given on the reconstruction of the cluster and its matching to the ID track. There are several identification "menus" with variable tightness on the electron reconstruction requirements. The menu that suits best for the central electrons of this analysis is the *multilepton*, as it was optimized for multi-electron analysis that include as well low energy electrons. Forward electrons must fulfill the *loose* menu.

In addition to the above requirements, central electrons must also fulfill the following requirements for the two impact parameters: $|z_0 \cdot sin(\theta)| < 0.5$ mm and $|\frac{d0}{\sigma_{d0}}| < 6$. The track isolation requirement is also applied to central electrons, and has the same value as for muons, i.e 0.15. No impact parameter and isolation requirements are applied to forward electrons.

Finally, if an electron is found within a cone of $\Delta R < 0.1$ with a muon or with some other higher energy electron, then it is removed in order to prevent double counting.

In table 5.2 the cumulative impact after each cut is presented for the two electron categories. The numbers are produced following the same procedure described for the muon cut efficiency computation.

Requirement	Central e [%]	Forward e [%]
Transv. momentum	97.2 ± 0.0	69.6 ± 0.4
Identification	89.5 ± 0.1	61.8 ± 0.4
$\|z_0 \cdot sin(\theta)\|$	88.9 ± 0.1	-
$\|d_0\|/\sigma(d_0)$	87.9 ± 0.1	-
Track isolation	86.9 ± 0.1	-

Table 5.2: Cumulative efficiency (%) of the successive selection requirements on the two electron types.

5.2.2 ZZ event selection

Preselection

In this section a set of general cuts, which are common between all the physics analysis are listed. These cuts are related to the global event features and have been already introduced in section 4.4.1.

- Good Runs List: Keep only events existing in the Good Runs List.

- Trigger: The event must pass an unprescaled single-electron or single-muon trigger. Those used are the lowest threshold triggers that remain unprescaled over the whole data taking period. Muons must pass the `EF_mu24i_tight` or `EF_mu36_tight` triggers. The first requires an isolated (12% in a cone of 0.2) muon with $P_T > 24$ GeV, while the second raises the P_T threshold to 36 GeV without looking at the muon isolation. Electron must pass the `EF_e24vhi_medium1` or `EF_e60_medium1` triggers. The first requires one isolated (10% in a cone of 0.2) $medium++$ electron with $P_T > 24$ GeV, while the second trigger requires $P_T > 60$ GeV and an identification $medium++$ without examining the isolation. In the $e^+e^-\mu^+\mu^-$ channel, either of the muon or electron triggers may be fulfilled. In table 5.3 the cut efficiency of these triggers on the ZZ selection is shown.

- Primary vertex: The primary vertex must have at least 3 tracks associated to it. By doing so it is more likely that the event corresponds to a hard scattering.

- Event cleaning and data corruptions: Remove events with: α) incomplete event information, β) noise bursts and data integrity errors in the Liquid Argon calorimeter, γ) corrupted tile information. These detector-related issues are taken into account in the integrated luminosity calculation.

	$eeee$ [%]	$\mu\mu\mu\mu$ [%]	$ee\mu\mu$ [%]	$\ell\ell\ell'\ell'$ [%]
Trigger efficiency	99.7± 0.1	97.5 ± 0.2	99.2 ± 0.1	98.8 ± 0.1

Table 5.3: Trigger Efficiency estimated on MC with all SF applied.

Selection

While the event pre-selection is similar among all physics analyses, the event selection that follows is specifically developed to identify the on-shell $ZZ \to \ell\ell\ell'\ell'$ events. Besides the selection of energetic high quality isolated leptons, discussed in previous section, a key to the signal identification is the study of the event as an ensemble. Requirements on the lepton system result to an enhancement of the signal over background ratio.

- Four leptons: The events must have exactly four leptons passing the selection criteria listed in section 5.2.1.

- Quadruplet Formation: There must be two lepton pairs, each one composed by two same flavor opposite sign leptons.

- ΔR between leptons: None of the selected four leptons should overlap with another lepton of the quadruplet within a cone of $\Delta R(\ell, \ell) > 0.2$.

- Extension leptons: In an event, the number of allowed extension leptons i.e of forward electrons, forward muons and calorimetric muons is limited to a maximum of one per type. It is also required that each lepton pair consists of at most one extension lepton.

- "Primary" Z candidate: The Z candidate closest to the Z pole mass must satisfy the mass cut $66 < m_{12} < 116$ GeV.

- "Secondary" Z candidate: The other Z candidate must fulfill the same mass cut, i.e $66 < m_{34} < 116$ GeV.

- Trigger matching: At least one lepton with $p_{\mathrm{T}} > 25$ GeV must be matched to a trigger object. If the trigger matched lepton is an electron it must fulfill the `Medium++` identification requirement. If the trigger matched lepton is a muon it is required to be a Combined muon in the central area, $|\eta| < 2.4$. A scale factor is applied on MC events to account for any mis-modeling of the single-lepton trigger efficiency compared to the data. It is calculated as:

$$SF = \frac{1 - \prod_{n=1}^{N_l}(1 - \epsilon_{\mathrm{data,l_n}})}{1 - \prod_{n=1}^{N_l}(1 - \epsilon_{\mathrm{MC,l_n}})} \tag{5.1}$$

where N_l is the number of leptons forming the ZZ candidate that are matched to a trigger object, $\epsilon_{\mathrm{data,l_n}}$ is the data trigger efficiency for a lepton of flavor l_n, and $\epsilon_{\mathrm{MC,l_n}}$ is the MC simulation trigger efficiency. For 2012 data the SFs are very close to 1 for any actual lepton composition, and the error associated to the central value is less than 0.2%.

- Partner electron: If one among the two electrons forming a Z is forward, then the "partner" central electron must have a transverse momentum above 20 GeV.

- J/ψ veto: A last cut is applied on the invariant mass of any combination of oppositely charged same flavor lepton pairs in order to exclude J/ψ events. This cut requires the dilepton mass to be above 5 GeV.

Table 5.4 shows the absolute impact of the ZZ event related cuts on the number of expected ZZ events. The numbers are obtained using the full statistics of our nominal ZZ signal simulation samples and are normalized to 20.3 fb^{-1}. It should be stressed that all event pre-selection and lepton selection requirements have been

Requirement	$eeee$	$\mu\mu\mu\mu$	$ee\mu\mu$	$\ell\ell\ell'\ell'$
Four leptons				605.73 ± 1.24
Quadruplet formation	126.53 ± 0.51	168.05 ± 0.59	287.61 ± 0.94	582.19 ± 1.22
ΔR between leptons	126.46 ± 0.51	168.0 ± 0.59	287.52 ± 0.94	581.98 ± 1.22
Extension leptons	108.35 ± 0.45	163.0 ± 0.57	266.49 ± 0.88	537.83 ± 1.14
"Primary" Z candidate	88.58 ± 0.41	125.95 ± 0.5	210.83 ± 0.78	425.36 ± 1.01
"Secondary" Z candidate	64.63 ± 0.35	84.35 ± 0.41	144.83 ± 0.65	293.82 ± 0.84
Trigger match	64.6 ± 0.35	83.8 ± 0.41	144.49 ± 0.64	292.89 ± 0.84
Partner electron	62.18 ± 0.34	83.8 ± 0.41	141.72 ± 0.64	287.7 ± 0.83
J/ψ veto	62.14 ± 0.34	83.74 ± 0.41	141.72 ± 0.64	287.6 ± 0.83

Table 5.4: Number of expected ZZ events normalized to 20.3 fb^{-1} after each selection requirement.

already applied along with all the event and lepton related corrections. Thus, the last row of the table indicated the expected number of ZZ events in the 2012 dataset.

It is of great interest to decompose the expected signal yield in order to quantify the contribution of the extension leptons. In table 5.5 the number of events containing at least one extension lepton is shown. The gain in the total yield is 17.5%. More specifically, in the four electron channel the gain from adding the forward electrons is almost 20%, while in the 2e2μ is 10%. The inclusion of the forward and calorimetric-tagged muons brought a 15% increase in the four muon channel, and 7% in the 2e2μ channel.

	$eeee$	$\mu\mu\mu\mu$	$ee\mu\mu$	$\ell\ell\ell'\ell'$
All Central e and μ	50.18 ± 0.3	71.35 ± 0.37	115.96± 0.58	237.49 ± 0.89
At least 1 Ext. e or μ	11.96 ± 0.15	12.39 ± 0.16	25.76 ± 0.27	50.11 ± 0.32
1 Forw. e	11.96 ± 0.15	-	14.321± 0.2	26.28 ± 0.25
1 Forw. μ	-	7.44 ± 0.12	5.92 ± 0.13	13.36 ± 0.18
1 Calo-Tag μ	-	4.81 ± 0.1	3.91 ± 0.11	8.72 ± 0.15
1 Forw. μ +1 Forw. e	-	-	1.31 ± 0.06	1.31 ± 0.06
1 Calo-Tag μ + 1 Forw. e	-	-	0.31 ± 0.03	0.31 ± 0.03
1 Forw μ + 1 Calo-Tag μ	-	0.14 ± 0.02	-	0.14 ± 0.02

Table 5.5: Signal yields decomposition in extension lepton contributions.

5.2.3 Reconstruction efficiency

In the previous sections all the selection cuts applied on the particles and on the event have been presented. These cuts will reject some of the ZZ events because of the limited reconstruction efficiency, this issue has been already discussed in

section 4.5.1. The reconstruction efficiency correction factor with respect to the defined fiducial volume, see sec. 4.5.3, is shown in the first row of table 5.6. In the second row the A_{ZZ} value already presented in section 4.5.3 is recalled.

	$eeee$	$\mu\mu\mu\mu$	$ee\mu\mu$
C_{ZZ}	0.496 ± 0.002	0.849± 0.002	0.644 ± 0.001
A_{ZZ}	0.817 ± 0.001	0.645± 0.001	0.726 ± 0.001

Table 5.6: The reconstruction correction factor C_{ZZ} and the acceptance factor A_{ZZ} per channel. Only the statistical error is shown.

The C_{ZZ} for the four muon channel is higher compared to the four electron channel. This is expected due to the lower electron reconstruction and identification efficiency. It is reminded that the 1-C_{ZZ} is not entirely due to limited lepton reconstruction efficiencies, since the C_{ZZ} also accounts for the differences between the defined fiducial volume and the selection at reconstruction level. For example, at the reconstruction level the partner of a forward electron must have a transverse momentum larger than 20 GeV while at truth level no such requirement is applied. This is done in order to keep the fiducial volume definition simple for the easier comparison with theory predictions.

5.3 The background estimation

The background sources to the $ZZ \to \ell\ell\ell'\ell'$ process have been already discussed in section 4.3. There exist MC simulations for all physics processes, thus we could estimate the expected contamination using those. However, this is not always suitable, especially when the contamination is due to fake leptons. These fake leptons are produced inside jets and since the jet fragmentation is difficult to model it is preferable not to rely on the simulation. Furthermore, as these are edge effects, the available MC statistics after applying the full ZZ selection is very low, and does not allow a reliable estimation. For these reasons, the reducible background estimation is based on the data, using so called data-driven methods. Contrariwise, the irreducible background containing four prompt leptons can be directly estimated from simulations, as no simulation or low statistics problems are involved[2].

[2]The only eventual problem is the high uncertainty on the cross section of the irreducible DPI background which can reach 50%. This however will not affect our measurement as the contamination is expected to be very small («1 event) for the 2012 LHC running conditions.

5.3.1 Background estimation from MC

In this section the background yields using MC simulations are presented. For the irreducible background i.e the tri-boson production ZZZ/ZWW, the $tt\bar{V}$ and the double-parton interactions, the obtained numbers are directly used for the cross section extraction. The MC estimations that will be shown hereafter for the reducible background i.e V+jets, VW and top, are given just for illustration, as a data-driven technique is used for their determination. The list of the MC background samples considered here is given in the appendix A.

In table 5.7 the progressive impact of the ZZ selection cuts on all types of backgrounds is shown for each ZZ decay channel separately. The numbers are normalised to 20.3 fb^{-1}. It can be seen that for all background processes the requirement of having two opposite sign same flavor (OSSF) lepton pairs eliminates a lot of background events, as does the mass requirement on the two Z bosons. The three first columns are for the reducible background, while the fourth column is for the irreducible background. In the last column the sum of all the backgrounds is shown. The last row shows the final MC background expectation for all channels. There are in total 14.0 $\pm$ 6.2 expected background events. This estimation suffers from high statistical errors, especially for the Z+jet background which is the dominant background in the four electron channel. For instance, these 9.1 V+jets events in the *eeee* channel are actually three events with important weights.

Table 5.8 shows the background decomposition in terms of extension lepton contributions for each final state. In the four electron channel the extension lepton contribution is found overwhelming, with however a very large statistical error. For the two other channels the statistical error is reasonable. In the $2e2\mu$ channel the background contribution seems to come equally from central and extension leptons, while in the 4μ channel, it comes mainly from central muons. Complementary investigation of the extension lepton background contamination will follow in the next section, where the data - driven estimation of the reducible background is presented.

Table 5.9 shows for each final state the irreducible background contamination decomposed in the three sources: double-parton interaction, tri-boson and $t\bar{t}$+V. As the tri-boson background and the $t\bar{t}+Z$ contain at least one Z boson, as expected the cut on the second Z is crucial for the background rejection. Only the statistical error is shown, which is less than 10% for the total estimation in each decay channel.

$ZZ \to eeee$					
Cut	V+jets	VW	top	$ZZZ/ZWW/ttV/DPI$	sum
Four Leptons	392.12 ± 36.99	26.13 ± 1.22	51.52 ± 2.93	11.26 ± 0.23	480.87 ± 37.13
OSSF	149.93 ± 23.91	4.85 ± 0.56	7.53 ± 1.30	1.20 ± 0.06	163.51 ± 23.95
DR	142.48 ± 23.58	4.85 ± 0.56	7.31 ± 1.29	1.20 ± 0.06	155.84 ± 23.62
Ext. lept	58.21 ± 15.55	3.46 ± 0.45	5.35 ± 1.12	1.03 ± 0.06	68.05 ± 15.6
$66 < M_1 < 116$ GeV	44.82 ± 13.85	2.96 ± 0.42	4.35 ± 1.05	0.93 ± 0.05	53.06 ± 13.89
$66 < M_2 < 116$ GeV	12.65 ± 6.48	1.04 ± 0.27	0.66 ± 0.29	0.42 ± 0.04	14.76 ± 6.5
J/ψ Veto/TrigMatch/F.el	9.14 ± 6.13	0.89 ± 0.25	0.43 ± 0.26	0.41 ± 0.04	10.87 ± 6.14
$ZZ \to \mu\mu\mu\mu$					
Cut	V+jets	VW	top	$ZZZ/WW/tt/DPI$	sum
Four Leptons	392.12 ± 36.99	26.13 ± 1.22	51.52 ± 2.93	11.1 ± 0.23	480.87 ± 37.13
OSSF	1.64 ± 1.19	0.29 ± 0.11	0.82 ± 0.32	1.46 ± 0.07	4.21 ± 1.24
DR	1.64 ± 1.19	0.28 ± 0.11	0.82 ± 0.32	1.46 ± 0.07	4.2 ± 1.24
Ext. lept	1.53 ± 1.12	0.26 ± 0.10	0.80 ± 0.31	1.41 ± 0.07	4.01 ± 1.17
$66 < M_1 < 116$ GeV	1.09 ± 1.02	0.24 ± 0.10	0.37 ± 0.19	1.29 ± 0.06	2.98 ± 1.05
$66 < M_2 < 116$ GeV	0.0 ± 0.0	0.05 ± 0.04	0.0 ± 0.0	0.50 ± 0.04	0.55 ± 0.06
J/ψ Veto/TrigMatch/F.el	0.0 ± 0.0	0.05 ± 0.04	0.0 ± 0.0	0.50 ± 0.04	0.54 ± 0.06
$ZZ \to ee\mu\mu$					
Cut	V+jets	VW	top	$ZZZ/WW/tt/DPI$	sum
Four Leptons	392.12 ± 36.99	26.13 ± 1.22	51.52 ± 2.93	11.1 ± 0.22	480.87 ± 37.13
OSSF	116.1 ± 18.0	5.58 ± 0.51	11.6 ± 1.32	3.17 ± 0.12	136.45 ± 18.06
DR	111.28 ± 17.65	5.55 ± 0.51	11.0 ± 1.29	3.16 ± 0.12	131.0 ± 17.71
Ext. lept	61.54 ± 12.31	4.67 ± 0.45	7.96 ± 1.10	2.92 ± 0.11	77.08 ± 12.37
$66 < M_1 < 116$ GeV	55.6 ± 12.28	3.58 ± 0.39	3.87 ± 0.75	2.66 ± 0.10	65.72 ± 12.31
$66 < M_2 < 116$ GeV	3.19 ± 0.96	0.75 ± 0.19	0.53 ± 0.28	0.95 ± 0.05	5.42 ± 1.02
J/ψ Veto/TrigMatch/F.el	0.79 ± 0.29	0.58 ± 0.16	0.28 ± 0.24	0.93 ± 0.05	2.58 ± 0.42
$ZZ \to \ell\ell\ell'\ell'$					
Total	9.93 ± 6.14	1.52 ± 0.30	0.71 ± 0.35	1.84 ± 0.06	13.99 ± 6.15

Table 5.7: MC predicted number of events normalized to 20.3 fb^{-1} passing the successive ZZ selection cuts for all types of background for the *eeee* (top), the $\mu\mu\mu\mu$ (middle) and $\mu\mu ee$ (bottom) channels. Only statistical errors are shown.

	$eeee$	$\mu\mu\mu\mu$	$ee\mu\mu$
Central e, μ	1.20 ± 0.32	0.48 ± 0.06	1.23 ± 0.19
Extension e, μ	9.67 ± 6.13	0.07 ± 0.01	1.35 ± 0.36
1 Forw. e	9.67 ± 6.13	-	1.08 ± 0.34
1 Forw. μ	-	0.05 ± 0.01	0.04 ± 0.01
1 Calo-Tag μ	-	0.02 ± 0.01	0.02 ± 0.01
1 Forw. μ +1 Forw. e	-	-	0.08 ± 0.05
1 Calo-Tag μ + 1 Forw. e	-	-	0.14 ± 0.13
1 Forw μ + 1 Calo-Tag μ	-	0.00 ± 0.00	-

Table 5.8: Background yields decomposition in extension lepton contributions.

$ZZ \to eeee$				
Cut	DPI	ZZZ/ZWW	$t\bar{t}+V$	sum
Four Leptons	1.40 ± 0.03	4.06 ± 0.06	5.65 ± 0.21	11.1 ± 0.22
OSSF	0.32 ± 0.01	0.49 ± 0.02	0.39 ± 0.06	1.20 ± 0.06
DR	0.32 ± 0.01	0.49 ± 0.02	0.39 ± 0.06	1.20 ± 0.06
Ext. lept	0.25 ± 0.01	0.44 ± 0.02	0.34 ± 0.05	1.03 ± 0.06
$66 < M_1 < 116$ GeV	0.24 ± 0.01	0.39 ± 0.02	0.30 ± 0.05	0.93 ± 0.05
$66 < M_2 < 116$ GeV	0.14 ± 0.01	0.12 ± 0.01	0.15 ± 0.03	0.42 ± 0.04
J/ψ Veto/TrigMatch/F.el	0.13 ± 0.01	0.12 ± 0.01	0.15 ± 0.03	0.41 ± 0.04
$ZZ \to \mu\mu\mu\mu$				
Cut	DPI	ZZZ/ZWW	$t\bar{t}+V$	sum
Four Leptons	1.40 ± 0.03	4.06 ± 0.06	5.65 ± 0.21	11.10 ± 0.22
OSSF	0.34 ± 0.01	0.54 ± 0.02	0.58 ± 0.06	1.46 ± 0.07
DR	0.34 ± 0.01	0.54 ± 0.02	0.58 ± 0.06	1.46 ± 0.07
Ext. lept	0.33 ± 0.01	0.52 ± 0.02	0.56 ± 0.06	1.41 ± 0.07
$66 < M_1 < 116$ GeV	0.31 ± 0.01	0.47 ± 0.02	0.52 ± 0.06	1.29 ± 0.06
$66 < M_2 < 116$ GeV	0.15 ± 0.01	0.19 ± 0.01	0.17 ± 0.03	0.5 ± 0.04
J/ψ Veto/TrigMatch/F.el	0.15 ± 0.01	0.18 ± 0.01	0.16 ± 0.03	0.5 ± 0.04
$ZZ \to ee\mu\mu$				
Cut	DPI	ZZZ/ZWW	$t\bar{t}+V$	sum
Four Leptons	1.40 ± 0.03	4.06 ± 0.06	5.65 ± 0.21	11.10 ± 0.22
OSSF	0.68 ± 0.02	1.04 ± 0.03	1.44 ± 0.11	3.17 ± 0.12
DR	0.68 ± 0.02	1.04 ± 0.03	1.44 ± 0.11	3.16 ± 0.12
Ext. lept	0.60 ± 0.02	0.98 ± 0.03	1.34 ± 0.10	2.92 ± 0.11
$66 < M_1 < 116$ GeV	0.58 ± 0.02	0.85 ± 0.03	1.23 ± 0.10	2.66 ± 0.10
$66 < M_2 < 116$ GeV	0.30 ± 0.01	0.28 ± 0.02	0.36 ± 0.05	0.95 ± 0.05
J/ψ Veto/TrigMatch/F.el	0.29 ± 0.01	0.28 ± 0.02	0.36 ± 0.05	0.93 ± 0.05
$ZZ \to \ell\ell\ell'\ell'$				
Total	0.57 ± 0.02	0.58 ± 0.02	0.67 ± 0.07	1.84 ± 0.08

Table 5.9: MC predicted number of events normalized to 20.3 fb^{-1} passing the successive ZZ selection requirements for the irreducible background originating from double-parton interactions, the decay of three gauge bosons and the tops produced in association with a Z or W boson, for the $eeee$ (top), the $\mu\mu\mu\mu$ (middle) and $\mu\mu ee$ (bottom) decay channels. Only statistical errors are shown.

5.3.2 Background estimation using a Data Driven method

In this section, the data driven method employed to estimate the background contamination due to events containing fake leptons is described and an estimation of the expected fake background is given. This method has been already used for the 7 TeV paper and is the baseline method in the $ZZ \to \ell\ell\ell'\ell'$ group.

The basic idea behind the many different existing data-driven methods can be summarized as follow. First, a control region is defined, as similar as possible to the signal one, in which no signal is expected. This is achieved by reversing some cuts closely related to the signal characteristics. Then, the yield estimated in this background dominated control region is extrapolated to the signal region. MC simulations are used to subtract the small signal contamination from the control region.

More specifically, all leptons coming from reducible background processes should normally fail the isolation, the d0 significance and/or the identification requirements. However, because of the very high cross section of the multijet backgrounds, it can happen that some objects finally pass the lepton requirements and contaminate our signal yield. The "fake" lepton background contamination is estimated separately for each channel, using a two dimensional data-driven method.

Because of the different origin of the electron and muon "fake" leptons, different variables are reversed in order to define the "control region". Fake muons mostly are real muons coming from hadron decays, while fake electrons are often the result of a misidentification when for instance an energy deposit in the calorimeter is wrongly matched with an ID track. For this reason, the variables examined for muons are the isolation and the d0-significance while for electrons the variables are the identification and the isolation.

Methodology

In an ideal world where the *true* "T" leptons could be distinguished from the *background* "B" leptons, one could obtain the background contribution by simply computing:

$$N_{bkg} = N_{TTTB} \times f + N_{TTBB} \times f^2 + N_{TBBB} \times f^3 + N_{BBBB} \times f^4 \qquad (5.2)$$

where "f" is the probability for a *background* lepton to pass all the selection requirements and be considered as a *true* lepton, and N_{XXXX} is the number of events passing all the selection requirements with their composition being made of n *true* leptons plus $4 - n$ *background* leptons.

To a good approximation, one can neglect the last two terms as the (already small) background contribution from the two first terms (events with at least two true leptons) is expected to be significantly higher. More in detail, processes giving three true leptons in the final state are the diboson $WZ + jet$ and the single top production in association with a W boson. Two true leptons in the final state mainly come from $Z + jets/\gamma$, WW and $t\bar{t}$ processes. There is a weak possibility to end up with a final state having one or even zero true lepton in combination with three or four background leptons, respectively, when one or more true leptons are outside the detector acceptance, or from processes such as $W + jets$ and top decaying in the semileptonic final state. Still, such events are much less likely to fulfill the on-shell mass requirement for the two Z bosons, and even if they finally do, they are much more suppressed because of the expansion in powers of f. Thus, it is legitimate to neglect contributions from events with three or more background leptons.

Since it is not possible to directly know the composition of each data event in terms of "T" and "B", the equation 5.2 can not be used as it is. It must be reworked such that all of its terms are experimentally computable. It is better, instead of working with *true* and *background* leptons, to work in a background sample with $true-like$ "L" and $background-like$ "J" objects. The latter are "fake" leptons that could potentially be mis-identified as good leptons.

Both "L" and "J" objects fulfill all the regular lepton requirements as listed in section 5.2.1, except the isolation and d0-significance for muons, and the isolation and identification for electrons. These pairs of requirements will determine whether an object is "L" or "J". An object identified as a muon is considered as "L" when in addition to the pre-selection cuts it passes both the isolation and the d0-significance cut i.e all the standard muon cuts. When it fails either the isolation or the d0-significance, it is considered as "J". In the case it fails both requirements, then it is too far away form our signal region and this object is not included in the study. The same reasoning is found in electron categorization. If an electron passes both the isolation and the identification requirements it is considered as "L" while when it fails one of the two requirements as "J". Electrons failing both requirements are not included in the analysis. Figure 5.2 illustrates the "L" and "J" definitions for muons and electrons. Note that all muon types share the same "L" and "J" definitions, while central and forward electrons do not. Forward electrons do not have an isolation cut, and thus only the identification criterion is examined for them: its is a $true-like$ if it passes the *Loose* requirement, while it is a $background-like$ if it fails.

One can now assume that in a background only sample the probability "f" can be written as the ratio of the sum of the $true-like$ leptons to the sum of $true-like$

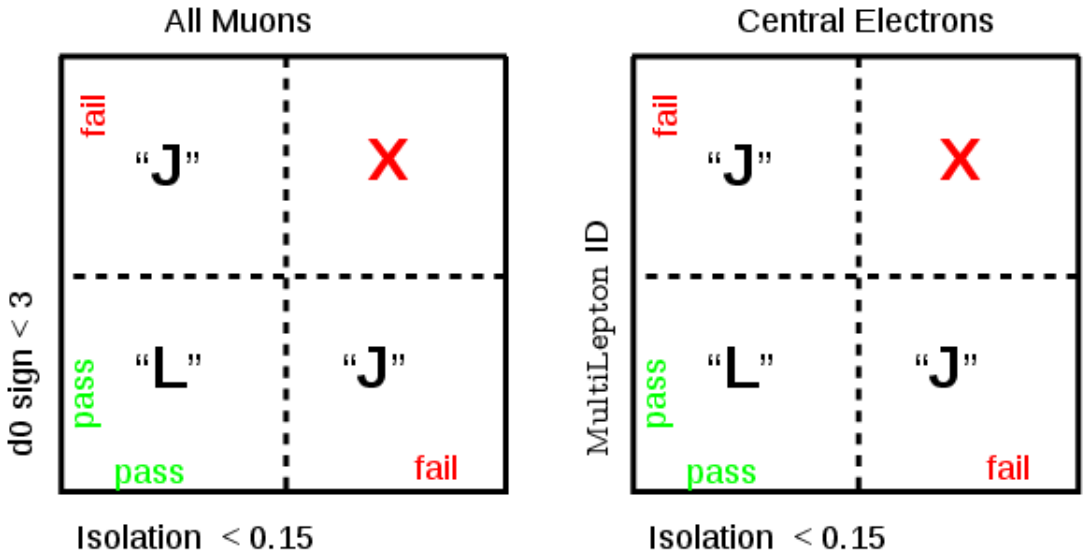

Figure 5.2: Illustration of the lepton type definitions for all types of muons (left), and central electrons (right).

plus $background-like$ leptons:

$$f = \frac{L}{L+J} \tag{5.3}$$

The N_{LLLJ} and N_{LLJJ} can be expressed as a function of N_{TTTB}, N_{TTBB} and f:

$$N_{LLLJ} = N_{TTTB} \times (1-f) + N_{TTBB} \times 2(1-f)f + \cdots \tag{5.4}$$

$$N_{LLJJ} = N_{TTBB} \times (1-f)^2 + \cdots \tag{5.5}$$

where the factor of two in the N_{TTBB} term accounts for the "B" combinatorial possibilities.

Here, a new quantity called fake factor "FF" is introduced, and represents the ratio of the probability of having a $true-like$ lepton versus the probability of having a $background-like$ lepton:

$$FF = \frac{L}{J} = \frac{f}{1-f} \tag{5.6}$$

When combining the above equations one gets the following:

$$N_{Bkg} = N_{LLLJ} \times FF - N_{LLJJ} \times FF^2 \tag{5.7}$$

Furthermore, potential signal contamination in the N_{LLJJ} and N_{LLLJ} terms must be subtracted using the MC signal predictions normalized to the 20 fb^{-1}. The final form of the equation for the background estimation is:

$$N_{Bkg} = (N_{LLLJ} - N^{MCZZ}_{LLLJ}) \times FF - (N_{LLJJ} - N^{MCZZ}_{LLJJ}) \times FF^2 \tag{5.8}$$

All terms in eq. 5.8 are experimentally computable. It should be noted that the FF and N_{LLXJ} (X=J or L) are estimated in a different sample of the full 2012 dataset. The FF is evaluated using a tag and probe method on Z+jet events, while the N_{LLXJ} terms are estimated applying the full ZZ selection. More details on these procedures are given in the following sections.

Fake factor computation

The fake factor, which is defined as the ratio of the $true-like$ versus the $background-like$ leptons, is computed using a tag-and-probe-like method on Z+jet events. First one searches for events having two good leptons "L" and can form a Z with an invariant mass inside a $\pm$ 25 GeV window around the pole. In order to have a region closer to the signal, one of the Z leptons must have triggered the event and the event missing energy must be below 25 GeV. Then, events with a "tagged" Z are scanned for additional "J" and "L" leptons. The sum of the "L" and "J" leptons found in the whole 2012 dataset is the numerator and denominator of the FF, respectively, see eq. 5.6. One has to correct for the contamination coming from ZZ and WZ leptonic decays, especially in the numerator "L". This J^{ZZ+WZ} and L^{ZZ+WZ} contamination is estimated from MC simulations and is subtracted from the denominator and numerator, respectively.

In figure 5.3 control plots of the P_T and η of the $background-like$ electrons and muons present in the Z-tagged events are shown. For both electrons and muons, as expected, the background contamination comes nearly 100% from $Z + jets$ events, while for muons there is also a small contribution from top events. The total number of fake electrons is more than three times higher than the number of fake muons. Figure 5.4 shows the same type of plots for the $true-like$ leptons. A small contribution from signal and WZ leptons is seen, which makes important its subtraction for the FF determination. In both $true-like$ and $background-like$ plots the data - MC agreement is poor due to the $Z+jet$ bad modeling. This justifies the usage of

a data-driven method that does not rely on the reducible background simulations.

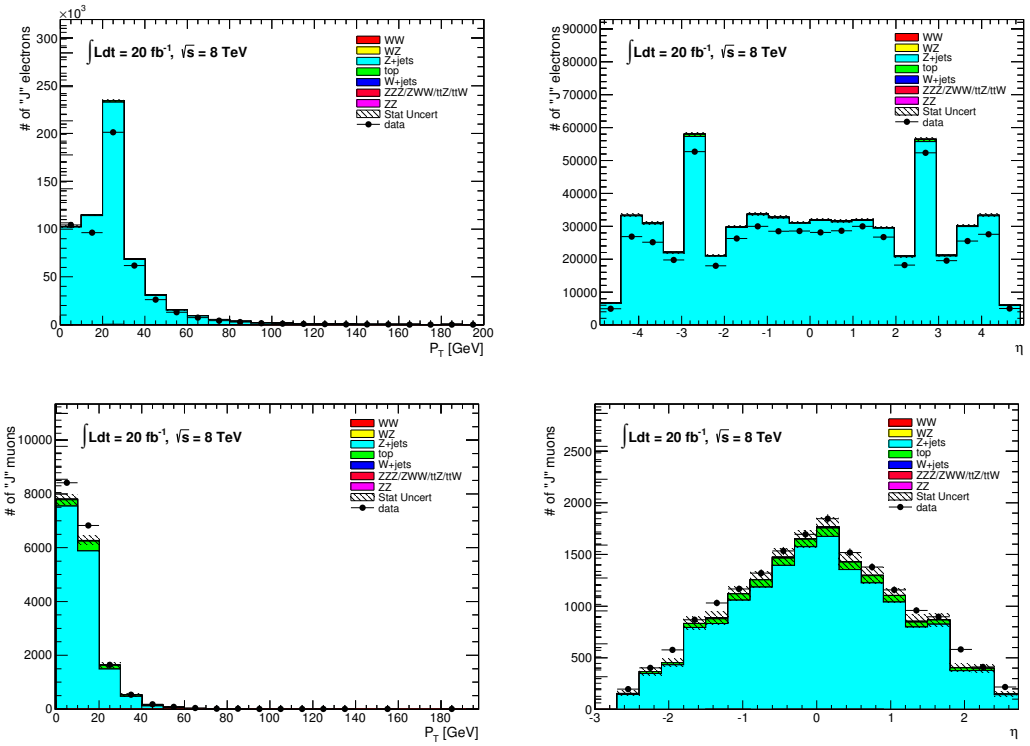

Figure 5.3: Control plots for the η (right) and P_{T} (left) of the "background like" electrons (top) and muons (bottom).

A dependence of the fake rate on the event kinematics is expected. Thus, in addition to the global fake factor, a differential fake factor in transverse momentum and η is also estimated. In each P_{T} and η bin i the fake factor is:

$$FF_i = \frac{L_i^{data} - L_i^{ZZ+WZ}}{J_i^{data} - J_i^{ZZ+WZ}}, \tag{5.9}$$

In table 5.10 the global fake factor for each lepton category is shown. The errors are the result of the numerator and denominator statistical error propagation. Electrons have much lower fake factors because of the strong discrimination power that the isolation and identification variables have against the very high number of background fake objects. On the other hand, there are much less background muons produced but it is harder to discriminate against them as usually these are true muons coming from hadron decays.

Figures 5.5 and 5.6 show the differential in P_{T} and η fake factor for muons and electrons, respectively. The dependence of the muon fake factor with both P_{T}

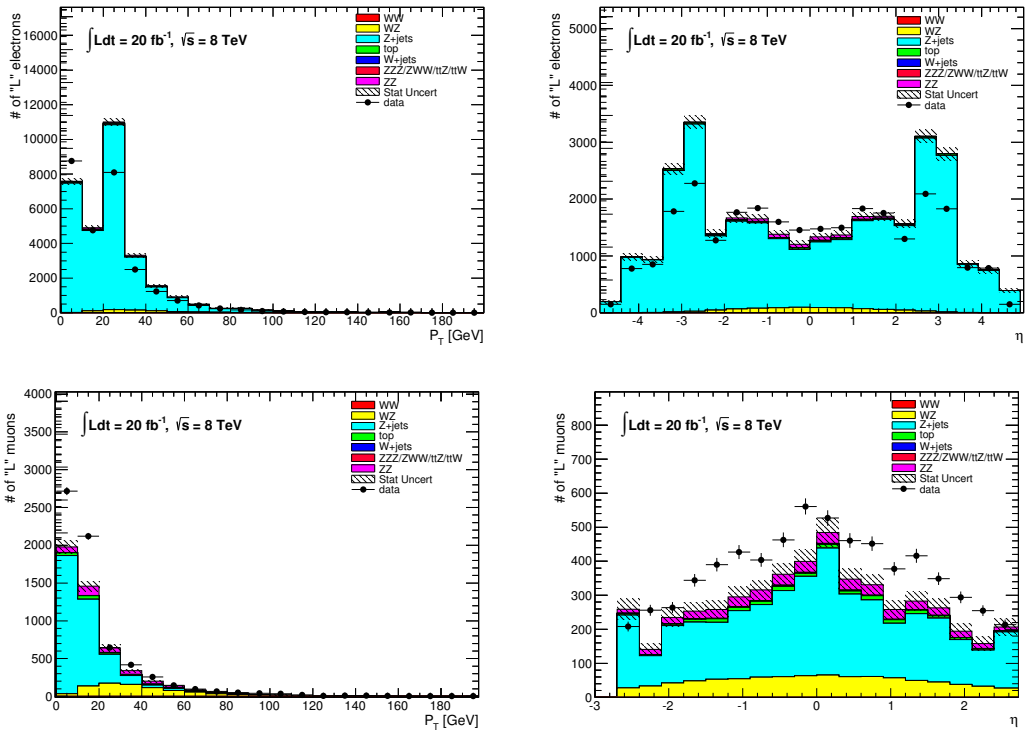

Figure 5.4: Control plots for the η (right) and P_{T} (left) of the "signal like" electrons (top) and muons (bottom).

Lepton type	Global fake factor <FF>
Central muons	0.289 ± 0.005
Forward muons	1.086 ± 0.112
Calorimeter muons	0.418 ± 0.033
Central electrons	0.056 ± 0.001
Forward muons	0.043 ± 0.000

Table 5.10: Global fake factor for the five different lepton types.

and η is more important compared to electrons. Again, this is expected as high energy background muons are more likely to be genuine muons coming from heavy flavor decays and thus are much more susceptible to pass the isolation requirements, resulting in high FF values.

N_{LLXJ} estimation - Results

In order to estimate the N_{LLLJ} and N_{LLJJ} one performs an identical event selection as the one used for the ZZ signal determination, except the leptons requirements. The event is required to have at least two good leptons "L" and at least two more

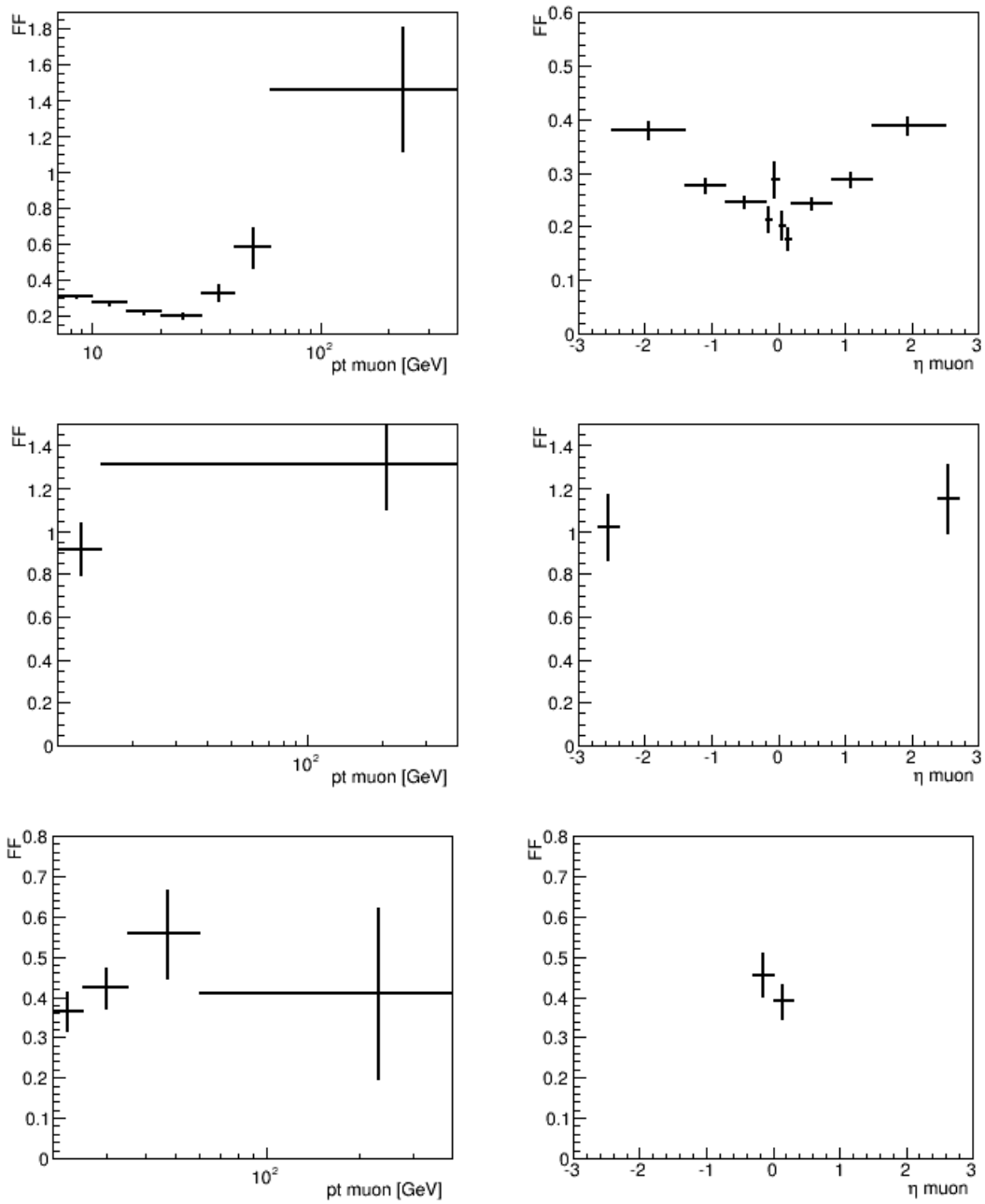

Figure 5.5: The FF for central (top), forward (middle) and calorimetric muons (bottom), as a function of η (right) and P_{T} (left).

"L" + "J" leptons. The leptons of the event are combined as for the regular ZZ analysis and all the criteria described in section 5.2.2 are applied on the event. An event with more that four "L"+"J" is double counted, if more than one combination of not-identical leptons can fulfill all the event requirements. In table 5.11 the total

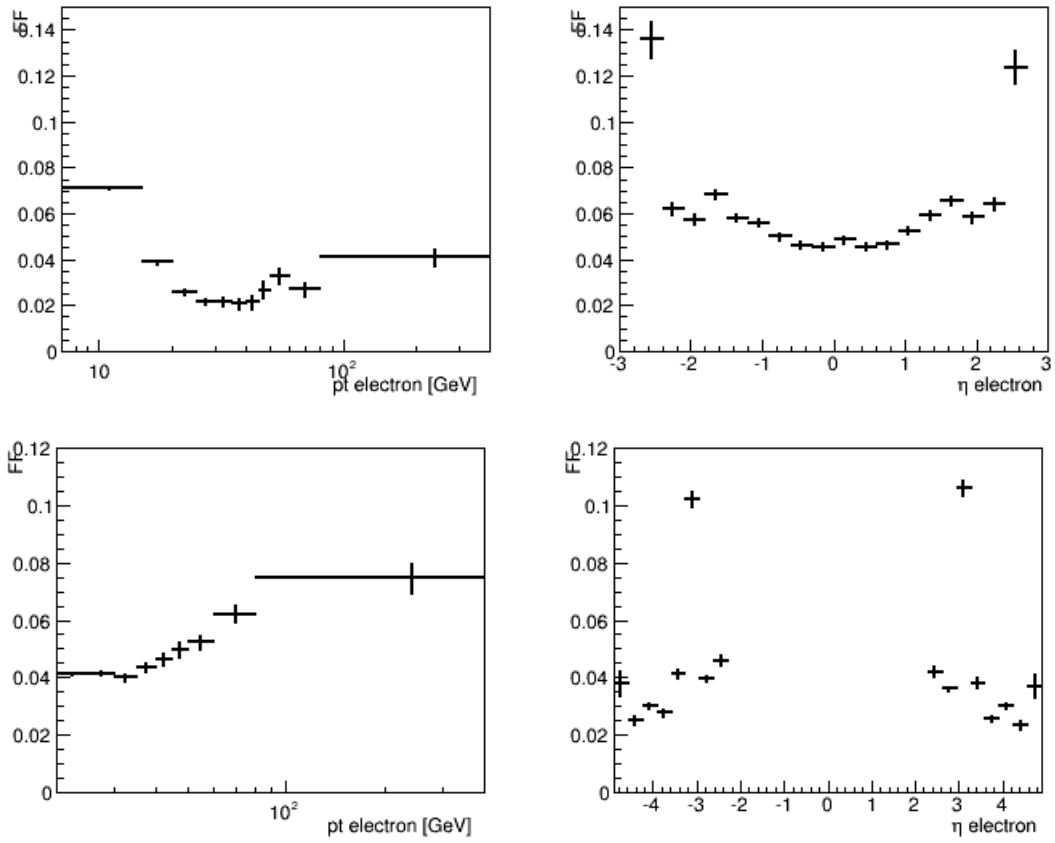

Figure 5.6: The FF for central (top) and forward (bottom) electrons, as a function of η (right) and P_{T} (left).

number of $LLLJ$ and $LLJJ$ events found in data and in the signal MC is shown.

As discussed, the fake rates are expected to depend on the event kinematics especially for muons. Therefore, instead of just inserting the number of fake events from table 5.11 and the global fake factors from table 5.10 in the formula 5.8, an event by event weight is applied. This weight is the combination of the differential P_{T} and η fake factors:

$$FF_{tot} = \sum_{j}^{N_j} FF_j(P_{\mathrm{T}}, \eta) = \sum_{j}^{N_j} \frac{FF_j(P_{\mathrm{T}}) \times FF_j(\eta)}{< FF_j >}, \tag{5.10}$$

where N_j is the number of "J" leptons in the ZZ event (up to two), $< FF_j >$ is the global fake factor for the j^{th} lepton, taken from table 5.10, and $FF_j(P_{\mathrm{T}})$, $FF_j(\eta)$ are the differential fake factors taken from the plots 5.5 and 5.6.

In table 5.12 the weighted data and MC yields are shown, and the final back-

	eeee	$\mu\mu\mu\mu$	$ee\mu\mu$
N_{LLLJ}	206	9	169
ZZ_{LLLJ}	20.43	4.09	25.50
N_{LLJJ}	2108	12	1621
ZZ_{LLJJ}	4.1	0.07	2.42

Table 5.11: Number of N_{LLLJ} and N_{LLJJ} events measured in data and in the ZZ MC. No fake factor weights were applied.

Ingredients in eq.5.8	eeee	$\mu\mu\mu\mu$	$2e2\mu$	$llll$
$(+)\ N_{LLLJ} \times FF$	8.42 ± 0.69	4.96 ± 2.03	14.61 ± 2.74	27.99 ± 3.48
$(-)ZZ_{LLLJ} \times FF$	0.60 ± 0.01	1.94 ± 0.06	2.8 ± 0.08	5.24 ± 0.10
$(-)N_{LLJJ} \times FF^2$	3.83 ± 0.12	1.40 ± 0.43	4.12 ± 0.54	9.35 ± 0.70
$(+)ZZ_{LLJJ} \times FF^2$	0.00 ± 0.00	0.02 ± 0.004	0.02 ± 0.003	0.04 ± 0.005
$N_{4\ell}^{\text{fake}}$	3.99 ± 0.70	1.63 ± 2.08	7.71 ± 2.79	13.34 ± 3.55

Table 5.12: ZZ reducible background estimate using the differential fake factors in 20 fb^{-1} of data.

ground estimate is given in the last row. The contamination due to fake leptons is estimated to be 13.34 ± 3.55 (stat. error). The statistical error shown is estimated by propagating the statistical uncertainty of each weighted N_{LLLJ} and N_{LLJJ} yield to the final estimation.

Table 5.13 shows the decomposition of the final background estimation in terms of extension lepton contributions for each channel. Only the statistical error is shown. The first row indicates the number of background events being composed exclusively by central leptons. The second row shows the number of events being composed by central leptons plus one forward electron or muon (in the $2e2\mu$ case it can be up to one forward lepton of each flavor). In the third row the number of events having one calorimetric muon is shown. Finally, in the fourth row the number of events being composed by central leptons plus a combination of different extension lepton types (up to two) is given. Even though the statistical error is important, it can be seen that more than half of the background events come from central leptons. This justifies the inclusion of extension leptons in this analysis since the ZZ signal gain is significant, see table 5.5, while the background is kept low.

As mentioned in the introduction of this section, this Data-Driven method has been already used by the ZZ group since the 7 TeV publication, and therefore, a "baseline" software framework exists since then. The results shown above were produced with an independent code that I developed in the context of this thesis.

type	$eeee$	$\mu\mu\mu\mu$	$ee\mu\mu$	$llll$
Central	1.21 ± 0.43	0.39 ± 1.50	5.59 ± 2.44	7.19 ± 2.90
Forward	2.78 ± 0.56	1.09 ± 1.38	1.34 ± 0.62	5.22 ± 1.61
Calo		0.16 ± 0.41	-0.07 ± 0.05	0.09 ± 0.42
Multi		-0.01 ± 0.00	0.85 ± 1.22	0.84 ± 1.22
$N_{4\ell}^{\text{fake}}$	3.99 ± 0.70	1.63 ± 2.08	7.71 ± 2.79	13.34 ± 3.55

Table 5.13: Decomposition of the background estimation in extension lepton contribution. Only statistical errors are shown.

	eeee	$\mu\mu\mu\mu$	$2e2\mu$	$llll$
$N_{4\ell}^{\text{fake}}$	4.40 ± 0.67 (st.) ± 2.80 (sy.)	1.95 ± 2.53 (st.) ± 1.0 (sy.)	9.17 ± 3.62 (st.) ± 4.06 (sy.)	15.52 ± 4.47 (st.) ± 7.33 (sy.)

Table 5.14: ZZ fake estimate as obtained with the official background estimator.

The aim was to perform a cross check of the baseline numbers that can be found in table 5.14. From the comparison of the last line of table 5.13 with the table 5.14, one observes that the numbers are in agreement within uncertainties. The statistical uncertainty observed in the baseline numbers is higher since the statistical error on the Fake Factor has been propagated. Hereafter, for the cross section measurement and the limit setting on the anomalous couplings, the reducible background numbers that will be used are those provided with the baseline software as these are currently used for the ongoing publication.

The systematic uncertainty on the Data-Driven measurement shown in table 5.14 has been evaluated by comparing the nominal estimation to the estimation one gets if instead of a differential fake factor the global fake factor is applied. The nominal estimation is also compared to the estimation one gets if instead of requiring both Zs of the N_{LLJJ} and N_{LLLJ} events to be composed of two *opposite* sign and same flavor leptons, one of them to be composed of *same* sign same flavor leptons. Finally, the greater discrepancy between the nominal estimate and the results of these two "alternative" methods is taken as the systematic uncertainty.

5.3.3 Total background estimation

In order to get the final expected background contamination one should add the irreducible and reducible background, the first estimated from MC and the latter estimated using the data-driven method. Table 5.15 summarizes these results. Only statistical errors are shown.

The background contamination with respect to the signal expectation gives a

	eeee	$\mu\mu\mu\mu$	$ee\mu\mu$	$llll$
Red. bkg. (data-driven)	4.40 ± 0.67	1.95 ± 2.53	9.17 ± 3.62	15.52 ± 4.47
Irred. bkg. (MC)	0.41 ± 0.04	0.5 ± 0.04	0.93 ± 0.05	1.84 ± 0.08
Total	4.81 ± 0.67	2.45 ± 2.53	10.1 ± 3.62	17.36 ± 4.47

Table 5.15: Total background estimation. Only statistical errors are shown.

high $\frac{S}{B}$ ratio of approximately 17 for the total yield. More in detail, the four muon channel is the cleanest one, with $\frac{S}{B}$ of about 34, while the four electron channel and the $2e2\mu$ have ≈ 13 and $\approx 2e2\mu \approx 14$, respectively.

5.4 Event yields

The number of expected and observed events after applying all selection cuts is shown in Table 5.16. Only the statistical uncertainties are given in the table. There are 321 data events passing the ZZ selection for 287.6 $\pm$0.8 [3] expected signal events and 17.4 ± 4.5 expected background events.

$ZZ \to \ell\ell\ell'\ell'$	$eeee$	$\mu\mu\mu\mu$	$ee\mu\mu$	$llll$
Observed ZZ	64	86	171	321
Expected ZZ	62.1 ± 0.3	83.7± 0.4	141.7 ± 0.6	287.6 ± 0.8
Expected Bkg	4.8 ± 0.7	2.5 ± 2.5	10.1 ± 3.6	17.4 ± 4.5
Total expected	67.0 ± 0.8	86.2± 2.6	151.8 ± 3.7	305.0 ± 4.6

Table 5.16: Summary of observed events and expected signal and background contributions in the individual sub-channels and combined for each channel. Only statistical errors are shown.

The agreement between the data and the expected events in the four electron and in the four muon channel is good whereas in the $2e2\mu$ channel we see a slight excess of data of $\approx 10\%$, which is however close to be covered by the large statistical error. The break down of the data yield to its extension lepton components is shown in table 5.17. The gain from adding the extension leptons is $\approx 17\%$, a number which is compatible with the MC signal predictions.

[3] If NLO EW corrections were NOT applied the expected number of signal events would have been 300.9 ± 0.9. In this case the SM expectation for each channel is: 65.0 (4e), 87.6 (4μ), 148.3 ($2e2\mu$).

	$eeee$	$\mu\mu\mu\mu$	$ee\mu\mu$	$llll$
Central e, μ	54	78	136	268
Extension e, μ	10	8	35	53
1 Forw. e	10	0	20	30
1 Forw. μ	-	3	8	11
1 Calo-Tag μ	-	5	6	11
1 Forw. μ +1 Forw. e	-	-	1	1
1 Calo-Tag μ + 1 Forw. e	-	-	0	0
1 Forw μ + 1 Calo-Tag μ	-	0	-	0

Table 5.17: Decomposition of data events in extension lepton contributions for each channel.

5.4.1 Kinematic distributions

In this section the kinematic distributions in which the data are compared to the MC signal plus background prediction, are presented. The distributions are made after performing the full selection. All the event and lepton weights are applied.

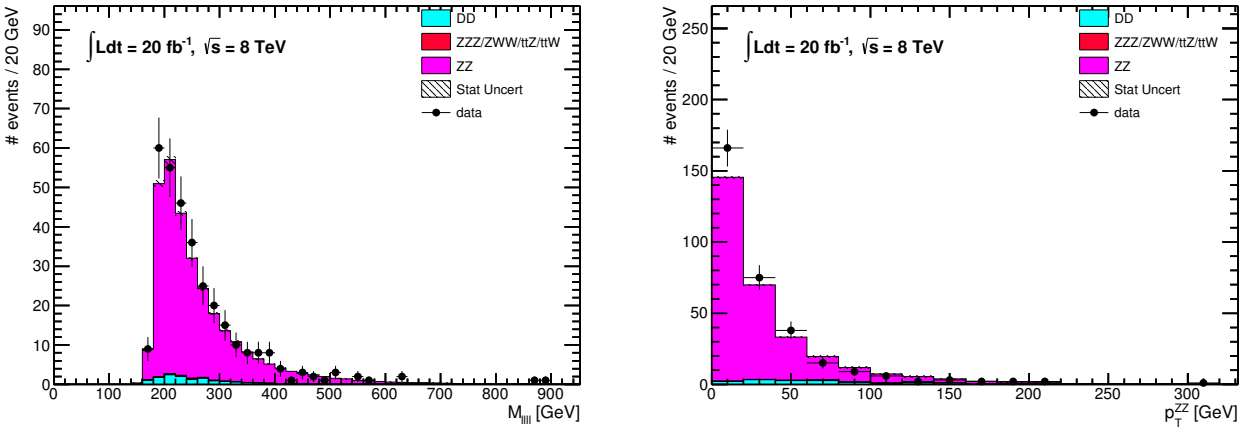

Figure 5.7: Kinematic distributions for the $ZZ \to \ell\ell\ell'\ell'$ candidates after applying the full ZZ selection, left: mass of the system, right: transverse momentum of the system. The DD indicates the reducible background contribution computed using the Data-Driven method.

In figures 5.7 and 5.8 the mass and the transverse momentum of the four lepton system and the leading Z are shown, respectively. In all cases a good data-prediction agreement is seen. Though, the statistical uncertainties are still large.

The distribution of the leading Z transverse momentum is shown separately for each decay channel is figure 5.9. The predictions describe the data fairly well.

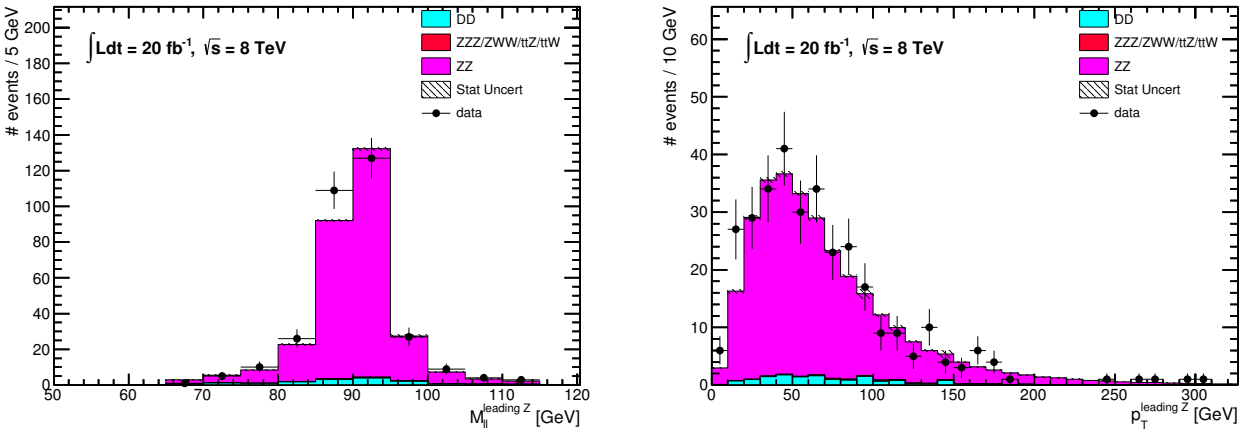

Figure 5.8: Kinematic distributions for the leading Z after applying the full ZZ selection, left: dilepton mass, right: transverse momentum. The DD indicates the reducible background contribution computed using the Data-Driven method.

5.5 Systematic Uncertainties

5.5.1 Particle uncertainties

In sec. 4.4.2, lepton properties have been discussed. It was mentioned that there are small discrepancies observed between the efficiencies (reconstruction, identification etc.) estimated on MC simulations and those estimated on data. To account for this mismodeling scale factors (SF) are applied on the MC simulations. In the case of the energy resolution and scale, the correction is applied directly on the energy value. In all cases, the central values of these corrections have uncertainties associated to their computation that have to be propagated on the C_{zz} estimation. The electron and muon performance groups, along with the correction central values, also provide the 1 σ error on them. The variation is usually asymmetric, and thus in order to calculate the impact on the final yield one need to re-perform the analysis twice, one for each variation "up" and "down". The final relative systematic error δ due to an uncertainty source i is given by:

$$\delta_i^{up(down)} = \frac{N_{ZZ,i}^{up(donw)} - N_{ZZ}}{N_{ZZ}} \tag{5.11}$$

where N_{ZZ} is the nominal signal yield, computed using the central values of the scale factors and the momentum/energy corrections. The systematic error is then symmetrised.

This work has to be done separately for each error source i as these are uncor-

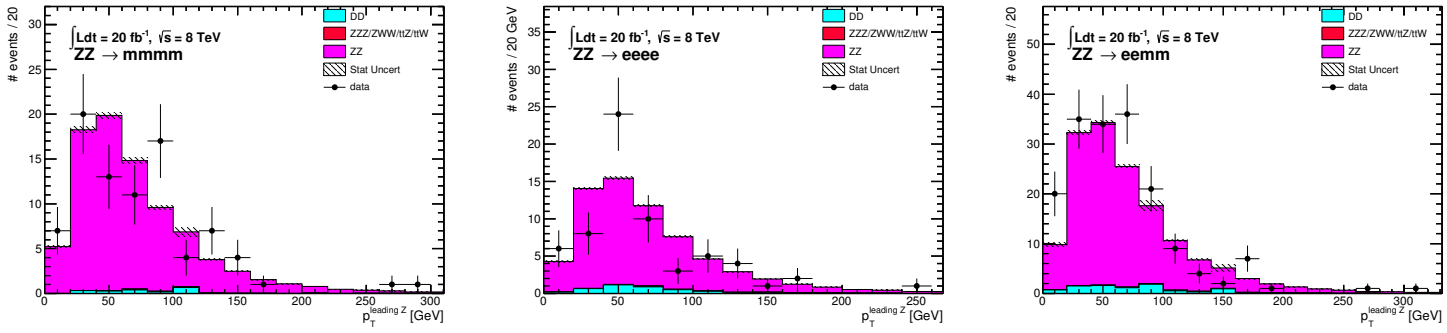

Figure 5.9: The transverse momentum of the leading Z for each channel after applying the full ZZselection: left: four electron, middle: four muon, right: $2e2\mu$ channels. The DD indicates the reducible background contribution computed using the Data-Driven method.

related. In the following the systematic errors coming from muons and electrons and their amplitude are discussed. All object-related systematics are computed separately for electrons and muons. The only exception is the trigger systematic, as a global event scale factor is applied according to equation 5.1. The amplitude of this systematic is less than 0.2% and can be found for each channel in the summary table 5.25. The impact of a systematic source is estimated separately in each decay channel and when entering the cross section calculation it is treated as fully correlated between the three channels.

Muon systematics

The uncertainty sources related to the muon reconstruction efficiency correction and the energy scale and smearing have been already presented in section 4.2.1. In addition to these main corrections, one more had to be applied to account for differences observed between the efficiency of the muon isolation and impact parameter (iso/ip) cuts in MC simulations compared to data. The iso/ip efficiencies have important uncertainties mainly due to the background subtraction in the tag-and-probe method, leading to large systematic errors on the SF. All the muon systematic errors on the C_{ZZ} along with the % impact on each channel separately are summarized in table 5.18.

The systematic error related to the isolation, z0 and d0Sig cut is by far the leading one, reaching 3.4% in the four muon channel[4], while the reconstruction systematic follows with 1.75%. The systematics related to the energy scale and smearing are

[4]It should be noted that the 1σ errors on the isolation, z0 and d0Sig scale factor are still preliminary.

Muon Reco. Uncert. [%]	*eeee*	$\mu\mu\mu\mu$	$ee\mu\mu$	*llll*
μ energy smearing	0.00	0.03	0.02	0.02
μ energy scale	0.00	0.02	0.01	0.02
μ reconstruction	0.00	1.75	0.88	0.95
μ isolation/z0/d0Sig	0.00	3.35	1.69	1.81

Table 5.18: Muon systematics on C_{ZZ}.

below the level of 0.1% and thus can be neglected in this analysis.

Electron systematics

As for the muons, the uncertainties related to the basic electron properties (reconstruction, identification and energy estimation) have been already discussed, see sec. 4.2.2. Electrons have as well an additional uncertainty due to the isolation and impact parameter SFs. However, this systematic is smaller, of the order of 1.4% in the four electron channel. All electron related systematics are listed in table 5.19. One sees that the leading systematic comes from the identification efficiency that reaches 3.6% in the four electron channel. This is not surprising as in section 4.2.2 it was discussed that several uncertainties are related to the identification efficiency estimation. The reconstruction uncertainty goes up to 1.7%.

Electron Reco. Uncert. [%]	*eeee*	$\mu\mu\mu\mu$	$ee\mu\mu$	*llll*
e momentum smearing	0.01	0.00	0.01	0.01
e energy scale	0.42	0.02	0.12	0.12
e identification efficiency	3.55	0.00	1.78	1.64
e isolation/z0/d0Sig	1.36	0.00	0.66	0.62
e reconstruction	1.69	0.00	0.83	0.77

Table 5.19: Electron systematics on C_{ZZ}.

5.5.2 Theory uncertainties

The nominal MC signal samples of this analysis are generated with *POWHEG* and *gg2VV*, both interfaced with *Pythia*. The factorisation and renormalization scales were set equal to m_{zz} and the PDF set used is the CT10. It is important to estimate the impact of these specific choices on the A_{ZZ} and C_{ZZ}, as these quantities are necessary for the cross section extraction.

PDF uncertainties

The correction factors are expected to depend on the PDFs. In order to evaluate the magnitude of the dependence the PDF experts recommend to estimate the following two errors:

- The first error is related to the 26 free parameters used for the CT10 PDF determination. The error associated to these free parameters can be estimated according to the CTEQ recommendations using the following formulas [71]:

$$\begin{aligned} \Delta X^{+} &= \sqrt{\sum_{i=1}^{n}[max(X_i^{+} - X_{ZZ}, X_i^{-} - X_{ZZ}, 0)]^2} \\ \Delta X^{-} &= \sqrt{\sum_{i=1}^{n}[max(X_{ZZ} - X_i^{+}, X_{ZZ} - X_i^{-}, 0)]^2} \end{aligned} \tag{5.12}$$

  where n is the number of free parameters, X_{ZZ} is the A_{ZZ} or C_{ZZ} evaluated using the central value of CT10 PDF. The X_i are the A_{ZZ} or C_{ZZ} estimated after applying an event-by-event PDF re-weighting to the ZZ signal samples using the *lhapdf* framework [88]. This computation is performed using the so-called 90% CL CT10 set. Thus, the obtained error corresponds to the 1.645 σ estimate of the effect and has to be scaled down accordingly.

- The second error is related to the choice of the PDF group. For its evaluation, the nominal sample is reweighed to the MSTW2008 PDF set [72], and the obtained difference is taken as a systematic error.

The above sources are considered uncorrelated and hence added in quadrature. Results on the error estimation for the A_{ZZ} and C_{ZZ} are shown in table 5.20 and 5.21, respectively. As it can be seen, the errors obtained with eq. 5.12 are quite symmetric, henceforth, they will be symmetrized.

A_{zz}	$eeee$	$\mu\mu\mu\mu$	$ee\mu\mu$
Error set [%]	$^{+0.32}_{-0.33}$	$^{+0.57}_{-0.55}$	$^{+0.38}_{-0.39}$
MSTW [%]	0.55	0.69	0.6
Total	0.64	0.89	0.71

Table 5.20: PDF systematics on the A_{ZZ}.

C_{zz}	$eeee$	$\mu\mu\mu\mu$	$ee\mu\mu$
Error set [%]	$^{+0.12}_{-0.12}$	$^{+0.03}_{-0.03}$	$^{+0.11}_{-0.10}$
MSTW [%]	0.1	0.01	0.08
Total	0.16	0.02	0.13

Table 5.21: PDF systematics on the C_{ZZ}.

The behavior of the PDF systematic error on the A_{ZZ} and C_{ZZ} seems consistent with what one would expect, i.e having larger errors when the correction factor performs a large extrapolation (small correction factor value).

QCD scale uncertainties

In order to assess the systematic uncertainty due to the QCD scale choices for which the signal samples have been generated, $\mu_R = \mu_F = m_{zz}$, here, $POWHEG$ samples have been re-generated for different QCD scales. The scales μ_R and μ_F have been set independently to 0.5 m_{zz}, m_{zz} and 2 m_{zz} for all possible configurations. This results to 8 combinations plus 1 for the nominal sample, i.e 9 samples for each channel. Since the full simulation of the MC samples is time consuming, only truth level simulations have been performed. Thus, a scale uncertainty can be assigned only to the acceptance correction factor, A_{ZZ}. This is not a problem though, as the QCD scale systematic is expected to be smaller for the C_{ZZ} compared to the A_{ZZ}. From the estimation of the PDF systematic error it was already shown that the reconstruction correction factor is less sensitive to theory uncertainties. Additionally, previous studies of the C_{ZZ} sensitivity on the scale choice support also this statement [89].

The systematic uncertainty on the A_{zz} is taken as the maximum deviation of the A_{zz} values computed using the "shifted" samples with respect to the nominal one ($\mu_R = \mu_F = m_{ZZ}$). In table 5.22 the systematics for each channel is shown. For all three channels the error is small, ranging between 0.15 and 0.26. This is expected because of canceling effects between the numerator and denominator of A_{ZZ}.

	$eeee$	$\mu\mu\mu\mu$	$ee\mu\mu$
scale uncertainties [%]	0.17	0.26	0.15

Table 5.22: Scale systematics on the A_{ZZ}.

Generator uncertainties

In order to estimate the systematic error associated to the choice of the simulation program, the nominal C_{ZZ} and A_{ZZ} values computed using the $POWHEG$

and $gg2VV$ samples are compared to the correction factors obtained with *Sherpa*, $PYTHIA$ and $MCFM$.

- *Sherpa* [90] is a stand alone $q\bar{q} \to ZZ$ LO generator at ME which performs the full simulation chain i.e the parton shower, underlying event, hadronisation etc.

- $PYTHIA$ is a $q\bar{q} \to ZZ$ LO generator that performs the full simulation chain as well, i.e showering, hadronisation and underlying event modeling. It can be also interfaced with NLO generators. In this case, it receives the hard process information and then implements the remaining simulation steps.

- $MCFM$ [40] is a $q\bar{q}+gg \to ZZ$ generator that performs a NLO matrix element computation. It is useful for the total and fiducial cross section computation and thus it can also be used for the A_{ZZ} computation. However, it does not incorporate the event simulation at reconstruction level.

The $MCFM$ generator is the only one modeling the ZZ production for both $q\bar{q}$ and gg initial states besides the nominal $POWHEG$+$gg2VV$ samples. However, as $MCFM$ does not perform a full event simulation it cannot be used for the estimation of the MC systematic on the C_{ZZ}. In order to still be able to extract this systematic, here we decided to compare the $q\bar{q}$ component of the nominal C_{ZZ} factor (computed with $POWHEG$ only) with the C_{ZZ} computed by the $q\bar{q}$ *Sherpa* and $PYTHIA$ generators.

It should be stressed that the consideration of a systematic error resulting from the comparison of all the available ZZ simulations with the nominal one is quite conservative. Several effects are assessed together, such as the hard process simulation framework, LO/NLO differences, the generation conditions and the modeling of the showering.

A_{ZZ}	$eeee$	$\mu\mu\mu\mu$	$ee\mu\mu$
Nominal ($q\bar{q}$+gg)	0.817 ± 0.001	0.645 ±0.001	0.726 ± 0.001
MCFM	0.824 ± 0.001	0.642 ±0.001	0.742 ± 0.001
[%] diff.	0.84	0.43	2.24
Nominal ($q\bar{q}$)	0.814 ± 0.001	0.639 ± 0.001	0.722 ± 0.001
Sherpa	0.798 ± 0.006	0.635 ± 0.005	0.735 ± 0.004
PYTHIA	0.799 ± 0.003	0.620 ± 0.004	0.733 ± 0.003
[%] diff.	1.97	2.97	1.80
[%] A_{ZZ} MC syst.	1.97	2.97	2.24

Table 5.23: Generator systematics on the A_{ZZ}.

In table 5.23 the A_{ZZ} systematics due to simulation differences are shown. The $MCFM$ A_{ZZ} values are compared with the nominal ($q\bar{q}$+gg) A_{ZZ}, while the *Sherpa* and $PYTHIA$ values are compared to the $q\bar{q}$ A_{ZZ} component, using $POWHEG$

only. The higher discrepancy observed in each channel is taken as the MC systematic, see last row of the table.

In table 5.24 the C_{ZZ} systematics due to generator differences are shown. The C_{ZZ} $q\bar{q}$ component, computed exclusively with $POWHEG$, is compared to *Sherpa* and $PYTHIA$ and the maximum difference is taken as a systematic.

C_{ZZ}	$eeee$	$\mu\mu\mu\mu$	$ee\mu\mu$
Nominal ($q\bar{q}$)	0.495 ± 0.002	0.849 ±0.001	0.644 ± 0.001
Sherpa	0.504 ± 0.006	0.859 ±0.005	0.655 ± 0.004
PYTHIA	0.493 ± 0.005	0.844 ±0.004	0.633 ± 0.003
[%] C_{ZZ} MC syst	1.82	1.18	1.71

Table 5.24: Generator systematics on the C_{ZZ}.

5.5.3 Systematic uncertainties summary

In this section all the systematics uncertainties entering the cross section extraction fit are summarized. The complete list of the signal systematics is found in table 5.25. The leading uncertainties come from the electron identification, reconstruction and the e, μ isolation/z0/d0Sig. Among the theory uncertainties the most important one is the generator difference. For the C_{ZZ} it is of the order of 1-2% depending on the channel, and for the A_{ZZ} is of the order of 2-3%. The luminosity uncertainty is also high, 2.8%.

All the above uncertainties are affecting the C_{zz} correction factor. In addition to those, the systematics uncertainties related to the background estimation must be also taken into account. The statistical and systematic errors on the reducible background estimation have been discussed in the data-driven section 5.3.2. For the irreducible background, in addition to the statistical error due to the limited MC statistics, the same reconstruction systematic sources and values as those computed for the C_{zz} are considered. It is legitimate to do so, as the final state is identical, and thus the same reconstruction uncertainties are expected. It should be stressed that in any case the effect of these systematics on the measurement will be negligible, since the number of expected irreducible background is very small, 1.8±0.1 events for 287.6± 0.8 expected ZZ events.

5.6 Cross-Section Combination

In chapter 4.1, the equations giving the total and fiducial cross section were presented, 4.1 and 4.2, respectively. These formulas do not prescribe how to combine

Source %	$eeee$	$\mu\mu\mu\mu$	$ee\mu\mu$	$llll$
Luminosity		2.8		
Reconstruction efficiency C_{ZZ}				
Particle-related systematics				
μ energy smearing	0.00	0.03	0.01	0.02
μ energy scale	0.00	0.05	0.03	0.02
μ reconstruction	0.00	1.75	0.88	0.95
μ isolation/z0/d0Sig	0.00	3.35	1.69	1.81
e momentum smearing	0.01	0.00	0.01	0.02
e energy scale	0.42	0.02	0.12	0.12
e ID efficiency	3.55	0.00	1.78	1.64
e isolation/z0/d0Sig	1.36	0.00	0.66	0.62
e reconstruction	1.69	0.00	0.83	0.77
trigger	0.04	0.20	0.10	0.11
Total object syst.	4.18	3.78	2.82	2.81
Theory-related systematics				
C_{ZZ} generator	1.82	1.18	1.71	
C_{ZZ} PDF	0.16	0.02	0.13	
Total C_{ZZ}	4.56	3.96	3.30	
Acceptance efficiency A_{ZZ} - Theory				
A_{ZZ} generator	1.97	2.97	2.24	
A_{ZZ} PDF	0.64	0.89	0.71	
A_{ZZ} QCD Scale	0.17	0.26	0.15	
Total A_{ZZ}	2.08	3.11	2.35	
Total	5.74	5.76	4.92	

Table 5.25: Reconstruction and theory systematic sources affecting the cross section measurement.

independent measurements, neither how to propagate the uncertainties. Therefore, a more explicit procedure is needed; here we adopt a minimum log-likelihood approach.

For a given channel i the likelihood is defined as the Poissonian probability of observing N_{obs} events when N_{exp} events are expected.

$$L_i = \frac{e^{-N_{exp}} \times (N_{exp})^{N_{obs}}}{N_{obs}!} \tag{5.13}$$

where

$$N^i_{exp} = N^i_s + N^i_b. \tag{5.14}$$

with N^i_b being the total number of background events and N^i_s being the number of expected signal events in the channel i. The N^i_s can be expressed as a function of the total cross-section, σ^{tot}_{ZZ}, which is the parameter that we want to determine:

$$N^i_s(\sigma^{tot}_{ZZ}) = \sigma^{tot}_{ZZ} \times BR^i(ZZ \to \ell\ell\ell'\ell') \times L \times A^i_{ZZ} \times C^i_{ZZ}, \tag{5.15}$$

The A^i_{ZZ}, C^i_{ZZ} and BR^i are respectively the acceptance factor, the reconstruction factor and the branching ratio of two Zs going to four leptons e or μ, all computed for the i channel. For the extraction of the fiducial cross-section the same formula is used, but with the total cross-section σ^{tot}_{ZZ} replaced by the fiducial cross-section $\sigma^{i\ fid}_{ZZ}$ and without the A^i_{ZZ} factor and the BR^i.

The impact of the systematic uncertainties, so called nuisance parameters, is taken into account by modifying the number of predicted signal and background events as follows:

$$N^i_s(\sigma^{tot}_{ZZ}, \{x_k\}) = \sigma^{tot}_{ZZ} \times BR^i \times L \times A^i_{ZZ} \times C^i_{ZZ} \times (1 + \sum_{k=1}^{n_s} x_k S^i_k) \tag{5.16}$$

and

$$N^i_b(\{x_k\}) = N^i_b(1 + \sum_{k=1}^{n_b} x_k B^i_k). \tag{5.17}$$

where n_s and n_b are the number of nuisance parameters affecting the signal and the background, respectively. The S^i_k and B^i_k represent the effect of the k^{th} nuisance on the channel i for the signal and the background, respectively. Finally, the x_k are the pulled nuisance parameters, i.e centered on 0, with an uncertainty of 1.

Moreover, a Gaussian constraint on the nuisance parameters x is applied, such that the nominal value of a systematic uncertainty corresponds to $x = 0$ and one standard deviation shift corresponds to $x \pm 1\sigma$.

$$L_c(x) = K \prod_{m=1}^{n_x} e^{-\frac{x^2}{2}} \tag{5.18}$$

The n_x is the number of nuisance parameters and K a normalization constant. This term is used to keep the nuisance parameters close to their central values.

The Likelihood described so far is appropriate for the cross section extraction of one single channel. For the combination of the three channels, the product of the three likelihoods should be used. Furthermore, as it is more convenient to work with the logarithm of the Likelihood function, finally one gets the following expression:

$$-\ln L(\sigma, \{x_k\}) = \sum_{i=1}^{3} -\ln\left(\frac{e^{-(N_s^i(\sigma,\{x_k\})+N_b^i(\{x_k\}))} \times (N_s^i(\sigma,\{x_k\}) + N_b^i(\{x_k\}))^{N_{obs}^i}}{(N_{obs}^i)!}\right) + \sum_{k=1}^{n} \frac{x_k^2}{2}. \tag{5.19}$$

Using the Minuit package [91], this quantity is minimized with respect to σ and x_k in order to get the best estimate of these parameters. The errors are obtained using the MINOS algorithm. All the actions described above are performed using the FLIT package [92].

5.6.1 Impact of systematic uncertainties

The full likelihood function with nuisance parameters will automatically take into account all the systematic errors, and propagate them to the final uncertainty.

First, a fit of all the parameters is performed. This fit, referred hereafter as the "main fit", gives the best estimate for the parameter values along with their total error. Then, the statistical error on the cross section is obtained by fixing all the parameters x_k to their fitted values in the main fit, and re-fitting the cross section. The cross section error extracted from this new fit is taken as the statistical error on the measurement. Finally, the "full systematic" error is obtained by quadratically subtracting the statistical error by the total error of the main fit.

In order to understand the contribution of each systematic error separately, a cycle of minimizations of the likelihood function is performed. Each nuisance parameter is in turn fixed and shifted from its value in the main fit by first $+1\ \sigma$ and then by -1 σ, while letting all the other parameters free. The change of the cross-section with respect to its value in the main fit represents the contribution of the considered uncertainty source to the total error. The "full systematic but luminosity" error is obtained by subtracting from the "full systematic" error the error due to the luminosity uncertainty.

5.7 Cross-Section Results

All the ingredients needed in order to perform the ZZ cross section measurement have been exposed in the previous sections. The compilation of these inputs result in the total and fiducial cross section measurements shown in tables 5.26 and 5.28, respectively.

The total ZZ on-shell cross section is found to be $6.98^{+0.42}_{-0.40}(stat.)^{+0.38}_{-0.33}(syst.)^{+0.20}_{-0.19}(lumi.)$. The quality of the fit (p-value) for the combined measurement is of about 50%.

Channel	Cross-Section [pb]
$eeee$	$6.35^{+0.89}_{-0.82}$(stat.) $^{+0.49}_{-0.42}$(syst.) $^{+0.18}_{-0.18}$(lumi.)
$ee\mu\mu$	$7.48^{+0.63}_{-0.59}$(stat.) $^{+0.42}_{-0.38}$(syst.) $^{+0.22}_{-0.21}$(lumi.)
$\mu\mu\mu\mu$	$6.64^{+0.77}_{-0.70}$(stat.) $^{+0.43}_{-0.38}$(syst.) $^{+0.19}_{-0.18}$(lumi.)
Combined	$6.98^{+0.42}_{-0.40}(stat.)^{+0.38}_{-0.33}(syst.)^{+0.20}_{-0.19}(lumi.)$

Table 5.26: Measured total cross-sections for each channel and combined.

The total error on the combined cross section is about 8.3% with the statistical error being still slightly higher than the total systematic one. It is of great interest to decompose the systematic error, as it was described in the previous section, so that the uncertainty sources with the higher contribution on the total systematic error are identified. This decomposition is shown in table 5.27. As expected, the uncertainties with the higher impact on the C_{ZZ} and the A_{ZZ}, see sec 5.5.3, are those having the major effect on the cross section measurement. More precisely, the luminosity, the MC generator differences [5], the electron identification and the muon isolation uncertainties have the leading roles.

In table 5.28, the fiducial cross sections for each decay channel is shown. These measurements are performed in the fiducial volumes defined in section 4.5.3. No combined measurement is possible, as each channel has a different volume definition.

[5]For a less conservative cross section extraction the MC generator difference error could be neglected. In this case the obtained result would be $6.98^{+0.42}_{-0.40}(stat.)^{+0.31}_{-0.28}(syst.)^{+0.20}_{-0.19}(lumi.)$, i.e the systematic error drops from 5.1% to 4.2% and the total error (stat+syst+lumi) drops from 8.3% to 7.8%.

Source	$eeee$	$ee\mu\mu$	$\mu\mu\mu\mu$	Combined
Luminosity	$^{+2.86}_{-2.78}$	$^{+2.88}_{-2.75}$	$^{+2.87}_{-2.77}$	$^{+2.87}_{-2.76}$
e - energy scale	$^{+0.38}_{-0.42}$	$^{+0.21}_{-0.20}$	$^{+0.0}_{-0.0}$	$^{+0.18}_{-0.18}$
e - identification efficiency	$^{+3.66}_{-3.49}$	$^{+1.82}_{-1.76}$	$^{+0.0}_{-0.0}$	$^{+1.63}_{-1.61}$
e - reconstruction efficiency	$^{+1.70}_{-1.70}$	$^{+0.84}_{-0.83}$	$^{+0.0}_{-0.0}$	$^{+0.76}_{-0.75}$
e - isolation and IP	$^{+1.36}_{-1.38}$	$^{+0.67}_{-0.66}$	$^{+0.0}_{-0.0}$	$^{+0.61}_{-0.60}$
μ - energy Scale	$^{+0.0}_{-0.0}$	$^{+0.0}_{-0.0}$	$^{+0.09}_{-0.11}$	$^{+0.04}_{-0.03}$
μ - rconstruction efficiency	$^{+0.0}_{-0.0}$	$^{+0.89}_{-0.87}$	$^{+1.78}_{-1.75}$	$^{+0.99}_{-0.98}$
μ - isolation and IP	$^{+0.0}_{-0.0}$	$^{+1.72}_{-1.67}$	$^{+3.45}_{-3.30}$	$^{+1.92}_{-1.89}$
Trigger efficiency	$^{+0.0}_{-0.0}$	$^{+0.11}_{-0.10}$	$^{+0.19}_{-0.21}$	$^{+0.12}_{-0.11}$
MC Generator Differences (C_{ZZ})	$^{+1.88}_{-1.87}$	$^{+1.81}_{-1.75}$	$^{+1.23}_{-1.22}$	$^{+1.64}_{-1.60}$
MC Generator Differences (A_{ZZ})	$^{+2.00}_{-1.98}$	$^{+2.28}_{-2.20}$	$^{+3.06}_{-2.94}$	$^{+2.48}_{-2.40}$
PDF (C_{ZZ})	$^{+0.14}_{-0.18}$	$^{+0.14}_{-0.13}$	$^{+0.01}_{-0.03}$	$^{+0.10}_{-0.10}$
PDF (A_{ZZ})	$^{+0.62}_{-0.66}$	$^{+0.72}_{-0.70}$	$^{+0.89}_{-0.89}$	$^{+0.76}_{-0.75}$
Scale (A_{ZZ})	$^{+0.15}_{-0.19}$	$^{+0.15}_{-0.15}$	$^{+0.25}_{-0.27}$	$^{+0.20}_{-0.19}$
Signal stat	$^{+0.53}_{-0.57}$	$^{+0.46}_{-0.45}$	$^{+0.48}_{-0.49}$	$^{+0.29}_{-0.28}$
Bkg syst (Data Driven)	$^{+4.64}_{-4.81}$	$^{+2.51}_{-2.54}$	$^{+1.19}_{-1.21}$	$^{+2.54}_{-2.58}$
Bkg stat (Data Driven)	$^{+1.11}_{-1.16}$	$^{+2.24}_{-2.26}$	$^{+2.99}_{-3.07}$	$^{+1.57}_{-1.53}$
Bkg stat (MC)	$^{+0.05}_{-0.09}$	$^{+0.04}_{-0.03}$	$^{+0.04}_{-0.05}$	$^{+0.03}_{-0.02}$

Table 5.27: Relative systematic uncertainties (%) on the total cross-section for each channel.

Channel	Cross-Section [fb]		
$eeee$	$5.88^{+0.83}_{-0.76}$(stat.)	$^{+0.43}_{-0.37}$(syst.)	$^{+0.17}_{-0.16}$(lumi.)
$ee\mu\mu$	$12.29^{+1.03}_{-0.97}$(stat.)	$^{+0.63}_{-0.55}$(syst.)	$^{+0.36}_{-0.33}$(lumi.)
$\mu\mu\mu\mu$	$4.84^{+0.56}_{-0.51}$(stat.)	$^{+0.28}_{-0.23}$(syst.)	$^{+0.14}_{-0.13}$(lumi.)

Table 5.28: Fiducial cross-sections measurement for each channel.

5.7.1 Evaluation of the results

Comparison with theory predictions

In order to compare the measured cross section with the theory prediction the MCFM generator is used. The on-shell ZZ cross section, computed with the CT10 PDF set and for the QCD scales equal to m_{ZZ}, it is found to be:

$$\sigma_{th} = 7.06 \pm 0.25\ pb. \quad MCFM\ (NLO\ QCD) \tag{5.20}$$

This prediction is in excellent agreement with the combined measurement. The uncertainties on the predicted value are due to the scale choice and the PDF set and are of the order of 3.95%.

As discussed in the introduction of this chapter, we decided to apply the available NLO EW correction on our nominal samples. The inclusion of the electroweak corrections decreased our signal by 4.4%. The MCFM cross section can be corrected for NLO EW effects by scaling the computed cross section by 0.956. Then one gets:

$$\sigma_{th} = 6.75 \pm\ 0.24\ pb \quad MCFM\ (NLO\ QCD\ +\ NLO\ EW)$$

This prediction is still in agreement with the measurement within uncertainties. One step further, a rough estimate of the impact of the newly computed NNLO QCD corrections on the MCFM NLO cross section could be made. In the paper by Grazzini et al [86], the ratio of the computed NLO to NNLO cross section was found to be 0.8895, i.e the ZZ cross section prediction increased by 11.04%. This percentage includes the gluon-gluon contribution, which is estimated to be responsible for the 60% of the correction. Thus, the bare NNLO $q\bar{q} \rightarrow ZZ$ correction is about 4.4%. Although this correction was not applied on the $POWHEG$ sample as no differential k-factors have been provided so far, it can be applied to the total expected cross section. One sees that the NLO EW and the NNLO QCD corrections on the total cross section are found to be of the same order, but to act in the opposite direction. Therefore, the canceling effects between those two corrections result in a "corrected" cross section for NNLO QCD and NLO EW effects of the same order as the NLO QCD MCFM cross section, which in any case is in agreement with the measurement.

In table 5.29 the expected NLO QCD fiducial cross sections are given for each decay channel. The numbers are obtained with MCFM using the same setup (QCD scales, PDF) as for the total cross section, and no corrections are applied to them since, as just discussed, the NNLO QCD and NLO EW corrections have canceling effects on the integrated cross section. One observes that the measured cross sections are again compatible with the theory predictions within uncertainties. The NLO QCD theory prediction is slightly higher than the measurement for the four electron

and four muon channel, while it is smaller for the 2e2μ channel. This behavior is expected if one compares the data yield per channel with the signal prediction without applying the EW corrections, see section 5.4.

Channel	$eeee$	$\mu\mu\mu\mu$	$ee\mu\mu$
Expected fidu. [fb]	6.58 ± 0.26	5.14 ± 0.20	11.87 ± 0.67

Table 5.29: The theoretical fiducial cross sections as estimated with MCFM. The errors account for the QCD scale and PDF choises.

Comparison with previous results

All ZZ cross section measurements conducted so far in ATLAS and CMS are in agreement with the theory predictions [36] [37] [89] [93]. This is also the case for the present measurement.

The direct comparison with the CMS 8 TeV measurement is not possible since CMS has different baseline choices for the QCD scales and the parton distribution function: m_Z and MSTW2008, respectively. Moreover, the on-shell definition is also different, requiring $m_z \in$ 60-120 GeV. With the above setup CMS finds a total on-shell cross section of $7.7^{+0.5}_{-0.5}(stat.)^{+0.5}_{-0.4}(syst.) \pm 0.4(theo.) \pm 0.3(lum.)$ pb [93] which is in agreement with the associated theory prediction of 7.7±0.6.

It is interesting to compare this measurement with the ATLAS preliminary 2012 total ZZ cross section measurement shown in Moriond 2013. The measured cross section was $7.1^{+0.5}_{-0.4}(stat.) \pm 0.3(syst.) \pm 0.2(lumi.)$ [89]. The two measurements are, as expected, in good agreement. One observes that including the extension leptons slightly reduced the statistical error from 0.5 pb to 0.4 pb while the systematic errors are slightly larger.

Chapter 6

Anomalous couplings

6.1 Introduction

The good agreement between the measured cross section and the SM prediction, as observed in chapter 5, is an evidence of the SM success. However, as seen in chapter 1, the effect of new physics is expected to be very small with respect to the SM ZZ production. With the present 8% error on the total cross section measurement, and even with an increased luminosity which would reduce the statistical error, the detection of such small effects on the cross-section is still excessively difficult. Therefore, in order to search for very subtle deviations from the SM dedicated studies have to be performed.

An interesting model independent scenario to examine, is the existence of the neutral anomalous triple gauge boson couplings (aTGC). As described in section 1.1.3, according to the SM, the neutral ZVV vertexes (V = γ or Z) are forbidden at tree level, and only a very small contribution of the order of $O(10^{-4})$ is expected from higher order SM diagrams. In section 1.2, the possibility of observing signs of new physics via aTGCs was discussed, and the four neutral anomalous coupling parameters, f_4^γ, f_4^Z, f_5^γ and f_5^Z which are associated to the ZZ final state were introduced. The aim of this analysis is to set limits on these parameters.

If the aTGCs are present, in addition to the enhancement in the observed number of events, the kinematic distributions are expected to be modified. Therefore, instead of working with the integrated number of events over all the spectrum, as done for the cross section extraction, here the aim is to identify the most sensitive observable and localise the part of its spectrum which has the higher discriminative power against the SM.

In the following sections the signal parametrisation, the statistical method used for the limit extraction, the search for the most sensitive observable and its most

interesting spectrum region are presented. Finally, the expected and observed limits on the anomalous coupling parameters are extracted.

6.2 Limits setting procedure

The procedure to follow in order to set limits on the anomalous couplings is similar to the one described in section 5.6 for the cross section extraction. Likewise, a fit is performed between the observed number of events (N_{obs}) and the expected number of events[1] (N_{exp}). The difference is that now the N_{exp} is expressed as a function of the coupling parameters f_i^V which are those that are being fitted. Moreover, the three decay channels are merged, and instead of working with the integrated number of events a binned analysis on the most sensitive observable is performed. Finally, the quoted value is the 95% Confidence Interval (CI) on the coupling, and not the one that minimises the fit and its 1σ error.

6.2.1 Signal parametrisation

The four neutral aTGC parameters appear linearly in the Lagrangian, see equation 1.13. Thus, the process cross section, after squaring the invariant amplitudes, becomes a function of four linear, six interference and four quadratic terms.

$$\begin{aligned} d\sigma_{SM+aTGC} &= F_{00} + f_4^\gamma F_{01} + f_4^Z F_{02} + f_5^\gamma F_{03} + f_5^Z F_{04} \\ &+ \left(f_4^\gamma\right)^2 F_{11} + f_4^\gamma f_4^Z F_{12} + f_4^\gamma f_5^\gamma F_{13} + f_4^\gamma f_5^Z F_{14} \\ &+ \left(f_4^Z\right)^2 F_{22} + f_4^Z f_5^\gamma F_{23} + f_4^Z f_5^Z F_{24} \\ &+ \left(f_5^\gamma\right)^2 F_{33} + f_5^\gamma f_5^Z F_{34} \\ &+ \left(f_5^Z\right)^2 F_{44} \end{aligned} \tag{6.1}$$

where F_{00} is the SM contribution, and the F_{ij} with $ij \neq 00$ are the coefficients of the aTGC terms. There are only 14 aTGC terms, since among the 24 F_{ij} possible coefficients, 10 of them are symmetric $F_{ij} = F_{ji}$.

Contrary to the SM amplitude and those associated to the f_5^V couplings which are CP-even, the amplitudes associated to the f_4^V couplings are CP-odd. Therefore the terms corresponding to interferences between the two sets of amplitudes, i.e F_{01},

[1] The N_{exp} is the sum of signal + background (reducible+irreducible) events: $N_S + N_B$. Hereafter, for simplicity instead of talking about N_S we will directly refer to N_{exp}, thus when one sees $N_{exp}(f)$ it should be interpreted as $N_{exp} = N_S(f) + N_B$

F_{02}, F_{13}, F_{14}, F_{23} and F_{24}, are expected to be null. A fact of experience is that the terms of interferences between the f_5^V and SM amplitudes, i.e F_{03} and F_{04}, are found very small as well.

The optimal way to get the parametrisation for the expected events as a function of the anomalous couplings, $N_{exp}(f)$, is to have MC simulations for which the cross section parametrisation of each event is known. There are MC samples that already contain this information, such as *MC@NLO*, however, the ZZ process is not implemented in it yet. An alternative is to use an external software framework which is able to compute the event cross section of an already generated sample using the event kinematics.

In this analysis, the F_{ij} coefficients for each event are obtained using the Baur, Han and Ohnemus (BHO) program [94] interfaced with *Sherpa*. The framework performing this interface is described here [95]. The *BHO* program takes as input the kinematics of the incoming partons and the outgoing particles and, for a given set of assumptions i (couplings, form factor etc), computes the cross section for the event kinematics, hereafter noted $d\sigma$. If the cross section is computed for 15 different sets of assumptions (aTGC configurations), by solving the system of 15 equations one gets the 15 F_{ij} coefficients of the equation 6.1. This is done by reversing the matrix equation: $\mathrm{d}\vec{\sigma} = \hat{A}\vec{F} \quad \Rightarrow \quad \vec{F} = \hat{A}^{-1}\mathrm{d}\vec{\sigma}$, where $\hat{A}$ is the matrix containing the coupling values, $\mathrm{d}\vec{\sigma}$ are the cross sections and $\vec{F}$ the terms to determine. A simple example of coefficient determination can be given if only one coupling constant is considered. In this case, there are 3 coefficients to determine $\mathrm{d}\sigma_{\mathrm{SM+TGC}} = F_{00} + fF_{01} + f^2F_{11}$. Then, by considering three different values for the anomalous coupling f, e.g $f_a = 0$, $f_b = 1$ and $f_c = 2$, and using the three associated cross sections $\mathrm{d}\sigma_i$ the BHO program has computed, three independent equations can be written. In the matrix-form one has:

$$\begin{pmatrix} \mathrm{d}\sigma_a \\ \mathrm{d}\sigma_b \\ \mathrm{d}\sigma_c \end{pmatrix} = \begin{bmatrix} 1 & 0 & 0 \\ 1 & 1 & 1 \\ 1 & 2 & 4 \end{bmatrix} \begin{pmatrix} F_{00} \\ F_{01} \\ F_{11} \end{pmatrix} \tag{6.2}$$

The values of the F_{00}, F_{01} and F_{11} are determined after inverting the eq. 6.2.

Once the F_{ij} terms of each event are known, one can obtain the associated cross section for any desirable value of the couplings. This is a step towards the parametrization of the number of expected events:

$$\begin{aligned} N_{exp} &= Y_{00} + f_4^\gamma Y_{01} + f_4^Z Y_{02} + f_5^\gamma Y_{03} + f_5^Z Y_{04} \\ &+ \left(f_4^\gamma\right)^2 Y_{11} + f_4^\gamma f_4^Z Y_{12} + f_4^\gamma f_5^\gamma Y_{13} + f_4^\gamma f_5^Z Y_{14} \\ &+ \left(f_4^Z\right)^2 Y_{22} + f_4^Z f_5^\gamma Y_{23} + f_4^Z f_5^Z Y_{24} \\ &+ \left(f_5^\gamma\right)^2 Y_{33} + f_5^\gamma f_5^Z Y_{34} \\ &+ \left(f_5^Z\right)^2 Y_{44} \end{aligned} \tag{6.3}$$

To determine the Y_{ij} terms one has to apply the regular analysis selection requirements on the full simulation sample, and sum over the F_{ij} weights of all the selected events. All the event related weights and the object scale factors have to be taken into account in the sum. Then, this yield has to be normalised to the expected luminosity:

$$Y_{ij} = [\sum_{e}^{N_{events}} (F_{ij}^e \cdot W^e)] \times \frac{20.3\sigma}{G} \tag{6.4}$$

where N_{events} is the total number of events that passed the full selection, W^e is the product of all event and object related weights of the current event e, σ and G are the sample generated cross section and the number of generated events, respectively, and finally 20.3 fb^{-1} is the integrated luminosity of our data sample.

As it will be shown in the next section, the sensitivity to new physics is at high transverse energies. Hence, as discussed, the aim is to localise the interesting part of the spectrum and split it into bins such that the bin combination gives the best possible (tighter) limits. This implies that the N_{exp} parametrisation (Yij coefficients) have to be estimated separately for each bin. Since it is important that the coefficients are precisely estimated in all bins, and especially in those with a high sensitivity, our nominal *POWHEG* generator is not suitable for the Y_{ij} coefficients computation. Indeed, being a SM generator gives only a limited number of events generated at high energies. In order to cope with this problem, one should use MC samples generated at "boosted" aTGCs points, in such a way that high event statistics is guaranteed at high energies. Of course, the F_{ij} coefficients of each event need to be corrected for the initial generation conditions, such that in the final parametrisation the F_{00} terms represent the SM cross section. This is done by dividing all of the obtained F_{ij} coefficients with the event cross section computed for the specific aTGCs point at which the sample was generated, $d\sigma(f_4^\gamma, f_4^Z, f_5^\gamma, f_5^Z)$.

The only generator that models the aTGCs for the ZZ process is *Sherpa*. Therefore *Sherpa* samples have been used, generated at various "boosted" aTGC points.

In table 6.1 the ID numbers of these samples and the aTGC points for which the samples have been generated are listed. It should be noted that no form factors have been used for the sample generation.

aTGC Sherpa Samples	f_4^γ	f_5^γ	f_4^Z	f_5^Z
147207_SM	0	0	0	0
147208_TGC0	0.1	0	0	0
147209_TGC1	0.1	0	0	0.1
147210_TGC2	0.1	0.1	0.1	0.1

Table 6.1: The *Sherpa* samples used for the Y_{ij} determination and the procedure validation.

When the cross section parametrisation of each event is known, it can be used to reweight the MC sample distributions from the generated aTGC point to another point by applying an event by event weight. The reweighing technique will be used in order to validate the F_{ij} extraction procedure. More in detail, this can be done using a pair of samples generated at different aTGC points, i.e for different sets of couplings, by comparing the distribution obtained after reweighing one of the sample to the aTGC point of the other. In the left plot of figure 6.1, the TGC0 sample was reweighed to the aTGCs points for which the SM, TGC1 and TGC2 samples were generated, as listed in table 6.1. These reweighed distributions are compared to the bare distributions of the SM, TGC1 and TGC2 samples (same color but different line type). As it can be seen from the ratio plot, the agreement between the bare and reweighed distributions is good. In the right plot, the TGC0 and TGC1 samples have been reweighed to all the aTGCs points of the four *Sherpa* samples (same color but different marker shape). Here again, the agreement between the distributions is good, as no specific tendency is shown besides statistical fluctuations.

Sherpa is a leading order $q\bar{q}$ generator, and thus the term Y_{00} lacks the gg contribution and the NLO QCD and EW corrections. As it was discussed in the cross section chapter, all these corrections exist in our nominal signal samples ($POWHEG$+$gg2VV$), see section 5.1. Hence, one should use instead this most accurate prediction for the SM term, Y_{00}. By doing so, one prevents from observing a "fake" excess in data, as evidence for aTGCs, while it is just due to the missing higher order terms in the SM prediction of the Leading Order *Sherpa* generator.

It should be noted that for the 7 TeV publication, all the terms of the N_{exp} parametrisation were normalized to the $Powheg + gg$ prediction, by scaling the whole polynomial with $Y_{00}^{Powheg+gg}/Y_{00}^{Sherpa}$. This methodology assumes that the behavior of the aTGCs at NLO is the same as for the SM, something that has not

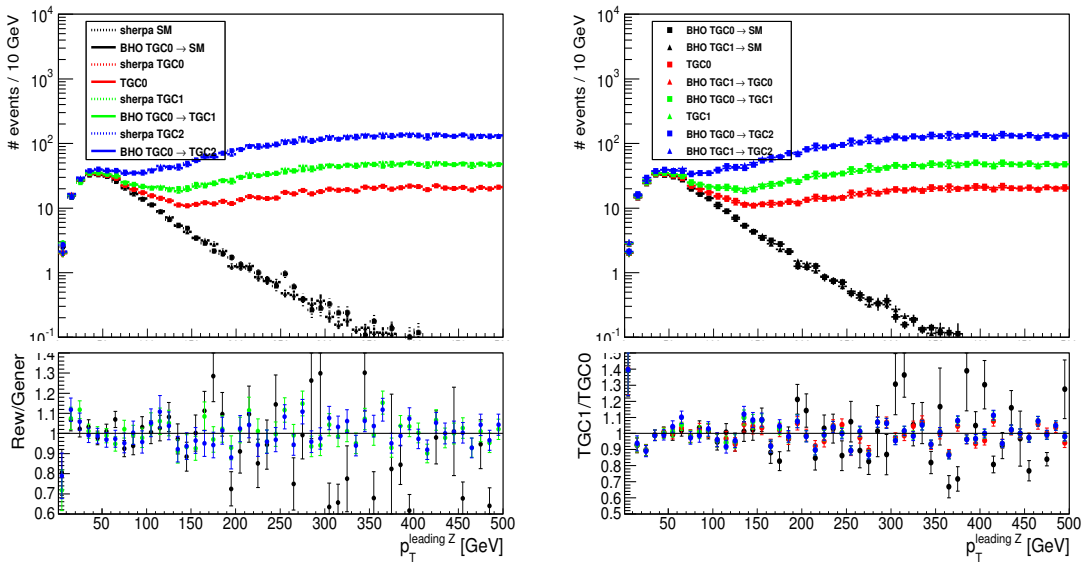

Figure 6.1: Coefficients extraction validation using the reconstructed P_T distribution. Left: comparison of the P_T distribution obtained after reweighting the TGC0 sample to another aTGC point X with the distribution of another sample generated at the X point. Right: comparison of the TGC0 and TGC1 P_T distributions, both re-weighted to some other X TGC point.

been proved yet, and thus, it is an arbitrary correction that should preferably not be applied anymore.

Cutoff scale

In section 1.2 where the aTGCs have been introduced, the unitarity violation issue was raised. It was said that anomalous couplings having a limit above some threshold may violate unitarity. Such situations without a physical meaning can be avoided using form factors that will impose the coupling straight to decrease with the energy.

Working in this direction, there is a possibility to compute the cross section parametrisation for each event for a finite Λ scale of the form factor. In this case, when estimating the F_{ij}, the dipole form factor is applied on the anomalous coupling in the matrix A. The form factor, $FF = \frac{1}{(1+\frac{\hat{s}}{\Lambda^2})^n}$, depends on the event mass scale $\hat{s}$ and an arbitrary number n that further suppresses the coupling. For the neutral anomalous couplings the number typically used is $n = 3$.

The inclusion of such a form factor has been actively discussed within the ATLAS and CMS communities. The argument is that even though the unitary is preserved, the way this form factor is introduced remains arbitrary and model dependant.

Furthermore, an advantage of not introducing a form factor is that only in this case the relations between the f_i^V and the effective field theory parameters C_i are valid, see section 1.2. This makes possible to deliver limits on the C_i parameters using the existing N_{exp} parametrization. Heretofore, there is not clear prescription on how to proceed within the ATLAS collaboration. In this document the limit behavior as a function of the cutoff scale Λ will be studied. However, special attention will be given in the case no form factor is used ($\Lambda = \infty$) as this is the baseline of the present analysis.

6.2.2 Statistical procedure

Likelihood definition

For the limit extraction a binned maximum log likelihood approach is used, similar to the one described for the cross section extraction. The only difference is the fitted parameters, which now are the anomalous couplings.

Again, in the aTGC case, for a better convenience instead of handling the bare Likelihood quantity, the negative-log-likelihood (nLL) is introduced. Furthermore, a normalization to the best possible predicted value (L_{best}) is done. The L_{best} corresponds to the likelihood of an unknown theory that would predict exactly the observations, i.e it is computed for N_{obs}= N_{exp}. Finally, the nLL is:

$$nLL(f,x) = -ln\frac{L}{L_{best}} = -\sum_{i}^{n_{bins}} \frac{e^{-N^i_{exp}(f,x)} \times (N^i_{exp}(f,x))^{N^i_{obs}}}{e^{-N^i_{obs}} \times {N^i_{obs}}^{N^i_{obs}}} + \sum_{m=1}^{n_x} \frac{x_m^2}{2} \qquad (6.5)$$

Once the nLL is defined, one can proceed to its minimization in order to find the values of the coupling ($\hat{f}$) and the nuisance parameters ($\hat{x}$) for which the best agreement between the observation and the expectation is achieved.

95% CL limits

Instead of quoting the best matching value for the parameters and their errors at 68% CL, as it is done for cross section, the common practice for the aTGC studies is to quote only the Confidence Domain at the 95% CL. In order to extract these limits the FLIT package is used [92] in which a fully Frequentist approach is followed as prescribed by J. Feldman and R. D. Cousins [96].

For the extraction of 95% CL limits one needs to proceed to a scan of the coupling values and find the one having a p-value equal to 5%. This procedure must be

repeated for both upper and lower end of the interval. Here are presented the steps to follow for the computation of the p-value of the parameter f, fixed at a test value (f^{test}), for a given N_{obs}.

One first defines the "test statistics":

$$q_{obs} = -ln\frac{L(N_{obs}|f^{test}, \hat{\hat{x}})}{L(N_{obs}|\hat{f}, \hat{x})} \tag{6.6}$$

In eq. 6.6 the numerator of the fraction is the likelihood value obtained after performing a minimization for a fixed coupling value equal to f^{test} and all nuisance parameters free (profile Likelihood). The denominator is the minimum value of the likelihood obtained after the free fit.

The next step is to generate 10K pseudo-experiments, each one for a new N^*_{obs} value. The N^*_{obs} is generated from a Poissonian PDF which has a mean value equal to the prediction for the given value of the coupling $N_{exp}(f^{test})$. For each pseudo-experiment the q^* is computed according to eq. 6.6 for the new N^*_{obs} value. Finally, the $p-value$ is defined as the fraction of the pseudo-experiments having $q^* > q_{obs}$ over the total number of pseudo-experiments. Therefore, the $p-value$ is the probability of obtaining an outcome at least as extreme as the actual observation. The scan stops once the f^{test} having $p-value$= 5% is found.

Limits to extract

There are two types of limits that need to be extracted:

- Observed limits: The ZZ data candidates (N_{obs}) are used for the extraction of the observed limits. In order to estimate the 95% CL limits on f, one fits the f and x_k parameters such that the function 6.5 gets minimal. The steps to follow are those described in the previous section i.e build the likelihood and then determine the limit for which $p-value$= 5%.

- Expected limits: It is important to know if the observed limits are compatible with the limits one would obtain from a SM-only scenario. For this reason one estimates the so called "expected" limits, such that they can be directly compared to the observed ones. The procedure to follow for the expected limit extraction requires some additional steps. One has to generate a large number of pseudo-experiments from a Poissonian PDF with a mean value equal to the SM prediction, and find for each pseudo-experiment the 95% CL limit. The obtained limits are histogrammed and the median of the distribution is considered as the "expected limit". The σ of the distribution with respect to

the median is also an important quantity. In the case where a discrepancy between the observed and the expected limits is found, it is used to quantify its significance i.e to estimate how likely it is the discrepancy to be due to a genuine fluctuation.

The observed and expected limits can be extracted either by fitting one coupling per time while all remaining three couplings are set to zero, or by fitting two couplings simultaneously, while the remaining two couplings are set to zero, giving six pairs of coupling combinations. The former limits are referred as 1D limits and the latter as 2D limits. The two dimensional graphs showing the 2D limits are of special interest as they can reveal correlations between the couplings. Ideally, the extraction of 3D and 4D limits is even more interesting, however, the results would have been hard to interpret due to the difficulty in visualizing such a multidimensional surface.

6.3 Optimisation study

As it was already mentioned in the previous sections, the anomalous triple gauge couplings, if any, will appear at high energy transfers. Therefore, the kinematic spectra expected to be mostly modified are those related to the event energy scale, such as the transverse momentum of the leading Z and the mass of the four lepton system. So far, in all ATLAS and CMS diboson analyses, one of these two variables has been used. In this document, besides the P_{T} of the leading Z and the m_{zz}, other variables will be also probed. Once the most sensitive observable is determined the next step will be to find the optimal binning giving the tighter limits.

Such optimisation studies must be always performed on the expected limits in order not to bias the analysis. The full Frequentist approach for the expected limits extraction, as described in the previous section, is time consuming due to the generation of pseudo-experiments. Therefore, for the investigation of several variables and binning configurations an alternative much quicker procedure was used. Once the optimal observable is identified and an indication of the optimal binning position is found, then, more advanced limit optimisation will be performed using the Frequentist approach.

6.3.1 Educated guess

The need for a fast and simple way to decide how to proceed with the limit optimization, led to the usage of an "educated guess" approach. In this approach the

significance of the signal (aTGCs) with respect to the background (SM), is used as a guideline for the optimization.

$$Signif. = \frac{S}{\sqrt{S+B}} = n \tag{6.7}$$

For simplicity, only one coupling is considered and the linear term can be neglected as it is negligible compared to the quadratic term. Thus the equation 6.3 which gives the number of expected events becomes $N_{exp} = Y_{00} + Y_{ij}f^2$, and the significance equivalence is: $S = Y_{ij}f^2$ and $B = Y_{00}$. The 95% CL limits (f) are obtained after solving the equation 6.7 for n = 1.96:

$$f_i = \pm\sqrt{\frac{n^2 + \sqrt{n^4 + 4n^2 Y_{00}}}{2Y_{IJ}}} \tag{6.8}$$

The equation 6.8 gives the limit for one inclusive bin. In the case of several bins, the simplest and conventional approach is to consider that the significance has a quadratic dependence on the parameter f. This assumption allows to use the weighed average formula:

$$\frac{1}{f^2} = \frac{1}{f_1^2} + \frac{1}{f_2^2} + ... + \frac{1}{f_n^2} \tag{6.9}$$

This way of combining the limits is valid for bins with dominant aTGC contribution, as $Signif \approx \sqrt{S} = \alpha f$. However, if the SM (B) expectation is not negligible in a bin, by assuming quadratic dependence one allows this bin a higher contribution than it really has.

The advantage of the "educated guess" procedure is that it is much quicker than the full procedure and technically easier to handle. However, this method does not take into account the systematics and makes a lot of approximations. Therefore, it should not be used for quoting an exact numerical result but only for comparing observables behavior, and to indicate the spectrum region where the binning seems optimal.

Observables study for $\Lambda = \infty$

The production mechanism of the $ZZ \to \ell\ell\ell'\ell'$ final state is via t and u channels for the SM and the s-channel for the aTGCs. Hence, the kinematic distributions are expected to be different. In order to set the tighter possible limits, one should select the most sensitive observable. The following observables will be examined:

- Transverse momentum of leading Z, $P_T^{leadingZ}$

- Mass of the ZZ system, M_{ZZ}
- Longitudinal momentum in center of mass frame (CM), P_z^{CM}
- Momentum in CM, P^{CM}
- Rapidity difference of the two Zs, $\Delta Y = |Y_{Z1} - Y_{Z2}|$, where $Y = 0.5ln(\frac{E+P_Z}{E-P_Z})$
- The polar angle of the Z in the CM, $\theta^* = tan^{-1}(\frac{P_T^{CM}}{P_z^{CM}})$

Plots in figure 6.2 show the distributions of the six observables under investigation for the SM and the case where all the anomalous coupling parameters are set to $f_i^V = 0.005$, for $\Lambda = \infty$. The SM distributions are drawn with black, while the aTGC distributions with red. One sees that especially the P_T , M_{ZZ} , Pz and P observables seem more discriminant compared to the rapidity and θ^*. In the following, the educated guess method is used in order to determine which observable is the most sensitive.

In order to identify which observable gives the most constraining limits two bins will be considered. A scan on the bin boundary x is performed, and for each bin configuration [0-x][x-∞] the 95% CL limit is computed using relation 6.8 and 6.9. All the pairs (bin configuration - limit) are plotted in the same graph. The results are shown in figure 6.3, where the x-axis represents the boundary x between the two bins and the y-axis the obtained limit for the given bin configuration.

These plots reveal two things. First, the behavior of all four coupling parameters is the same, independently of the observable under examination. Consequently, hereafter, the optimization will be performed on just one coupling parameters and the conclusions will be applied on the remaining three. In this document the f_4^γ coupling will be used. Second, the observables directly related to the energy scale of the ZZ process, i.e $P_T^{leadingZ}$, M_{ZZ}, P_z^{CM} and P^{CM}, have the same high sensitivity to the aTGCs, while ΔY and θ^* are much less sensitive. These results are consistent with what was shown in figures 6.2. As all the energy related variables have the same sensitivity, it is legitimate to use either of them. In this analysis we will proceed to the limit extraction using the $P_T^{leadingZ}$ as it is the one used so far within the ATLAS collaboration.

A more accurate estimation can be obtained by solving numerically the significance sum over all bins $Signif.^2$:

$$\sum_{i=1}^{Nbins} Signif._i^2 = \frac{Y_{IJ0}^2 f^4}{Y_{IJ0} f^2 + Y_{000}} + \frac{Y_{IJ1}^2 f^4}{Y_{IJ1} f^2 + Y_{001}} + ... + \frac{Y_{IJN}^2 f^4}{Y_{IJN} f^2 + Y_{00N}} = n^2 \quad (6.10)$$

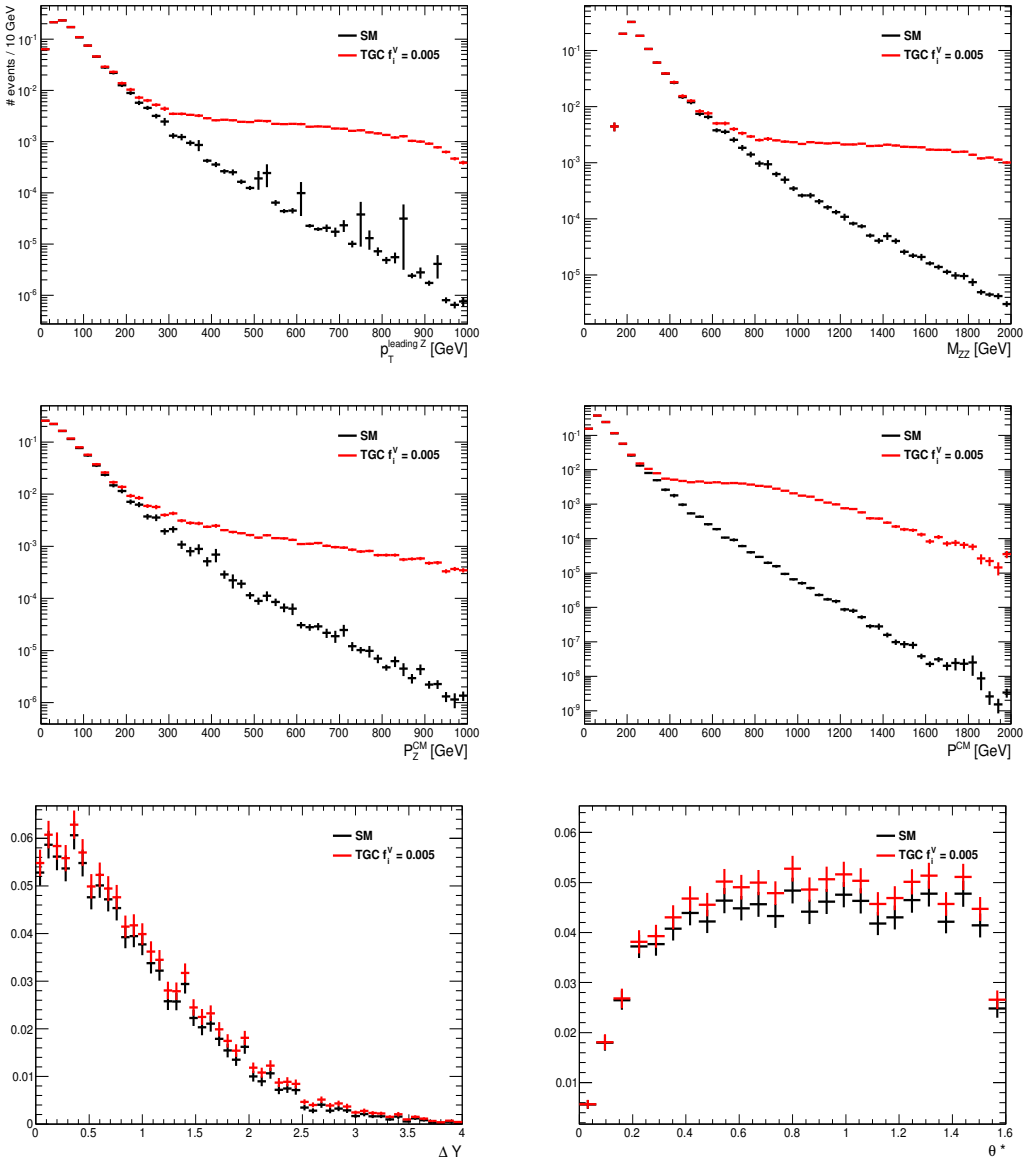

Figure 6.2: Comparison of various SM distributions (black) with the equivalent distribution when all aTGC parameters are set to 0.005 (red).

For each bin configuration a scan of f is performed in the range [0.003 - 0.018] with a step of 0.00005. The value minimizing equation 6.10 is finally retained. In figure 6.4 the optimization results on the P_{T} observable obtained with eq.6.10 (cyan) are compared to the results obtained with the weighted average formula 6.9 (red) for the f_4^γ parameter. Both methods are consistent and only a small difference is seen at very high bin boundaries where the weighted average method gives slightly tighter limits. This is expected because at these high P_{T} bin boundaries the first

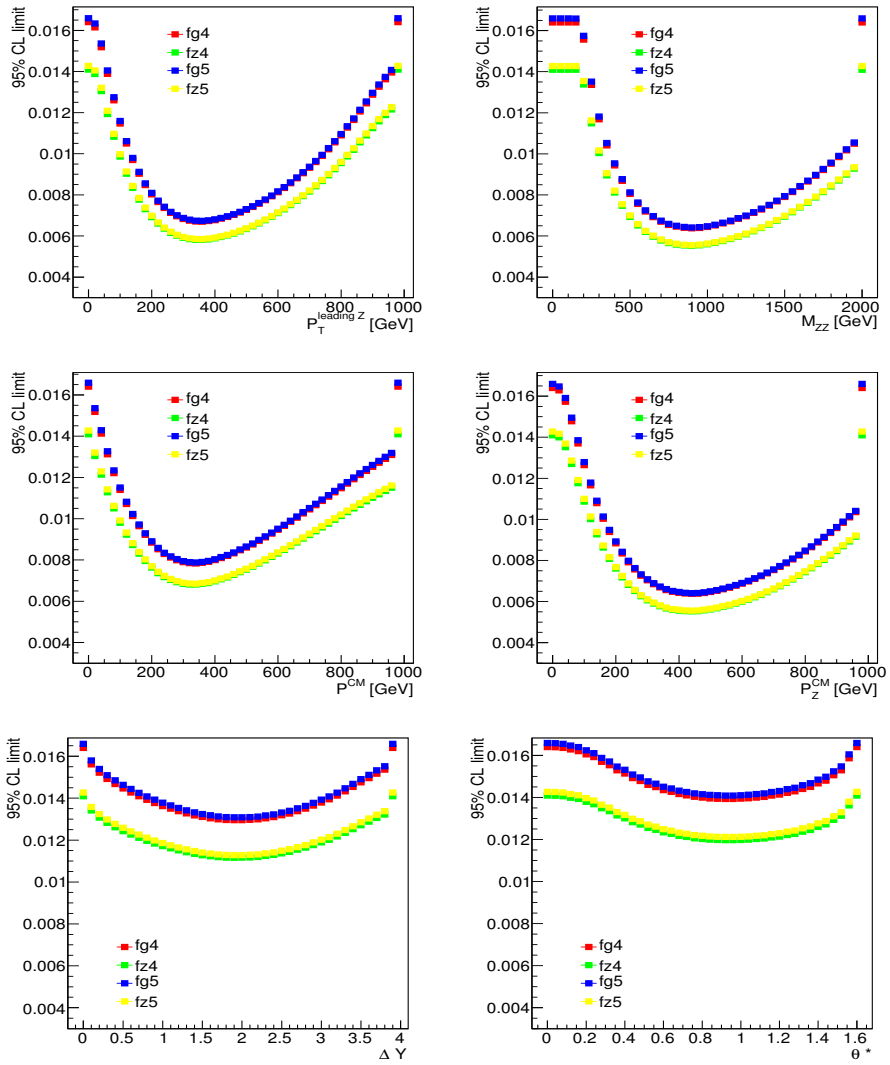

Figure 6.3: Limit estimation as a function of the boundary between the two bins for various observables.

bin becomes more sensitive and thus the weighted average method tends to enhance its contribution.

In addition to the above study that compares the observables sensitivity, I have also worked with two observables per time, i.e M_{ZZ} vs P_{T}, P_{T} vs θ^* etc. In this two dimensional configurations four bins have been considered. The boundaries of x and y axis were moved simultaneously, so that the optimal four bin configuration is found. The study showed that there is a gain of at most 4% with respect to the limit one obtains using only one variable with 2 bins. Finally, the two variables configuration was not adopted for practical reasons. Such reasons are the high

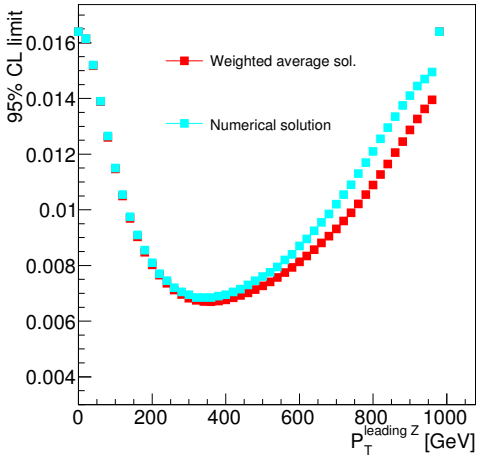

Figure 6.4: Comparison of the weighted average method (red) with the numerical one (blue) for the f_4^γ parameter.

statistical uncertainties on the optimal binning SM prediction and the complications in computing the data-driven background in those 2D bins.

P_T binning optimization for $\Lambda = \infty$

Now that the P_{T} observable has been selected, the next step is to determine the optimal bin boundaries. So far, only two bins have been used and from plot 6.4 one deduces that the optimal last bin boundary is around 360 GeV. Here, one more bin will be introduced. In order to determine what should be the lower bin boundary of the penultimate bin the same strategy will be employed, i.e the binning configuration to be probed is: [0-x][x-360]. In this study the bin [360-∞] is not considered because its great significance would shadow the optimisation.

The left plot in figure 6.5 shows the result for the penultimate binning optimisation. The plot indicates that the optimal lower boundary of the penultimate bin is around 250 GeV. Furthermore, one observes that the best limit obtained for the configuration [0-x][x-360] is about twice looser compared to the best limit obtained with the configuration [0-x][x-∞]. This indicates that the last bin will drive the analysis results and thus, adding more bins will probably not further improve the limits. The right plot of fig. 6.5 verifies this guess, as it illustrates the result of a three bin optimization where a scan of the type [0-x][x-(x+100)][(x+100)-∞] is performed. The best limit of the three bin optimisation is less than 3% tighter, compared to the best limit obtained with the two P_{T} bin optimisation [0-x][x-∞], shown in the figure 6.4. Furthermore, one sees that the exact position of the sec-

ond bin boundary is not clearly defined anymore, as now the third bin drives the result. More three-bin configurations of the type [0-x][x-(x+$x^{'}$)][(x+$x^{'}$)-∞], where $x^{'} \in [40-160]$ GeV with a 20 GeV step, have been studied as well. The results were optimal for $x^{'} \in [80-100]$.

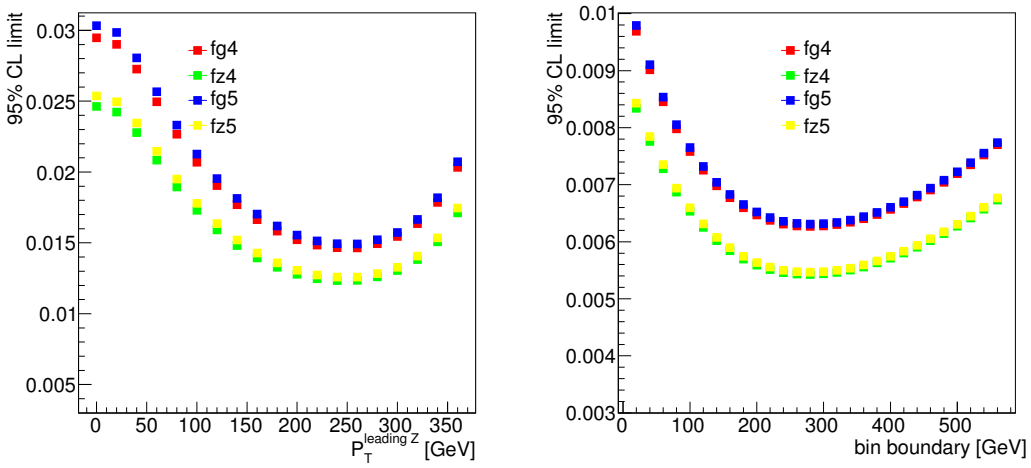

Figure 6.5: Binning optimisation for the penultimate binning boundary. Left: optimization of [0-x][x-360], Right: optimization of [0-x][x-(x+100)][(x+100)-∞]

The conclusion of the above binning optimisation study is that the optimal bin boundaries, when no form factor is applied, should be around 360 GeV for the last bin, and around 250 GeV for the penultimate bin. These numbers are an outcome of an "educated guess" study, and thus before proceeding to the limit extraction, one should first validate this choice using the Frequentist approach. Once this is done the accurate estimate of the expected and observed limits can be realized taking in account all the systematics and using a fully Frequentist approach.

P_T binning optimisation as a function of Λ

So far, the optimisation study was performed on limits without form factor. In figure 6.6 the P_{T} distribution is shown in the case all couplings have a value of the order of the expected limits i.e $f_i^V = 0.005$. The blue curve is for the no form factor case, while the red curve is for $\Lambda = 2$ TeV. As the form factor significantly modifies the kinematic distributions, the binning optimisation is expected to point to a different optimal binning.

Here a bin optimization on the P_{T} observable for various values of the Λ scale is shown. The optimisation is restricted on finding the bin boundary between two

bins [0-x][x-∞], since in the previous section it was shown that the last bin drives the analysis.

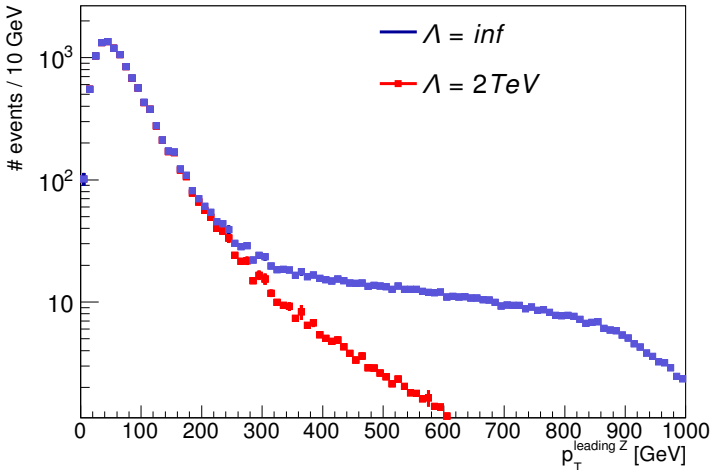

Figure 6.6: P_T distribution for $f_i^V = 0.005$ when no form factor is used (blue) and when $\Lambda = 2$ TeV (red).

Figure 6.7 shows the results of the two bin optimization for various values of the cutoff scale. As predicted, the optimal bin boundary depends on the cutoff scale. The bin boundary goes towards lower P_{T} values as Λ decreases. The two-bin optimization results shown in plot 6.7 will be used in section 6.6 for the aTGC limit extraction as a function of the Λ scale.

Λ scale [TeV]	2	2.5	3	4	5	6	8	∞
P_{T} bin boundary [GeV]	280	300	300	320	340	340	340	360

Table 6.2: Optimal bin boundary for each Λ scale, based on the findings of figure 6.7.

6.3.2 Asimov datasets

In section 6.2.2, the procedure to follow in order to extract the expected limits was described. This approach requires the generation of pseudo-experiment from a Poissonian PDF with a mean value equal to the SM prediction. Then, the median of the distribution of the 95% CL limits obtained by all these pseudo experiments is considered as the expected limit.

To bypass this time consuming procedure it has become common practice in LHC analyses to use an "Asimov Data set", i.e a single input data which is supposed to give forthwith the median of the pseudo-experiments without performing them. In

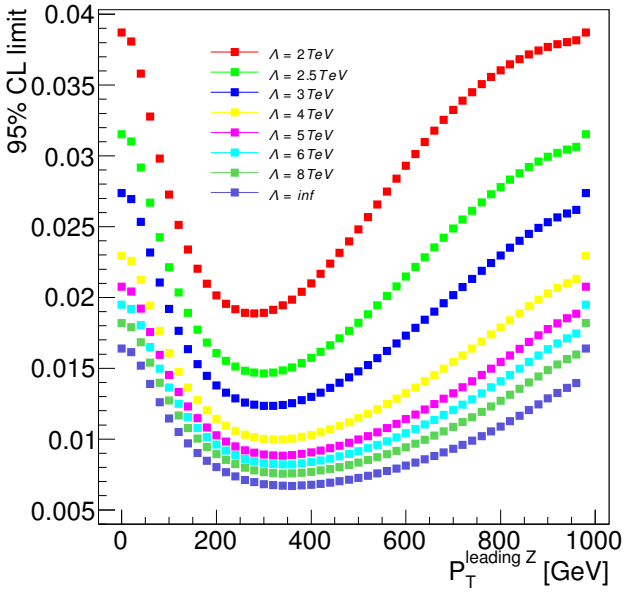

Figure 6.7: Two bin optimization as a function of the Λ scale.

the aTGC case, one can follow the spirit of this approach and take as "observation" input the exact SM prediction. Intuitively one can guess that this "average" input will return the "average" output, i.e the expected limit [97]. This assumption can be checked a posteriori.

When using an Asimov dataset, the N_{obs} is not an integer anymore since by definition it has the exact value the theory predicts. Technically, this is a problem due to N_{obs} factorial present in the Poissonian PDF. This problem is avoided when the Likelihood is divided by the L_{best} term, since the factorials cancel each other out, see equation 6.5. The advantage of working with an Asimov dataset is that it is about N times quicker, with N being the number of pseudo-experiments one would generate when using the full approach.

In this section the findings of the "educated guess" approach will be used as a guideline in order to finalise the binning optimization using the Asimov datatset for the case where no form factor is applied ($\Lambda = \infty$). It was shown that the best sensitivity is achieved when the last bin boundary is around 360 GeV and the penultimate bin boundary is around 250 GeV. In this paragraph the same study will be re-done, but now focusing around these areas. All systematics sources have been considered in this study[2].

[2]The systematics used were roughly estimated: the same values were used for all the first bins, as computed in the bin [0-200], and the same for all the last bins, as computed in the bin [200-∞]

Figure 6.8 shows the obtained limit versus the bin boundary. In the left plot the last bin boundary is tested. One sees that the best bin boundary is at 380 GeV; a result wich is very close to the "educative guess" findings. In the right plot the penultimate lower bin boundary was optimized for an upper bin boundary fixed as 380 GeV. The result again validates the educative guess method. The favorable bin boundary is at 260 GeV.

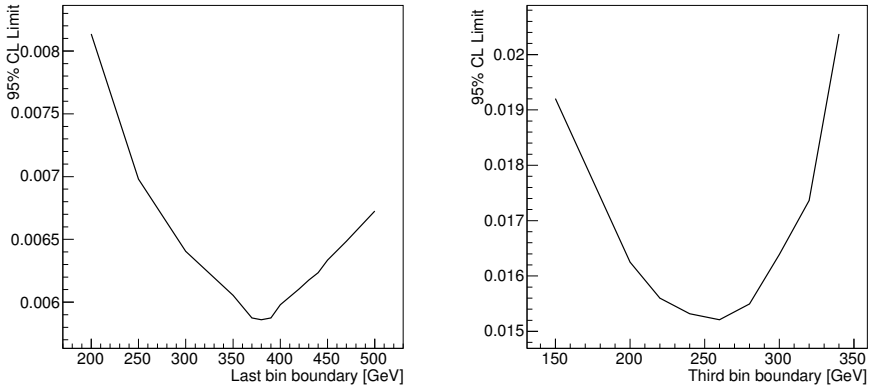

Figure 6.8: Two-bin optimisation on the f_4^γ parameter. Left: last bin optimization [0-x][x-∞], Right: penultimate bin optimization [0-x][x-380].

As it was already discussed, the last bin is by far the most sensitive one and thus there is no need continuing the optimisation for lower P_{T} bins. The top left plot in figure 6.2 indicates that the aTGC sensitivity starts around 200 GeV. Hence, based on the findings of the above studies, the binning configuration: [0-200][200-260][260-380][380-∞] was finally adopted, as it seems to be the most appropriate one for the limit extraction.

Figure 6.9 shows the nLL versus the coupling value for each of the four selected bins (colored) while the combined nLL is drawn in black. As it can be seen, the contribution of the last bin [380-∞] (cyan) is the dominant one since it practically overlaps with the combined (black) curve.

6.4 Inputs for the selected binning

So far, the optimisation has been performed without looking into the details of the bin content. Now that the optimal binning has been determined the data, SM and background yields in each of the four selected bins will be shown. Furthermore, special attention will be given to the binned systematics.

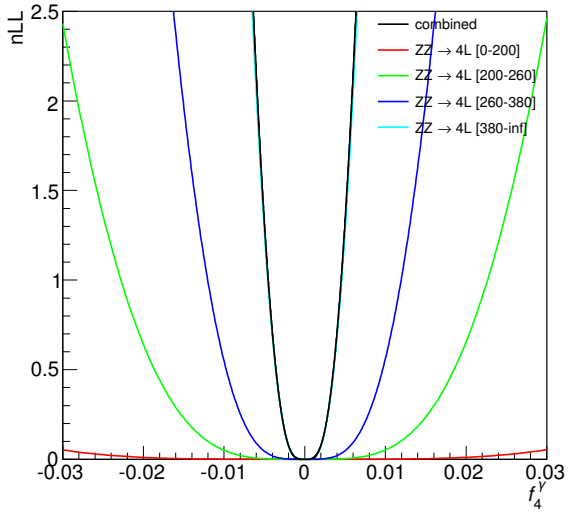

Figure 6.9: nLL value as a function of the coupling f_4^γ for the selected binning. The nLL for each of the four bins (coloured) and the combination (black) are plotted separately.

6.4.1 Data, SM and background Yields

The data yields, the SM expectation and the background contamination in each bin are extracted from the histogram shown in figure 6.10. It is the P_{T} distribution already shown in the cross section chapter, see section 5.4, with the y-axis being in logarithmic scale for a better view of the region of interest, and the P_{T} distribution for a scenario for which all coupling parameters are set to 0.005 superimposed. The exact content of each of the four bins is shown in table 6.3.

As it can be seen, the optimum binning is "unlucky" with respect to the actual data distribution. Even though the integral of data events in the last three bins is lower than the integral of the expected SM events, the data are not distributed evenly, something that is expected to deteriorate the quality of the fit. If for instance the third bin lower boundary would have been at 280 GeV instead of 260 GeV, the third bin would have had 2 observed events to be compared with 1.8 expected SM events and the second bin would have had 3 data events to be compared with 6.3 expected SM events, which is a more convenient configuration, in terms of fit quality.

In table 6.4 the SM prediction is compared to two aTGCs scenarios. In the first scenario all the f_i^V parameters are set to 0.001, while in the second $f_i^V = 0.005$.

[3]If the EW corrections wouldn't have been applied the expected number of events in each bin would be: 290.86 , 6.15 , 3.06 , 0.80

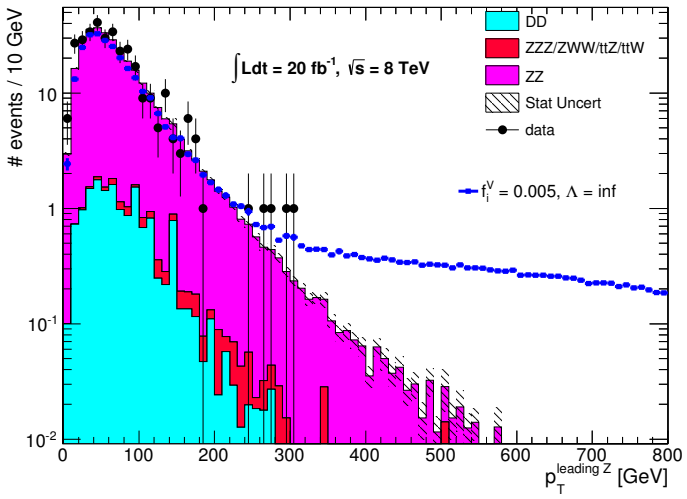

Figure 6.10: Data MC comparison and the aTGC expectation for $f_i^V = 0.005$.

$ZZ \to \ell\ell\ell'\ell'$	[0-200]	[200-260]	[260-380]	[380-∞]
Observed ZZ	316.0	1.0	4.0	0.0
Expected ZZ [3]	279.12 $\pm$0.80	5.43 $\pm$ 0.1	2.58 $\pm$ 0.07	0.63 $\pm$ 0.03
Expected MC Bkg	1.68 $\pm$0.07	0.09 $\pm$ 0.02	0.05 $\pm$ 0.01	0.02 $\pm$ 0.01
Expected DD Bkg	15.26 $\pm$4.57	0.17 $\pm$ 0.17	0.08 $\pm$ 0.08	0.02 $\pm$ 0.02
Total Expected	296.06 $\pm$4.64	5.69 $\pm$ 0.20	2.71 $\pm$ 0.11	0.67 $\pm$ 0.04

Table 6.3: Summary of observed events and expected signal and background contributions in each P_{T} bin. Only statistical errors are shown.

One sees that for $f_i^V = 0.001$, the number of events in the last bin has doubled. However, this number is still very small. The image is better for $f_i^V = 0.005$, however, as already discussed such large values of the neutral anomalous couplings are unlikely to be observed as neutral anomalous couplings are highly suppressed.

6.4.2 Systematic uncertainties

The same systematic sources affecting the cross section measurement also affect the aTGC limits extraction. However, there is an important difference between the two measurements. The cross section measurement relies on the MC simulation only for the computation of the correction factors C_{ZZ} and A_{ZZ}. Consequently, the theory systematics tend to cancel out as they are affecting both the numerator and the denominator of these factors. This is not the case for the aTGC limit extraction, since now one directly relies on the MC simulations for the Y_{00} term estimation.

$ZZ \to \ell\ell\ell'\ell'$	[0-200]	[200-260]	[260-380]	[380-∞]	total
SM $N_s(f_i^V = 0)$	279.12	5.43	2.58	0.63	287.7
$N_s(f_i^V = 0.001)$	279.18	5.49	2.72	1.22	288.45
$N_s(f_i^V = 0.005)$	280.55	6.79	6.12	15.36	308.66

Table 6.4: Comparison of the SM prediction in each bin with the expected SM+signal for two aTGC scenarios. In the first scenario the couplings f_i^V are set to 0.001 and in the second scenario $f_i^V = 0.005$.

As a result, the full theory uncertainty is propagated on the limit and thus it is expected to be the dominant among the systematics. On the other hand, as the reconstruction systematics are affecting only the numerator of the C_{zz}, their value would have been exactly the same if only one inclusive P_{T} bin would have been used for the aTGC extraction. However, here we perform a binned analysis and as both reconstruction and theory systematics are expected to vary with P_{T} they need to be all estimated separately in each bin.

The systematics on the object reconstruction are estimated according to what has been described in section 5.5. The theory systematics are also computed according to what was described in this section. The only difference is that now the scale and PDF systematics are deduced from the variation of the SM prediction, instead of the C_{ZZ} and A_{ZZ} variation. It should be noted that no simulation systematic is consider here since a simulation framework having the same features as the nominal $POWHEG$ + $gg2VV$ would have been needed. So far, no fully reconstructed $q\bar{q}$+gg NLO (QCD and EW) samples modeling the $ZZ \to \ell\ell\ell'\ell'$ process exist. The available frameworks which simulate the ZZ production lack these features. For instance *Sherpa* and $PYTHIA$ are LO generators, and the NLO QCD $MCFM$ is only a true level generator. Furthermore, none of them incorporates the EW corrections.

Table 6.5 lists all the systematic sources affecting the aTGC limit extraction. The major systematic is due to the QCD scale choice. It grows importantly with the P_{T} and reaches 10% in the last bin. Then, the systematics on the PDF and muon isolation/IP cut efficiencies follow, with a value of approximately 4% in the last bin. Still, it should be stressed that the dominant uncertainty on the aTGC extraction is the very large statistical error due to the small expected number of events in the driving bin.

Finally, statistical and systematic errors on the irreducible and data-driven background estimations are also taken into account. The errors associated to the very small number of irreducible background events are the statistical uncertainty on the MC estimation and the particle reconstruction uncertainties. As the final state of

Source %	[0-200]	[200-260]	[260-380]	[380-∞]
Luminosity		2.8		
Reconstruction efficiency				
Particle-related systematics				
e momentum smearing	0.08	0.97	1.50	1.29
e energy scale	0.12	1.13	1.72	2.40
e ID efficiency	1.64	1.77	1.73	1.65
e isolation/z0/d0Sig	0.61	0.94	0.91	0.43
e reconstruction	0.76	1.06	1.04	0.87
μ energy smearing	0.02	0.10	0.42	1.23
μ energy scale	0.01	0.28	0.22	0.39
μ isolation/z0/d0Sig	1.75	3.61	3.89	3.96
μ reconstruction	0.95	1.02	1.00	0.97
trigger	0.11	0.09	0.07	0.05
Theory-related systematics				
PDF	2.76	3.64	3.80	4.06
QCD Scales	2.81	4.75	7.21	9.63

Table 6.5: Systematic errors per bin.

the irreducible background is the same as the signal, the same reconstruction uncertainties have been considered, i.e those shown in table 6.5. No theory uncertainties have been taken into account. For the data-driven background the estimation of the uncertainties per bin is not possible due to the limited data statistics in the control region. For this reason it has been chosen to consider the systematic uncertainties to be the same in each bin, equal to the one computed for the total background estimation. The statistical error in the first bin is set equal to the statistical error of the total estimation while it is set equal to 100% for the last three bins. As the background estimation in the $ZZ \to \ell\ell\ell'\ell'$ channel is very small, especially in the high P_{T} bins, the large uncertainties attributed to them are not expected to have an impact on the measurement.

In section 6.5.1 it will be demonstrated that the impact of both signal and background uncertainties on the limits is very small. This justifies neglecting the theory systematics on the small irreducible background (about 0.02 events in the last bin), and the conservative rough estimate of the data-driven errors per bin.

6.5 Results for $\Lambda = \infty$

In the previous sections all the elements needed in order to perform the extraction of the expected and observed limits have been discussed. This includes the description

Parameter	Observed	Expected
f_4^γ	[-0.0046, 0.0046]	[-0.0056$^{+0.0013}_{-0.0017}$, 0.0056$^{+0.0017}_{-0.0013}$]
f_4^Z	[-0.0041, 0.0040]	[-0.0049$^{+0.0011}_{-0.0014}$, 0.0049$^{+0.0014}_{-0.0011}$]
f_5^γ	[-0.0046, 0.0047]	[-0.0056$^{+0.0013}_{-0.0017}$, 0.0056$^{+0.0017}_{-0.0013}$]
f_5^Z	[-0.0040, 0.0040]	[-0.0048$^{+0.0011}_{-0.0015}$, 0.0048$^{+0.0015}_{-0.0011}$]

Table 6.6: Observed and expected limits.

of the signal parametrisation and the Frequentist 95% CL limits extraction procedure in section 6.2, the binning optimization in section 6.3, and finally all the binned yields in section 6.4. Here, based on all the above, the expected and observed limits on the anomalous couplings f_i^V and the EFT parameters C_i are presented in the case where no form factors are used.

6.5.1 Expected and Observed limits on f_i^V

In figure 6.11 the 1-dimensional expected and observed limits are shown. For each of the four couplings there are two distributions, one for the *lower end* (left plots), and one for the *upper end* (right plots) of the limit interval. Each plot shows the 95% CL limits obtained from the 5000 pseudo-experiments generated around the SM prediction. The *expected limit* for each coupling is the median of the distribution, and it is drawn with long dashed black line. The Asimov result is shown as a solid black line. One checks that as expected, it is very close to the expected limit. The observed limit, drawn in red, is superposed on this histogram in order to be able to compare its position with respect to the expected one. The significance of the discrepancy between the observed and the expected limits is assessed from the 1 and 2 σ bands of the pseudo-experiment distributions, drawn with short dashed lines.

It should be noted that since the pseudo-experiment distributions are noticeably asymmetric, we quote asymmetric 1 and 2 σ errors. The reason of this asymmetry is the low SM event prediction of the driving bin, which gives 0.6 expected SM events in the last bin. As a result, the Poissonian PDF used for the 5000 pseudo-experiment generation is far from being Gaussian, as it consists of three spikes, squeezed toward the 0 value, see figure 6.12. The combined fit of the four bins along with the impact of the systematic uncertainties result in a smearing of the limit distribution, which however keeps the features of the Poissonian PDF used for the psudo-experiments

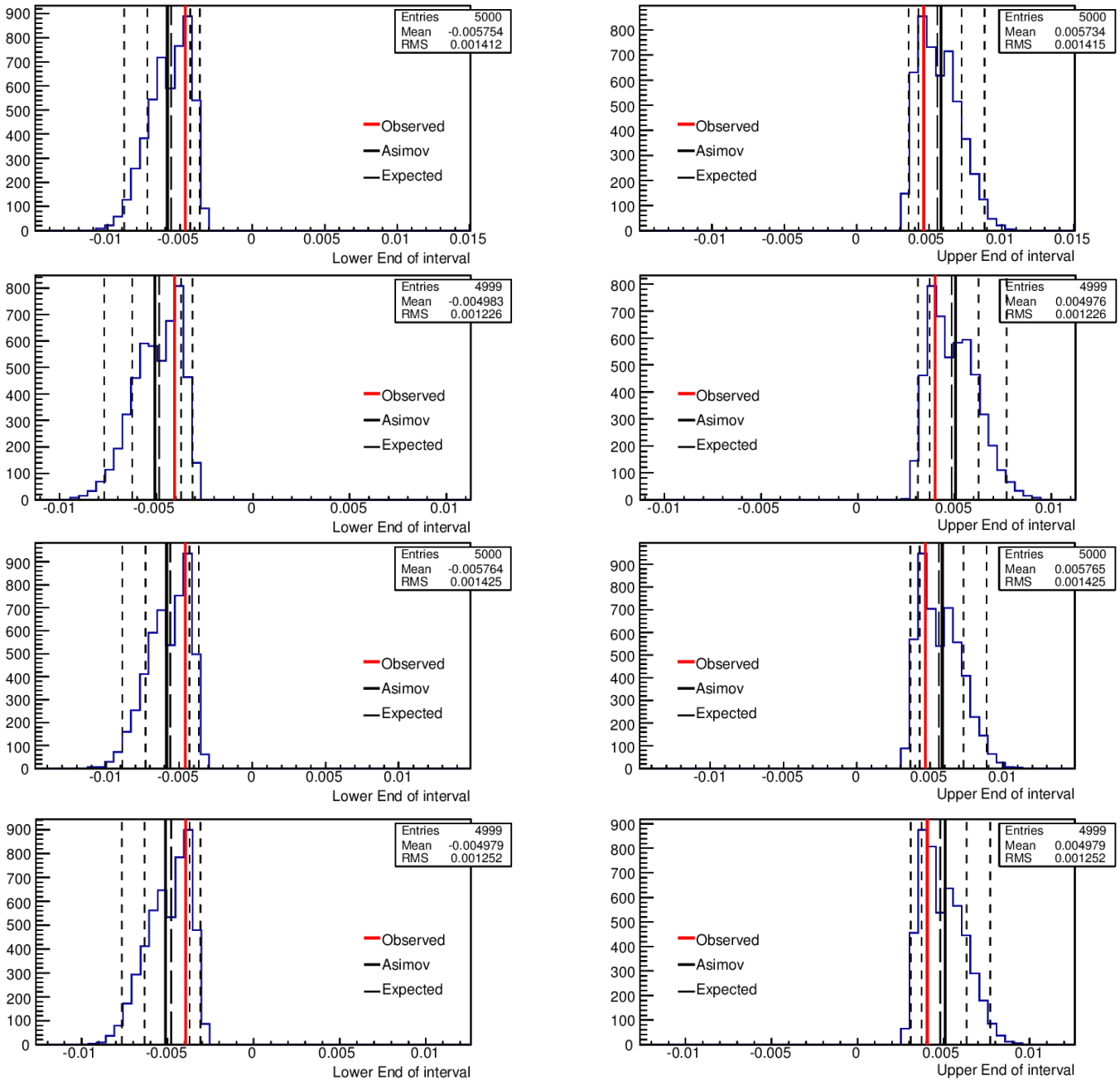

Figure 6.11: One dimensional expected and observed limits. From the top to the bottom the plots correspond to the couplings f_4^γ, f_4^Z, f_5^γ and f_5^Z.

generation.

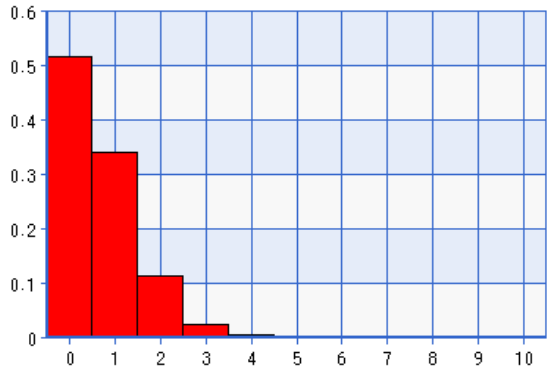

Figure 6.12: Poissonian PDF for a mean value of 0.63.

The exact values of the 1-dimensional observed and the expected limits are shown in table 6.6 [4] [5]. From both the figures and the table it can be seen that the observed limits are for all couplings tighter than the expected limits, still within the 1 σ band. This is not surprising, since the last bin which drives the analysis contains zero observed events for a non zero SM expectation.

In figure 6.13 the six pairs of 2-dimensional limits are shown. The observed limits are systematically tighter than the expected limits, within the 1σ band, something which is in line with the 1D limits behavior.

P-value and systematics impact

An interesting feature to examine is the quality of the aTGC fit. As already discussed, the driving bin is the last bin, and thus the disagreement between the data and the SM expectation in the three first bins is not expected to directly impact the limit. Nevertheless, it can have an impact on the p-value of the fit. In order to estimate the p-value a test statistics S is defined as:

$$S = -ln[\frac{L(f_i^V = 0, \hat{\boldsymbol{\eta}})}{L_{best}}] \tag{6.11}$$

where f_i^V are the anomalous coupling parameters and η the nuisance parameters.

[4] The observed (symmetrised) limits if only two bins are considered i.e [0-380][380-∞] are: 0.0047, 0.0041, 0.0048 and 0.0041, for the couplings f_4^γ, f_4^Z, f_5^γ and f_5^Z, respectively

[5] The observed (symmetrised) limits when no EW corrections are applied to the SM prediction for the nominal binning are : 0.0045, 0.0039, 0.0045 and 0.0039, for the couplings f_4^γ, f_4^Z, f_5^γ and f_5^Z, respectively

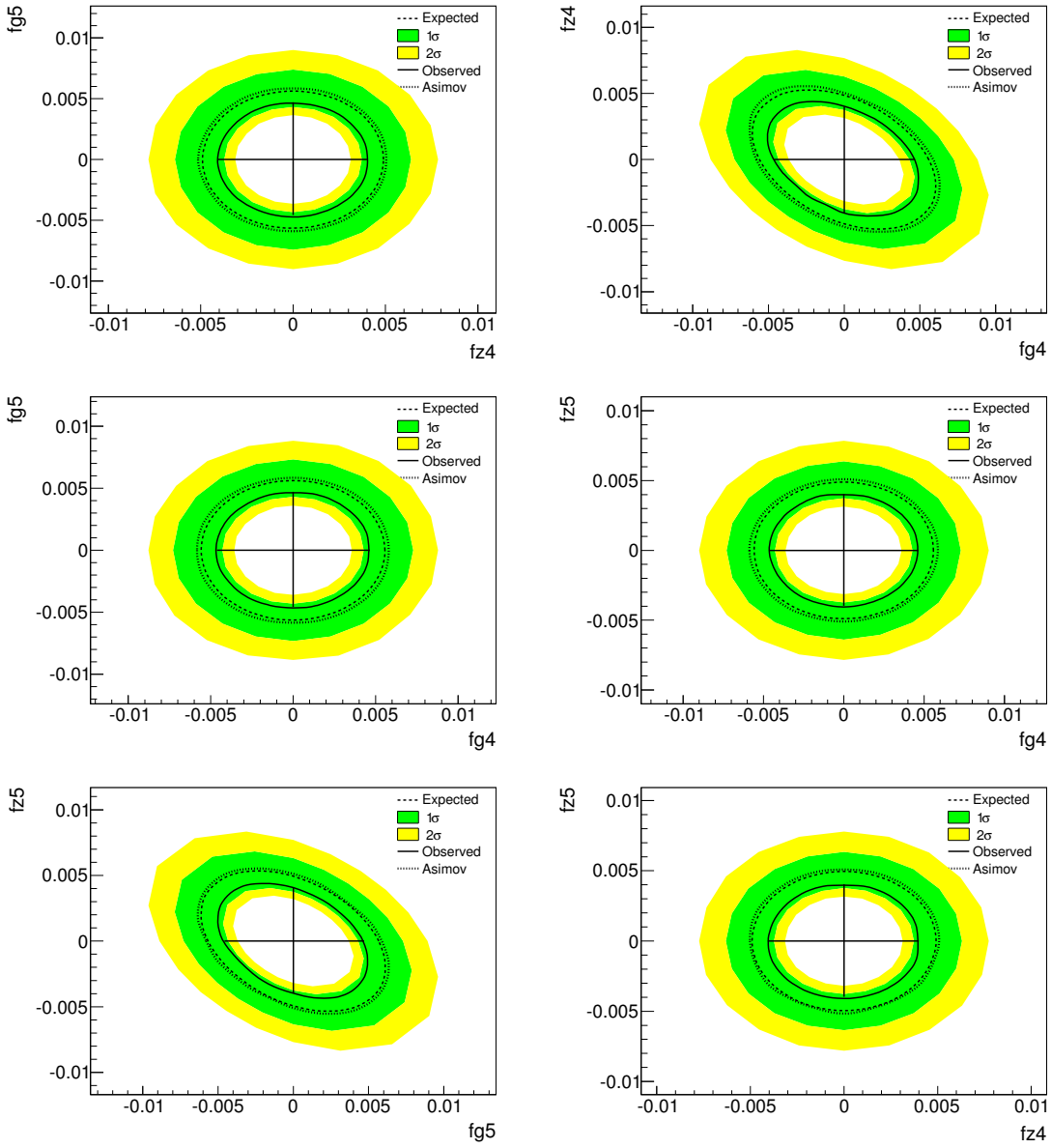

Figure 6.13: 2D limits.

$L(f = 0, \hat{\boldsymbol{\eta}})$ is the likelihood value for a fit of N_{obs} with N_{exp} for which all the coupling parameters are set to 0, and the nuisance parameters are let free to vary. L_{best} is the best value the likelihood can have, and it is obtained by setting the N_{exp} equal to the observation N_{obs}. First one computes the S_{obs} for the observed data. Then, 100K pseudo-experiments are performed, each one for N'_{obs} generated from a Poissonian PDF with a mean value equal to the SM prediction. The S' is computed for all pseudo-experiments according to 6.11. The p-value is the number of pseudo-experiments having $S' > S_{obs}$ over the total number of pseudo-experiments.

The data yields and predictions for the optimal binning, as described in section 6.4.1, indicate an uneven distribution of the data with respect to the expected events. This is reflected in the p-value that was found to be about 7% [6]. The left plot in figure 6.14 shows the distribution of S', while the right plot shows the cumulative distribution of the same quantity. In both plots the dashed straight line represents the S_{obs} position and the solid curve is the χ^2 asymptotic law for four (number of bins) degrees of freedom.

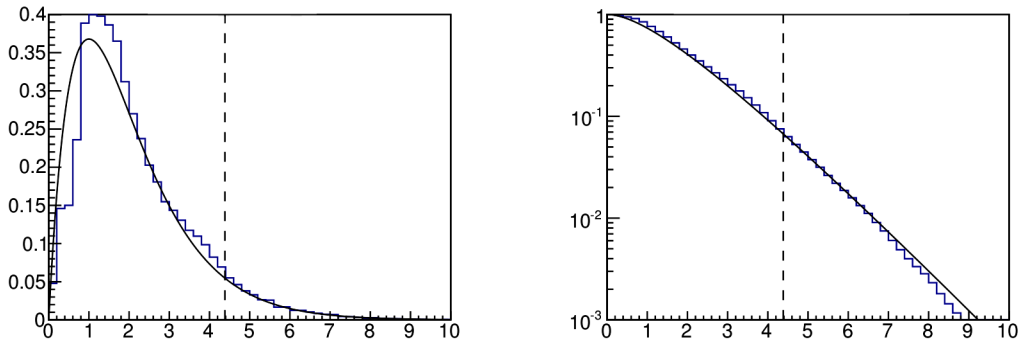

Figure 6.14: S' distribution (left) and S' cumulative distribution (right). The position of the S_{obs} with respect to the pseudo experiments is indicated with a dashed line.

It is of great interest to investigate the impact of the systematic uncertainties on the limits and the fit p-value. In order to estimate this contribution, the optimal binning is used and the limits are extracted for all systematic sources deactivated. The statistical error on the signal MC and the backgrounds are considered as systematic uncertainties. Therefore, this estimation will only take in account the error due to limited data statistics.

In table 6.7 the limits on the f_4^γ coupling are shown in the two cases, i.e when

[6] It is interesting to note that the bin configuration having a third bin lower boundary at 280 GeV instead of 260 GeV have been tested and yield a 30% p-value

configuration	Expected	Observed	p-value
Systematics ON	[-0.0056, 0.0056] , $\sigma = \pm$ 0.0014	[-0.0046, 0.0046]	≈7%
Systematics OFF	[-0.0055, 0.0055] , $\sigma = \pm$ 0.0014	[-0.0048, 0.0047]	≈6%

Table 6.7: Comparison of the nominal observed and expected limits with limits obtained when systematics are turned off.

the systematics are taken into account in the fit and when they are not [7]. As it is supposed to happen, the expected limits are getting tighter when the systematic uncertainties are turned off. Though, the improvement is very small, of the order of 2%, because the statistical error is by far the dominant one. A very interesting feature is seen on the observed limits where the limits are getting looser of about 4% when the systematic uncertainties are turned off. Such uncommon behavior can be the outcome of specific data configuration. In this analysis, the phenomenon is due to the discrepancy between the expectation (SM+Bkgd) and the observation in the first bin. There are about 295 expected events for 316 observed. As the first bin is not sensitive to the aTGCs it can not regulate this discrepancy by adjusting the f_i^V parameters and thus this is done by pulling the nuisance parameters to high values. As the systematics are correlated between the bins, the trend in the first bin causes the rise of the expected number of events in the last bin. This amplifies the data-prediction discrepancy, and hence results to tighter limits. Nonetheless, this strange data behavior is covered by the large 1 σ width of the expected distribution which reaches 25% of the limit value.

Besides the change in the observed and expected limit values, the quality of the fit also changes. The p-value drops from 7% down to 5.8%. This is foreseen, since by deactivating the nuisance parameters the fit looses its flexibility to adjust the expectation with the observation.

Limit precision

In the previous sub-section it was shown that the impact of the systematic uncertainties is small, of the order of 2% for the expected limits and -4% for the observed limits. It is interesting to compare these small variations with the numerical precision of the limit. The major reason which could affect the numerical result on the observed or the Asimov limits is the seed value of the random generator. The seed value is used for the generation of the 10K pseudo-experiments that are needed for the estimation of the p-value of a test parameter, f^{test}. In order to estimate the

[7] It has been shown that all couplings have the same behavior and thus the study is performed on one coupling, the f_4^γ

impact of the seed choice, the observed limits have been re-extracted for 1K different seed values. The obtained 1K limits *lower* and *upper ends* are shown in figure 6.15. The 1σ width of both distributions is about 0.00004, i.e approximately 1% of the limit value. This result indicates that the quoted limits should not contain more than four digits.

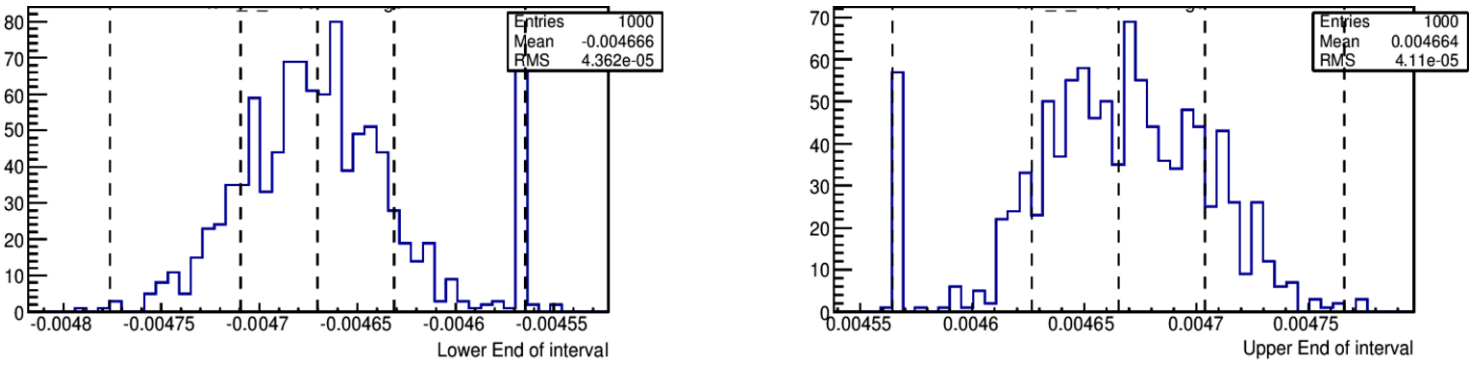

Figure 6.15: Distribution of the lower and upper interval ends of the observed limits for modified seed values of the random generator.

6.5.2 Expected and Observed limits on C_i

In the first chapter of this document the relations between the anomalous coupling parameters f_i^V and the Effective Field Theory parameters, C_i, have been presented. Thanks to these relations one can express the existing $N_{exp}(f_i^V)$ parametrisation, described in section 6.2.1, in terms of the C_i parameters, $N_{exp}(C_i)$. Here, the C_i parameters have been fitted, each one independently of the other. The results are shown in table 6.8.

Among the four parameters, only the $C_{\tilde{B}W}/\Lambda^4$ could have been directly computed using the f_5^γ results as these two parameters have a 1-1 relation. The remaining three parameters have dependencies on two neutral anomalous coupling parameters, among which the h_1^V parameters associated to the vertex $VZ\gamma$. Hence, only a direct fit can provide limits on the C_i parameters.

6.6 Results as a function of Λ

In this section the observed and expected limits as a function of the cutoff scale for $n = 3$ will be presented. Only two bins will be considered since the optimization

Parameter	Observed	Expected
$C_{\tilde{B}W}/\Lambda^4$	[-15.53 , 15.65]	[-18.86$^{+4.48}_{-5.53}$, 18.87$^{+5.55}_{-4.47}$]
C_{BB}/Λ^4	[-7.98 , 7.83]	[-9.53$^{+2.24}_{-2.72}$, 9.52$^{+2.71}_{-2.24}$]
C_{BW}/Λ^4	[-8.43 , 8.56]	[-10.34$^{+2.45}_{-3.12}$, 10.35$^{+3.12}_{-2.43}$]
C_{WW}/Λ^4	[-7.07 , 7.17]	[-8.57$^{+1.95}_{-2.73}$, 8.60$^{+2.71}_{-1.95}$]

Table 6.8: Observed and expected limits on the C_i/Λ^4 parameters.

studies have shown that adding more bins does not importantly improve the limits. The boundary between the two bins for the various Λ values is taken from the "Educative guess" approach, see table 6.2. As the bin boundary for all Λ choices lies in a narrow region, between 280 and 380, to a good approximation one can assume that the uncertainties on each bin will have the same values for all Λ bin configurations. More specifically, the systematics of the first bin are taken from the first column of table 6.5, while the systematics of the second bin are taken from the last column of the same table. The above assumption is valid as it was shown that the systematic uncertainties have a very small impact on the limit, and thus small inaccuracies on their values are not expected to affect the results.

Figure 6.16 shows the value of the limit as a function of the Λ scale. The solid black line is the observed limit while the dashed black line is the expected limit. The green band represents the 1σ width of the expected value, while the yellow band represents the 2σ width. The red line represents the unitarity bound above which the unitarity is violated. This curve was computed according to the formulas 1.17 and 1.18 for the f_i^γ and f_i^Z couplings, respectively. These plots indicate that the limits we quote for Λ above 5 TeV does not have physical meaning as they have values violating unitarity.

6.7 Assessment of the results

In this last section the limits on the coupling parameters shown in sec. 6.5 are compared to the ATLAS limits obtained using the 2011 7 TeV data and also with the latest CMS 8 TeV results.

In table 6.9 the limits on the f_i^V coupling parameters extracted in this document (first row) for the case where no form factor is used, are compared to the ATLAS

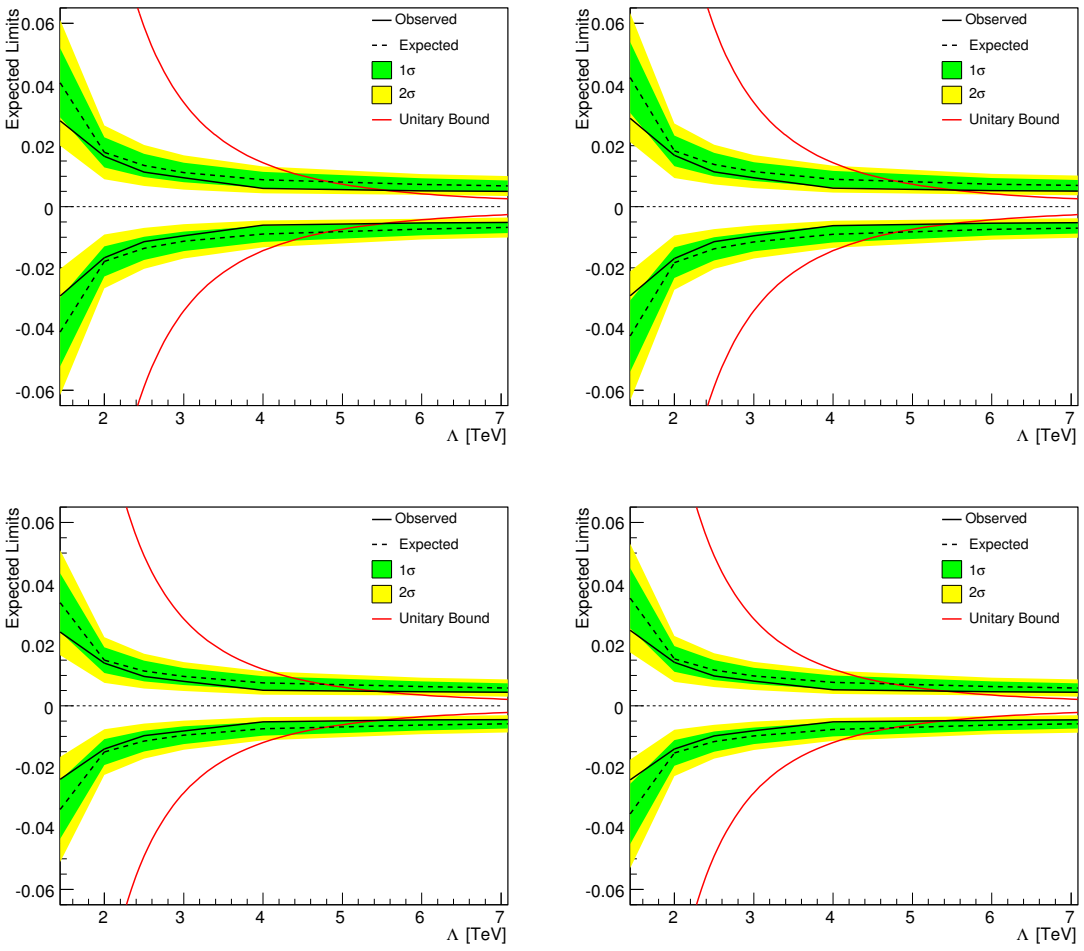

Figure 6.16: Expected and observed limits as a function of the Λ scale. Top left plot is for the f_4^γ coupling, top right plot is for the f_5^γ, bottom left plot is for the f_4^Z and bottom right plot is for the f_5^z coupling.

combined (4l and 2l2ν) [8] 7 TeV limits [37]. The present limits are found to be about 3.3 times tighter than the ATLAS combined.

In the third row of the same table, the CMS 8 TeV limits using the 4l final state are presented [93]. The comparison between our limits and CMS limits is straight forward as in both cases the limits are extracted using the same channel. One observes that the results are compatible.

Limits on the C_i EFT parameters shown in this document are extracted for the first time within the LHC collaborations and thus no comparison can be performed.

coupling $\Lambda = \infty$	f_4^γ	f_4^Z	f_5^γ	f_5^Z
4l 8 TeV	[-0.0046, 0.0046]	[-0.0041, 0.0040]	[-0.0046, 0.0047]	[-0.0040, 0.0040]
ATLAS combined 7 TeV	[-0.015, 0.015]	[-0.013, 0.013]	[-0.016, 0.015]	[-0.013, 0.013]
CMS 4l 8 TeV	[-0.004, 0.004]	[-0.004, 0.004]	[-0.005, 0.005]	[-0.005, 0.005]

Table 6.9: Observed limits for 8 TeV data as computed in this document, ATLAS combined (4l and 2l2ν) 7 TeV limits and CMS 4l 8 TeV limits.

[8] The exclusive 4l 7 TeV limits are not available for comparison

Conclusions

In the context of this thesis two main studies have been conducted. In chronological order, the first one was an assessment of the Toroid magnetic field sensors, and the second was the study of the production of pairs of Z bosons. Conclusions on the sensor assessment studies have been given in section 3.9

The on-shell ZZ diboson process has been probed in the leptonic decay channel using 20 fb^{-1} of data, collected by the ATLAS detector during 2012, at a center of mass energy of 8 TeV. The very clean final state signature allows a precise test of the Standard Model. However, the small cross section of the ZZ process, of 7.06± 0.25 pb (NLO MCFM) at a CME of 8 TeV, results to a measurement that is expected to be still statistically limited. For this reason, the analysis strategy was to maximise the acceptance by including all types of leptons that can be potentially detected by the ATLAS detector, i.e in a pseudorapidity range up to 4.9 for electrons and up to 2.7 for muons. There have been 321 ZZ candidates observed, with a background prediction of the order of 17 events.

The total ZZ on-shell cross section measurement is:

$$6.98^{+0.42}_{-0.40}(stat.)^{+0.38}_{-0.33}(syst.)^{+0.20}_{-0.19}(lumi.) \quad pb \tag{6.12}$$

which is compatible with the NLO MCFM prediction. The statistical uncertainty is still of the same order as the total systematic uncertainty. The measurements performed using the data from each decay channel separately are also in agreement with the theory predictions within uncertainties. The cross section measurement was also performed in a "fiducial", close to the reconstruction, volume for each decay channel. The results are again in agreement with the theory predictions.

The study of the neutral triple gauge couplings is of great interest, as these are forbidden within the Standard Model. Thus, any sign of anomalous TGC will provide evidence for the existence of new physics. Here, 95% CL limits have been extracted on the anomalous coupling parameters, of both frameworks introducing the aTGCs, f_i^V and C_i/Λ^4.

The limits on the f_i^V have been extracted as a function of the Λ scale. For the case where $\Lambda = \infty$ (no form factor) the limits are:

$$\text{-}0.0046 < f_4^\gamma < 0.0046, \qquad \text{-}0.0041 < f_4^Z < 0.0040$$
$$\text{-}0.0046 < f_5^\gamma < 0.0047, \qquad \text{-}0.0040 < f_5^Z < 0.0040$$

The limits on the C_i/Λ^4 parameters are:

$$\text{-}15.53 < C_{\tilde{B}W}/\Lambda^4 < 15.65, \qquad \text{-}7.98 < C_{BB}/\Lambda^4 < 7.83$$
$$\text{-}8.43 < C_{BW}/\Lambda^4 < 8.56, \qquad \text{-}7.07 < C_{WW}/\Lambda^4 < 7.17$$

All the limits on the aTGC parameters have been found to be compatible with the SM.

Appendix A

MC samples

MC sampels

MCID	Process	Generator	PDF	k-factor	ϵ_{filter}	cross section [pb]
126937	$ZZ \to eeee$	PowhegBox	CT10	1	0.91	0.077
126938	$ZZ \to ee\mu\mu$	PowhegBox	CT10	1	0.83	0.176
126939	$ZZ \to ee\tau\tau$	PowhegBox	CT10	1	0.58	0.175
126940	$ZZ \to \mu\mu\mu\mu$	PowhegBox	CT10	1	0.91	0.077
126941	$ZZ \to \mu\mu\tau\tau$	PowhegBox	CT10	1	0.59	0.175
126942	$ZZ \to \tau\tau\tau\tau$	PowhegBox	CT10	1	0.11	0.077
116601	$gg \to VV \to eeee$	gg2VV	CT10	1	1.00	0.003
116602	$gg \to VV \to \mu\mu\mu\mu$	gg2VV	CT10	1	1.00	0.003
116603	$gg \to VV \to eee\mu\mu$	gg2VV	CT10	1	1.00	0.012
		Other signal samples				
161962	$ZZ \to \ell\ell\ell'\ell'$	Sherpa	CT10	1	1.00	0.777
146903	$ZZ \to \ell\ell\ell'\ell'$	Pythia 8	CTEQ6L1	1	1.00	0.114

Table A.1: The ZZ signal used in this analysis.

MCID	Process	Generator	PDF	k-factor	ϵ_{filter}	cross section [pb]
147285	MPI Z + Z	Pythia	CTEQ6L1	1	0.054	0.213
119353	ttbarW	MadGraphPythia	CTEQ6L1	1.175	1	0.104
119355	ttbarZ	MadGraphPythia	CTEQ6L1	1.35	1	0.0677
119583	ttbarWW	MadGraphPythia	CTEQ6L1	2.07	1	0.0009
167007	ZWWStar_lllnulnu	MadGraphPythia	CTEQ6L1	1	1	0.0016
167008	ZZZStar_nunullll	MadGraphPythia	CTEQ6L1	1	1	0.0003

Table A.2: Irreducible MC datasets used as background samples.

MCID	Process	Generator	PDF	k-factor	ϵ_{filter}	cross section [pb]
108343	SingleTopSChanWenu	McAtNlo+Herwig	CT10	1.00	1.00	0.564
108344	SingleTopSChanWmunu	McAtNlo+Herwig	CT10	1.00	1.00	0.564
108345	SingleTopSChanWtaunu	McAtNlo+Herwig	CT10	1.00	1.00	0.564
117360	singletop_tchan_e	AcerMC+Pythia	CTEQ6L1	1.00	1.00	9.48
117361	singletop_tchan_mu	AcerMC+Pythia	CTEQ6L1	1.00	1.00	9.48
117362	singletop_tchan_tau	AcerMC+Pythia	CTEQ6L1	1.00	1.00	9.48
110001	ttbar_dilepton	McAtNlo+Herwig	CT10	1.15	1.00	21.81
129477	WZ_Wm11Z11	Powheg+Pythia8	CT10	1.00	0.295	1.407
129478	WZ_Wm11Z13	Powheg+Pythia8	CT10	1.00	0.352	0.938
129479	WZ_Wm11Z15	Powheg+Pythia8	CT10	1.00	0.167	0.175
129480	WZ_Wm13Z11	Powheg+Pythia8	CT10	1.00	0.294	1.399
129481	WZ_Wm13Z13	Powheg+Pythia8	CT10	1.00	0.351	0.954
129482	WZ_Wm13Z15	Powheg+Pythia8	CT10	1.00	0.169	0.175
129483	WZ_Wm15Z11	Powheg+Pythia8	CT10	1.00	0.143	1.399
129484	WZ_Wm15Z13	Powheg+Pythia8	CT10	1.00	0.183	0.938
129485	WZ_Wm15Z15	Powheg+Pythia8	CT10	1.00	0.585	0.172
129486	WZ_W11Z11	Powheg+Pythia8	CT10	1.00	0.297	0.980
129487	WZ_W11Z13	Powheg+Pythia8	CT10	1.00	0.353	0.639
129488	WZ_W11Z15	Powheg+Pythia8	CT10	1.00	0.160	0.113
129489	WZ_W13Z11	Powheg+Pythia8	CT10	1.00	0.298	0.936
129490	WZ_W13Z13	Powheg+Pythia8	CT10	1.00	0.354	0.649
129491	WZ_W13Z15	Powheg+Pythia8	CT10	1.00	0.160	0.113
129492	WZ_W15Z11	Powheg+Pythia8	CT10	1.00	0.148	0.936
129493	WZ_W15Z13	Powheg+Pythia8	CT10	1.00	0.187	0.639
129494	WZ_W15Z15	Powheg+Pythia8	CT10	1.00	0.057	0.111
126928	WpWm_ee	Powheg+Pythia8	CT10	1.0	1.00	0.62
126929	WpWm_me	Powheg+Pythia8	CT10	1.0	1.00	0.62
126930	WpWm_te	Powheg+Pythia8	CT10	1.0	1.00	0.62
126931	WpWm_em	Powheg+Pythia8	CT10	1.0	1.00	0.62
126932	WpWm_mm	Powheg+Pythia8	CT10	1.0	1.00	0.62
126933	WpWm_tm	Powheg+Pythia8	CT10	1.0	1.00	0.62
126934	WpWm_et	Powheg+Pythia8	CT10	1.0	1.00	0.62
126935	WpWm_mt	Powheg+Pythia8	CT10	1.0	1.00	0.62
126936	WpWm_tt	Powheg+Pythia8	CT10	1.0	1.00	0.62
146430	WgammaNp0	Photos+Herwig	CTEQ6L1	1.15	1.00	230.09
146431	WgammaNp1	Photos+Herwig	CTEQ6L1	1.15	1.00	59.34
146432	WgammaNp2	Photos+Herwig	CTEQ6L1	1.15	1.00	21.47
146433	WgammaNp3	Photos+Herwig	CTEQ6L1	1.15	1.00	7.10
146434	WgammaNp4	Photos+Herwig	CTEQ6L1	1.15	1.00	2.12
146435	WgammaNp5	Photos+Herwig	CTEQ6L1	1.15	1.00	0.466
145161	Zeegamma	Sherpa	CT10	1	1	32.26
145162	Zmumugamma	Sherpa	CT10	1	1	32.32
126854	Ztautaugamma	Sherpa	CT10	1	1	32.33

Table A.3: Top and Diboson MC datasets used as background samples.

MCID	Process	Generator	PDF	k-factor	ϵ_{filter}	cross section [pb]
117650	ZeeNp0	Alpgen+Pythia	CTEQ6L1	1.18	1.00	718.890
117651	ZeeNp1	Alpgen+Pythia	CTEQ6L1	1.18	1.00	175.600
117652	ZeeNp2	Alpgen+Pythia	CTEQ6L1	1.18	1.00	58.849
117653	ZeeNp3	Alpgen+Pythia	CTEQ6L1	1.18	1.00	15.560
117654	ZeeNp4	Alpgen+Pythia	CTEQ6L1	1.18	1.00	3.932
117655	ZeeNp5	Alpgen+Pythia	CTEQ6L1	1.18	1.00	1.199
117660	ZmumuNp0	Alpgen+Pythia	CTEQ6L1	1.18	1.00	718.910
117661	ZmumuNp1	Alpgen+Pythia	CTEQ6L1	1.18	1.00	175.810
117662	ZmumuNp2	Alpgen+Pythia	CTEQ6L1	1.18	1.00	58.805
117663	ZmumuNp3	Alpgen+Pythia	CTEQ6L1	1.18	1.00	15.589
117664	ZmumuNp4	Alpgen+Pythia	CTEQ6L1	1.18	1.00	3.907
117665	ZmumuNp5	Alpgen+Pythia	CTEQ6L1	1.18	1.00	1.193
117670	ZtautauNp0	Alpgen+Pythia	CTEQ6L1	1.18	1.00	718.850
117671	ZtautauNp1	Alpgen+Pythia	CTEQ6L1	1.18	1.00	175.830
117672	ZtautauNp2	Alpgen+Pythia	CTEQ6L1	1.18	1.00	58.630
117673	ZtautauNp3	Alpgen+Pythia	CTEQ6L1	1.18	1.00	15.508
117674	ZtautauNp4	Alpgen+Pythia	CTEQ6L1	1.18	1.00	3.953
117675	ZtautauNp5	Alpgen+Pythia	CTEQ6L1	1.18	1.00	1.181
110817	ZeebbNp0	Alpgen+Pythia	CTEQ6L1	1.15	1.00	8.040
110818	ZeebbNp1	Alpgen+Pythia	CTEQ6L1	1.15	1.00	3.235
110819	ZeebbNp2	Alpgen+Pythia	CTEQ6L1	1.15	1.00	1.139
110820	ZeebbNp3	Alpgen+Pythia	CTEQ6L1	1.15	1.00	0.491
110821	ZmumubbNp0	Alpgen+Pythia	CTEQ6L1	1.15	1.00	8.042
110822	ZmumubbNp1	Alpgen+Pythia	CTEQ6L1	1.18	1.00	3.216
110823	ZmumubbNp2	Alpgen+Pythia	CTEQ6L1	1.18	1.00	1.140
110824	ZmumubbNp3	Alpgen+Pythia	CTEQ6L1	1.18	1.00	0.509
110825	ZtautaubbNp0	Alpgen+Pythia	CTEQ6L1	1.18	1.00	8.036
110826	ZtautaubbNp1	Alpgen+Pythia	CTEQ6L1	1.18	1.00	3.230
110827	ZtautaubbNp2	Alpgen+Pythia	CTEQ6L1	1.18	1.00	1.145
110828	ZtautaubbNp3	Alpgen+Pythia	CTEQ6L1	1.18	1.00	0.493
117680	WenuNp0	Alpgen+Pythia	CTEQ6L1	1.19	1.00	8136.800
117681	WenuNp1	Alpgen+Pythia	CTEQ6L1	1.19	1.00	1791.500
117682	WenuNp2	Alpgen+Pythia	CTEQ6L1	1.19	1.00	541.600
117683	WenuNp3	Alpgen+Pythia	CTEQ6L1	1.19	1.00	146.650
117684	WenuNp4	Alpgen+Pythia	CTEQ6L1	1.19	1.00	37.334
117685	WenuNp5	Alpgen+Pythia	CTEQ6L1	1.19	1.00	11.355
117690	WmunuNp0	Alpgen+Pythia	CTEQ6L1	1.19	1.00	8133.400
117691	WmunuNp1	Alpgen+Pythia	CTEQ6L1	1.19	1.00	1792.700
117692	WmunuNp2	Alpgen+Pythia	CTEQ6L1	1.19	1.00	541.270
117693	WmunuNp3	Alpgen+Pythia	CTEQ6L1	1.19	1.00	146.490
117694	WmunuNp4	Alpgen+Pythia	CTEQ6L1	1.19	1.00	37.341
117695	WmunuNp5	Alpgen+Pythia	CTEQ6L1	1.19	1.00	11.364
117700	WtaunuNp0	Alpgen+Pythia	CTEQ6L1	1.19	1.00	8135.700
117702	WtaunuNp2	Alpgen+Pythia	CTEQ6L1	1.19	1.00	541.240
117703	WtaunuNp3	Alpgen+Pythia	CTEQ6L1	1.19	1.00	146.480
117704	WtaunuNp4	Alpgen+Pythia	CTEQ6L1	1.19	1.00	37.344
117705	WtaunuNp5	Alpgen+Pythia	CTEQ6L1	1.19	1.00	11.477
126601	WcNp0	Alpgen+Pythia	CTEQ6L1	1.19	1.00	758.930
126602	WcNp1	Alpgen+Pythia	CTEQ6L1	1.19	1.00	274.240
126603	WcNp2	Alpgen+Pythia	CTEQ6L1	1.19	1.00	71.634
126604	WcNp3	Alpgen+Pythia	CTEQ6L1	1.19	1.00	16.425
126605	WcNp4	Alpgen+Pythia	CTEQ6L1	1.19	1.00	4.747
126606	WccNp0	Alpgen+Pythia	CTEQ6L1	1.19	1.00	143.070
126607	WccNp1	Alpgen+Pythia	CTEQ6L1	1.19	1.00	143.680
126608	WccNp2	Alpgen+Pythia	CTEQ6L1	1.19	1.00	80.762
126609	WccNp3	Alpgen+Pythia	CTEQ6L1	1.19	1.00	35.932
110801	WbbNp0	Alpgen+Pythia	CTEQ6L1	1.15	1.00	52.255
110802	WbbNp1	Alpgen+Pythia	CTEQ6L1	1.15	1.00	45.540
110803	WbbNp2	Alpgen+Pythia	CTEQ6L1	1.15	1.00	23.671

Table A.4: MC datasets for Z+jets and W+jets.

Bibliography

[1] S. Protopapadaki, L. Chevalier, A. Formica, and J. Laporte, *B-field sensors assessment, B-map study, sensors monitoring*, Tech. Rep. ATL-COM-MUON-2012-027, CERN, Geneva, Nov, 2012.

[2] N. Benekos, R. Caputo, S. Chouridou, N. Edwards, C. Gumpert, G. Hesketh, D. Iliadis, E. Jansen, S. Kaneti, K. Kordas, V. Kouskoura, D. Kyriazopoulos, J. Laporte, B. Li, Z. Liang, J. Manjarres, A. Mangarelli, H. Merritt, J. Meyer, D. Moreno, J. Moss, I. Nomidis, A. Oh, A. Ouraou, C. Petridou, E. Protopapadaki, P. Sommer, D. Su, P. Ward, L. Xu, H. Yang, B. Zhou, and Z. Zhao, *Measurement of the total ZZ production cross section in proton-proton collisions at $\sqrt{s} = 8$ TeV using the llll decay channel with the ATLAS detector*, Tech. Rep. ATL-COM-PHYS-2013-142, CERN, Geneva, Feb, 2013.

[3] N. Benekos, R. Caputo, S. Chouridou, N. Edwards, G. Hesketh, D. Iliadis, E. Jansen, S. Kaneti, K. Kordas, V. Kouskoura, D. Kyriazopoulos, J. Laporte, B. Li, Z. Liang, J. Manjarres, A. Mangarelli, H. Merritt, J. Meyer, D. Moreno, J. Moss, I. Nomidis, A. Oh, A. Ouraou, C. Petridou, E. Protopapadaki, D. Su, P. Ward, L. Xu, H. Yang, B. Zhou, and Z. Zhao, *Measurement of the total ZZ production cross section in proton-proton collisions at $\sqrt{s} = 8$ TeV in 20 fb^{-1} with the ATLAS detector*, Tech. Rep. ATLAS-COM-CONF-2013-020, CERN, Geneva, Feb, 2013.

[4] F. Halzen and A. D. Martin, *Quarks and Leptons*, Wiley, 1985.

[5] W. N. Cottinghamand and D. A. Greenwood, *An Introduction to the Standard Model of Particle Physics*, Cambridge university press, 1988.

[6] D. Griffiths, *Introduction to Elementary Particles*, Wiley, 2008.

[7] F. Englert and R. Brout, *Broken Symmetry and the Mass of Gauge Vector Mesons*, Phys.Rev.Lett. **13** (1964) 321–323.

[8] P. W. Higgs, *Broken Symmetries and the Masses of Gauge Bosons*, Phys.Rev.Lett. **13** (1964) 508–509.

[9] R. Brout and F. Englert, *Spontaneous symmetry breaking in gauge theories: A Historical survey*, `arXiv:hep-th/9802142 [hep-th]`.

[10] F. L. Wilson, *Fermi's theory of Beta Decay*, AJP **36** (1968) .

[11] C. Wu, E. Ambler, R. Hayward, D. Hoppes, and R. Hudson, *Experimental Test of Parity Conservation in Beta Decay*, Phys.Rev. **105** (1957) 1413–1414.

[12] ALEPH Collaboration, DELPHI Collaboration, L3 Collaboration, OPAL Collaboration, LEP Electroweak Working Group Collaboration, J. Alcaraz et al., *A Combination of Preliminary Electroweak Measurements and Constraints on the Standard Model, 2006*, Tech. Rep. hep-ex/0612034. ALEPH-2006-001 PHYSICS-2006-001. CERN-L3-310. CERN-PH-EP-2006-042. DELPHI-2006-014 PHYS-948. L3-Note-2833. LEPEWWG-2006-01. OPAL-PR-419, CERN, Geneva, Dec, 2006.

[13] CDF Collaboration, D0 Collaboration Collaboration, T. E. W. Group, *2012 Update of the Combination of CDF and D0 Results for the Mass of the W Boson*, `arXiv:1204.0042 [hep-ex]`.

[14] Particle Data Group Collaboration, J. Beringer et al., *Review of Particle Physics (RPP)*, Phys.Rev. **D86** (2012) 010001.

[15] ALEPH Collaboration, DELPHI Collaboration, L3 Collaboration, OPAL Collaboration, LEP Electroweak Working Group Collaboration, *A Combination of preliminary electroweak measurements and constraints on the standard model*, `arXiv:hep-ex/0511027 [hep-ex]`.

[16] J. D. Lykken, *Beyond the Standard Model*, `arXiv:1005.1676 [hep-ph]`.

[17] D. E. Morrissey, T. Plehn, and T. M. Tait, *Physics searches at the LHC*, Phys.Rept. **515** (2012) 1–113, `arXiv:0912.3259 [hep-ph]`.

[18] J. Hewett, T. Takeuchi, and S. D. Thomas, *Indirect probes of new physics*, `arXiv:hep-ph/9603391 [hep-ph]`.

[19] K. Hagiwara, R. Peccei, D. Zeppenfeld, and K. Hikasa, *Probing the Weak Boson Sector in e+ e- -> W+ W-*, Nucl.Phys. **B282** (1987) 253.

[20] K. Gaemers and G. Gounaris, *Polarization amplitudes for e+ e- -> W+ W- and e+ e- -> ZZ*, Zeitschrift fur Physik C Particles and Fileds **1** (1979) no. 3, 259–268. `http://dx.doi.org/10.1007/BF01440226`.

[21] W.-Y. Keung, I. Low, and J. Shu, *Landau-Yang Theorem and Decays of a Z' Boson into Two Z Bosons*, Phys.Rev.Lett. **101** (2008) 091802, `arXiv:0806.2864 [hep-ph]`.

[22] U. Baur and E. L. Berger, *Probing the weak-boson sector in Z gamma production at hadron colliders*, Phys. Rev. D (1993) 4889. http://link.aps.org/doi/10.1103/PhysRevD.47.4889.

[23] U. Baur and D. L. Rainwater, *Probing neutral gauge boson selfinteractions in ZZ production at hadron colliders*, Phys.Rev. **D62** (2000) 113011, arXiv:hep-ph/0008063 [hep-ph].

[24] K. Hagiwara, S. Ishihara, R. Szalapski, and D. Zeppenfeld, *Low-energy effects of new interactions in the electroweak boson sector*, Phys.Rev. **D48** (1993) 2182–2203.

[25] J. Wudka, *Electroweak effective Lagrangians*, Int.J.Mod.Phys. **A9** (1994) 2301–2362, arXiv:hep-ph/9406205 [hep-ph].

[26] C. Degrande, N. Greiner, W. Kilian, O. Mattelaer, H. Mebane, et al., *Effective Field Theory: A Modern Approach to Anomalous Couplings*, Annals Phys. **335** (2013) 21–32, arXiv:1205.4231 [hep-ph].

[27] ATLAS Collaboration Collaboration, G. Aad et al., *Combined search for the Standard Model Higgs boson using up to 4.9 fb^{-1} of pp collision data at $\sqrt{s} = 7$ TeV with the ATLAS detector at the LHC*, Phys.Lett. **B710** (2012) 49–66, arXiv:1202.1408 [hep-ex].

[28] T. Corbett, O. Eboli, J. Gonzalez-Fraile, and M. Gonzalez-Garcia, *Robust Determination of the Higgs Couplings: Power to the Data*, Phys.Rev. **D87** (2013) 015022, arXiv:1211.4580 [hep-ph].

[29] T. Corbett, O. Eboli, J. Gonzalez-Fraile, and M. Gonzalez-Garcia, *Determining Triple Gauge Boson Couplings from Higgs Data*, Phys.Rev.Lett. **111** (2013) 011801, arXiv:1304.1151 [hep-ph].

[30] C. Degrande, *A basis of dimension-eight operators for anomalous neutral triple gauge boson interactions*, arXiv:1308.6323 [hep-ph].

[31] G. Gounaris, J. Layssac, and F. Renard, *New and standard physics contributions to anomalous Z and gamma selfcouplings*, Phys.Rev. **D62** (2000) 073013, arXiv:hep-ph/0003143 [hep-ph].

[32] ALEPH Collaboration Collaboration, D. Fayolle, J. Jousset, and B. Trocme, *Limits on anomalous neutral gauge couplings using data from ZZ and*

Zgamma production between 183-208 GeV, Tech. Rep. CERN-ALEPH-2001-061, CERN, Geneva, Jul, 2001.

[33] P. Bambade, G. Borissov, C. Matteuzzi, V. Verzi, L. Pieri, A. Baroncelli, E. Graziani, J. Rehn, I. Van Vulpen, M. Witek, and O. P. Yushchenko, *Study of Trilinear Gauge Boson Couplings, ZZZ, ZZv and Zvv*, Tech. Rep. DELPHI-2001-097-CONF-525. CERN-DELPHI-2001-097-CONF-525, CERN, Geneva, Jul, 2001.

[34] OPAL Collaboration Collaboration, G. Abbiendi et al., *Search for trilinear neutral gauge boson couplings in Z^- gamma production at $S^{(1/2)}$ = 189-GeV at LEP*, Eur.Phys.J. **C17** (2000) 553–566, arXiv:hep-ex/0007016 [hep-ex].

[35] ALEPH Collaboration, DELPHI Collaboration, L3 Collaboration, OPAL Collaboration, LEP Electroweak Working Group Collaboration, J. Alcaraz et al., *A Combination of preliminary electroweak measurements and constraints on the standard model*, arXiv:hep-ex/0612034 [hep-ex].

[36] CMS Collaboration Collaboration, S. Chatrchyan et al., *Measurement of the ZZ production cross section and search for anomalous couplings in 2l2l final states in pp collisions at $\sqrt{s} = 7$ TeV*, JHEP **1301** (2013) 063, arXiv:1211.4890 [hep-ex].

[37] ATLAS Collaboration Collaboration, G. Aad et al., *Measurement of ZZ production in pp collisions at $\sqrt{s} = 7$ TeV and limits on anomalous ZZZ and $ZZ\gamma$ couplings with the ATLAS detector*, JHEP **1303** (2013) 128, arXiv:1211.6096 [hep-ex].

[38] ATLAS Collaboration Collaboration, G. Aad et al., *Measurement of $W\gamma$ and $Z\gamma$ production cross sections in pp collisions at $\sqrt{s} = 7$ TeV and limits on anomalous triple gauge couplings with the ATLAS detector*, Phys.Lett. **B717** (2012) 49–69, arXiv:1205.2531 [hep-ex].

[39] CMS Collaboration Collaboration, S. Chatrchyan et al., *Measurement of the production cross section for $Z\gamma \to \nu\bar{\nu}\gamma$ in pp collisions at $\sqrt{s} = 7$ TeV and limits on $ZZ\gamma$ and $Z\gamma\gamma$ triple gauge boson couplings*, JHEP **1310** (2013) 164, arXiv:1309.1117 [hep-ex].

[40] J. M. Campbell, R. K. Ellis, and C. Williams, *Vector boson pair production at the LHC*, JHEP **1107** (2011) 018, arXiv:1105.0020 [hep-ph].

[41] The ATLAS Collaboration et al., *Luminosity Determination in pp Collisions at sqrt(s)=7 TeV Using the ATLAS Detector at the LHC*, EPJC **J.C71:1630** (2011) .

[42] ATLAS Collaboration, G. Aad et al., *Improved luminosity determination in pp collisions at $\sqrt{s}$ = 7 TeV using the ATLAS detector at the LHC*, Eur.Phys.J. **C73** (2013) 2518, `arXiv:1302.4393 [hep-ex]`.

[43] *Design and Development of the ATLAS Central Solenoid Magnet*, http://cds.cern.ch/record/404719/files/cer-000331439.pdf (1999) .

[44] ATLAS Collaboration Collaboration, *ATLAS calorimeter performance: Technical Design Report*. Technical Design Report ATLAS. CERN, Geneva, 1996.

[45] ATLAS Collaboration Collaboration, *ATLAS muon spectrometer: Technical Design Report*. Technical Design Report ATLAS. CERN, Geneva, 1997. distribution.

[46] T. Nikitina and F. Bergsma, *A program to calculate the ATLAS magnetic field*, Tech. Rep. ATL-MAGNET-2001-002, CERN, Geneva, Apr, 2001.

[47] *Vector Fields Limited, The TOSCA Reference Manual*, tech. rep., 24 Bankside, Kidlington, Oxford, OX5 1JE, England.

[48] The ATLAS Collaboration et al., *Muon Spectrometer technical design report, chapter 1, Overview*, http://atlasinfo.cern.ch/Atlas/GROUPS/MUON/TDR/pdf_final/overview.pdf (1997) .

[49] The ATLAS Collaboration et al., *The ATLAS Experiment at the CERN Large Hadron Collider*, Journal of Instrumentation **JINST-3-S08003** (2008) .

[50] The ATLAS Collaboration et al., *Muon Spectrometer technical design report, chapter 10, Magnetic field measurement*, http://atlasinfo.cern.ch/Atlas/GROUPS/MUON/TDR/pdf_final/aux-systems.pdf (1997)
.

[51] F. Bergsma, *Hall probes: physics and application to magnetometry*, arxiv.org/pdf/1103.1271 (2008) .

[52] PF Giraud, A.Formica, F.Bauer, *Privet conversation*, .

[53] F. Bergsma, *Privet conversation*, .

[54] J.C. Barriere, F. Bauer, M. Fontaine, A. Formica, V. Gautard, P.F. Giraud, C. Guyot, R. Hart, S. Horvat, O. Kortner, S. Kotov, H. Kroha, F.Linde, P. Ponsot, I.Potrap, Ph. Schune, H. van der Graaf, *The alignment system of the ATLAS barrel muon spectrometer*, .

[55] G. Unal and D. Froidevaux, *Higgs mass measurements and uncertainties in 2011 and 2012 data*, Tech. Rep. ATL-COM-PHYS-2012-1774, CERN, Geneva, Dec, 2012.

[56] G. Artoni, M. Corradi, A. Dimitrievska, F. Sforza, N. Vranjes, and P. Fleischmann, *Muon momentum scale and resolution corrections evaluated with Z->mumu 2 and J/psi->mumu decays on Run I ATLAS data*, Tech. Rep. ATL-COM-MUON-2014-001, CERN, Geneva, Jan, 2014.

[57] R. Nicolaidou, L. Chevalier, S. Hassani, J. Laporte, E. Le Menedeu, et al., *Muon identification procedure for the ATLAS detector at the LHC using Muonboy reconstruction package and tests of its performance using cosmic rays and single beam data*, J.Phys.Conf.Ser. **219** (2010) 032052.

[58] S. Hassani, L. Chevalier, E. Lancon, J. Laporte, R. Nicolaidou, et al., *A muon identification and combined reconstruction procedure for the ATLAS detector at the LHC using the (MUONBOY, STACO, MuTag) reconstruction packages*, Nucl.Instrum.Meth. **A572** (2007) 77–79.

[59] ATLAS Collaboration Collaboration, G. Aad et al., *Measurement of the muon reconstruction performance of the ATLAS detector using 2011 and 2012 LHC proton-proton collision data*, `arXiv:1407.3935 [hep-ex]`.

[60] ATLAS Collaboration Collaboration, *Muon Momentum Resolution in First Pass Reconstruction of pp Collision Data Recorded by ATLAS in 2010*, Tech. Rep. ATLAS-CONF-2011-046, CERN, Geneva, Mar, 2011.

[61] ATLAS Collaboration Collaboration, *Expected electron performance in the ATLAS experiment*, Tech. Rep. ATL-PHYS-PUB-2011-006, CERN, Geneva, 2011.

[62] W. Lampl, S. Laplace, D. Lelas, P. Loch, H. Ma, S. Menke, S. Rajagopalan, D. Rousseau, S. Snyder, and G. Unal, *Calorimeter Clustering Algorithms:*

Description and Performance, Tech. Rep. ATL-LARG-PUB-2008-002. ATL-COM-LARG-2008-003, CERN, Geneva, Apr, 2008.

[63] *Electron efficiency measurements with the ATLAS detector using the 2012 LHC proton-proton collision data*, Tech. Rep. ATLAS-CONF-2014-032, CERN, Geneva, Jun, 2014.

[64] ATLAS Collaboration Collaboration, G. Aad et al., *Electron performance measurements with the ATLAS detector using the 2010 LHC proton-proton collision data*, Eur.Phys.J. **C72** (2012) 1909, `arXiv:1110.3174 [hep-ex]`.

[65] ATLAS Collaboration Collaboration, G. Aad et al., *Electron reconstruction and identification efficiency measurements with the ATLAS detector using the 2011 LHC proton-proton collision data*, Eur.Phys.J. **C74** (2014) 2941, `arXiv:1404.2240 [hep-ex]`.

[66] Z. Sullivan and E. L. Berger, *Isolated leptons from heavy flavor decays - theory and data*, Phys.Rev. **D82** (2010) 014001, `arXiv:1003.4997 [hep-ph]`.

[67] M. Woudstra, *Performance of the ATLAS muon trigger in p-p collisions at* $\sqrt{s} = 8$ *TeV*, Tech. Rep. ATL-DAQ-PROC-2013-034, CERN, Geneva, Nov, 2013.

[68] M. Wielers, R. Mantifel, A. Tricoli, and P. Bell, *Single Electron Trigger Performance Plots*, Tech. Rep. ATL-COM-DAQ-2012-146, CERN, Geneva, Jun, 2012.

[69] ATLAS Collaboration Collaboration, *Performance of the Electron and Photon Trigger in p-p Collisions at sqrt(s) = 7 TeV*, Tech. Rep. ATLAS-CONF-2011-114, CERN, Geneva, Aug, 2011.

[70] G. Piacquadio, K. Prokofiev, and A. Wildauer, *Primary vertex reconstruction in the ATLAS experiment at LHC*, J.Phys.Conf.Ser. **119** (2008) 032033.

[71] H.-L. Lai, M. Guzzi, J. Huston, Z. Li, P. M. Nadolsky, et al., *New parton distributions for collider physics*, Phys.Rev. **D82** (2010) 074024, `arXiv:1007.2241 [hep-ph]`.

[72] A. Martin, W. Stirling, R. Thorne, and G. Watt, *Parton distributions for the LHC*, Eur.Phys.J. **C63** (2009) 189–285, `arXiv:0901.0002 [hep-ph]`.

[73] H1 and ZEUS Collaboration Collaboration, F. Aaron et al., *Combined Measurement and QCD Analysis of the Inclusive e+- p Scattering Cross Sections at HERA*, JHEP **1001** (2010) 109, arXiv:0911.0884 [hep-ex].

[74] G. Moreno, C. Brown, W. Cooper, D. Finley, Y. Hsiung, et al., *Dimuon production in proton - copper collisions at $\sqrt{s}$ = 38.8-GeV*, Phys.Rev. **D43** (1991) 2815–2836.

[75] NuSea Collaboration Collaboration, E. Hawker et al., *Measurement of the light anti-quark flavor asymmetry in the nucleon sea*, Phys.Rev.Lett. **80** (1998) 3715–3718, arXiv:hep-ex/9803011 [hep-ex].

[76] NuSea Collaboration Collaboration, J. Webb et al., *Absolute Drell-Yan dimuon cross-sections in 800 GeV / c pp and pd collisions*, arXiv:hep-ex/0302019 [hep-ex].

[77] T. Melia, P. Nason, R. Rontsch, and G. Zanderighi, *W+W-, WZ and ZZ production in the POWHEG BOX*, JHEP **1111** (2011) 078, arXiv:1107.5051 [hep-ph].

[78] N. Kauer, *Interference effects for $H \to WW/ZZ \to \ell\bar{\nu}_\ell\bar{\ell}\nu_\ell$ searches in gluon fusion at the LHC*, JHEP **1312** (2013) 082, arXiv:1310.7011 [hep-ph].

[79] G. Passarino, *Higgs Interference Effects in $gg \to ZZ$ and their Uncertainty*, JHEP **1208** (2012) 146, arXiv:1206.3824 [hep-ph].

[80] T. Sjostrand, S. Mrenna, and P. Z. Skands, *A Brief Introduction to PYTHIA 8.1*, Comput.Phys.Commun. **178** (2008) 852–867, arXiv:0710.3820 [hep-ph].

[81] P. Golonka and Z. Was, *PHOTOS Monte Carlo: A precision tool for QED corrections in Z and W decays*, Eur. Phys. J. **C45** (2006) 97–107, hep-ph/0506026.

[82] A. Bierweiler, T. Kasprzik, and J. H. Kuhn, *Vector-boson pair production at the LHC to $\mathcal{O}(\alpha^3)$ accuracy*, JHEP **1312** (2013) 071, arXiv:1305.5402 [hep-ph].

[83] A. Bierweiler, T. Kasprzik, and J. H. Kuhn, *Electroweak accuracy in V-pair production at the LHC*, PoS **ICHEP2012** (2013) 078, arXiv:1208.3404 [hep-ph].

[84] S. Gieseke, T. Kasprzik, and J. H. Kuhn, *Vector-boson pair production and electroweak corrections in HERWIG++*, arXiv:1401.3964 [hep-ph].

[85] J. Meyer, *Reweighting method to incorporate higher order electroweak corrections into resonant heavy gauge boson pair production predictions*, Tech. Rep. ATL-COM-PHYS-2014-152, CERN, Geneva, Feb, 2014.

[86] F. Cascioli, T. Gehrmann, M. Grazzini, S. Kallweit, P. Maierhofer, et al., *ZZ production at hadron colliders in NNLO QCD*, arXiv:1405.2219 [hep-ph].

[87] G. Ordonez Sanz, *Muon identification in the ATLAS calorimeters.* PhD thesis, Nijmegen U., Amsterdam, 2009. Presented on 12 Jun 2009.

[88] D. Bourilkov, R. C. Group, and M. R. Whalley, *LHAPDF: PDF use from the Tevatron to the LHC*, arXiv:hep-ph/0605240 [hep-ph].

[89] ATLAS Collaboration Collaboration, *Measurement of the total ZZ production cross section in proton-proton collisions at $\sqrt{s}$ = 8 TeV in 20 fb^{-1} with the ATLAS detector*, Tech. Rep. ATLAS-CONF-2013-020, CERN, Geneva, Mar, 2013.

[90] T. Gleisberg, S. Hoeche, F. Krauss, M. Schonherr, S. Schumann, et al., *Event generation with SHERPA 1.1*, JHEP **0902** (2009) 007, arXiv:0811.4622 [hep-ph].

[91] F. James, *MINUIT Function Minimization and Error Analysis: Reference Manual Version 94.1*, .

[92] J.-F. Laporte et al., *https://laportej.web.cern.ch/laportej/Flit/doc/html/pages.html.*

[93] CMS Collaboration Collaboration, V. Khachatryan et al., *Measurement of the pp to ZZ production cross section and constraints on anomalous triple gauge couplings in four-lepton final states at $\sqrt{s}$ = 8 TeV*, arXiv:1406.0113 [hep-ex].

[94] U. Baur, T. Han, and J. Ohnemus, *QCD corrections and anomalous couplings in $Z\gamma$ production at hadron colliders*, Phys.Rev. **D57** (1998) 2823–2836, arXiv:hep-ph/9710416 [hep-ph].

[95] G. Bella, *Weighting Di-Boson Monte Carlo Events in Hadron Colliders*, arXiv:0803.3307 [hep-ph].

[96] G. J. Feldman and R. D. Cousins, *A Unified approach to the classical statistical analysis of small signals*, Phys.Rev. **D57** (1998) 3873–3889, arXiv:physics/9711021 [physics.data-an].

[97] G. Cowan, K. Cranmer, E. Gross, and O. Vitells, *Asymptotic formulae for likelihood-based tests of new physics*, Eur.Phys.J. **C71** (2011) 1554, arXiv:1007.1727 [physics.data-an].

Acknowledgements

First, I would like to warmly thank my PhD supervisor, Jean-François Laporte, for his support and guidance throughout these years, helping me to progress and become a better scientist. I deeply appreciate his motivation and willingness to share with me his vast knowledge on multiple subjects, during all the exciting conversations we had. I am also grateful to Laurent Chevalier for his co-supervision during my service task. His expertise on the ATLAS toroidal magnetic field illuminated our discussions. I would also like to thank Andrea Formica for helping me to collect all the data needed for the realisation of my service task, and Jean Ernwein for carefully going through the supporting document.

I thank the Particle Physics division (SPP) of the CEA Saclay for providing a workplace for my thesis, and particularly the former and latter directors of the SPP, Ursula Bassler and Isabelle Etienvre, respectively. Many thanks to all the members of the ATLAS Saclay group and the group leader Claude Guyot. Special thanks to the participants of the Tuesday ATLAS diboson meetings, Pierre-Francois Giraud, Samira Hassani and Ahmimed Ouraou for their advices and their availability for answering all my questions. I am also grateful to the "younger" members of the diboson group, the post-docs: Dimitra, Camilla and Joao, and former students: Joany and Meng, for all the constructive discussions we had and for the great company!

I would like to thank the ATLAS collaboration for giving me the opportunity to work for such an interesting experiment. I also thank the members of the ATLAS ZZ group for the great collaboration, the actual group convenors, Joshua Moss and Sofia Chouridou, and also the former convenor Kostas Kordas. Special thanks to Vasiliki Kouskoura for helping me on my first steps on the aTGC studies, to Joshua Moss for introducing me to the data-driven background estimation method and to Jochen Meyer for all the interesting conversations we had on the electroweak corrections. I also acknowledge and thank the ATLAS group of Thesaloniki, and particularly Chara Petridou for inspiring me to explore particle physics and for encouraging me to pursue a PhD.

I would also like to thank Lucia Di Ciaccio and Emmanuelle Perez for being my referees, and for their constructive comments and suggestions. I also thank Stéphane Lavignac, Georges Mikenberg and Fabien Zomer for composing my thesis committee.

I also thank my family who, even though many kilometers away, was always there when I needed support. Finally, my heartfelt thanks to Manos for his presence all these years, through both good and bad moments.